Technische Universität München

Fakultät für Physik

New magnetic phases under extreme conditions in transition metal compounds

Pau Jorba Cabré, M. Sc.

Vollständiger Abdruck der von der
Fakultät für Physik der Technischen Universität München
zur Erlangung des akademischen Grades eines

Doktors der Naturwissenschaften (Dr. rer. nat.)

genehmigten Dissertation.

Vorsitzender:		Prof. Dr. Frank Pollmann
Prüfer der Dissertation:	1.	Prof. Dr. Christian Pfleiderer
	2.	Prof. Dr. James S. Schilling

Die Dissertation wurde am 08.03.2021 der Technischen Universität München eingereicht
und durch die Fakultät für Physik am 01.12.2021 angenommen.

Contents

CHAPTER 1

Scientific motivation

1.1 Quantum matter

1.1.1 General Introduction

Solid state physics aims to understand the physical properties of solids (crystals, glasses, ceramics, etc) and the relation of these properties with the building blocks of matter. Although the individual components, atoms and electrons, obey the laws of quantum mechanics, many macroscopic properties of solids can be expressed in terms of classical statistical physics. The molecular (or covalent) bonding that keeps carbon atoms together to form a diamond crystal are quantum mechanical in nature. To understand covalent bonding the electron needs to be described as a wave function rather than a particle and the Pauli exclusion principle has to be taken in account. Nonetheless, the mechanical properties of a diamond can be described in terms of classical mechanics, its position and velocity are well defined, and the sound velocity through the crystal can be properly characterized and described by statistical mechanics.

Furthermore, if one were to use quantum mechanics to calculate the different configurations carbon crystals can take, we would discover that diamond is actually a meta-stable state, and that graphite is the stable structure that carbon takes at ambient conditions. Regardless of this troublesome revelation, bankers are quite confident that the diamonds they keep in their vault will not spontaneously decay into less lucrative graphite. In spite of the quantum mechanical nature of its constituents, diamond has a well defined classical state. Typical bulk samples comprise over 10^{23} atoms whereas the coherence of quantum mechanics is generally limited to a relatively small numbers of particles, therefore quantum effects are not expected to take an important role in the properties of bulk samples and limited to very low temperatures where thermal fluctuations are too small to break quantum coherence. A good example of these low temperature states is the quantum Hall effect observed in two dimensional electron systems at very low temperatures and high magnetic fields, where the conductance takes quantized discrete values.

Although the laws of quantum mechanics are well known, solid state physicists are far from

being able to describe and understand the properties of all materials. Inside a crystal, structural, orbital, electronic, and magnetic degrees of freedom may interact with each other in a complex way retrieving an intricate final state which is difficult to predict. For example, physicists where puzzled for a long time during the twentieth century because some materials like NiO which were predicted to be conductors by the electronic band theory, which accurately describes the properties of many semiconductors and metals, turned out to be insulators [1]. The theory describing these so called Mott insulators is rather complex and requires, for instance, Coulomb repulsion between electrons, and antiferromagnetic order [2].

The behavior of electrons in solids, and in particular Mott insulators are a good example where quantum effects can determine the properties of a bulk material even at high temperatures. Theoretical models and experimental observations need to be contrasted and improved in order to increase the understanding of solid state systems. Our understanding of existing theories might help to design materials with the desired properties, while the observation of new physical phenomenon challenges some of these existing theories.

In the last decades, the fascinating field of quantum phase transitions (QPT) has grown considerably. Phase transitions can be described as a drastic change in one of the order parameters of a system induced by thermal fluctuations. Good examples are the melting of ice above 0 degree Celsius (273.15 degree Kelvin), or the loss of ferromagnetic order in iron above its Curie temperature of 1043 Kelvin. Unlike thermal phase transitions, quantum phase transitions occur at absolute zero temperature under the change of a control parameter such as hydrostatic pressure, electron doping, or transverse magnetic field. At the quantum critical point (QCP), where this transition occurs, there are no thermal fluctuations, the transition is driven instead by quantum fluctuations that originate in the uncertainty principles governing quantum mechanics. Interestingly, at the QCP, the quantum coherence length becomes arbitrarily large, the individual components become entangled according to quantum physics with one another across the whole crystal. The state of the crystal cannot be defined in terms of classical physics.

Surprisingly, these quantum critical states seem to survive at finite temperatures. The study of the nature of these states has an inherent interest in itself, it offers a simple playground for quantum correlations to be studied, as an alternative to complex experimental setups needed for super cooled trapped ion systems [3]. Moreover, experimental investigations of QCP suggest that when possible, quantum criticality is avoided and instead new phases appear around the QCP. These phases emerge as consequence of the strong quantum fluctuations coupling with an available degree of freedom in the system, and have been the source of new types of order previously unknown. Not only these new types of order are a good challenge pushing to improve previously known theories, but they also constitute an unique source of new material properties that can be used in material science to potentially develop novel technology. The understanding of semiconductor physics and giant magnetoresistance have allowed some of the biggest technological revolutions of the twentieth century, with the advent of hard drives and random access memories. Similarly, newly discovered phases like high temperature superconductivity, or skyrmion lattices are expected to drastically change future technologies.

1.1.2 Quantum criticality

An extended description of quantum phase transitions and quantum criticality can be found in references [4, 5]. Following these references we summarize here the main concepts that set the theoretical framework for this thesis.

Classical phase transitions are generally classified into first and second order transitions. In both cases an order parameter, for example magnetization or lattice volume, is drastically changed across the transition. The main difference relies on the free energy landscape, while in first order phase transitions an energy barrier separates the two states, second order phase transitions are continuous, meaning that at the critical temperature no energy barrier needs to be overcome. A good example of first order phase transitions is the melting of ice, while the transition takes place the temperature remains constant and the two phases coexist, the latent heat necessary to melt ice accounts for the energy needed to overcome the mentioned energy barrier. Phase coexistence is hence a good indicator that a phase transition is first order.

Second other phase transitions in the other hand show no phase coexistence, the magnetic order in a typical ferromagnet can be continuously suppressed, in the whole crystal at once, as the temperature is increased across the Curie temperature. In second order phase transitions, the energy fluctuations go asymptotically to zero as the transition temperature is approached from both sides. Second order phase transitions are critical phenomena, the length scale and time scale of the energy fluctuations diverges at the transition temperature. At the critical point, fluctuations occur on all length scales and timescales, and the system is said to be scale-invariant. As a consequence, all observables depend via power laws on the external parameters. A set of corresponding exponents, called critical exponents, completely characterizes the critical behavior near a particular phase transition [5].

We differentiate here, classical phase transitions that occur at finite temperature, from quantum phase transitions (QPT) that occur at zero temperature. The origin of the interactions in place is quantum in nature for both cases, but the difference relies on what is driving the critical

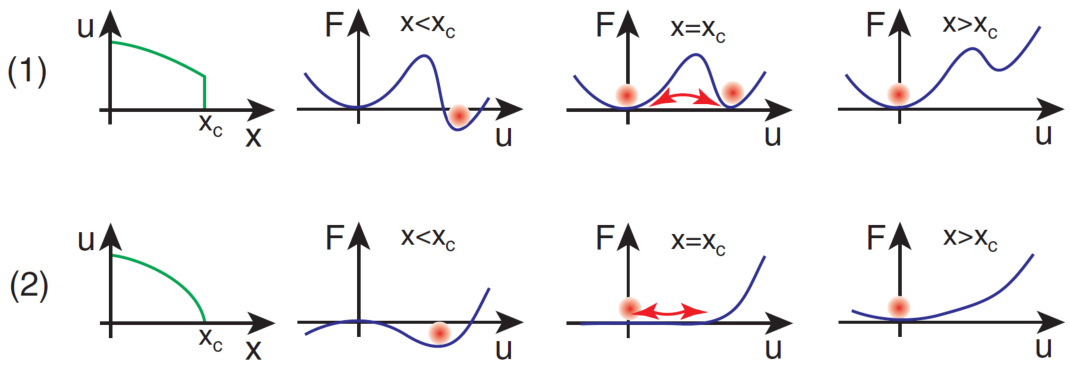

Figure 1.1: Phase transitions. Qualitative illustration of the first (1) and second (2) order behavior of the order parameter (u) and the free energy (F), respectively. The x would represent the temperature in the case of classical phase transition, and a non-thermal control parameter (magnetic field, pressure, etc.) for QPTs [6].

behavior at the phase transition. The thermal energy at a given finite critical temperature T_C would be $k_B T_C$, which is always larger than the energy scale of the fluctuations in a second order phase transition. Critical transitions at finite temperature are thus driven by thermal fluctuations.

The renormalization group, a mathematical tool that takes advantage of the scale invariance of the system at the critical temperature, is used to explain these critical phenomenon and is commonly taught as part of theoretical physics courses. An introduction to these topics can be found in references [7, 8]. In the other hand, when second order phase transitions occurs at zero temperature as a function of a non-thermal parameter g like pressure or magnetic field, there are no thermal fluctuations and the behavior is dominated by quantum fluctuations. Transitions at zero temperature are thus called QPT. Here only second order phase transitions are considered, the continuity of the transition (i.e. no energy barrier) is essential to allow quantum fluctuations to dominate. First order quantum phase transitions are, in principle, a contradiction.

Both, finite temperature and quantum critical phenomena have a similar formalism governed by a set of critical exponents. Whereas thermal phase transition are driven by the thermal quantity $t = |T - T_C| / T_C$ which goes to zero at the transition, QPT transitions are driven by a non-thermal parameter (or control parameter) g. Consider a Hamiltonian H which depends on g as $H = H_0 + gH_1$ (where H_0 and H_1 commute), there can be a level-crossing at a given value of $g = g_c$ where the ground state of the Hamiltonian changes. The correlation length ξ of the fluctuations (the length at which a cross-over between the two states occur) and its correlation time τ (decay time of the fluctuations), depend on g as follows:

$$\xi \propto |g - g_c|^{-\nu} \tag{1.1}$$

$$\tau \propto \xi^z \propto |g - g_c|^{-\nu z} \tag{1.2}$$

where ν is the correlation length critical exponent, and z is the dynamic critical exponent.

The interplay of classical and quantum fluctuations leads to an interesting phase diagram in the vicinity of the QCP. Figure 1.2 shows a typical phase diagram of the transition from an ordered state to a disordered state. As described earlier, the system can be driven to a thermally disordered state by increasing the temperature across a classical phase transition (solid line in figure 1.2), or to a quantum disordered state (i.e. dominated by quantum fluctuations) by varying a control parameter g. In an intermediate region above the QCP, a quantum critical region appears at finite temperatures where both quantum and thermal fluctuations are important. The correlation time of the quantum fluctuations diverges close to the critical point as indicated by equation 1.2 and the energy scale of the criticality increases away from the QCP as $\hbar\omega_c \propto |g - g_c|^{\nu z}$. The quantum critical regions is delimited by crossover lines (short dashed lines in figure 1.2) within which the thermal energy $k_B T_C$ is larger than the energy scale of the fluctuations.

Surprisingly, the physics in the quantum critical region is controlled by the thermal excitation of the quantum critical ground state. This extends the properties of the QCP, which is characterized by the absence of classical particle-like excitations, to much higher temperatures. None of the theoretical methods of condensed-matter physics yield an accurate description, except

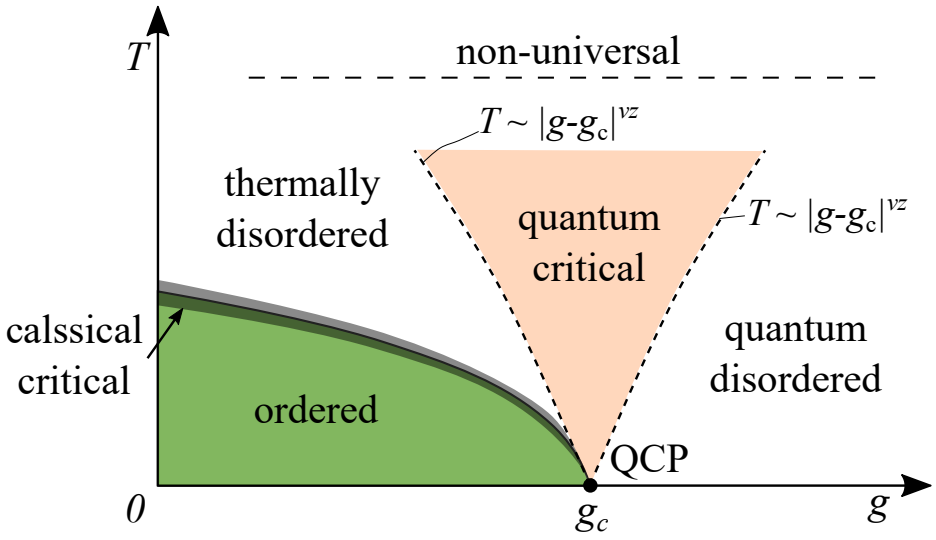

Figure 1.2: Schematic phase diagram in the vicinity of a quantum critical point (QCP). The system is controlled by the temperature T and the control parameter g. Thermal criticality (gray area) dominates the classical phase transition at finite temperatures. At g_c and zero temperature (the QCP) the transition is driven solely by quantum fluctuations. A quantum critical region appears above the QCP where thermal and quantum excitation can couple leading to unexpected new behavior. Quantum criticality breaks down when the thermal energy is close to the characteristic energies of the system (i.e. it becomes non-universal) [5].

for some special cases in lower dimensions. Moreover, unusual finite-temperature properties appear around the quantum critical region, such as unconventional power laws, non-Fermi liquid behavior, etc. This universal behavior is only observable as long as the thermal energy does not become larger than the characteristic microscopic energy scales of the problem, such as the exchange energy in magnetic systems or the Fermi energy in electronic systems.

1.1.3 Experimental examples

Experimental studies of QPT have both driven and challenged the theory of quantum criticality. For instance, a large variety of materials show non-Fermi liquid behavior as a consequence of quantum criticality arising from the suppression of a certain type of order via a control parameter [9], in good agreement with theoretical predictions. Meanwhile recent experimental findings challenge some of the basic theoretical concepts, suggesting that very weakly first order transition might have a nearly quantum critical behavior[6]. The emergence of new phases around QCPs mediated by quantum criticality is also of great interest. For instance, unconventional superconductivity arises at the expected QCP of several compounds containing f-electron elements [10].

An archetypal example would be the AFM metal $CePd_2Si_2$ under pressure, where a superconducting dome appears at the pressure range where the Néel temperature tends to zero (see figure 1.3 a). This new type of superconductivity strongly differs from conventional superconduc-

tors where the binding of electrons into the paired states that collectively carry the supercurrent is mediated by phonons, in the case of the heavy fermion superconductors it is believed that the charge carriers are bound together in pairs by magnetic interactions [11]. Although the extensive work on the pursue of high-temperature superconductors with ever higher transition temperatures has brought both great insights into the mechanisms of this phenomenon and an expanding horizon of technological applications, a complete theory of unconventional superconductivity is still not established [12].

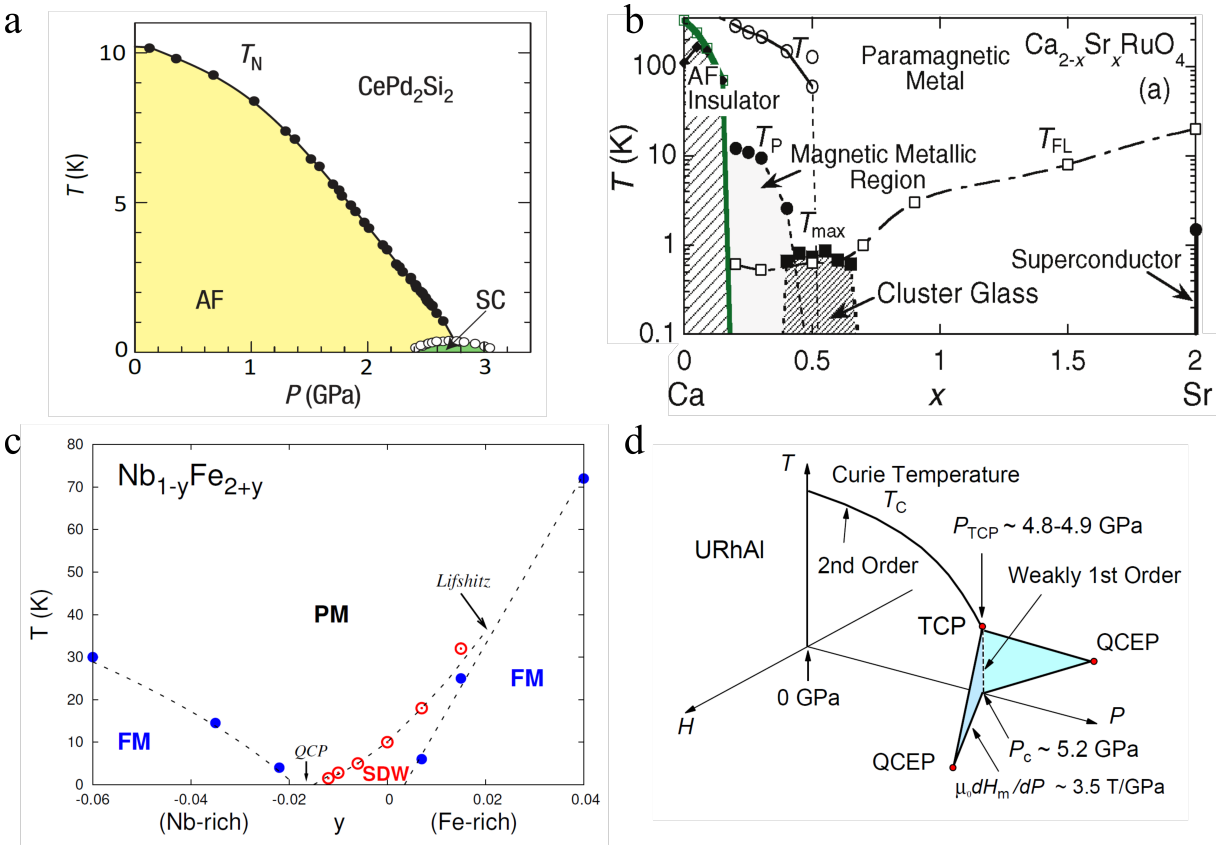

Figure 1.3: Experimental observations of QPTs. (a) Pressure phase diagram of $CePd_2Si_2$. Néel temperature (T_N) is suppressed and a superconducting phase (SC) emerges around the QCP. [13] (b) Phase diagram of $Ca_{2-x}Sr_xRuO_4$. T_{FL} indicates the temperature up to which the paramagnetic metal has a well defined Fermi-liquid behavior. T_O and T_P are structural transition temperatures and peaks in the magnetic susceptibility, respectively. [14] (c) Magnetic phase diagram of $Nb_{1-y}Fe_{2+y}$ as a function of composition y. Niobium and iron rich compounds order ferromagnetically (FM) at low temperatures, while a spin density wave order appears at compositions around the stoichiometrically pure Nb_1Fe_2. [15] (d) Schematic phase diagram of URhAl as a function of pressure (P) and magnetic field (H). The Curie temperature (T_C) of this ferromagnet is suppressed under pressure to a tricritical point (TCP) where metamagnetic wings expand with increasing field and pressure to lower temperatures down to a quantum critical end points (QCEP). [16]

Beyond superconductivity, a large variety of systems show unconventional emergent phenomenon at, or close to, QCP. For example, in the layered Ruthenate system $Ca_{2-x}Sr_xRuO_4$, a second order structural transition [17] reaches a QCP at $x = 0.5$ around which a Cluster Glass phase with strong FM fluctuations appears (see figure 1.3 b), seemingly as a consequence of orbital reorganization [14]. This very interesting compound series ranges from an AFM Mott insulator (Ca_2RuO_4) to a Hund's metal with a superconducting ground state (Sr_2RuO_4), as function of composition x. The interplay between different degrees of freedom, like in the ruthenates, increases the complexity of the phase diagram.

Not all these new phases are dome shaped. For instance, studying the system $Nb_{1-y}Fe_{2+y}$ close to the stoichiometrically pure Nb_1Fe_2 shows that while both niobium and iron rich compounds order ferromagnetically (FM) at low temperatures, the pure compound is actually not a FM. The Curie temperature decreases when the pure Nb_1Fe_2 is approached from both sides and a spin density wave (SDW) order appears between the two FM phases (see figure 1.3 c). Typically, in high purity itinerant ferromagnetic metals, where the Curie temperature is suppressed as function of pressure, a tricritical point is reached at finite temperature where magnetic order is suddenly suppressed, the transition becomes first order, and metamagnetic wings appear as a function of magnetic field and pressure [18]. As an example, the schematic phase diagram of URhAl is shown in figure 1.3 d where the critical wings expand with increasing field and pressure to lower temperatures down to a quantum critical end point (QCEP). The metamagnetism in these compounds is testimony of the strong fluctuations induced by quantum criticality [16]. Although seemingly contradictory with the previously described theory, QPT in two dimensional and three dimensional metallic systems from ferromagnetic to paramagnetic order are generically first order if the material is sufficiently clean [19].

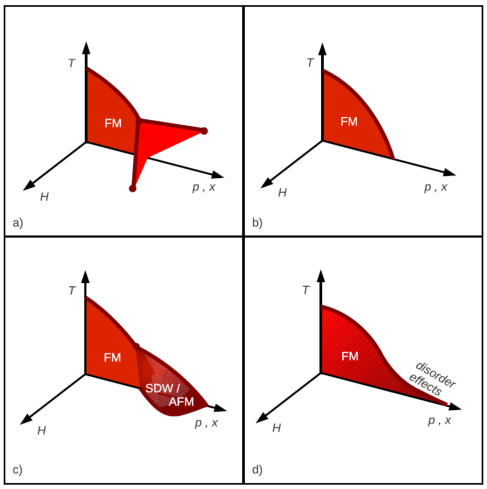

Figure 1.4: Schematic phase diagrams observed in FM systems as function of pressure/composition (p/x) and magnetic field (H) that show: a) a discontinuous transition and tricritical wings in a magnetic field, b) a continuous transition, c) a change to spin-density-wave or AFM order, d) a continuous transition in strongly disordered systems that may be accompanied by quantum Griffiths effects or spin-glass freezing in the tail of the phase diagram. Taken from [18].

These representative examples of QPT suggest that the experimental realization of a QCP is usually avoided through multiple escape routes. Brando *et al.* give an overview on QPT in metallic FMs discussing numerous experimental results and theoretical predictions. They classify the different QPTs with respect to the presence and strength of quenched disorder. Clean systems generically show a discontinuous, or first-order, QPTs from a ferromagnetic to a paramagnetic state as a function of some control parameter, as predicted by theory. Disordered systems are much more complicated, depending on the disorder strength and the distance from the QPT. In many disordered materials the QPT is continuous. In other systems the transition from the ferromagnetic state at low temperatures is to a different type of long-range order, such as an antiferromagnetic or a spin-density-wave state [18].

Figure 1.4 show a schematic representation of the different ways FM order can be suppressed by a control parameter. A clean suppression of the FM order with a second order phase transition decreasing down to a QCP (as seen in figure 1.4 b) is generally not realized and the systems tends to follow different escape routes. It seems that, if the degrees of freedom of the system allow it, the strong quantum fluctuations arising from the QCP drive the system to an emergent new phase which is more stable or energetically more favorable.

A good analogy can be found in a recent discovery within the investigation of the high pressure hydride LaH_{10}, which was found to be superconducting up to 250 K in the pressure range between 137 and 218 gigapascals. Classical *ab initio* structural calculations predict a complex energy landscape with many local minima yielding a low symmetry distorted structure which is incompatible with superconductivity and experimental observations [20]. By introducing quantum fluctuations into the calculation, which arise from the nature of the protons involved, the energy landscape strongly simplifies, and the high-symmetry Fm-3m crystal structure consistent with experiments is found to be the true ground state [21]. Figure 1.5 illustrates the impact of quantum effects into the energy landscape of high presssure LaH_{10}, highlighting the relevance of quantum fluctuations and how they can help stabilize otherwise unforeseen phases.

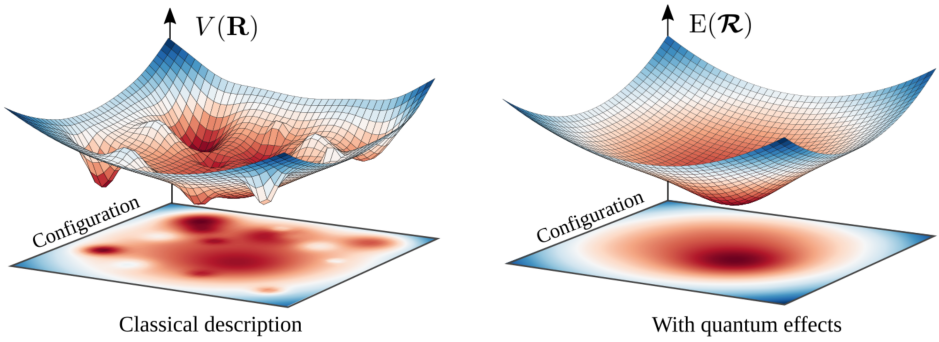

Figure 1.5: Quantum effects stabilize the symmetric Fm-3m phase of LaH_{10}. Left: Sketch of a Born-Oppenheimer energy surface $V(\mathbf{R})$ exemplifying the presence of many local minima for many distorted structures. $\mathbf{R}$ represents the positions of atoms treated classically as simple points. Right: sketch of the configurational $E(\boldsymbol{\mathcal{R}})$ energy surface including quantum effects. $\boldsymbol{\mathcal{R}}$ represents the quantum centroid positions, which determine the center of the ionic wave functions, i.e., the average atomic positions. Taken from [21].

1.2 Experimental methods

To experimentally map quantum phase transitions, several measurement methods are necessary, as well as the tuning of the control parameter through the change of a physical property of the system. Most common thermodynamic measurements (e.g. magnetic susceptibility, magnetization density, resistivity, heat capacity, etc.) are very useful to map the size of the order parameter and changes in the overall state of bulk samples. More complex spectroscopic techniques are sometimes needed, for example the ordered moment in an antiferromagnet can only be inferred from neutron diffraction experiments. As for the tuning parameters, chemical substitution, hydrostatic pressure, and magnetic field, are by far the most used. Each of these control parameters presents a series of experimental challenges which can limit the range of measurement techniques used. Given their relevance in this work, the use of hydrostatic pressure as a tuning parameter, and neutron depolarization imaging are introduced in this section.

1.2.1 Hydrostatic pressure

Pressure results from the application of a force (F) distributed over surface (A) in a direction perpendicular to the surface. Pressure P in Pascals (Pa) is defined as $P = F/A$, where the force is in Newtons and the area in square meters. This section focuses on static pressure as opposed to dynamic pressure. Although the field of dynamic compression has given recent impressive results with record high pressures using shock waves [22], the techniques tend to be destructive to the sample and the pressure can only be maintained for very short amounts of time, which make it unsuitable for many experiments. We also differentiate uniaxial pressure where the force is applied in a single direction, from hydrostatic pressure where the force is is applied isotropically onto the sample. Here only hydrostatic pressure will be described. To achieve hydrostatic pressure, a pressure transmitting medium (PTM) is used to redistribute the force equally around the sample. In real experiments, and depending on the quality (hydrostaticity) of the PTM, there is a significant contribution from uniaxial components.

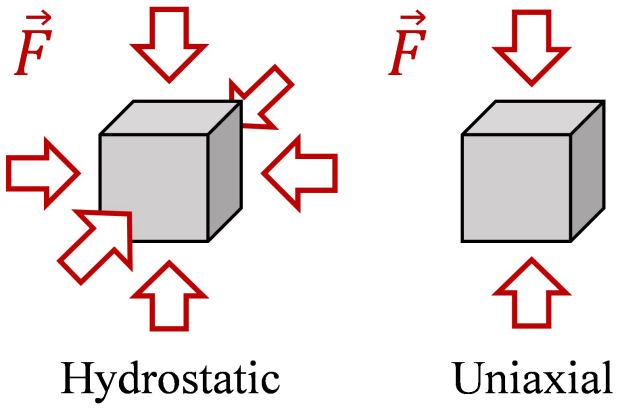

Figure 1.6: Schematic drawing highlighting the difference between uniaxial and hydrostatic pressure.

The volume of a solid is decreased by hydrostatic pressure according to its equation of state. Figure 1.7 shows the volume change under pressure for different elements, including diamond (C) and helium 3 (^{3}H), the least and most compressible substances, respectively. The equations of state of all known matter lie somewhere in between these two extremes [23]. The change of the inter-atomic distances as a consequence of the volume change can in turn potentially change different physical properties of the system. The simplest process is the increase of the internal energy which can then be spent. In materials presenting covalent bonding, pressure causes an increased overlap of orbitals broadening the energy bands and thus reducing the band gap, this effect is known as metallization. The change of inter-atomic distances can also change the strength of the magnetic interactions between ions [24]. Structural transitions also occur under pressure as a lower energy configuration is reached.

Compared to the chemical substitution, hydrostatic pressure allows for a mostly continuous and much clean tuning parameter. Chemical substitution is more likely to change more than one variable at a time, and more importantly, it might result in structural disorder which can potentially smear out the QPT [25]. Hydrostatic pressure is usually not a destructive technique, thus a large set of measurements can be done with the same sample, increasing the comparability of the data obtained. Magnetic field is also a powerful tuning parameter that can be finely tuned, but unlike hydrostatic pressure it is mostly limited to magnetic systems. Magnetic field is often used in combination of pressure as a secondary tuning parameter [16, 26].

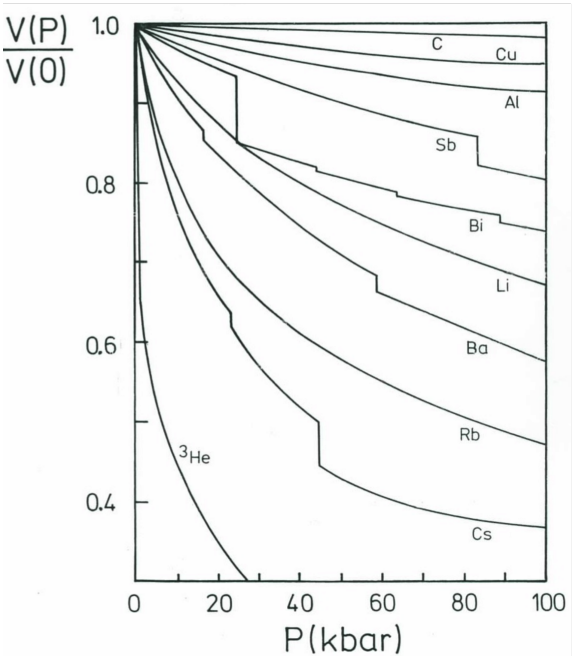

Figure 1.7: Equation of state of representative solids, showing the volume change versus hydrostatic pressure. Pressure is given in units of kbar (1 kbar = 0.1 GPa). Vertical jumps for Sb, Bi, Ba and Cs signal structural phase transformation. Taken from [23].

The main drawback of pressure as a tuning parameter is that it requires high pressure apparatus (pressure cells) to be applied which tend to be bulky and usually limit the type of

measurements that can be performed. A large variety of pressure cells have been developed since the middle of the twentieth century when high pressure physics became an important part of experimental physics as recognized by the concession of the 1946 Nobel prize in physics to Percy Williams Bridgman "for the invention of an apparatus to produce extremely high pressures, and for the discoveries he made therewith in the field of high pressure physics". The book by Mikhail Eremets, "High pressure experimental methods" [27] describes the design and use of the most common high pressure cells, as well as some of the measurement techniques adapted to these cells.

Pressure cells designs can be divided into two general groups, closed vessel cells and opposite anvil cells (figure 1.8), although some specialized designs fall somewhat in between. The first group is characterized by having an enclosed cylindrical sample space, where pressure is usually applied by pushing a piston into it. These cells typically offer a large sample volume but a limited pressure range, 2 - 4 GPa depending on construction material. In opposite anvil cells, two anvils are pressed together squeezing a thin disc of a hard malleable material (gasket) into which the sample space is enclosed. This second overall design allows for much higher pressures to be achieved, mostly due to the fact that the anvil material is working mainly under compression, and very hard materials (diamond, WC, sapphire) can be used which have a much larger compression yield strength than tensile yield strength. Moreover, the gasket is supported by the anvils (being squeezed), which adds additional forces (e.g. friction), at small thicknesses these forces dominate allowing the gasket material to hold pressures beyond its intrinsic mechanical properties [27]. The maximum pressure range achievable with opposite anvil cells depends largely on the cell design and the anvil material. Maximum achievable pressures range from 10 GPa for Bridgman pressure cells using large tungsten-carbide (WC) anvils, to the record high 600 GPa in diamond anvil cells (DACs) using small diamond anvils with toroidal tips shaped with a focused ion beam [28].

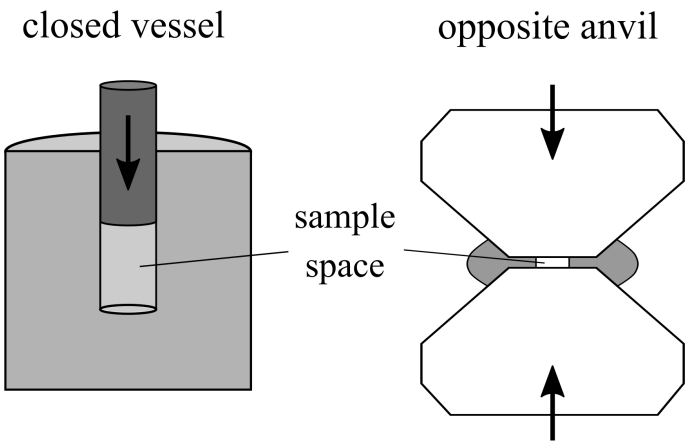

Figure 1.8: Section view of two drawings depicting the main concept of closed vessel and opposite anvil cells respectively. The force applied in the direction indicated by the black arrows builds up pressure inside the sample space thanks to the pressure transmitting medium (PTM).

To achieve large pressures bulky metallic structures, necessary to support large mechanical loads, surround the sample space limiting its accessibility. The large variety of designs does not arise solely due to a chronological evolution towards higher achievable pressures, but more importantly it originates from the need to adapt the preexisting designs to the required experiment. For example, transparent windows need to be installed in closed vessel cells to allow for optical measurements, high thermal conductivity materials are needed for low temperature measurements, electrical leads need to be funneled into the sample space for transport measurements, and large solid angle apertures are needed to allow scattered X-rays to leave diamond anvil cells without being absorbed into the metallic body. In the following chapter, there is a section (2.1) dedicated to describe the choice, design, and use of the pressure cells developed within the framework of this thesis.

1.2.2 Neutron depolarization

Neutron scattering is a unique tool to investigate condensed matter. The properties of the neutron, namely its neutral electric charge, its mass which gives it the right proportion between momentum and energy, and its magnetic moment, make it very suitable for a large set of measurement [29]. Neutron depolarization (ND) takes advantage of two of these properties in a rather unconventional way. In a ND experiment the change of the polarization of the neutron beam (which is defined by the average projection of the neutron spins onto a quantization axis) is analyzed after transmission through a magnetic medium. During transmission, the neutron spin, and thus the polarization vector of a neutron beam is affected by the local magnetization of the medium. Additionally, neutrons have a large penetration depth across most materials (due partly to its electrical neutrality), allowing bulk samples and samples inside large pressure cells to be studied.

In the presence of a magnetic field acting as a quantization axis, neutron spins will align either parallel (spin-up) or anti-parallel (spin-down) to the field direction. The beam polarization P is defined as $P = 2f - 1$, where f is the fraction of neutrons with spin-up. In unpolarized beams, i.e. same population of spin-up and spin-down, the polarization is zero. A fully polarized beam, with only spin-up neutrons, is defined by a polarization $P = 1$. A neutron polarizer is an instrument that absorbs mostly neutrons with one spin state, while allowing more neutrons with the other spin state to go through, giving the transmitted neutron beam a finite polarization ($0 < P \leq 1$).

To maintain the quantization axis and thus the neutron polarization, a magnetic field, at least one order of magnitude larger than the earth's magnetic field (i.e. a guide field circa 0.5 mT), has to be maintained along the neutron path. If the change in direction of the guide field along the neutron path is slow in comparison to the Larmor precession in that given field, the neutron polarization will simply follow the new field direction. On the other hand when a neutron non-adiabatically enters a magnetic field (i.e. the field changes faster than the Larmor period in that field), its magnetic moment undergoes Larmor precession around the new field direction [30].

It is important here to differentiate between two cases: (1) When a neutron beam enters non-adiabatically a homogeneous magnetic region with a beam direction different than the local guide field, as inside a Mezei flipper [31], it results in a net precessional motion of the beam

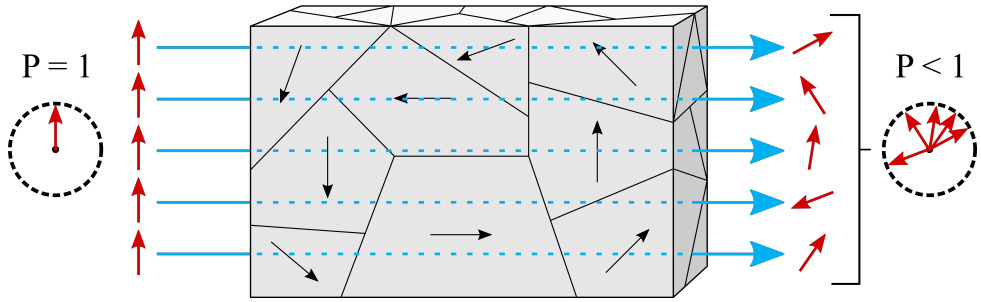

Figure 1.9: Schematic visualization of the depolarization process of a neutron beam by a magnetically inhomogeneous sample. A bulk sample is partitioned in different areas where the arrow indicates the direction of the magnetic field in the area. This configuration is similar to magnetic domains inside a FM. Different neutrons with the same initial polarization sense different magnetic fields along their paths and experience different spin precession, the overall polarization vector after transmission is thus reduced.

polarization (all neutrons at once) around the new field direction. (2) When a neutron beam enters a region with magnetic inhomogeneities, i.e. small regions with a local magnetic field in various different directions than the average magnetic field, different neutrons with different neutron paths will precess in different directions, resulting in a shortening of the beam polarization vector called depolarization. This process is illustrated in figure 1.9 and is the result of the spatial (and time) averaging of several neutrons. Single neutron detection is technically not feasible, state of the art spatially resolved ND measurements, neutron depolarization imaging (NDI), have a spatial resolution not better than 0.1 mm [32]. In ND experiments, both rotation and reduction of the polarization vector can take place, nevertheless this section will focus on the second case being the most relevant for the experiments undertaken during this thesis.

Changes in the neutron spin direction can take place if the length scale of the magnetic inhomogeneities is bound between the upper limit of non-adiabaticity, i.e. small/fast enough that the magnetic field change felt by the neutron along the path is considered non-adiabatic, and the lower limit of the coherence volume. As a quantum mechanical particle, the position of the neutron is derived from its wave-function and is expressed as a probability distribution, the magnetic field sensed by the neutron is thus a pondered average over this distribution. The coherence volume of a neutron beam encloses a volume which is comparable to the volume expansion of the probability distribution. This volume has an ellipsoidal shape as the coherence length along the beam direction (longitudinal coherence length L_l) is different from the one in the transverse direction (transverse coherence length L_t). For a neutron source with a given wavelength λ and a wavelength spread $\Delta\lambda$, the longitudinal and transverse coherence lengths, respectively, can be approximated by:

$$L_\mathrm{l} = \frac{\lambda^2}{\Delta\lambda} \qquad (1.3) \qquad\qquad L_\mathrm{t} = \frac{\lambda}{\Theta} \qquad (1.4)$$

where Θ is the angle sustained by the source as seen from the sample (i.e. divergence) [33]. The order of magnitude of the length scale bounds within which neutron depolarization can occur can be calculated for usual experimental conditions. For the upper limit, magnetic inhomogeneities with significant changes in the field direction taking place within few millimeters can already be considered non-adiabatic. In the other end of the spectrum, typical coherence

lengths, within which the magnetic field is averaged, are in the order of tens to hundreds of Angstroms. Meaning that the strong variations of the magnetic field strength H at the atomic scale are somewhat averaged over a larger volume. This is one of the reasons why paramagnets and antiferromagnets do not depolarize a neutron beam. Nonetheless a large amount of magnetic textures show inhomogeneities within the mentioned bounds and can be probed with ND. Changes in the polarization state of the transmitted neutron beam have been used to probe the magnetic domain distribution inside a ferromagnet [32, 34, 35], magnetic islands in spin glasses [36, 37], or the magnetic shielding effect outside a superconductor [38, 39]. These texture can easily be differentiated by their characteristic behavior under applied field.

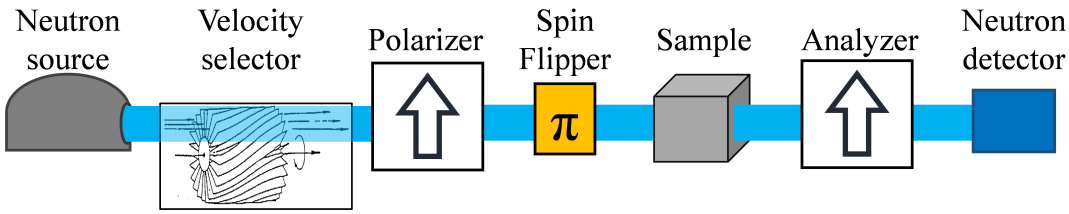

Figure 1.10: Schematic description of a neutron depolarization experiment highlighting the relative position of the different components. The neutron beam going from left to right is depicted in light blue.

Figure 1.10 shows a schematic description of the ND experiments performed in this thesis. Similarly to an optical experiment, two polarizers are needed to study the changes in the beam polarization, one is placed before the sample (polarizer), and the second one is placed after the sample (analyzer). Polarizers have their internal magnetic guide field by construction, but a set of guide fields, usually made with electromagnetic coils or permanent magnets, is needed to cover the whole path between the polarizer and the analyzer. A spin flipper placed after the polarizer can turn the neutron polarization by π (flip the spin from spin-up to spin-down and vice versa) when turned on. The beam intensity measured at the detector is a combination of the loss of beam polarization and the nuclear absorption. By combining the neutron intensity measured with the spin flipper turned off $I_\uparrow$ (spin-up) and with the spin flipper turned on $I_\downarrow$ (spin-down), the nuclear absorption of the sample can be removed and the beam polarization P can be obtained experimentally:

$$P = \frac{I_\uparrow - I_\downarrow}{I_\uparrow + I_\downarrow} \tag{1.5}$$

This value is then normalized to 1 to account for the efficiency of the polarizers and the flipping ratio of the spin flipper. Commonly used spin flippers, like the Mezei flippers, use electromagnetic coils to turn the beam polarization via Larmor precession. A monochromator is necessary to flip the neutron polarization efficiently, as neutrons with different velocities would spend different times inside the spin flipper and gather a different phase shift in their spin rotation. Depending on the experimental requirements, different monochromators can be used. Here a velocity selector is used, it acts as a band pass filter allowing neutrons with wavelength spread $\Delta\lambda$ of 10 % around a nominal value λ to go through. In comparison to monochromators using Bragg scattering, the beam intensity is at least an order of magnitude higher when suing the velocity selector, while the flipping ratio of the spin flipper is still very good. Moreover,

having a defined neutron wavelength is also necessary to be able to quantitatively analyze the measurements.

Assumptions on the nature of the magnetic inhomogeneities have to be made as a first step to theoretically model the depolarization process through a sample. For instance we focus here exclusively on ferromagnetic samples. The decay of the neutron beam polarization due to a ferromagnet was first described theoretically in a publication by Halpern and Holstein in 1941, "On the passage of neutrons through ferromagnets" [34]. To describe the changes in the neutron spin direction $\vec{S}$, they use the so-called Larmor approach where the quantum mechanical operators acting on the neutron spin can be reduced to the Larmor equation:

$$\frac{\mathrm{d}}{\mathrm{d}T}\vec{S} = \gamma\vec{S} \times \vec{H}(r) \tag{1.6}$$

where γ is the neutron gyromagnetic ratio. Different magnetic domain configurations are then assumed, most notably Ising and Heisenberg ferromagnets. The successive Larmor precessions in these domains are treated statistically to give the ratio between the beam polarization before and after passing through the sample, with respect to the relevant parameters of the problem. In order to do this approximation, 3 assumptions are made: (1) The size of the regions over which the magnetic field suffers appreciable variation (μm) is much larger than the wave length of the neutron (2 - 5 Å). This circumstance allows to treat the positional motion classically. (2) The quantity determining the neutron polarization as measured in the transmission experiments is the expectation value of the spin, i.e., the classical observable. (3) Since the equation is linear in the operators (all the other quantities being ordinary numbers), no error is incurred by replacing each by its expectation value [34].

A purely quantum mechanical approach also exists, it is called the scattering approach as it also describes, in addition to the neutron spin rotation inside a given domain, the change in polarization due to very small angle scattering, still reaching the detector (i.e. smaller than the beam angular width), which occurs at the domain boundaries [40, 41]. Upon a detailed analysis, including stray fields outside magnetic domains, Larmor and the scattering approach are generally equivalent and retrieve the same equations. A notable exception would be in the presence of the helical order, in this case one of the terms of the equation of the scattering approach becomes non-zero making it substantially different than the equation obtained with the Larmor approach [42]. As the focus is marked on neutron depolarization due to ferromagnets, the Larmor approach will be used henceforth.

The equations derived by Halpern and Holstein on the neutron depolarization due to a Heisenberg ferromagnet are sufficient to interpret qualitatively ND experiments performed in this thesis. Two main assumptions are made on the magnetic domain distribution. First, the domains walls are ignored. Secondly, the magnetic field within a magnetic domain has the same amplitude B (i.e. saturated magnetization) for all domains, is random in direction, but constant both in magnitude and direction within each magnetic domain. Moreover, the domain directions are distributed isotropically, and the field average over the sample is zero, as it is in a bulk Heisenberg ferromagnet at zero magnetic field. As a neutron traverses the sample at a velocity v it spends an average amount of time τ inside each domain of average size δ with $v = \delta/\tau$. Successively applying equation 1.6 across the whole sample thickness d, which is assumed to be much larger than the mean domain size δ, i.e. large number of domains, two different solutions

are found at two distinct regimes. The first regime defined by $\tau \ll \frac{1}{\gamma B}$, and more commonly realized experimentally, is when the time spent inside a domain is much smaller than the period for a full Larmor precession inside this domain (i.e. small spin rotation). In this case, the final beam polarization P_f can be expressed with respect to the initial beam polarization P_0 as:

$$P_\mathrm{f} = P_0 \exp(-\frac{1}{3}\gamma^2 B^2 d\delta/v^2) = P_0 \exp(-\frac{1}{3}\gamma^2 B^2 d\tau/v) \tag{1.7}$$

In the second regime defined by $\tau \geq \frac{1}{\gamma B}$, where the time spent inside a domain is larger than the period for a full Larmor precession inside this domain (i.e. large spin rotation) the equation obtained is much simple:

$$P_\mathrm{f} = P_0 \exp(-\frac{d}{\delta}) \tag{1.8}$$

In the case of large spin rotation, as we have assumed that there is a large number of domains (i.e. $\delta \ll d$), the polarization decreases rapidly to zero at the transition temperature retrieving an almost step-like function. This second case can be considered a limiting case of the first one where the depolarization is very strong, indeed when the product $\tau\gamma B$ is large, the term in the exponent of equation 1.7 becomes also large, retrieving a step like function.

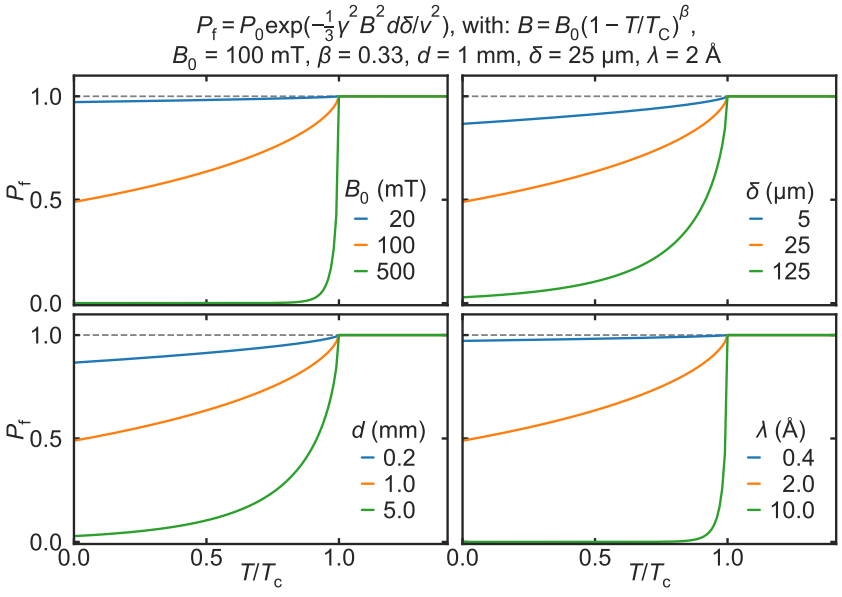

Figure 1.11: Temperature dependence of the final beam polarization P_f through a ferromagnetic sample, for different experimental and parameters calculated with the equation 1.7. The temperature dependence of the magnetic field inside a domain B is taken from a 3D Heisenberg model, where B_0 is the saturated field at 0 Kelvin. The parameters indicated above (B_0, mean domain size δ, sample thickness d, and neutron wavelength λ) are used unless otherwise indicated in the legend. The horizontal dashed line indicates the initial polarization P_0 which has been normalized to 1.

The main parameters that play a role in the depolarization values are the magnetic field inside a domain, the distance traveled by the neutron across the sample (sample thickness), the

mean domain size, and the neutron velocity. In figure 1.11, the effect of these 4 parameters on the polarization profile is presented by introducing different values into equation 1.7. The depolarization depends strongly on the magnetic field inside the domain, but also in a smaller degree on the domain size. This makes ND a unique tool to investigate ferromagnetic materials. Temperature sweeps are specially suited to identify the transition temperature, as the saturated magnetization increases drastically at the Curie temperature, the neutron polarization decreases even more sharply. Moreover, if the saturation magnetization at each temperature is known, the mean domain size can also be retrieved, or vice versa. The other two parameters, sample thickness and neutron wavelength (inversely proportional to neutron velocity) are experimental parameters that can be adjusted to highlight the dependence on the sample parameters. Ideally they are adjusted to retrieve a polarization profile which is neither saturated, i.e. the sample will strongly depolarize the beam independently of the other quantities, neither too small to be resolved experimentally.

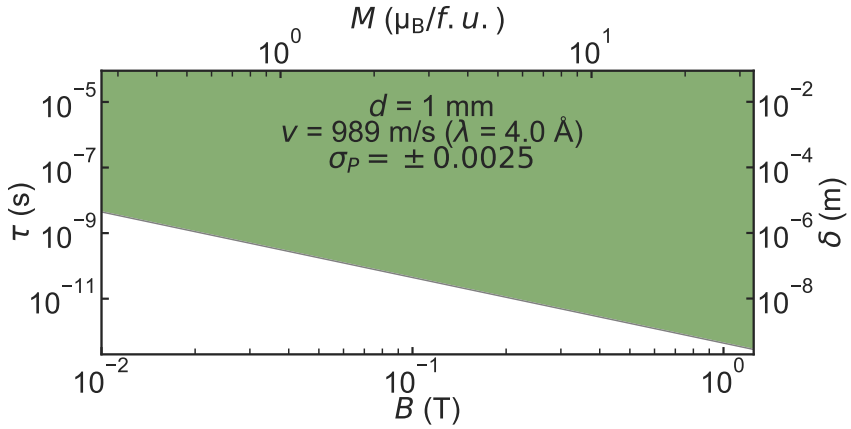

Figure 1.12: Accessible critical times τ and average size δ of magnetic domains by ND (in green) depending on the strength of the saturated magnetic field. Equation 1.7 is, the sample thickness d and neutron velocity v is fixed, the detection threshold is set to a polarization drop of at least 0.25 %. The magnetic field B is also expressed as ordered moment M for the particular case of $HgCr_2Se_4$.

Note that equation 1.7 is also valid for fluctuating domains where the field direction is constant only within a mean time τ [34] but random otherwise. ND has been used to study critical fluctuations around the Curie temperature of a FM retrieving the dynamic properties of the system [43]. Indeed the theoretical treatment of the magnetic domain inside a FM can be extrapolated to fluctuating ferromagnetic domains around thermal or quantum criticality, where the mean time τ and the mean domain size δ can be interpreted as the correlation length and correlation times, respectively. Figure 1.12 shows what is the time or length scale of magnetic inhomogeneities that can be resolved by a ND experiment depending on the strength of the magnetic field inside the domain (i.e. strength of the ordered moment) when the detection threshold is set at 0.25 % of the incoming beam polarization. The fastest accessible correlation times range from a few picoseconds (10^{-12} s) to a few nanoseconds (10^{-9} s) depending on the strength of the magnetic field inside the domains. The accessible length scales covers a large range from macroscopic dimensions down to a few nanometers, making ND somewhat a complementary technique to small angle neutron scattering (SANS).

1.3 Goals of the thesis

The first goal of this thesis and what has driven most of the technical developments undertaken, is to follow the suppression of the Curie temperature under hydrostatic pressure in the FM semiconductor $HgCr_2Se_4$. This compound is the member of the chromium spinel family (ACr_2X_4 with A = Zn, Cd, Hg and X = O, S, Se) with the largest lattice parameter [44]. Chromium spinels show diverse magnetic ground states mostly due to the competition of the AFM exchange between the Chromium ions and the FM superexchange mediated by the X nonmagnetic atoms [44–46]. While the AFM exchange increases with smaller Cr-Cr separation, the FM superexchange remains almost unchanged. $HgCr_2Se_4$ orders ferromagnetically below 105 K, and for moderate applied pressures, the Curie temperature decreases at a constant rate of 10 K/GPa [24]. This linear suppression of transition temperature was recently confirmed and extended up to 1.8 GPa via vibrating sample magnetometry (VSM) under pressure [47]. A simple extrapolation of this trend places a possible QCP around 10 GPa. The study of the high pressure magnetic phase diagram of $HgCr_2Se_4$ will increase the experimental examples of QPT of local moment FMs. Moreover, hydrostatic pressure is a clean tuning parameter in comparison to chemical substitution, this study can reveal interesting insights into the competing magnetic interactions in the chromium spinels as the lattice parameter is varied continuously without changes in the chemical composition.

Ca_2RuO_4, one of the end members of the series shown in figure 1.3 b, has recently been the object of renewed interest due to its unusual transport properties. This AFM Mott insulator appears to be at the verge of a structural instability which makes it very susceptible to chemical substitution [48, 49], hydrostatic pressure [50, 51], or even electrical current [52, 53]. Pressures as low as 0.5 GPa are sufficient to suppress AFM order, and a metallic FM phase with an apparent dome shape appears at higher pressures [54]. AFM order can also be suppressed with current densities j as low as 1.3 A/cm^2. Interestingly, despite being two very different control parameters, pressure and current seem to drive the system through similar structural transformations [55, 56]. In search of a better understanding of the interplay of the structural, magnetic, and electronic degrees of freedom in Ca_2RuO_4, we aim to study the high pressure FM phase with help of neutron depolarization measurements, and changes in the temperature dependence of the magnetization and resistivity as function of current density. Although similar measurements have already been performed, we expect to obtain unique insights by exploring the high pressure FM phase with a new probe, and extending the current density measurements to lower temperatures.

In order to successfully map FM phases to pressures up to 10 GPa, two main technical challenges had to be faced. First, a pressure cell capable of routinely reaching pressures in excess of 10 GPa had to be designed and constructed. Secondly, the strength of the saturated magnetization (i.e. the order parameter) of the sample inside this pressure cell had to be measured. Chapter 2 describes in detail the technical improvements undertaken as part of this thesis. Diamond (and moissanite) anvil cells fitting the experimental constrains of the problem at hand, have been designed, constructed, and characterized. These type of cells are able to achieve very high pressures, but offer a very limited sample space with thicknesses typically below 100 µm. In prediction of a strong reduction of the neutron depolarization signal due to limited sample thickness as deduced from equation 1.7, a module with focusing neutron guides was also built in parallel to enhance the resolution of neutron depolarization measurements.

CHAPTER 2

Technical Developments

2.1 Diamond Anvil Cells

This section describes the technical developments in high pressure instrumentation that have been implemented to reach the necessary pressure range for the studies presented in this thesis. First, the choice of diamond anvil cells as the more suitable pressure cell type for the problem at hand is addressed. Then, the different cells used in this thesis are described, and a short account of their performance is given. The most relevant construction and utilization details are also explained. Finally, a detailed account on the low temperature behavior of the cells is given.

2.1.1 Pressure cell type

There is a wide range of pressure cells designs used to apply hydrostatic pressure to a bulk sample [27]. Choosing the appropriate pressure cell type depends on the pressure range that is targeted, the sample environment required, and the experimental techniques used to measure a given sample. All these constrains determine which design and construction materials are the most suitable.

The initial motivation for this thesis is to extend a previous study by Michael Wagner [47] up to 10 GPa to follow the expected decrease of the Curie temperature of the chromium spinel $HgCr_2Se_4$ down to very low temperatures. This pressure range is significantly high, although many different pressure devices can be used to reach pressures below 2-3 GPa, only opposite anvil type cells (see figure 1.8) are able to deliver such high pressures. Regarding the sample environment, the cells have to be compatible with cryogenic temperatures, and magnetic fields. This limits both the size and the materials used for the cells. Standard cryostats and electromagnets limit the sample space to a few tenths of millimeter in diameter. To properly cool the cells down to the lowest temperatures, the building materials must have a relatively high thermal conductivity at low temperatures, and in order to not disturb applied magnetic fields, the building materials have to be nonmagnetic (i.e. magnetic permeability close to 1).

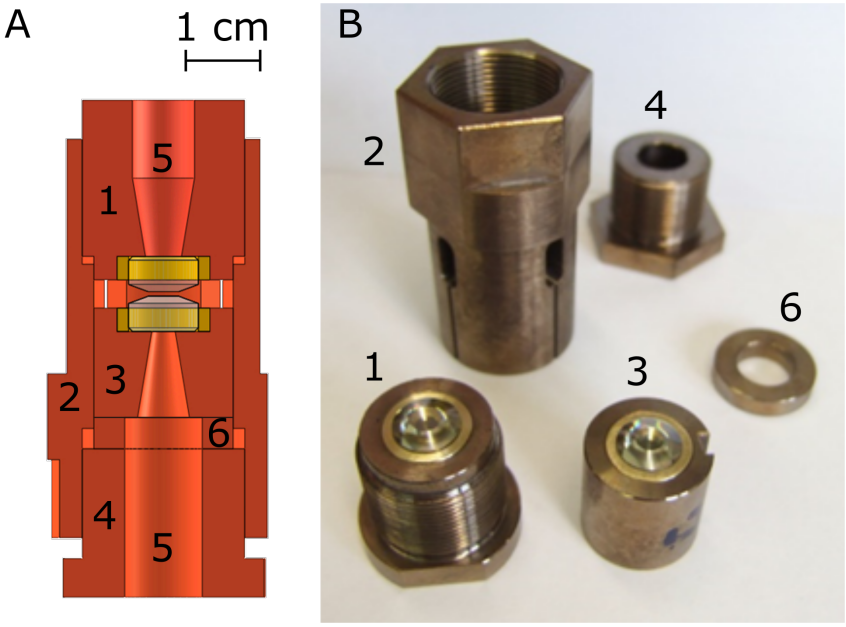

Figure 2.1: Bridgman cell mounted with large moissanite anvils. A: Drawing showing a transverse cut of a mounted cell. The bottom anvil is mounted on a nut (1) screwed into the cell body (2). The top anvil is mounted on a piston (3) that slides tightly into the cell body. The pressure is applied with an hydraulic press on the piston, and locked in place with the locking nut (4). The apertures in the cell body (5) allow for optical access to the back of the moissanite anvils on both sides. A large ring (6) is used as a washer to decrease the transmission of any torque from the locking nut to the piston. B: Photograph of the cell with the different elements.

Bridgman cells, using large tungsten-carbide anvils which are pressed against each other with very large loads, difficultly reach pressures as high as 10 GPa [57]. More importantly, Bridgman cells are almost only suitable for transport measurements. The anvils are opaque impeding any optical access, and although non-magnetic tungsten-carbide can be manufactured, these so called non-magnetic materials still have a relatively large magnetic component at low temperatures rending any magnetic induction measurement impossible. Some attempts where made at replacing the tungsten-carbide anvils by synthetic moissanite anvils in these cells in order to increase the accessible pressure range, and at the same time provide optical access to the sample. With a hardness (Knoop scale) of 3000, synthetic moissanite (hexagonal silicon carbide) is harder than sapphire (2000) and cubic zirconia (1370) but softer than diamond (5700 to 10,400 in the Knoop scale) [58]. Large, gem-quality, single-crystal synthetic moissanite anvils are available in the market. Figure 2.1 shows a picture of different parts of the modified Bridgman cell with moissanite anvils, and a drawing depicting the mounted cell.

Unfortunately, this attempts were unsuccessful and the anvils constantly failed with very little applied load. Many reasons can be given to explain this, here the two main lessons that have been learned from this attempt are summarized. First, although moissanite is an extremely hard material, only surpassed by diamond, it is far from being tough and can break easily when stress is accumulated in a small surface or an edge. Therefore, the alignment and parallelism between

the two anvils must be very well adjusted, and the piston-cylinder fit of the cell made to about 10 µm difference in diameter. Secondly, as already known for diamonds but also applicable to moissanite, the larger the anvil the higher the probability that a flaw of sufficient size exist in the anvil leading to anvil failure [59]. The anvils were made identical in dimensions as the Tungsten-Carbide anvils originally used in these cells and had a diameter of 10 mm at the base, and a culet of 3.5 mm, which is much larger than the typical moissanite/diamond anvils used in high pressure experiments.

One way to alleviate this problem would be to use supported anvils which would allow much higher pressures to be reached while keeping a relatively large sample volume. The principle of supported moissanite anvils is to force fit an anvil with slightly conical sides (circa 2°) into a matching steel ring of slightly smaller dimension. The side force provided by the the ring, strengthens the anvil, allowing it to reach far higher pressures than otherwise achievable, without breaking [60]. This solution was not suitable to us. First of all, the technical difficulty to manufacture perfectly matching pairs of anvils and rings with a conical shape is to be considered. The time needed to perfect such a design, and the elevated costs when considering the large number of anvil breaking that usually happens during the learning process, would certainly be very considerable. Secondly, the aligning mechanisms for these already large diamonds would further increase the total size of the pressure cell. Standard cryostats, where these pressure cells are intended to be used, have limited available space and the current design is already close to the limit.

Paris-Edinburgh cells are specially designed for neutron scattering techniques, achieving pressures as high as 25 GPa while still allowing for large sample spaces in the order of tenths of cubic millimeters [61]. Here the technical challenges and construction costs are comparable to the previous case. Even so, these cells are extremely large and weight between 10 and 100 kilograms, they are subsequently very difficult to operate and to cool down to cryogenic temperatures. Moreover, dedicated cryostats and magnets would have to be constructed.

Diamond anvil cells (DACs) exist in many different configurations and sizes. They are adapted to a wide variety of experimental techniques from X-ray scattering, to all sort of spectroscopic and thermodynamic measurements. DACs can also be used to explore samples in an extremely wide range of temperatures, from the millikelvin regime [62], to earth's deep mantle temperatures (circa 5000 Kelvin) achieved via CO_2 laser heating [63]. Using relatively small anvils, around 3 mm diameter and 3.5 mm height, these anvils are less prone to failure. The force is typically applied over a small surface (culet) of 1 mm diameter and smaller, thus the load needed to achieve a certain pressure is strongly reduced, decreasing the overall mechanical demands on the cell design which allows for small cells to be built. For the smaller culet sizes (below 100 µm), pressures as high as 200 GPa (megabar regime) can be achieved [64]. The main drawback of the DAC is the extremely limited sample space, in the order of 0.05 mm^3 to reach 10 GPa, which can seriously limit the signal to noise ratio for some experimental techniques. Due to the definition of pressure $P = F/A$ (load divided by area), and as diamond can only sustain a given load until it breaks, the area on which the load is applied has to be decreased in order to increase the maximum achievable pressure.

Given the previous considerations, the diamond anvil cell (DAC) is the most suitable type of pressure cell for the experiment at hand. DACs can easily reach the pressure range needed,

the design can be adapted to the sample environment required, and they are compatible with many experimental techniques. Both diamond and moissanite anvils can be mounted on the cells that have been designed, but for all the measurements discussed in this thesis the chosen anvil material was moissanite. These type of cells are called Moissanite anvil cells (MACs). At first only moissanite anvils were purchased given the smaller price per carat. As further experiments required us to reach higher pressures, natural diamonds were also purchased. Synthetic moissanite anvils are more prone to failure than diamonds, specially in presence of shear forces, and are thus less forgiving of design flaws or inexperienced users. When taking in account anvil failures, diamond becomes more cost effective than moissanite and therefore is the chosen anvil material for future measurements.

Though, less technically challenging to build than the other considered cell types, designing and building DACs is far from being trivial. There are many commercially available DACs from different companies. Buying ready to use pressure cells from a reliable manufacturer is a very convenient option to consider as it can save time and resources. A self-made design has been chosen in this case, allowing us not only to adapt the design to our needs, but also to accumulate a know how in DACs design and construction. An interesting and comprehensive article by Dunstan and Spain [59] describes the principles, design and construction of DACs.

2.1.2 Diamond anvil cell designs

First, the choice of an appropriate anvil design has to be addressed. One of the most critical dimensions of the anvil is the culet diameter. The culet is the flat top of the anvil, the part of the anvil that withstands the highest stress. The smaller the culet diameter, the higher the pressure that can be achieved before anvil failure. In order to maintain the biggest possible sample space, one has to chose the biggest possible culet size that will allow to reach the aimed pressure. Dunstan and Spain propose a formula [59], generally accepted in the high pressure community, which gives the maximum achievable pressure with a DAC for a given culet diameter (d) in usual conditions:

$$P_{max}(\text{GPa}) = \frac{12.5}{(d(\text{mm}))^2} \tag{2.1}$$

In order to avoid anvil failure, it is common practice to stay 20 % below this value. A culet diameter of 0.8 mm should therefore be sufficient to reach 15 GPa comfortably.

As discussed in the previous section, although both diamond and moissanite anvils can be mounted on the pressure cells, all experiments covered in this thesis have been performed with moissanite anvils. The maximum achievable pressure with moissanite anvils is significantly lower than what is predicted by equation 2.1 due to the lower material strength. The moissanite anvils are manufactured by Charles & Colvard. The so called standard design was chosen, as it is simple and offers a very good performance. Figure 2.2 shows a detailed drawing and 2 pictures of these anvils. Unlike natural diamonds which have either 8 or 16 facets, these anvils seem perfectly smooth. They are actually cut with a much larger number of facets and then polished. This reduces the possibility of anvil failure by removing sharp edges where stress could accumulate. The culet has an 8 degree bevel which extends outwards, this further reduces the stress at the edges making the anvils more sturdy. Beveled angles of 6 - 9 degrees are accepted as optimal

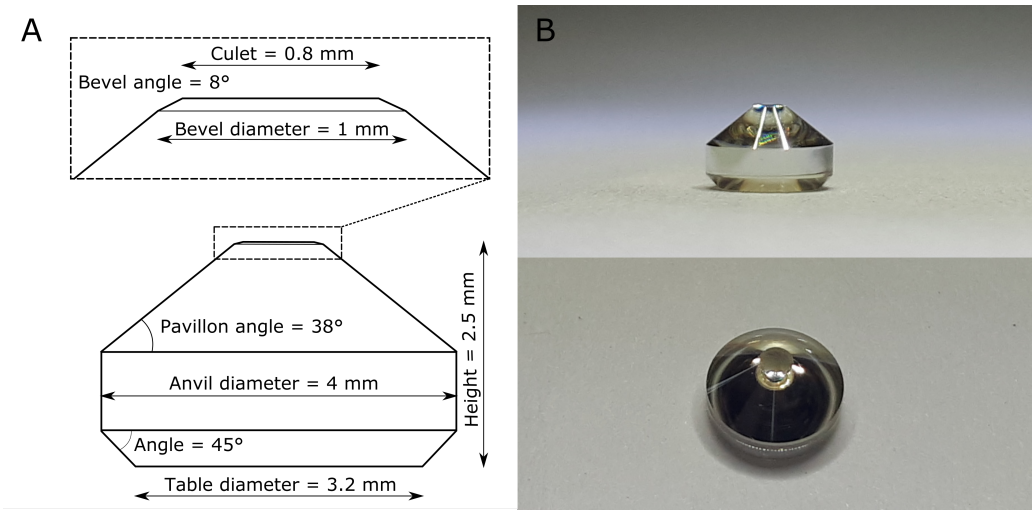

Figure 2.2: Moissanite anvils used in this thesis. A: Drawing of the moissanite anvils with the relevant dimensions. The inset details the culet area to highlight the 8 degree bevel. B: Two images of one of the anvils highlighting the high quality finish, the facets are almost imperceptible.

towards achieving maximum pressure and homogeneous pressure distribution within the sample space [27]. Beveled anvils are also recommended when transport measurements are intended as they reduce the possibility that electric wires are cut during operation. The culet surface is not perfectly flat, as revealed by concentric Newton rings when getting two anvils together, most likely presenting a slight concave curvature due to the polishing technique used.

The cell body has two main roles, apply a compressing force between the anvils, and align the anvils so that the culet faces are parallel (tilt alignment) and concentric (xy alignment). Again there is a large variety of designs and construction materials available. It is important to make the best choices for a particular experiment.

To generate a force, the two most common solutions are hydraulic/pneumatic drive and direct screw drive. It is very common to use small helium gas membranes that allow for an in situ pressure change by regulating the gas pressure delivered to the membrane. This option was discarded mostly due to size constrains, the helium pressure that can safely be delivered in such membranes is limited, and thus to achieve a given load force the membrane must cover a large area. Typical sizes for such cells are usually 50 mm in diameter which is too large to fit inside the intended cryostats. Screw driven cells are more adapted to our needs, they can be designed in a more compact way. The main drawback is that these cells have to be removed from the cryostat to change the pressure. Additionally, the pressure might change upon cooling, fortunately, these changes happen in a controlled and mostly reproducible way. Below 100 Kelvin, where the magnetic phases under study are expected to be, the changes in the sample pressure are marginal [65, 66]. The following sections deal with the pressure changes upon cooling with more detail.

From the culet area of the anvils (0.5 mm^2), and the maximum aimed pressure (15 GPa),

an estimate of the maximum load that needs to be applied can be calculated. Rounding up to account for losses due to friction, a value around 10 kN is found. This is a considerable load, therefore the parts of the cell under load and the screws that generate the force have to be sufficiently strong. Copper-beryllium (Cu-Be) is easy to machine in its unhardened state, shows great mechanical properties (similar to stainless steel) after heat aging, is non-magnetic, and shows a thermal conductivity below 100 Kelvin of at least one order of magnitude higher than stainless steel [67]. It is therefore the chosen material for the cell body. It is important to notice that beryllium can be a health hazard, specially when it is airborne, and great care has to be taken when machining it.

Using the same material for the loading screws and the cell body would be unwise, the friction coefficient between identical materials tends to be much stronger. Titanium grade 5 (Ti-6Al-4V) is used instead for the screws, it is nonmagnetic and has mechanical properties comparable to steel. Moreover, titanium has a rather small thermal expansion coefficient which will prove useful in limiting the pressure change upon cooling. As for the size of the screws themselves, the maximum load the threads and the screws can sustain depend mostly on the thread size and the yield strength of the materials. As a broad estimation, M3 and M4 titanium screws would support tensile loads up to 3 kN and 5 kN, respectively. When the load is applied by tightening the screws, the strain on the thread parts is much larger than if they were only used to keep the load in place. This substantially reduces the maximum load that should be applied on the screws. By using 4 screws one gets a maximum load capacity around 8 and 14 kN for the M3 and M4 screws, respectively.

Backing plates made of non-magnetic Tungsten-Carbide (WC) are installed in all designs. Backing plates made of a very hard material are very commonly used in DACs, they are placed between the diamonds and the cell body. Diamonds are not directly fixed on the cell body but rather glued using low temperature composite glue (stycast) to these larger backing plates. Although the table surface of the diamonds is much larger than the culet and they redistribute the load efficiently, it is still possible that the load in the back of the anvils is sufficient to deform the Cu-Be cell body and create indents in it. Tungsten-carbide backing plates are able to withstand higher loads without deformation, and further redistribute the load on an even larger surface reducing the risk of deforming the cell body. This practice also allows for an easy re-utilization of the cell body when the anvils are damaged.

To allow a proper optical access to the sample, the backing plates have an axial aperture, usually cone shaped to allow for a larger opening angle. The diameter of the aperture giving to the back of the anvils should be at least 3 times smaller than the table diameter of the anvils [59]. The backing plates have two slightly different designs. The backing plate that will be mounted on the side of the pressure cell where the xyalignment is performed have a slightly conical shape with a 5 degree angle whereas the other ones are cylindrical.

During this thesis, 3 different cell body designs have been tested. At first, 2 designs with a piston-cylinder drive were built. More recently a third design with a dowel pin drive and based on the experience accumulated with the first designs has been constructed.

The smaller design, with 22 mm diameter and 34 mm height, was meant to fit in a Physical Property Measurement System (PPMS) from Quantum Design, it is therefore called "PPMS

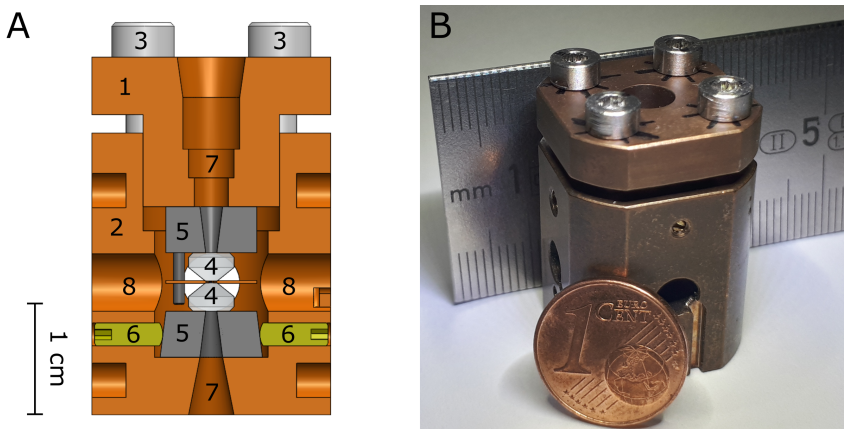

Figure 2.3: PPMS moissanite anvil cell. A: Section view of the 3D model of a PPMS cell. The top cell body (1) is pressed into the bottom cell body (2) by 4 M3 titanium screws (3). The moissanite anvils (4) are fixed on top of the tungsten-carbide backing plates (5). x-y alignment between the anvils is ensured by 4 M2 set screws (6) made of brass. Both sides of the cell body have axial apertures (7) to allow for optical access into the sample space. On the sides, 4 lateral apertures (8) allow the inspection of the gasket during operation. B: Photograph of a loaded PPMS cell with a coin and a ruler as scale.

cell". In figure 2.3 a side cut of the cell model and a picture of a loaded cell are shown. In this cell 4 M3 hexagonal socket screws are used to push the top part of the cell into the lower one. Although only moderated loads were applied, some of the screws became slightly damaged after repeated use. This design is rather simple and only lateral (x-y) alignment of the anvils is allowed. For a proper functioning of the cells the faces of the anvil culets must be parallel. Therefore both sides of each anvil and backing plates must be perfectly parallel, the surfaces where the backing plates sit have also to be parallel, and the fit between the piston (top part) and the cylinder (bottom part) of the cell body has to be very good in order to avoid the piston from tilting. Unfortunately, the sufficient machining accuracy was not reached. This cell is very prone to anvil failure and only very low pressures have been achieved. Since there has not been any experiment inside a PPMS these cells were not used beyond the test phase.

The second design, is larger with 30 mm radius and 35 mm height, it is labeled as the V2 cell, which stands for version 2. The outer body shape is based on a cylinder where 4 faces have been milled out in the sides to allow sample holders and thermometers to be easily mounted. In figure 2.4 a section view of the 3D model and a picture of a loaded V2 cell are shown. As before, a piston cylinder mechanism with the top part of the cell being pushed into the lower one with 4 screws is used. This time 4 M4 hexagonal socket screws are used to apply the load, they are sufficiently sturdy as no damage can be seen after repeated use. The main particularity of this cell, with respect to the previous one is that it accommodates a hemispherical rocker driven by 3 M2 brass screws, the hemisphere can be titled a few degrees in any direction by adjusting these 3 screws. The advantage of this construction is that it allows to adjust the parallelism of the anvils without applying load on the adjustment screws. A total of 6 of these cells have been manufactured, but due to the large machining tolerances only the 3 cells with the best piston cylinder fit are used. Most of the high pressure measurements presented in this thesis

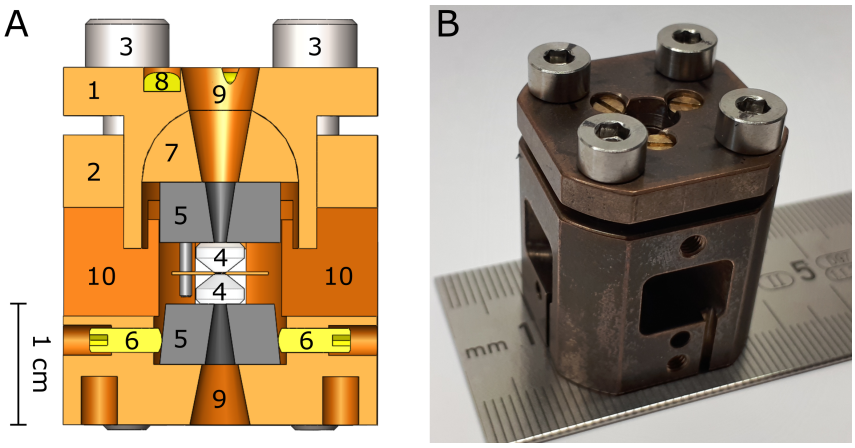

Figure 2.4: V2 moissanite anvil cell. A: Section view of the 3D model of the V2 cell. The top cell body (1) is pressed into the bottom cell body (2) by 4 M4 titanium screws (3). The moissanite anvils (4) are fixed on top of the tungsten-carbide backing plates (5). x-y alignment between the anvils is ensured by 4 M2 set screws (6) made of brass. The tilt alignment between the anvils is ensured by a hemispherical rocker (7) adjusted with the help of 3 M2 brass screws (8). Both parts of the cell body have axial apertures (9) to allow for optical access into the sample space. On the sides, 4 lateral apertures (10) allow the inspection of the gasket during operation. B: Photograph of a loaded V2 cell with a ruler as scale.

were obtained using these 3 cells. With the described 0.8 mm moissanite culet anvils, they can reliably be used up to 6 GPa, and record pressure of 9 GPa has been achieved.

The performance of this design proved sufficient for the measurements intended. Despite this success, during the operation of this cell, a few design flaws have become obvious. First of all, and as it can be read in the article of Dunstan and Spain [59], the hemispherical rocker should actually not be a half sphere, but designed such that the center of the sphere coincides with the tip of the anvil to avoid it from moving laterally when the tilt is adjusted. In the V2 cell, when adjusting the tilt alignment, the lateral alignment is lost, this makes the aligning procedure more time consuming, as the alignment process needs to be iterated several times. The second design flaw is the piston cylinder fit. It is very challenging to machine a very tight fit between the two parts of the cell body, and even when the fit is reasonably good, the piston is still able to wobble. As the screws are tightened to increase the pressure, slight differences in he load applied by the 4 screws very easily tilt the piston. As a consequence, pressure experiments have to be prematurely terminated when the gasket gets deformed asymmetrically and the sample space starts to squeeze out. In the extreme case of a perfect piston-cylinder fit, where piston and cylinder have almost the same dimension, we encounter another problem. Under load, due to the Poisson effect, the piston becomes larger and the cylinder shrinks, making the two parts jam into each other. In order to reach the original targeted pressure of 15 GPa, a third cell with a significantly different design has been built.

The third design is similar, in dimension, to the second one, with 30 mm diameter and a height of 33 mm. As it can be seen in figure 2.5, this design retains some features of the previous ones,

as the x-y aligning mechanism, but instead of using a piston-cylinder fit, 3 titanium dowel pins are used to maintain the two parts of the cell body parallel to each other. Therefore this design is called GP cell, which stands for guide pin cell. This guiding mechanism allows for a much tighter fit between the pins and the cell body as no load is applied on the pins and therefore they do not suffer Poisson expansion.

Further improvements have also been implemented in this new design. First, the hemispherical rocker is constructed such as the center of the sphere and the tip of the anvils coincide. This makes the anvil alignment procedure much faster as the tilt and x-y alignment are decoupled. Another significant change is the use of M4 fine threaded screws, this allows for a finer tuning of the pressure, and smaller torque is needed to apply the same load. A copper layer of a few micrometer has also been sputtered on the backing plates before attaching the anvils on top. This soft layer between the backing plates and the anvils should further improve the durability of the anvils by helping to re distribute any local stress due to imperfections on these surfaces. Finally, as a cosmetic detail, the Cu-Be parts have been treated with an etching solution that removes the outer oxide layer that appears after the heat aging treatment. Despite this, a layer of oxide is created on the copper beryllium over time, which beyond aesthetically considerations decreases the quality of the thermal contact when attaching the cell to a cryostat. To prevent this, the cell parts can be gold plated after removing the oxide with an etching solution. For this purpose, commercially available gold plating kits can be easily purchased at reasonable prices.

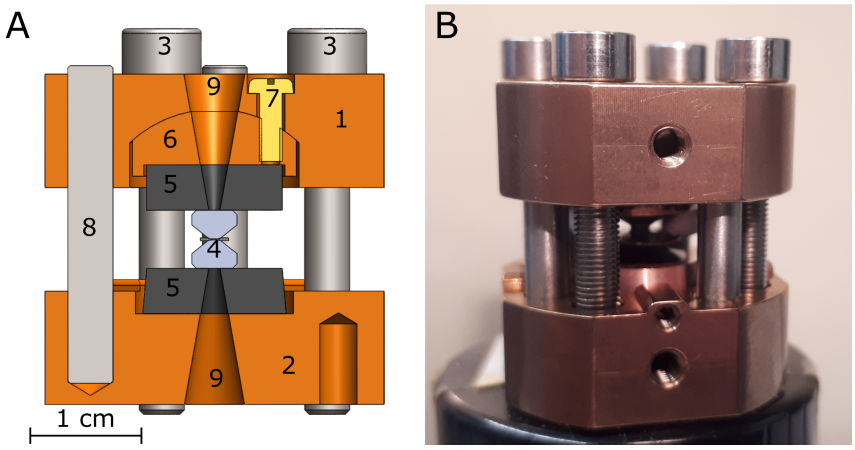

Figure 2.5: GP moissanite anvil cell. A: Section view of the 3D model of the GP cell. The top cell body (1) is pressed into the bottom cell body (2) with 4 M4 fine threaded titanium screws (3). The moissanite anvils (4) are fixed on top of the tungsten-carbide backing plates (5). The x-y alignment between the anvils is ensured by 4 M2 set screws made of brass. The tilt alignment between the anvils is ensured by a hemispherical rocker (6) adjusted with the help of 3 M2 brass screws (7). The parallelism between the two cell parts is maintained by 3 M4 titanium dowel pins. Both parts of the cell body have axial apertures (9) to allow for optical access into the sample space. B: Photograph of a loaded GP cell.

The GP cell has proved to be very reliable, and pressures up to 17 GPa have been reached when using 0.5 mm culet diamond anvils. It is clear that the improvement in the guiding mech-

anism has been crucial. Each pair of bottom and top parts of the GP cells are unique and identified with a number engraved on the side. The two parts have been drilled together to ensure that the pin holes are perfectly aligned. The holes have been drilled with a slightly smaller diameter than the pins, afterwards each pin has been polished until a perfect fit was reached. A small amount of glue is sufficient to attach the pins to the bottom part of the cell. As a perk, the new design also allows a much easier access to the sample area from the sides. A small coil set for susceptibility measurements that fits around the anvils has been designed by Anh Tong. Details on the construction and characteristics of these coil sets can be found in the Bachelor thesis report [68] performed under the author's supervision.

2.1.3 Utilization and characteristics

The procedure of aligning, mounting, and loading anvil cells is quite general. An excellent pedagogical account of the operation and use of DACs has been reported by Dunstan and Spain [69]. Only relevant aspects of the gasket preparation and cell loading will be described in detail during the following paragraphs. We give here a short summary of the main steps undertaken when preparing a DAC experiment.

First of all, the anvils must be glued with cryogenic epoxy (stycast) on the backing plates with great care of having both pieces concentric, usually a small tool is used for this purpose. One of the backing plates (with straight sides) is glued on the hemispherical rocker while the other one is just maintained in position by the x-y alignment screws. At this point the cell can be assembled carefully to avoid the diamonds to strike each other, they could be easily damaged this way. The anvils are then aligned by inspecting them carefully with a microscope while adjusting the alignment screws accordingly. The x-y alignment is done with the axis of the cell perpendicular to the microscope, the cell is repetitively rotated 90 degrees along its axis to switch from x to y point of view. The tilt alignment is usually performed by observing the anvil culets through the optical aperture along the cell axis. Newton interference fringes created when the two culets are in contact can be seen and need to be reduced to minimum. After each pressure experiment the alignment needs to be checked again.

Once the cell alignment is satisfactory, the cell can be used to indent the gasket, this procedure is very important and quite delicate. A blank gasket, with 0.25 mm thickness, is centered between the two anvils and load is applied on the cell until the desired gasket thickness is achieved (usually 100 to 80 µm for 0.8 mm culet sizes), or a similar load to the intended maximum load during the experiment has been applied. The cell is opened to take out the gasket, and the sample space can then be made into it by drilling a cylindrical hole at the center of the gasket indentation with a diameter usually half of the culet diameter. The gasket can then be carefully placed back on the anvil at the same position it was during the indent. The sample and a small ruby crystal are loaded into the sample space which is then filled with the pressure transmitting medium (PTM). At this point the cell needs to be closed quickly before the PTM flows away or evaporates. Once the cell is firmly closed the pressure can be inspected and the load is increased until the desired pressure is achieved.

For most of the experiments hardened (cold rolling and heat treatment) copper beryllium has been used as gasket material. It offers a good compromise as its hardness is similar to steel, it is

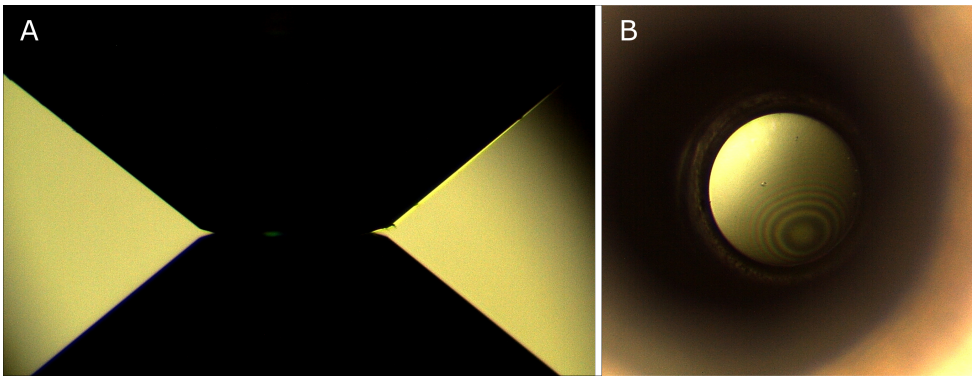

Figure 2.6: Anvil alignment. A: Picture of the two moissanite anvils from the side during the x-y alignment. B: Picture obtained through the optical aperture of the cell showing the Neuton interference rings created when the two anvils are brought together.

very easy to use and drill, and it is non-magnetic. The Cu-Be gaskets have an initial thickness of 250 µm and diameter of 8 mm. They are indented to an average thickness of 100 µm by applying load on the cell with the gasket being centered between the two anvils. The higher the maximum aimed pressure, the thinner the indentation should be made. The indentation is carried out in two steps, releasing the loading screws between the two, to avoid excessive stress. For the V2 and GP cells the screws are turned 90° and 135° respectively in each step. Each of these steps is done in a succession of small turns (circa 10°) applied on 2 opposite screws simultaneously (cross pattern) to help keeping the two main cell parts parallel to each other. The gasket thickness is then measured, further indentation steps can be done if necessary.

Next, the gasket is drilled using an electronic discharge machine (EDM) with a tungsten electrode of 380 µm in diameter. The result is a gasket with a 400 µm hole. Both the diameter of the gasket hole, and the thickness of the indent, seem to be very appropriate for culets with a diameter of 800 µm, reaching the desired pressures. When a relatively thicker sample space is needed and/or higher pressures want to be achieved, a rhenium gasket can be used instead as it is a much harder material than Cu-Be and it will be capable of withstanding higher pressures. Depending on the rolling quality, rhenium may crack when indented, rendering the gasket unusable. It is also much harder to drill, the EDM machine needs to be tuned to a different polarity and voltage, the drilling process is much longer, and the EDM electrode degrades more rapidly. Moreover rhenium becomes superconductor, with a transition temperature up to 4 K under load, which makes it unpractical to use for magnetic measurements at very low temperatures.

During our experiments 2 different pressure transmitting mediums have been used. Daphne oil was used for the initial test experiments as it is relatively easy to handle. Later, a 4:1 mixture of methanol and ethanol was used instead. The methanol ethanol mixture provides more hydrostatic conditions at low temperature [70]. Once the sample space is filled with the pressure medium, the cell is closed and a small clamping mechanism (e.g. a small vise) is used to keep a hand tight force on it while the M4 screws are tightened. This helps avoiding the sample fluid to escape or boil off. As methanol and ethanol have a high vapor pressure they tend to evaporate quickly, if the closing operation is too slow gas pockets can be trapped in the sample space, leading to a collapse of the sample space when load is applied.

The pressure is increased applying load to the cell by turning the 4 screws to a certain angle from a zero position defined as when the screw heads are in contact with the cell body but have not been tightened. This process is done in a succession of small turns (circa 10°) applied on 2 opposite screws simultaneously (cross pattern) to help keeping the two main cell parts parallel to each other. The load is increased until the desired pressure is reached. Using lubricant on the screws to reduce the friction with the cell body proves to be very helpful as most of the torque applied to the screws can be transmitted to the cell. Solid lubricants like molybdenum disulfide (MoS_2) are specially recommended.

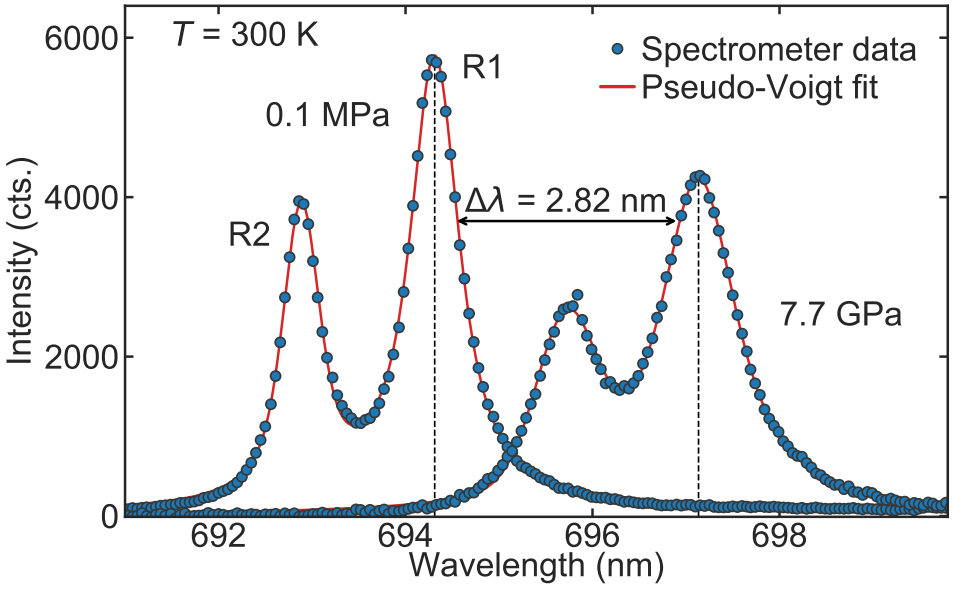

Figure 2.7: Ruby fluorescence spectra obtained at ambient pressure (left) and inside a loaded pressure cell (right). The spectrum is characterized by the R2 (lower intensity) and R1 lines (higher intensity). The exact position of the R1 lines (shown by the dashed line) is obtained by fitting the sum of two Pseudo-Voight functions. The pressure is obtained form the wavelength shift of the R1 line.

The pressure is determined using ruby fluorescence, where the pressure is extracted from the wavelength shift of the the R1 photoluminescence line of a ruby crystal. This is a widely used technique in high pressure experiments which allows for an accurate determination of the pressure. An excellent review of this technique and its applicable range has been reported by Syassen [71]. In this work, the linear ruby scale originally proposed by Piermarini et al. [72] and confirmed by Syassen to be valid up to 20 GPa, is used. The pressure increase (ΔP) is directly proportional to the wavelength shift ($\Delta\lambda$) as:

$$\frac{\Delta P}{\Delta \lambda} = 2.746 \pm 0.014 \text{ GPa/nm} \tag{2.2}$$

The accuracy of this scale (1.5 %) is much higher than the real experimental accuracy that is achieved. Depending on the hydrostaticity of the pressure medium, pressure gradients might build within the sample space where the pressure is maximum at the center and decreases out-

wards, meaning that sample and ruby might be at slightly different pressures.

Luminescence spectra on the high quality ruby crystals which are placed next to the sample are measured using a standard photo luminescence setup with a solid state laser and a small high resolution spectrometer. A camera and an optical lens are used to observe the sample space and align the ruby crystals with the laser. This setup was designed and constructed by Alexander Regnat, and is well described in his doctoral thesis [73]. A typical ruby spectrum obtained during a high pressure measurement is shown in figure 2.7. Ruby fluorescence is characterized by 2 lines, R1 and R2, the R1 line is used for pressure determination as it is the more intense, moreover the R2 line loses its intensity at low temperatures. The best fit of the photoluminescence lines is obtained by a Pseudo-Voigt function. The exact position of the R1 and R2 lines, as well as their FWHM is obtained by fitting the sum of two Pseudo-Voight functions. The pressure is then calculated form the wavelength shift of the R1 line via equation 2.2. The cell temperature is also measured, as the R1 and R2 lines also shift with temperature [71] which needs to be corrected for. Although the shift is small, depending on the conditions the cell temperature can vary greatly (usually from 22° to 28° Celsius). Note that the high pressure spectrum has a larger FWHM, this increase can be related to the increase of pressure anisotropies and pressure gradients across the ruby crystal [70].

2.1.4 Low temperature characterization

In figure 2.8 the relative thermal contraction (from 293 down to 20 Kelvin) of relevant materials used for the construction of pressure cells is shown. The temperature dependence of the thermal expansion for moissanite was not found, but we can confidently assume it is similar to diamond. The softer metals contract much more than the harder sintered materials. It is known that DACs tend to increase pressure upon cooling [66]. Given the construction of these cells, it seems intuitive that when the the cell is cooled down, due to the higher thermal contraction of the loading screws than the cell body, made of harder materials, the load of the cell will increase. Note that titanium's relative thermal contraction is close to the average between Cu-Be and WC/diamond. The choice of material for the loading screws has been made partially expecting that the overall thermal contraction difference between the cell body and the loading screws is reduced by the use of titanium screws (instead of stainless steel) and thus the change of pressure upon cooling is also reduced. The thermal coefficient changes linearly with applied load within the elastic limit [74], thus we don't expect that the load will change the relative difference between the thermal expansion of these materials.

As mentioned before, in-situ pressure determination during the measurements is not possible. The pressure is therefore measured at room temperature before and after every measurement. To extrapolate the pressure at low temperature, a characterization measurement of the pressure change is performed. To this purpose, a dedicated setup that allowed us to measure ruby photoluminescence inside the pressure cells as function of temperature has been constructed. Details of this setup are shown in figure 2.9. The sample stick of a variation temperature insert (VTI) from Oxford instruments has been customized by carefully placing a cryogenic-compatible fiber optic. The pressure cell can be mounted at the bottom of the sample stick and with the help of a small collimator, the sample space of the pressure cell is coupled to the standard photoluminescence device through multi-mode fiber optics. The VTI is installed inside a standard oxford

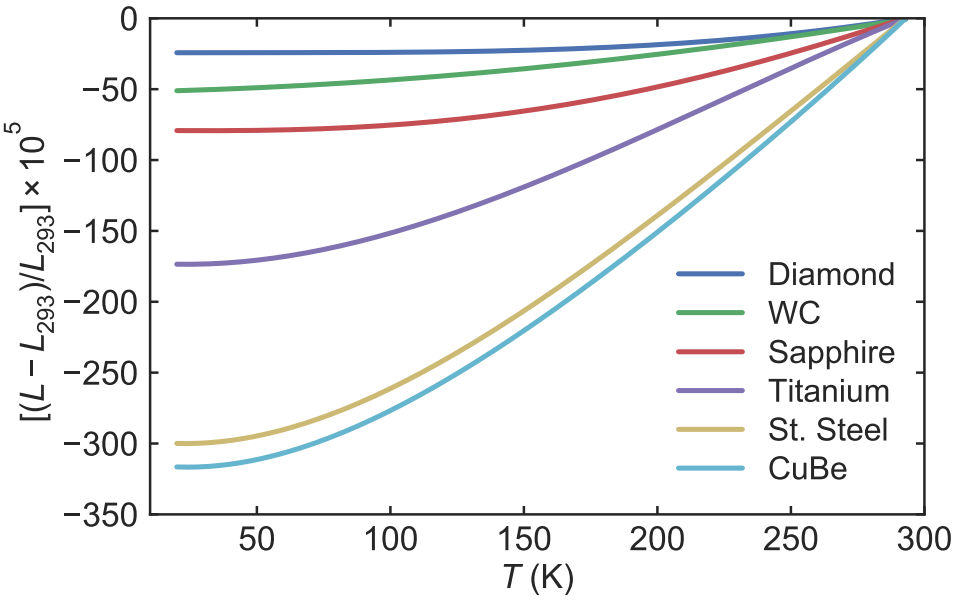

Figure 2.8: Relative linear expansion of various materials at different temperatures. The length at 293 K is used as reference. Values extracted from [75–77].

wet cryostat with a Helium bath. A cernox thermometer directly attached on the pressure cell is used to measure the exact temperature of the cell as, due to its relatively large thermal mass, large temperature gradients can exist between the cell and the temperature measured at the sample stick. More details on this setup can be found in the bachelor thesis of Florian Sigger [78] who designed and mounted the customized sample stick.

Due to the large losses (circa 50 % at each coupling point), only when the sample space inside the pressure cell is fully loaded with ruby crystals it is possible to have a measurable signal through the sample stick. The cells are loaded at a given pressure and subsequently cooled to 10 K and heated to room temperature while the ruby luminescence lines are measured every 50 K. The spectra measured during the cooling of a V2 pressure cell loaded to 2.5 GPa at room temperature are shown in figure 2.10. A single fluorescence spectrum is measured with 60 seconds of integrated intensity, then a dark spectrum obtained with the laser turned off and the same exposure time is subtracted. The final spectrum (shown in figure 2.10) is obtained by repeating this procedure 3 times and calculating the average. Again, the sum of two Pseudo-Voight functions is used to fit the spectra and obtain exact values of the R1 and R2 lines. The wavelength of the R1 and R2 lines decreases with temperature, the shift of the frequency $\nu(T)$ can be calculated as:

$$\nu(T) = \nu_0 - \alpha_\nu N(\frac{T}{\Theta_\nu}) \tag{2.3}$$

with

$$N(\frac{T}{\Theta_\nu}) = \frac{1}{\exp(\Theta_\nu/T) - 1} \tag{2.4}$$

where the values used for ν_0, α_ν, and Θ_ν, are 14421.9 cm^{-1}, 76.6 cm^{-1}, and 482 K, respectively [71]. The width of the lines also decreases with temperature making it easier to measure

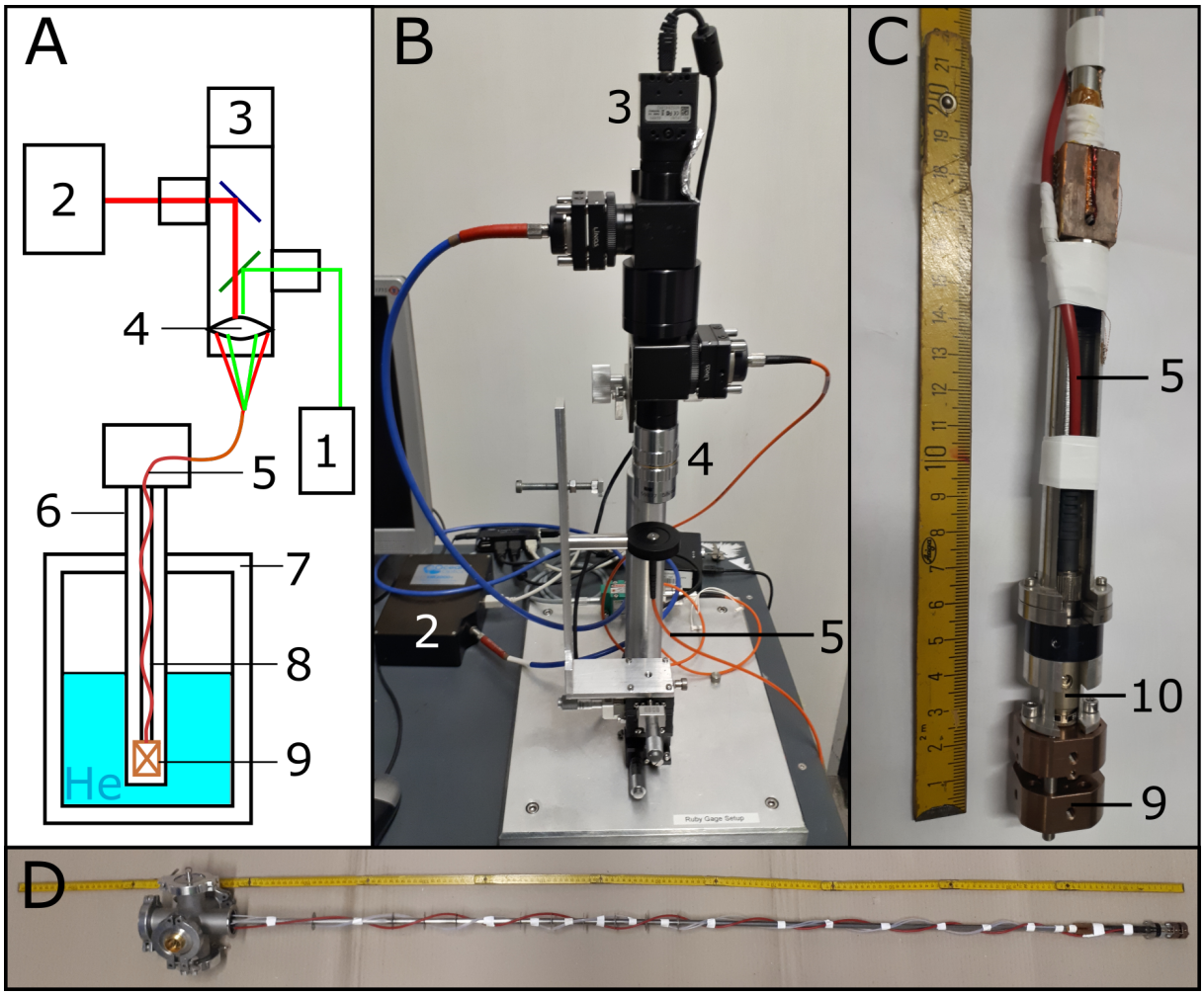

Figure 2.9: Details on the low temperature photoluminescence setup. A: Schematic drawing describing the different elements: solid state laser (1), spectrometer (2), CCD camera (3), optical lens (4), fiber optic (5), VTI (6), wet cryostat (7), sample stick (8), and pressure cell (9). B: Picture detailing the coupling of the photoluminescence setup with the fiber optic. C: Picture of the end of the sample stick, where a collimator (10) is used to optically couple the fiber optics to the sample space of the pressure cell. D: Detail of the sample stick compared with a 2 meter long ruler.

them as they become sharper. Below 50 K the line width of the peaks is mainly limited by the spectrometer resolution and residual internal strain. At 5 K the R2 line is not observed since its intensity goes to zero at very low temperatures [71]. The wavelength of the R1 ruby line changes both with pressure and temperature, fortunately, the two changes are independent from each other [79]. To retrieve the pressure in the sample space at a given temperature, it is sufficient to calculate what would be the ruby line wavelength at ambient pressure for this temperature using equations 2.3 and 2.4, and then compute the pressure from the wavelength shift between the measured value and the computed value according to equation 2.2.

In figure 2.11 the results of the characterization measurements of the V2 pressure cell are

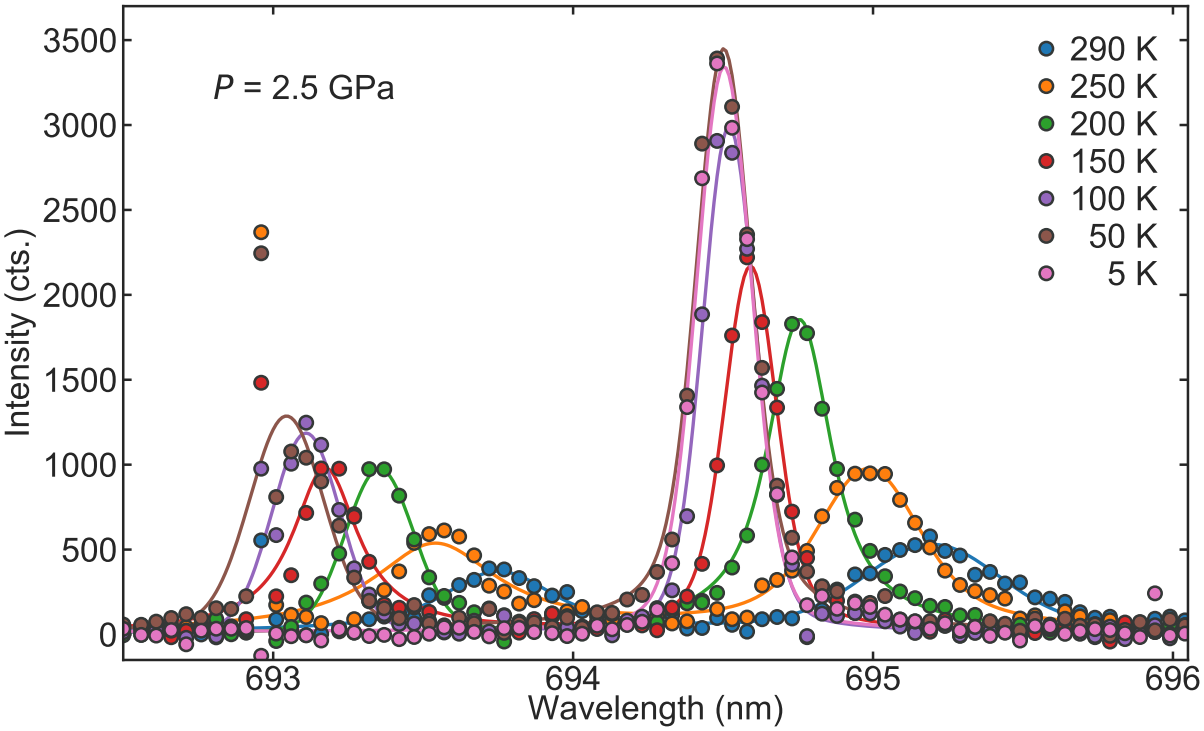

Figure 2.10: Ruby fluorescence spectra obtained with the experimental setup shown in figure 2.9. These spectra are obtained by cooling a V2 pressure cell loaded to 2.5 GPa at room temperature. The spectrometer data (colored circles) is fitted using the sum of two Pseudo-Voigt functions (colored lines). The total integration time for each spectrum is 6 minutes.

shown. The pressure cell is cooled and heated at 3 different pressures. The R1 luminescence line becomes sharper upon cooling, which makes it easier and more precise to measure at low temperatures. Interestingly, the trend is similar for the different pressure suggesting a reproducible behavior. When cooling, the pressure increases more or less linearly until it reaches a plateau somewhere between 100 and 50 Kelvin. When warming the cell, the pressure remains constant at first but between 50 and 100 Kelvin it starts to decrease in a hysteretic way, ending up at room temperature with a slightly higher pressure than the initial one. When looking at the relative change in pressure, from 300 K to base temperature, it becomes smaller for higher pressures, nominally it changes by 25 % at 1.7 GPa, 18 % at 2.5 GPa, and 15 % at 4.5 GPa.

We propose a rather simple explanation for this behavior by considering the thermal expansion of the different elements in the cell. With the values of figure 2.8, and the exact dimensions of the cell, one can compute how the different elements of the pressure cell will contract upon cooling. Figure 2.12 shows the difference between the contraction of the cell parts that are in compression (anvils, backing plate, and parts of the CuBe body) and the cell parts that are under tension (Titanium screws and parts of the bottom CuBe body), alongside the relative change in pressure measured in the experiment. An arbitrary normalization value is applied to the thermal expansion part to make it coincide with the measured data. Despite this, the trend between measured data and calculated thermal contraction is in excellent agreement. This

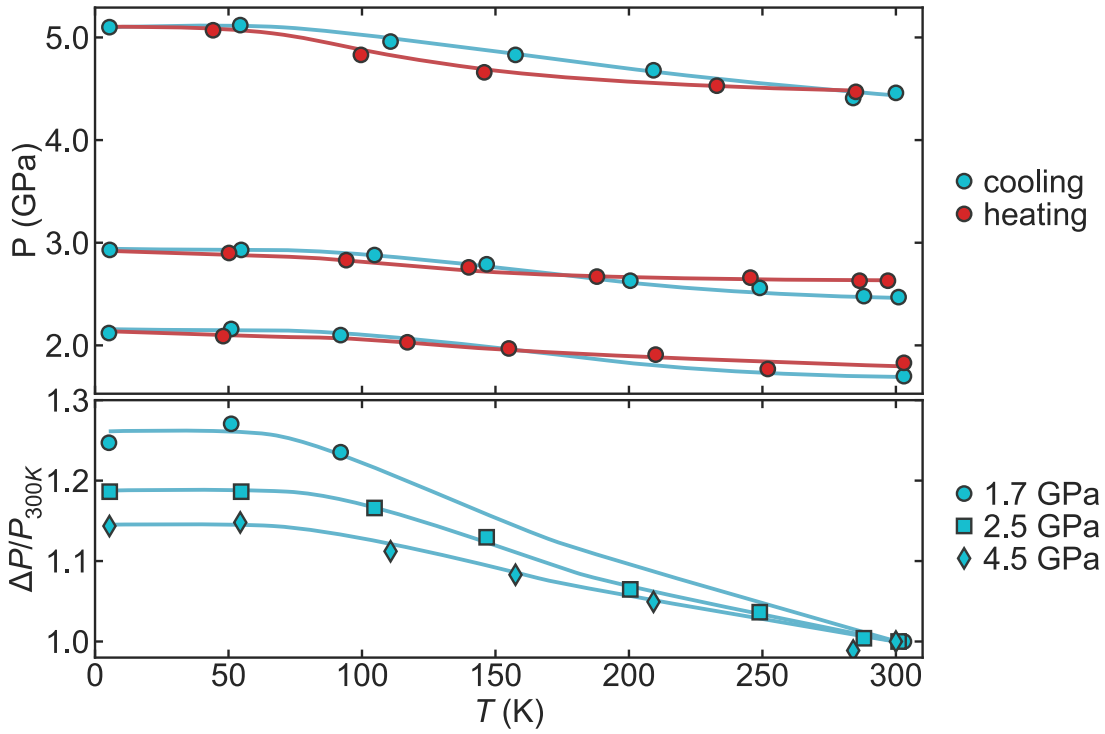

Figure 2.11: Characterization of pressure change upon cooling of the V2 pressure cells. Top panel shows the pressure values along the 3 cooling and heating cycles started at 1.7, 2.5, and 4.5 GPa. The bottom panel shows the relative change of pressure with respect to the initial room temperature measurement for the 3 cooling cycles. The lines are a guide to the eye.

strongly suggests that the difference in the thermal expansion of the various elements of the cell is the dominating factor in the change of pressure with temperature in these type of cells. Similar results are also reproduced in other studies [66]. This also explains why at low temperatures (below 70 K), where most of the phonons are frozen and the thermal contraction is minimal, the pressure changes very small.

Another relevant observation is that, when the pressure is higher, the effect of the thermal contraction becomes smaller. Figure 2.13 shows clearly how the relative pressure change drops quickly at the lowest pressures, from values above 20 % change below 2 GPa, to a more or less constant value around a 15 % increase above 2.5 GPa. It seems that stronger the load is, the smaller the effect of the thermal expansion. For the pressure and temperature range studied in this thesis (from 2 to 7 Giga Pascals, and 20 to 120 Kelvin), 15 % increase from the room temperature measurement has been used to extrapolate the in-situ pressure at low temperatures.

The hysteretic behavior observed in figure 2.11 is hard to explain. In the other hand, it is interesting to see how the pressure is always higher after the cooling cycle. After the slight load increase, parts of the gasket are deformed plastically and do not recover the initial shape, thus not recovering the initial pressure. This hysteretic behavior of the pressure when ramping up and down the load is well known [69]. It can be expected, that after each temperature

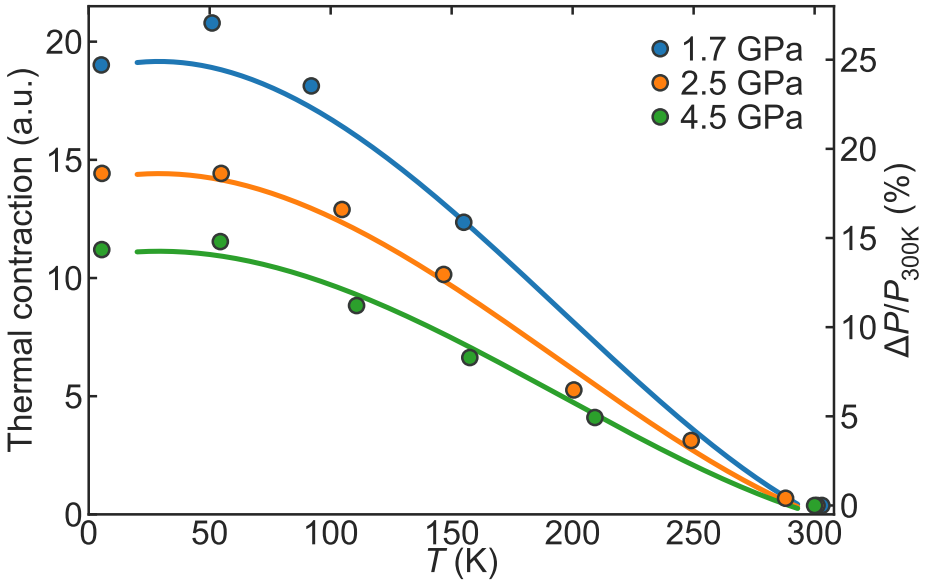

Figure 2.12: Difference between the thermal contraction of the loading screws and the cell body (solid lines), compared with the relative pressure change at 3 different pressures (circles). The difference in thermal expansion curve is obtained taking into account the dimension of the the V2 cell parts and the relative thermal expansion of the different materials shown in figure 2.8. An arbitrary normalizing coefficient is used to scale the curve to the 3 data sets obtained at different pressures (from figure 2.11).

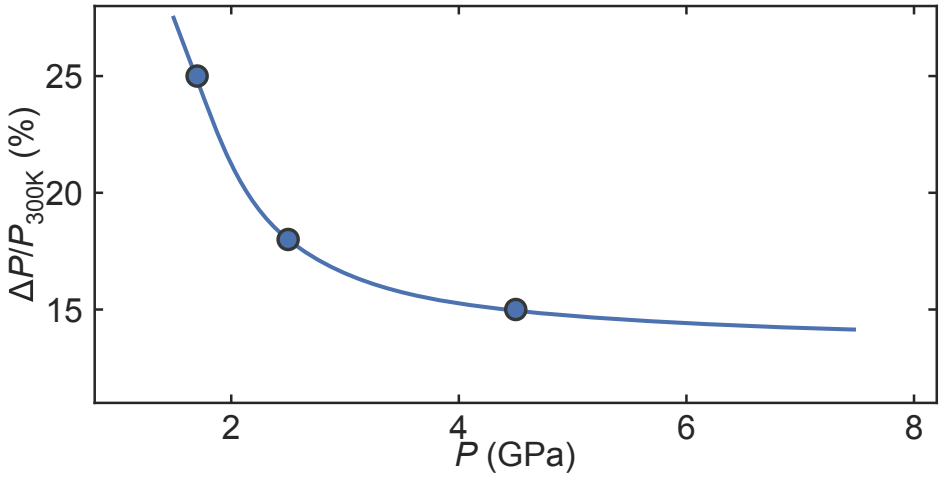

Figure 2.13: Relative change of pressure upon cooling in percent versus the applied load at room temperature. The line is a guide to the eye.

cycle the pressure change with temperature becomes smaller. This highlights the importance of controlling at all times the cooling history of the pressure cells. If the cell is warmed up to room temperature after the first cooling cycle, the pressure should be measured again before proceeding with the experiment even if the load hasn't been changed.

From the width of the R1 photoluminescence lines of ruby, relevant information on the pressure homogeneity inside the sample space can be extracted. When there is anisotropies in the sample space, giving a gradient of pressures around a central value, the width of the R1 lines becomes much wider as it is convoluted with the pressure dispersion across the large ruby crystal. This is strongly dependent on the hydrostaticity of the pressure medium. Moreover, when a liquid pressure medium freezes at a given temperature and pressure, it becomes much less hydrostatic. The higher the pressure the higher the freezing temperature. For instance, the pressure medium used here is Daphne oil, it freezes at 200 K at ambient pressure, and the freezing temperature rises to 300 K at only 2 GPa [80]. In figure 2.14 the relative change of the standard deviation σ of the Pseudo-Voigt fit upon cooling for the 3 pressure ranges measured is shown. At 4.5 GPa and low temperatures the width of the R1 lines is comparatively larger than for the other 2 pressures studied, revealing that strong pressure anisotropies can be present. Daphne oil is indeed not recommended to use for pressures above 2 GPa.

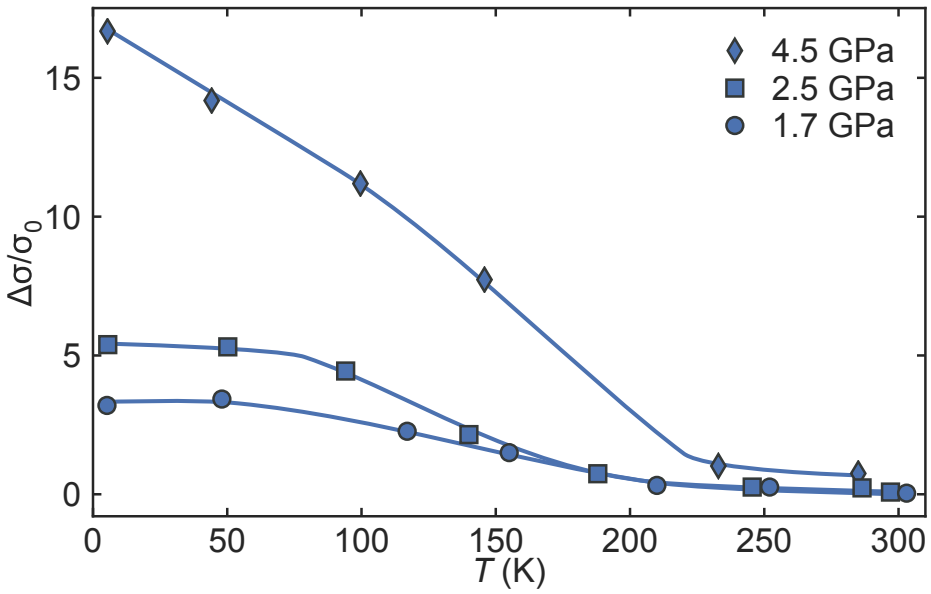

Figure 2.14: Relative change of the standard deviation σ of the Pseudo-Voigt fit of the R1 ruby luminescence lines versus temperature at 3 different pressure ranges. The lines are a guide to the eye.

2.1.5 Summary and outlook

A comprehensive account of the technical developments that have been carried out to improve the high pressure capacities available in our research group have been presented. The pressure cell designs shown are optimized to be used in cryogenic conditions with limited available space and under strong magnetic fields. Despite the relatively small size of the cells, the pressure range needed for the measurements is reached. The utilization procedure of these cells has been described in sufficient detail. The low temperature behavior of the cell has been studied thoroughly in order to predict with reasonable accuracy the pressure and hydrostaticity in the sample space at all the pressure and temperature ranges measured.

Further technical improvements could be implemented. First, as we already mentioned, the use of natural diamonds is preferable to synthetic moissanites. Although the later are more economic and have almost the same hardness as diamond, they tend to break easier specially under shear forces. Secondly, the loading screws system could be improved further. When the load is applied by tightening the screws, the cell needs to be clamped with a vise to prevent it from turning due to the torque forces. This could be avoided by using right and left handed threads on opposite corners of the cell. This way, when tightening the two opposite screws, as it is intended, the torque applied on each screw would be exactly compensated by the other one, thus not requiring the cell to be clamped. In order to improve the hydrostaticity, specially at higher pressures, is is recommended to use incompressible fluids with lower freezing temperatures. The use of 4:1 methanol:ethanol mixture is already a significant improvement with respect to Daphne oil, but when reaching pressure in excess of 10 GPa only cryogenic fluids such as argon, nitrogen, or helium, can guarantee sufficient hydrostatic conditions [70]. The use of nitrogen, with a relatively high boiling point and reasonably good hydrostaticity is preferable. A cryogenic loading system to allow the cell to be closed while being submerged inside a cryogenic liquid, so the liquid gets trapped in the sample space, is needed. One of the most simple solutions is to place the cell inside a polystyrene container, carefully fill it with nitrogen, and close the cell once it has reached liquid nitrogen temperatures. More sophisticated solutions, including high pressure chambers for liquid helium loading, are also available. Helium has the disadvantage of being strongly compressible, thus the sample space is strongly reduced under load.

Finally, a major improvement in the loading procedure, would be to use a small press to apply the load. The screws should only be used to lock the load in place, using them as driving force strongly increases the stress on all mechanical parts. Only relatively small loads are needed to load a DAC (less than 20 kN), thus large hydraulic presses commonly used for Bridgman cells are not sensitive enough. An important aspect of such press is that it should keep both sides of the pressure cell perfectly parallel when applying the load. Moreover, making the press compatible with the ruby photoluminescence setup, allowing a direct measurement of the pressure inside the cell as the load is applied, would strongly facilitate the loading procedure.

2.2 Enhanced neutron depolarization

Investigating magnetic materials under large pressures is challenging. The use of induction techniques around pressure cells becomes difficult as the small sample signal is usually lost in the background produced by the cell parts. Optical or transport techniques are also difficult to implement, and only offer indirect measurements of the magnetic state. In the other hand, Neutron Depolarization (ND) offers the possibility to investigate accurately the transition temperature of the sample, and gives an estimation of the evolution of the magnetic moment, even inside a pressure cell. Neutrons readily penetrate the cryogenic equipment, and can access the sample through the optical aperture of the cell body. The moissanite anvils, through which the beam is transmitted, have a small neutron absorption while they leave the polarization state of neutrons completely unchanged.

ND is based on pinhole optics, where a collimated beam produced by a small aperture illuminates a sample placed in front of a detector. The spatial distribution of the magnetic inhomogeneities can be obtained with neutron depolarization imaging (NDI) by using a 2D detector and a highly collimated beam. NDI can provide a spatially-resolved thermodynamic probe of a sample's magnetic state [81, 82], and potentially a three-dimensional distribution of the magnetic field [35, 83–85]. The main drawbacks of NDI are poor spatial resolution and long integration times. The highest images resolution is obtained when the sample is placed as close as possible to the detector, unfortunately in NDI a bulky neutron analyzer needs to be placed between the sample and the detector. Another way to mitigate the poor spatial resolution is to increase the collimation of the neutron beam which, subsequently decreases the neutron flux at the sample position. Moreover, the neutron beam is usually monochromatic decreasing further the neutron flux. As a consequence, in order to achieve good counting statistics with reasonable integration times, the highest resolution achieved in NDI is $\approx$ 500 µm [81, 86], which is larger than the sample space available in our pressure cells. Furthermore, measurements with particularly good statistics, i.e. long exposure times, will be needed. The depolarization signal depends exponentially on the sample thickness (see equation 1.7), considering then the 60 µm thickness limitation inside the cells, the signal amplitude is expected to drop considerably.

To overcome these limitations, a focusing neutron depolarization module has been developed where the neutron beam is condensed in a small cross section in order to significantly increase the neutron flux at the sample position. The improved statistics allows for an increased signal to noise ratio while decreasing the exposition time. As a drawback, due to the shape of the focusing guides, the imaging component is lost and only one dimensional information can be retrieved. In this particular case, as the spatial resolution is larger than the sample space inside the pressure cells, this loss of spatial resolution is thus irrelevant.

This section starts with the description of the focusing guides module, and the whole neutron depolarization instrumentation. Then, the exact functioning of the focusing guides module is explained with help of neutron ray tracing simulations. Afterwards, its operation details, i.e. alignment, measurement procedure, and data treatment, are described. The characteristics and performance of this module are also discusses. And finally, a proof of principle experiment on very small superconductors is presented.

2.2.1 Instrumental details

All enhanced neutron depolarization measurements were performed in the ANTARES beamline at the Heinz Maier-Leibnitz Zentrum (MLZ) neutron source. ANTARES is a cold-neutron imaging beamline. In figure 2.15 a drawing of the beamline with the main elements necessary for NDI measurements is shown. This beamline is very adequate for this experiment for several reasons. Most importantly, it offers a high flux of cold neutrons, which are preferred when measuring neutron depolarization. Cold neutrons have a smaller velocity, therefore according to equation 1.7 give stronger depolarization signal. In addition, cold neutrons are favorable when using neutron supermirror guides as they have larger total reflection angles. At the entrance of ANTARES a large collimator drum with several collimators of different sizes shape the beam divergence to different values. A velocity selector allows to select a neutron wavelength while maintaining a relatively large flux. Being an imaging beamline it also has high preforming 2D neutron detectors which make the whole aligning process easier, or even possible at all. Last but not least, many NDI experiments are carried out in this beamline, so it already has available many of the instrumentation necessary for polarized neutron beams. The focusing guides module presented below could be modifiable to fit any other cold neutron source that offers at least some of the mentioned features.

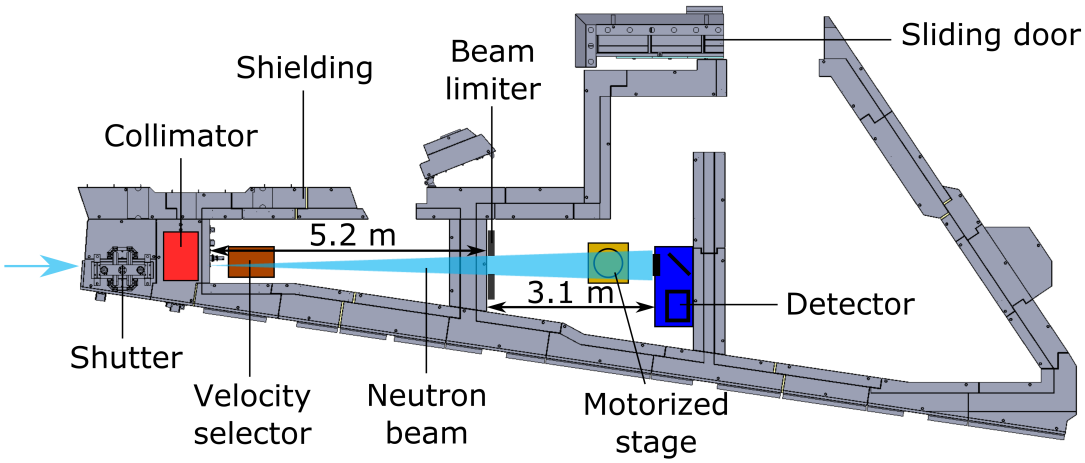

Figure 2.15: Drawing of the ANTARES beamline at the Heinz Maier-Leibnitz Zentrum (MLZ) neutron source. The beamline is presented with the elements that usually are already in place. The first chamber in the left is the beam preparation chamber. The module is mounted on to the motorized stage in the measuring chamber 1 (middle). The measuring chamber 2 (right) is only used for imaging of very large samples. Due to the large neutron fluxes obtained during neutron imaging, the whole instrument is surrounded by thick neutron absorbing shielding.

The use of a pair of focusing neutron supermirror guides manufactured by SwissNeutronics is at the core of this technical improvements. The geometry of the focusing guides is shown in figure 2.16. The guides are made of 4 solid blocks with a wedge shape where one of the side walls has a slight parabolic curvature which is covered by supermirror coating. The blocks are attached together in a cross configuration, leaving the parabolic side (the actual guides) on the inside, creating a square cross section. The blocks are made of N-BK7 glass, a borosilicate glass

with high level of purity, also known as Borkon glass. The parabolic surfaces have an optical quality polish with a waviness of 0.15 mrad RMS. Besides its optical qualities, this glass has a very low coefficient of thermal expansion. It therefore keeps its unique shape even when subjected to thermal gradients. A slightly different defocusing guide is also used in the experiment. The second guide has the same geometry as the first one, where the last 40 mm at the thin end of it have been removed. This difference has little impact for the experiment as both guides have the same curvature.

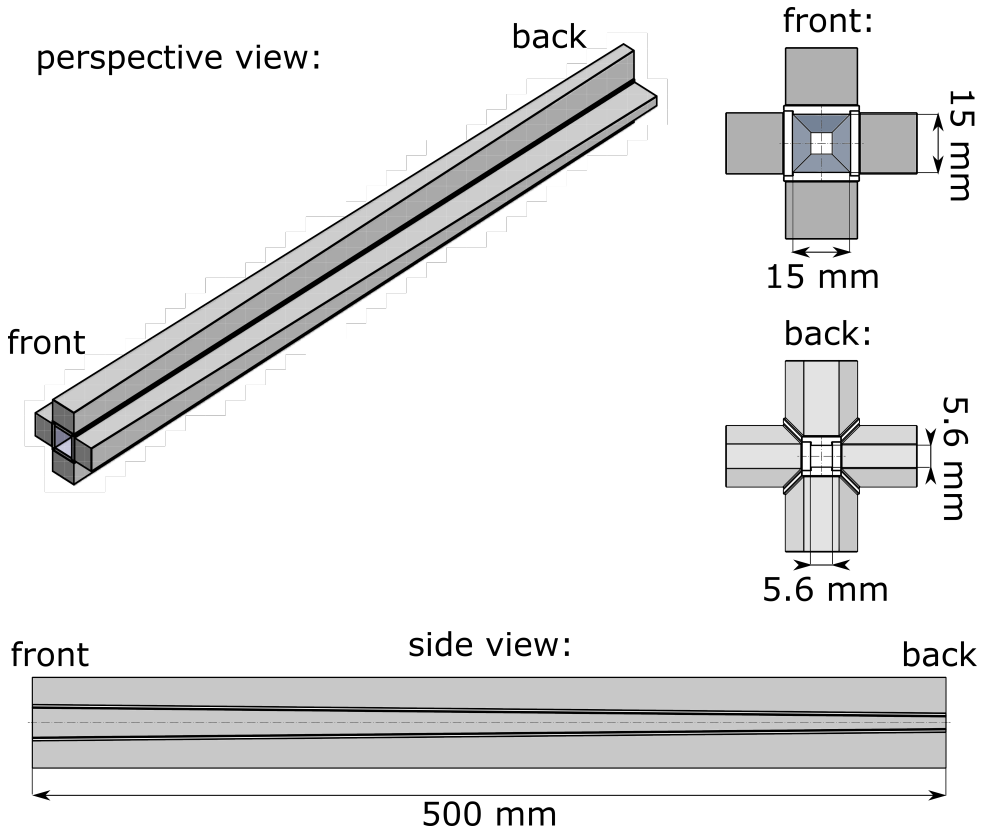

Figure 2.16: Technical drawing of the neutron supermirror guide. The front view shows the guide entrance where the inside of the guide, which is covered with supermirror coating, can be seen. The back view shows the guide exit.

To highlight the true parabolic nature of the guides and their confocal configuration, a not-to-scale schematic is shown in figure 2.17 together with the equation of the parabola. Both guides are placed facing each other and share the focal spot. Any neutron with a direction parallel to the guide (z direction) and reflected by the focusing guide walls is directed towards the focal spot and then reflected again by the second guide in the z direction. The smaller size of the defocusing guide means that some neutrons reflected by the first guide are lost, simulations indicate that these losses are small.

From the curvature of the guides, one can compute that neutrons with a direction perfectly parallel to the guide's axis, would meet its walls at angles ranging from 0.37° to 0.99°. Nickel, the most common coating for neutron guides, allows for a total reflection angle of about 0.5°

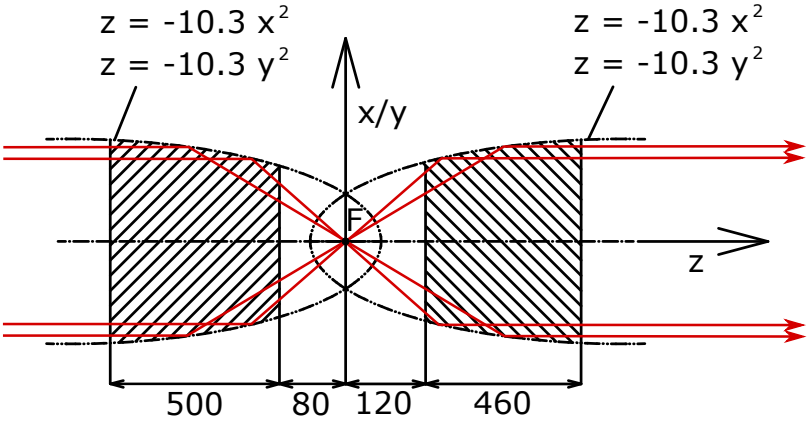

Figure 2.17: Schematic depiction highlighting the true curved nature of the inner guides sections and their confocal geometry. The focusing guide (left), with 500 mm length, and the defocusing guide (right), with 460 mm length, share the same focal point (F). The dashed area denotes the parts of the parabolic curve that are reproduced in the guides. The red arrows exemplify the trajectories of collimated neutrons. The values given are in millimeter, drawing is not to scale.

for neutrons with a wavelength of 5 Å as the ones used in this study. With a complex coating system, neutron supermirrors can be created. By stacking successively thinner layers alternating between a high positive (e.g. nickel) and negative (e.g. titanium) neutron scattering length density material, positive interference peaks are stacked together strongly increasing the total refection angle. The m-value determines the quality of the supermirror coating, and indicates the factor by which the original total reflection angle is increased. The inside of the focusing guide is covered with $m = 6$ nickel/titanium (Ni/Ti) supermirror coating, giving a total reflection angle of about 3° for neutrons with a wavelength of 5 Å. The defocusing guide is a bit more complex, as it is also used as analyzer. The top and bottom sections of the guide are also coated wit $m = 6$ Ni/Ti coating, but the side sections are coated with $m = 5$ iron/silicon (Fe/Si) layers. This coating has the particularity, when sufficient magnetic field (circa 30 mT) is applied to saturate the magnetization of the iron layers, to only reflect neutrons with a certain spin state (up or down) while being virtually transparent to the rest. More impressively it does so with an efficiency close to 100 %, meaning that the reflected neutrons are close to 100 % in the same spin direction.

A casing was designed and built to accommodate the guides and protect them from possible damage during utilization. The casing has various functionalities, for instance, it allows for very fine aligning of the guides by adjusting a set of crews and spring plungers. A misalignment of a few tenths of a degree with respect to the neutron beam is sufficient to cripple the efficiency of the guides. Moreover, the casing has to provide an homogeneous magnetic guide field to maintain the polarization of the neutron beam. Usually, a field of 0.5 mT (5 Gauss) should be sufficient, but for the defocusing guide, a field of at least 30 mT (300 G) to make the Fe/Si supermirror coating effective is needed. Permanent neodymium magnets (N42) with 1.4 Tesla residual magnetic flux at the surface were used to create the guide fields. As it is commonly done, large iron plates were placed at the top and bottom of the guides, they are connected with stacked magnets (with the same polarity) along the side of the guides. The magnetic

flux induced by the magnets inside the iron plates is distributed evenly along each plate, creating a straight and homogeneous magnetic field between the two plates of 43 mT. Small iron pieces were alternated between the magnets as a way to increase the distance between the 2 iron plates without losing magnetic flux, while keeping the number of stacked magnets low. Finite element simulations have been performed with COMSOL Multiphysics to optimize the guide field.

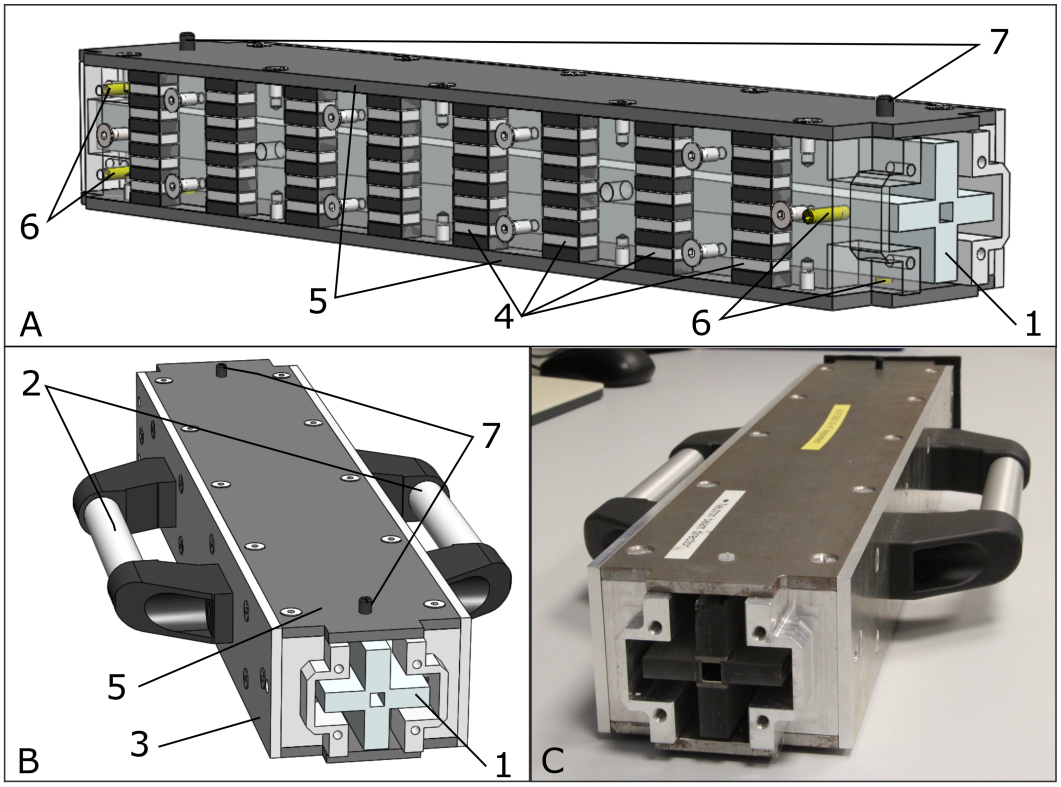

Figure 2.18: Focusing guides and casing. A: Schematic view of a focusing guide (1) inside its casing. Handle (2) and side plate (3) are made transparent to show the stacks (4) of iron pieces (dark gray) and neodymium magnets (light gray) on the sides of the guide. Top and bottom plates (5) are made of iron, the other parts are made of aluminum. For the aligning mechanism, brass screws (6) and plastic spring plunger (7) are used. B: Schematic view of the 3D model, where the handles (2) can be seen. C: Picture of the guide in its casing.

Details of the guide casing can be seen in figure 2.18. Due to the thick iron plates and the large number of magnets, the guides are relatively heavy, therefore large handles were installed for ease of operation. In order to not disturb the magnetic field created between the plates, all guides parts, except magnets and iron plates, are made of nonmagnetic materials. Most notably, aluminum was used for the frame and the screws. A thick boron rubber frame with a 16x16 mm window was used as a mask at the entrance of the focusing guide absorbing all neutrons not going through the guide entrance. The same frame was also mounted on the exiting side of the defocusing analyzing guide to absorb all neutrons not being properly defocused (i.e. reflected by the inner section of the guide) and leaving the guide by its aperture.

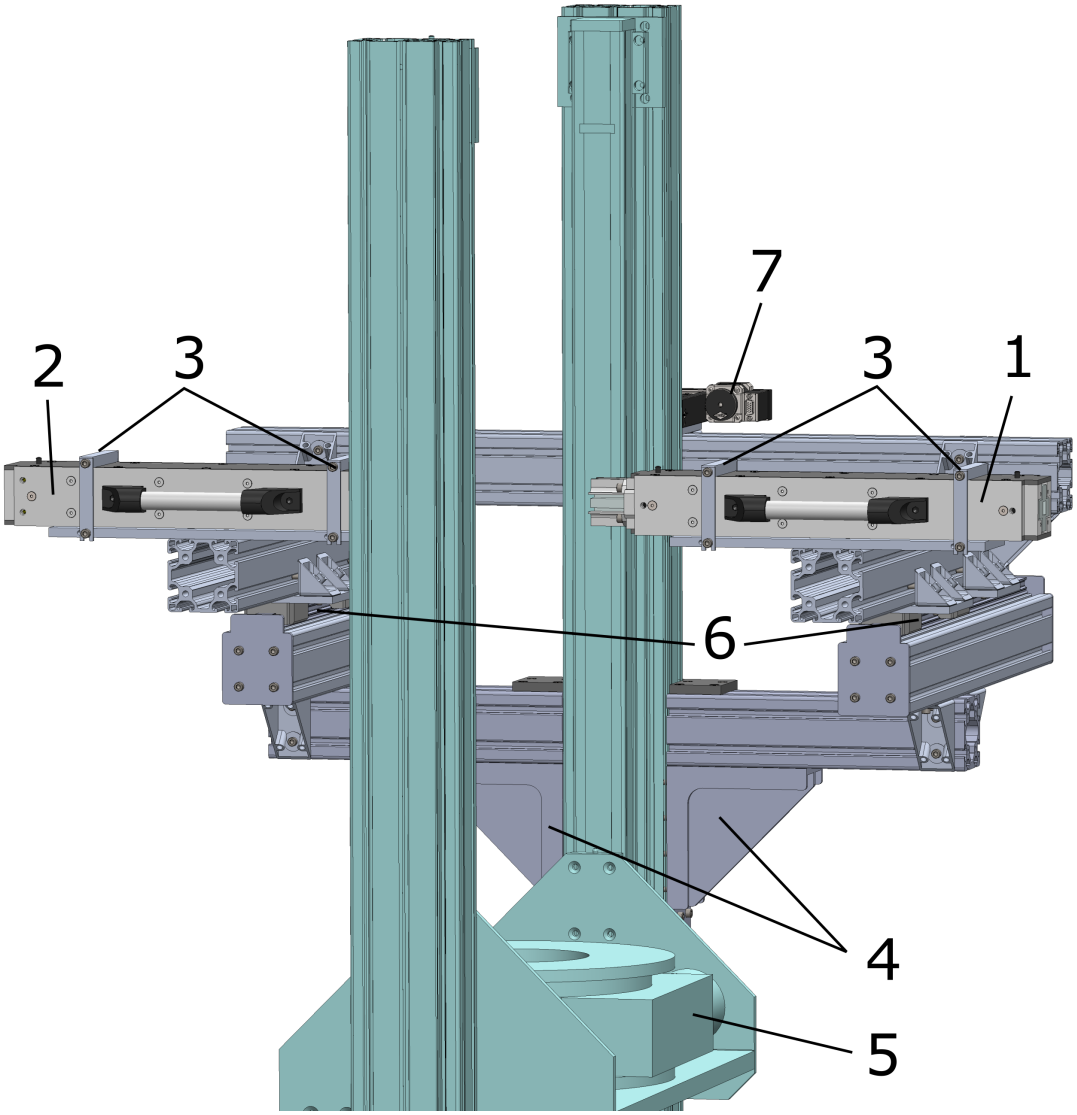

Figure 2.19: Drawing of the module constructed to support and align the neutron guides. The focusing (1) and defocusing (2) guides are carefully placed on the module, and secured in place with a simple clamping mechanism (3). The bottom part of the module is firmly anchored with right angle brackets (4) to the motorized stage (5) highlighted in blue. The top part, where the guides are places, can slide in the horizontal direction thanks to a rail (6) system. The movement in this direction can be precisely controlled with a stepper motor (7).

The guides have to be placed with high precision with respect to each other and aligned with the direction of the neutron beam within less than a 0.1°. At the same time, the focal spot (cross section of less than 1 mm diameter) should be precisely placed to coincide with the sample space in the pressure cells (about 400 µm in diameter). To fulfill these goals, a module was built that allows the guides to be placed and aligned with high accuracy. Figure 2.19 shows a detailed drawing of this module. It was made with large (80x80 mm) aluminum Item profiles to ensure stability. The coarse positioning of the two guides with respect to each other and the incoming

neutron beam was achieved mostly by having the module designed and built with accuracy and mounted on the motorized stage at the right height (so that the guides are at the center of the beam). Two aluminum plates, on which the module can be rested when mounting it, are permanently left on the motorized stage as a reference to allow for an easier and reproducible positioning of the module between experiments. The screws and spring plungers built into the guide casing (see figure 2.18) are used for the fine alignment of the guides with the incoming neutron beam and their relative position. This procedure is usually repeated once at the beginning of a new experiment and will be described in the following section.

The bottom of the guides casings have 3 steel spheres that fit perfectly into slots carved in the resting plates firmly anchored to the guides module. This 3 point mount ensures that the guides can be removed and placed back at the same exact position and angle. This is specially important when tanking in account that the guides are being removed many times in the course of an experiment in order to access the cryostat and change the sample or increase pressure. This feature increases strongly the time efficiency and consistency of the experiment by allowing the initial alignment to be recovered once the guide is placed back on the 3 point mount.

The module is strongly anchored on the side of the motorized stage (see figure 2.15) onto which the cryostat is placed. The motorized stage allows for automatized movements in transverse direction (x and y), and rotation along the vertical axis (y). Due to the location where the module is attached to the motorized stage, they move together in the horizontal (x) direction. Therefore, a rail system driven by a high precision motor was implemented (see figure 2.19) to allow the guides to be moved in the x direction with respect to the motorized stage were the cryostat sits. Moving the guides in x and y directions with respect to the sample table, allows for the precise alignment of the sample and the focal spot of the guides. The relative alignment of the focal spot and sample along the beam direction (z) is less demanding as it will be demonstrated in the following subsection. Nonetheless, two important details have to be considered. First, when mounting the samples (or pressure cells) into the cryostat, the sample must be well centered with respect to the rotation axis of the cryostat. Secondly, the cryostat must be placed equidistant of the two guides with help of a standard ruler. As a security measure, the guides and the cryostat are fixed in place with a simple clamping mechanism.

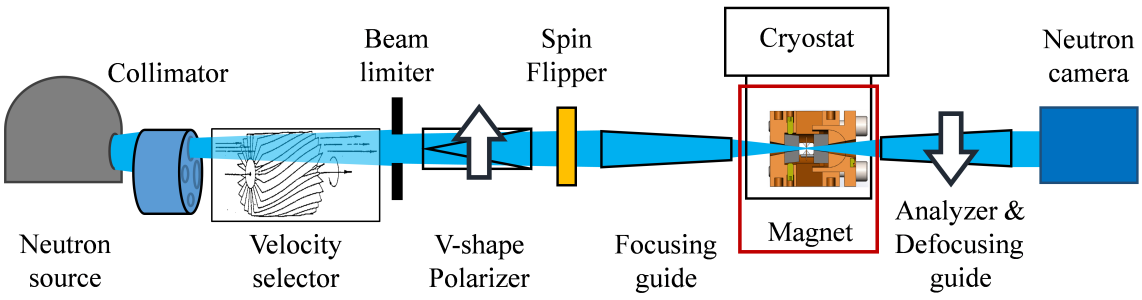

Figure 2.20: Schematic view of the focused neutron depolarization experiment with the relative position of the different elements. The arrows on polarizer and analyzer indicate which neutron spin state they absorb. The pressure cell is mounted in the cryostat and placed such that the neutron beam goes through its optical aperture.

A schematic view of the complete experimental setup is presented in figure 2.20 where the relative position of all the elements can be seen. Figure 2.21 shows pictures of the setup inside the measuring chamber 1 of the ANTARES beamline (see figure 2.15) during an experiment.

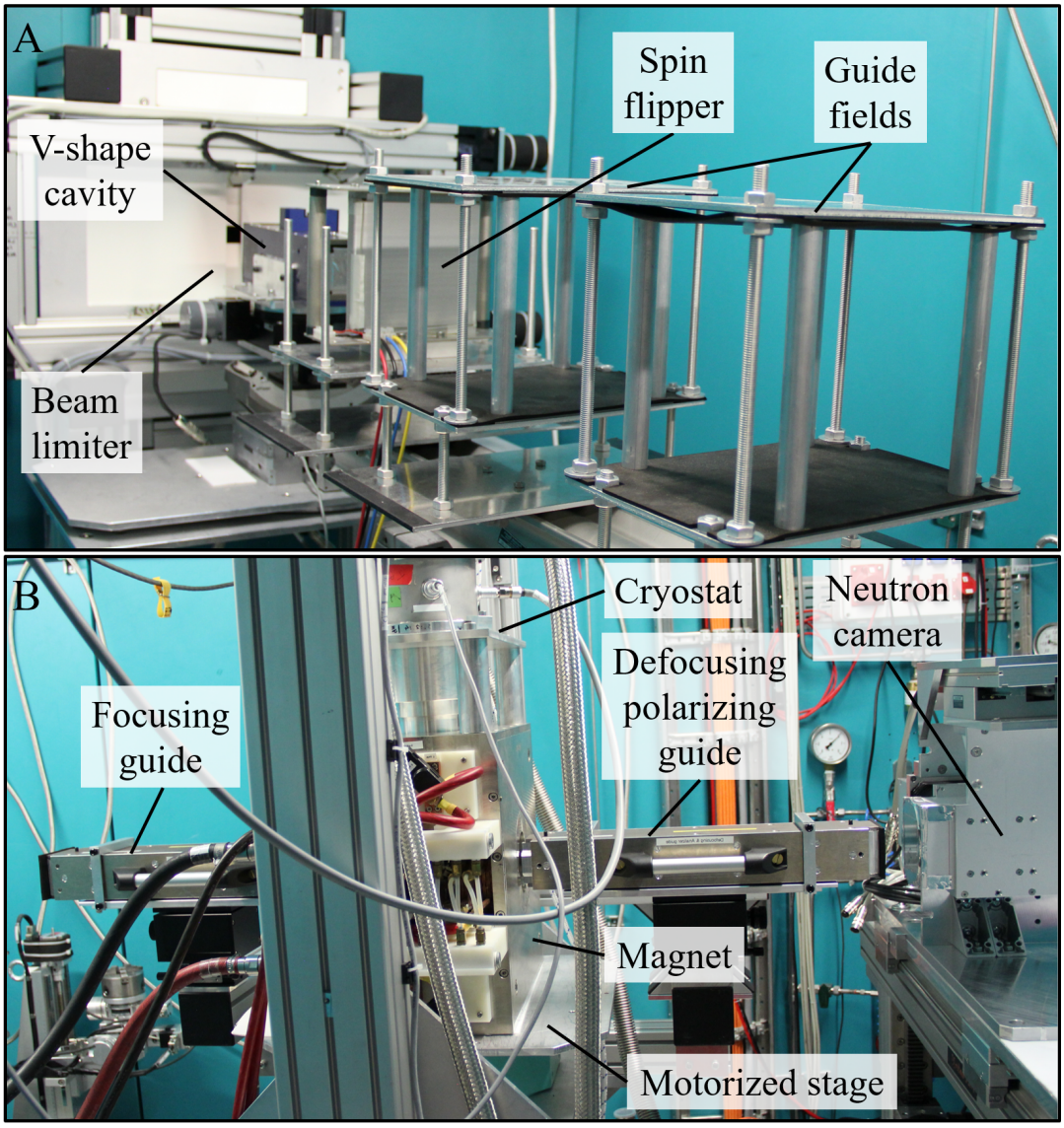

Figure 2.21: Pictures of the enhanced neutron depolarization setup being used. A: The Beam limiter is placed at the entrance of the chamber. Two guide fields help to maintain the magnetic field between the spin flipper a and the focusing guide which is 1.5 m downstream. B: The cryostat and the electromagnet sit on the motorized stage, while the guides are place onto the aligning module. The neutron camera is placed a few centimeters after the defocusing guide.

The divergence of the incoming beam is controlled with a collimator drum where different pinhole diameters are available. The energy spectrum of the cold neutron source is then shaped with a velocity selector that acts as a band-pass filter centered around a wavelength λ with a

bandwidth $\Delta\lambda/\lambda$ of about 10 %. A beam limiter shapes the cross section of the neutron beam to the desired size. The beam is then polarized with the use of a polarizing supermirror v-shape cavity, which stops the neutrons with spins aligned to the local magnetic field (spin-up). The polarizer itself, the casings of focusing guides, and two vertical guide fields made with permanent magnets, create an overlapping magnetic fields in the vertical direction along the path between analyzer and polarizer which maintains the polarization state of the neutron beam. A Mezei spin flipper changes the polarization state of the beam from down to up (π-flip) when it is turned on. The pressure cell, placed inside a cryostat, is brought to the focal spot of the focusing guides. A water cooled electromagnet can apply a magnetic field up to 0.3 Tesla at the sample position. The polarizing-supermirror defocusing guide acts also as analyzer as only neutrons with their spin aligned along the local guide field (spin-up) will be transmitted through it, the rest (spin-down) will be absorbed in the casing with help of a boron frame around the exit of the guide. An ANDOR cooled CCD camera with 2048 $\times$ 2048 pixels is used to measure the transmitted beam. All the elements are placed inside the measuring chamber 1, except the collimator and velocity selector which stand inside the preparation chamber (see figure 2.15).

2.2.2 McStas simulations

McStas is a neutron-ray tracing package that allows for a specific instrument to be defined and performs a Monte Carlo simulations of the neutron scattering experiment [87, 88]. Several McStas simulations have been used before and during the design of this experimental setup in order to have a better understanding of the experiment and how to tune the key parameters. A script that reproduces reliably the parameters inside the ANTARES beamline, as it is described in figure 2.15, with a collimator drum, a velocity selector and a beam limiter, has been modified to reproduced the current experimental setup. McStas allows for the proper definition of several neutron instrumentation, for example, the focusing guides described in the previous section can be defined with great detail. Virtual neutron detectors along the beam path have been used to retrieve information on the shape of the neutron beam and its divergence. To help understanding the exact functioning of the instrument, here below some of the most relevant results are presented. For simplicity, the neutron spin has not been included it into the simulations as the spin manipulation is almost identical to a standard NDI experiment and mostly independent of the neutron ray trajectories.

In a first simple simulation, a 500 mm long focusing guide is added at 7 m from the exit of the collimator (where it is intended to be used), into the script describing the ANTARES beamline. A virtual 2D detector is placed at the focal plane, 80 mm after the exit of the focusing guide, to observe the dimensions of the focal spot when using different collimation values. Figure 2.22 shows the main results of this simulations, where collimator sizes of 18 and 36 mm are compared, the velocity selector is centered to 5 Å. A cross-shaped cross section can be seen, although when looking at the high neutron intensity part (in bright yellow), i.e. the part of the beam that is efficiently focused, it has a disk-shaped cross section as expected. At half of the maximum intensity value, the intensity profile describes a circle with diameters of 0.25 and 0.7 mm for the 18 and 36 mm collimation values, respectively. The larger pinhole value seems to be more adapted to the typical size of the sample space inside a DAC (0.4 mm). Not only the intensity is slightly higher with the larger collimation, but it is also almost constant across the sample space. A highly collimated beam is in principle preferable when using parabolic guides, as the

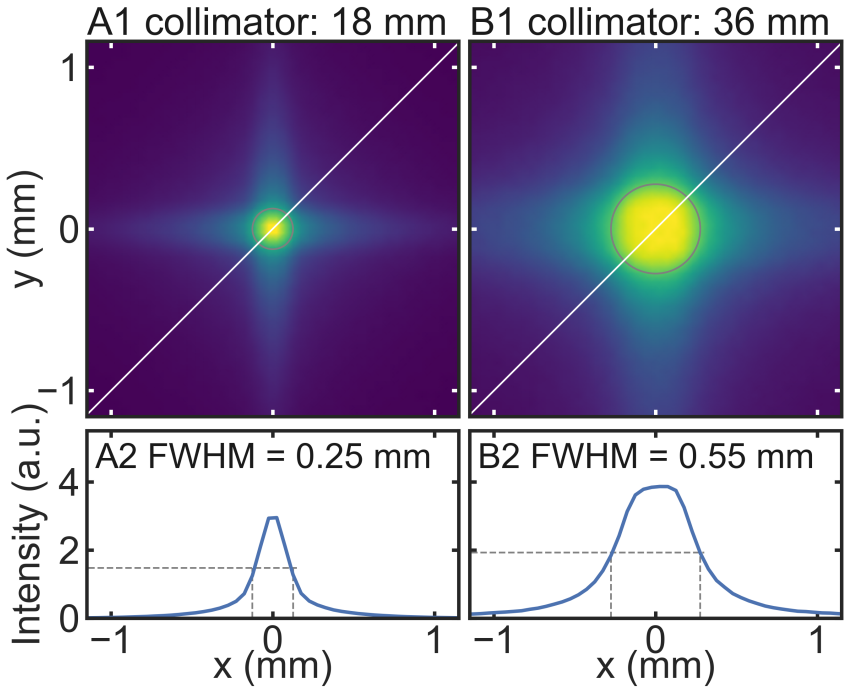

Figure 2.22: Simulation of the focal spot profile produced by the guides with two viable collimator sizes 18 mm (A1) and 36 mm (B1). For each collimation an image of the neutron profile and a a section cut across the center of the images (white line) is shown in A2 and B2, for the 18 mm and 36 mm collimators, respectively. The diameter of the intensity's full width half maximum (FWHM) is indicated and highlighted with a gray ring on the image.

extremely small focal spot indicates. In this particular case, the use of a slightly more divergent beam seems to be preferable. Not only the intensity is increased as we can expect form a larger pinhole size, but the slightly off axis neutrons produce a larger more convenient focal spot size which homogeneously covers the sample space. The use of an even larger collimator aperture (71 mm) is not recommended at ANTARES due to the critical increase of radiation (gamma rays and high energy particles) coming from the rector core.

Another interesting simulation has been performed with the same virtual instrument as the one previously described, i.e. with the basic ANTARES setup and the focusing guide. The collimator is set to 36 mm, as for the rest of the simulations. This time, many virtual 2D detectors are placed at 1 mm intervals before and after the focal spot. In figure 2.23 many of these beam slices are shown centered around the focal plane at $z = 0$. The beam profile changes more slowly along the beam direction than in the transverse direction. While the focal cross section is smaller than a millimeter, changes in the longitudinal direction of a few millimeters barely have any impact on the beam profile. Interestingly it is not symmetric with respect to the focal plane and the beam seems to remain more focused before the focal spot ($z < 0$) than after ($z > 0$). The main conclusion to be extracted is that the focal spot extends over several millimeters around the focal plane in the beam direction. There is therefore no need for a very precise adjustment of the position of the focusing guides with respect to the sample along the beam direction. Placing

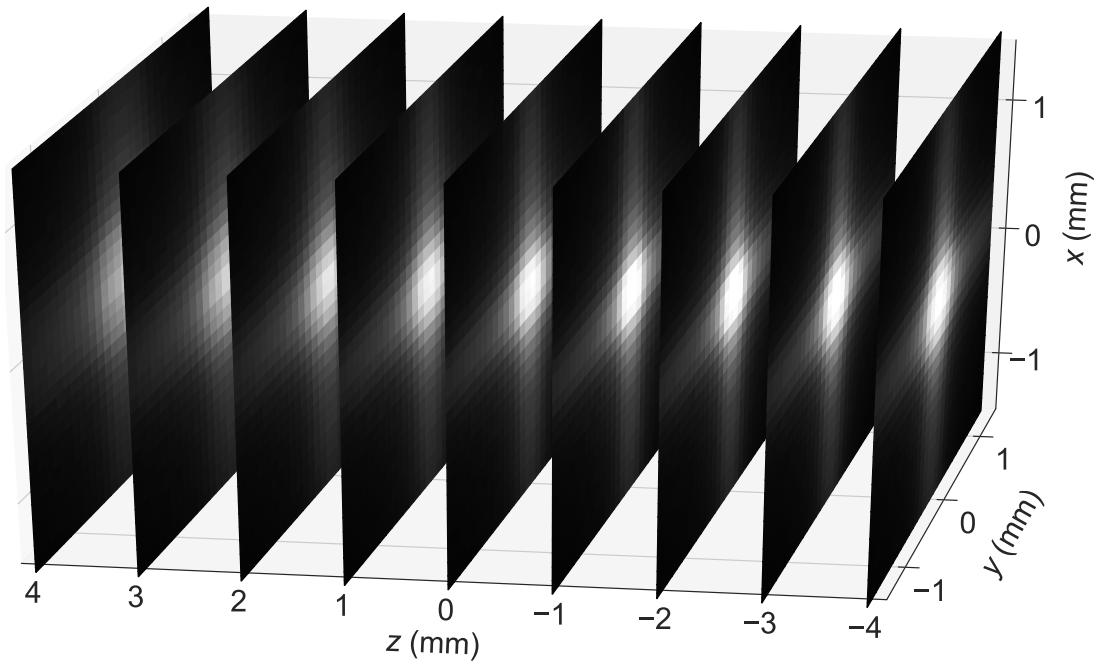

Figure 2.23: Simulation of the beam profile at several planes around the focal plane ($z = 0$). The gray scale intensity is normalized to the maximum intensity at the focal plane.

the cryostat equidistant of the two guides with help of a standard ruler, and ensuring that the sample space is centered with respect to the cryostat is sufficient. The accumulated error of these two procedures is in the range of 1 to 2 millimeters, within which the beam remains well focused.

Figure 2.24 shows the results of a simulation of the ANTARES beamline including both guides and a pinhole at the sample position. The collimator drum is set to 36 mm aperture and the velocity selector tuned to 5 Å. The pinhole, with 1.6 mm diameter, emulates the effect that the pressure cell has on the neutron beam. The pair of 5 mm thick tungsten carbide backing plates have a large absorption length (≈ 0.3 mm^{-1}), and have a conical aperture ranging from 2.5 to 1 mm in diameter, thus 1.6 mm pinhole is a good approximation. The changes on the neutron beam profile (i.e. spatial distribution) and the beam divergence are shown. With a finite beam divergence, the spatial distribution of the neutron cross section changes constantly, even in the absence of any optical element. In contrast, the neutron divergence changes only when the beam is reflected by neutron optical elements like the neutron guides.

Before the guides the beam intensity is homogeneously distributed and the divergence is contained in a 0.2° cone centered around 0. At the focal plane, the beam intensity is mostly condensed on the focal spot, although there is a significant cross-shaped intensity spread, as seen previously. The divergence is divided into 9 differentiated features with a 90° rotation symmetry. These features can be assigned to 3 distinct groups. The 4 spots at the corners correspond to neutrons with large divergence values in the x and y directions simultaneously, they have been focused on these 2 directions by 2 adjacent sections of the guides. Between these corner features, we can see 4 narrower features set in a cross shape. These only have large divergence values in one direction, thus have only been focused by one section of the mirror. Finally, the

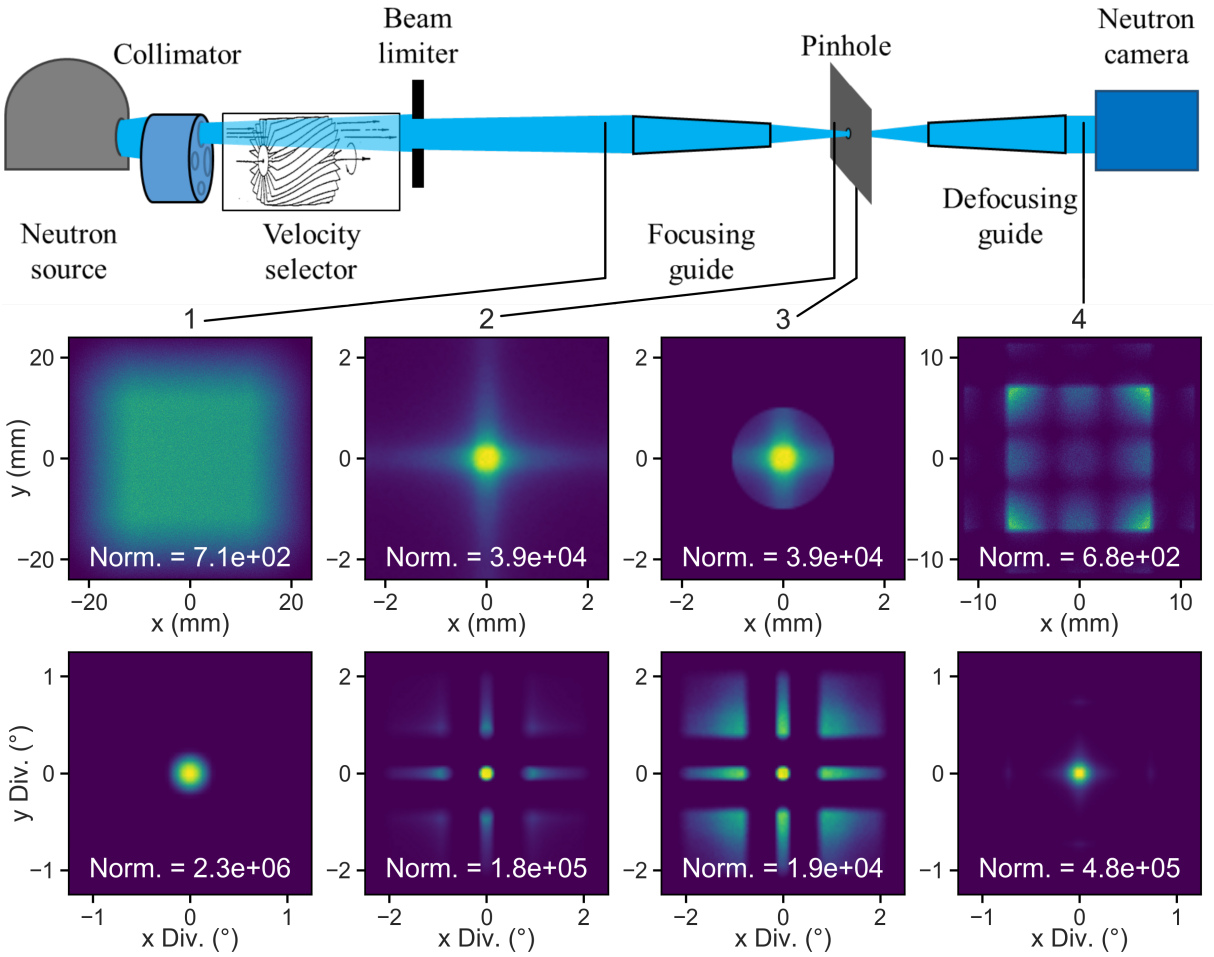

Figure 2.24: Simulation of the neutron profile, and beam divergence along the focusing and defocusing guides. The top drawing shows a schematic view of the elements used in this simulation. The bottom panels show the beam profile (top) and divergence (bottom) at 4 different places along the beam path: right before the first guide (1), right before the pinhole (2), right after the pinhole (3), and 200 mm after the defocusing guide (4). All the images are normalized to the maximum intensity value (Norm.). A 1.6 mm pinhole simulates the effect that the pressure cell has on the beam.

small bright spot at the center corresponds to highly collimated neutrons that have simply flown straight through the entrance and exit apertures of the focusing guide without interacting with it.

Interestingly, after the pinhole, the relative intensity of the different spots in the divergence plot is completely changed. Most of the highly collimated neutrons which are not focused by the guides are absorbed, whereas the highly divergent neutrons, because they have been focused by the neutron guide go through the focal spot and are transmitted. Note that the absolute value of the divergence of the focused neutrons in a given direction (x or y) is distributed between 0.74° and 2°, as it could be expected from the reflection over a curved mirror with angles ranging

from 0.37° to 0.99°.

After the defocusing guide the situation with respect to the one at the focal spot is reversed, the neutron profile shows 9 different features, while the divergence distribution is condensed in a narrow cone around 0°. The beam has efficiently been defocused. Interestingly, these 9 features can be mapped to the ones observed on the divergence plot at the focal plane. There are 4 corner features which correspond to the previously highly divergent neutrons in both x and y direction that have been defocused (i.e. brought again to a small divergence value) by being reflected on two adjacent sections of the guide. The integrated intensity over the corners account actually for most of the intensity transmitted through the instrument. There are also 4 features in between the corner ones, as before distributed in a cross shape. They correspond to the previously highly divergent neutrons in either x (right and left) or y (top and bottom) direction that have been defocused (i.e. brought again to a small divergence value) by being reflected on only one guide section. The spot in the center corresponds to neutrons that have simply flown through the apertures of the guides and the pinhole without interacting with them. The divergence of the beam after going through the focusing guides is even smaller than before. Only neutrons with small initial divergence values are correctly focused and defocused by parabolic mirrors, thus not being absorbed by the pinhole.

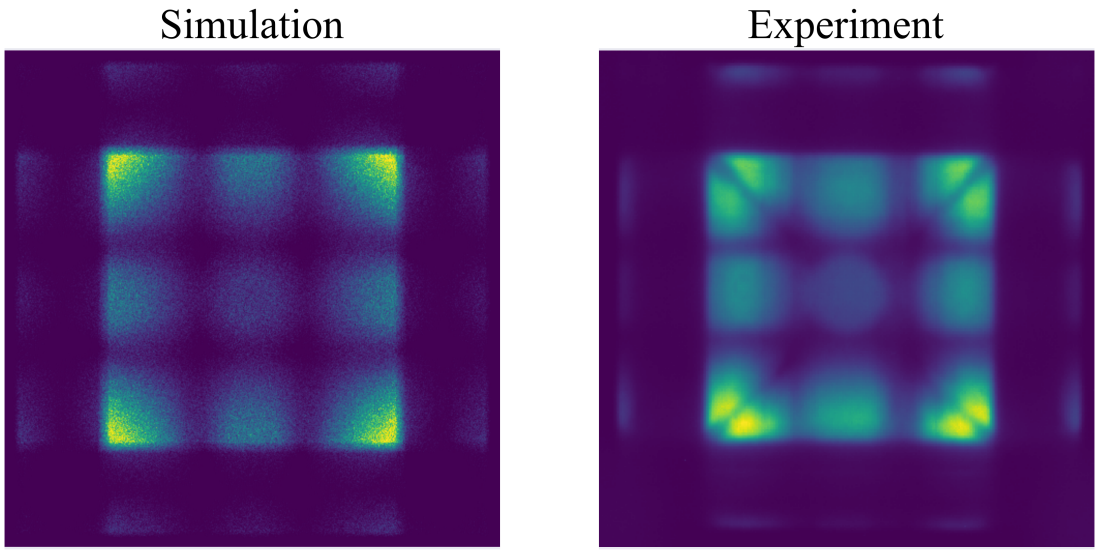

Figure 2.25: Comparison between the simulated neutron beam (left) at the detector position, and a neutron image (right) obtained with the experimental setup as described in figure 2.20.

The validity of these simulations can be demonstrated by comparing the image produced by the simulations at the detector position with the neutron images obtained during the experiments. In figure 2.25, the strong resemblance of the two images suggests that the simulations are indeed pertinent. The neutron image reproduces the 9 main features observed in the simulations, as well as the intensity distribution which is maximal in both cases around the corner features. It even reproduces a detail which has been previously overlooked, a small intensity

frame close to the edges of the images, made of 12 small regions. These are neutrons that have a large divergence in either x or y direction, thus this frame becomes larger further away from the defocusing guide. They can be identified in the divergence distribution at the detector position in figure 2.24 as 4 small spots with low intensity and with large divergence in either x or y direction. Their origin is not clear, but they can also be observed when illuminating the guides with laser light. The main difference that can be observed between simulation and experiment, is that in the measured image the corner spots are divided by a low intensity line along their diagonal. This artifact is most likely due to poor mirror efficiency at the junction points between the guide sections.

A quantitative measure of the efficiency of the focusing guide module, can be given by how much the measured intensity has been increased at the detector position with respect to a standard NDI experiment. This can be obtained by comparing the relative value between the the total intensity flying through the pinhole aperture in a standard NDi experiment to the total intensity in an experiment using the focusing neutron guides. Comparing, in the experimental image of figure 2.25, the integrated intensity of the central dot (i.e. neutrons flying through a pinhole in a standard NDI experiment), to the integrated intensity of the 8 spots around it (neutrons focused by the guides and going through the pinhole), a significant gain factor of 20 is obtained. This value is also reproduced by the simulations.

2.2.3 Set-up and operation

This section details some of the mounting and operation procedure of the enhanced neutron depolarization experiments. The standard beamline procedures performed at ANTARES, like adjusting the velocity selector, are usually managed by the instrument scientists and will not be covered in this discussion.

The first step is to install the guides module where the focusing guides will sit. The guides module is then mounted on the motorized stage as seen in the inset of figure 2.19. The adjustment of the guides in their casing is limited, thus the module has to be fixed as horizontal as possible to allow the guides to be aligned with the horizontal neutron beam. Additionally, the height has to be adjusted to place the guides at the height of the center of the incoming neutron beam. This is made easier with the help of 2 aluminum plates, permanently attached to the sample stage, where the module can be rested on before tightening the large angle brackets that fix it to the motorized stage. Once firmly attached, the module is reasonably leveled and at the right height. The position of the sample stage is then adjusted horizontally to leave the sample space (i.e. center of the rotation table) aligned with the center of the neutron beam.

If the electromagnet will be used, it should be placed first on the motorized stage (or sample stage) as once the guides module is mounted there is usually not enough space to put it in place. The electromagnet can be used in two positions, horizontal and vertical, with the applied field being perpendicular and parallel to the neutron beam, respectively. The horizontal position, with the magnetic field perpendicular to the neutron beam (and along the guide field) is preferable as it gives better signals and the access on the side of the electromagnet is easier. As a drawback the polarity of the magnetic field has to be set to coincide with the polarity of the guide field and cannot be reversed. If the polarity is reversed, the neutron guide field will be

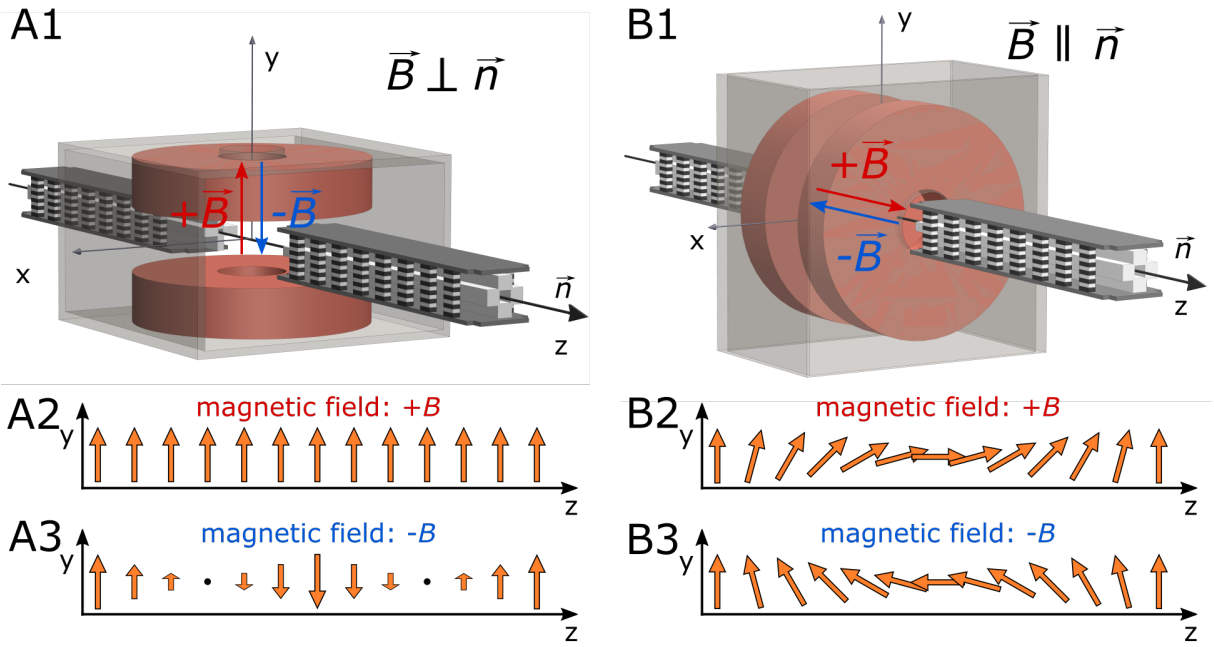

Figure 2.26: Interplay between neutron guide field and magnetic field. A1: Schematic view of neutron guides and electromagnet in the perpendicular configuration. A2 and A3: Direction of the neutron guide field along the neutron path for a positive and negative polarity of the electromagnet, respectively. The black dots indicate points where the neutron guide field may be suppressed. B1: Schematic view of neutron guides and electromagnet in the parallel configuration. B2 and B3: Direction of the neutron guide field along the neutron path for a positive and negative polarity of the electromagnet, respectively.

canceled at two points along the neutron beam and depolarize it. The vertical position is more complicated to operate as the magnet yoke gets in the way of the guides. In the other hand, since the field is applied along the beam and at a right angle with respect to the guide field, the polarity can be reversed without canceling the guide field, it will just be rotated in either direction inside the magnet without ever being zero. The main drawback is that, in the vertical position, when the electromagnet is turned off, the guide field is not able to penetrate deep enough in the electromagnet due to the yoke, thus depolarizing the neutron beam. Therefore, in the vertical position, a field of at least 20 mT, in either polarity, has to be applied in order to maintain the polarization of the neutron beam.

The electromagnet, or the cryostat when no magnet is being used, should be placed in the exact center (within a millimeter) between the two arms of the guides module manually and then strongly fixed. The position of the guides with respect to the sample can be adjusted in the direction transverse to the beam, but not in the longitudinal direction. The alignment in this direction is ensured by centering the electromagnet correctly, then centering the cryostat to the electromagnet, and having the sample space of the cell centered within the axis of the cryostat. The precision obtained with this method is in the order of 1 or 2 millimeters, but as it is shown in the previous section, this accuracy is sufficient. Given the short focal distances of

the focusing (80 mm) and defocusing guides (120 mm), they are very close to the cryostat and electromagnet. There is a real danger of damaging the guides or the motors if they drive into the electromagnet. To prevent this, with the focusing guides placed on the module, all motors should be moved carefully in all directions stopping before a collision might occur. Knowing these limit positions, motor limits can then be defined in the controlling software which allow them to be moved safely for the rest of the experiment.

The focusing guides can then be finely aligned with respect to the neutron beam and to each other, the procedure is illustrated by figure 2.27. First, the incoming guide (focusing guide) alone has to be aligned to the neutron beam, thus the defocusing guide is temporary removed. The focusing guide is roughly brought at the central beam position with the stepper motor of the guides module, and then the tilt is finely adjusted using the set screws of the guide casing. The adjustment procedure is done by observing the neutron beam pattern created by the guide at the detector position, and tuning the screws until it becomes perfectly symmetric as in panel 1 of figure 2.27. The corner features are quite irregular as they are superposed to neutrons flying through the screw holes in the boron rubber used as a mask in front of the guides, they can be seen in the right image as well. The alignment procedure is usually done with only a few iterations steps, specially when the guides module is properly leveled. Nonetheless, it can be quite time consuming to an inexperienced user because the experimental chamber needs to be opened and sealed between each screw adjustment to get a neutron image. Once the incoming guide is aligned to the neutron beam, it should be fixed with a clamping mechanism to keep the alignment.

Next, the defocusing guide has to be aligned to the focusing guide. A laser lamp with collimated red light is used to allow for a visual and faster alignment rather than using the neutron beam. The lamp is pointed at the focusing guide from its entrance and is adjusted with help of a manual goniometer to reproduce a symmetric pattern as in the previous step (see panel 2 of figure 2.27). This way the lamp light is made colinear with the neutron beam. The defocusing guide can then be placed on the module, the distance between the two guides should be exactly 200 mm, the sum of the 2 focal distances. If not the position of the resting plates where the guides are installed should be slightly adjusted by taking advantage of the loose fit of the screw clearance holes. The entrance (smaller aperture) of the defocusing guide is placed into the center of the beam with help of the screws and spring plungers present on the guides casing (see panel 3 of figure 2.27) at the entrance side (smaller aperture). As seen in the figure, the laser light shines at the rim of the guide entrance. The entrance of the guide is properly placed when the light is equally bright on the 4 edges. Finally, the alignment of defocusing guide can be adjusted with the screws and spring plungers on the guide casing situated the exit side of the guide (larger aperture). A good alignment is reached when a symmetric picture is obtained (see panel 4 of figure 2.27). When adjusting the alignment with the screws at the exit of the guide, the position of the entrance of the guide might be slightly off, therefore a couple of iterations over the last two steps are usually required.

The accurate alignment of both neutron guides is finally tested with the neutron beam (after removing the laser lamp). A typical neutron image obtained after a successful alignment can be seen in panel 5 of figure 2.27. If the pattern obtained is not symmetric, the whole alignment procedure should be repeated. Note that unlike the image obtained with laser light, this image has not a 4 fold rotation symmetry, the right and left sides of the pattern obtained are

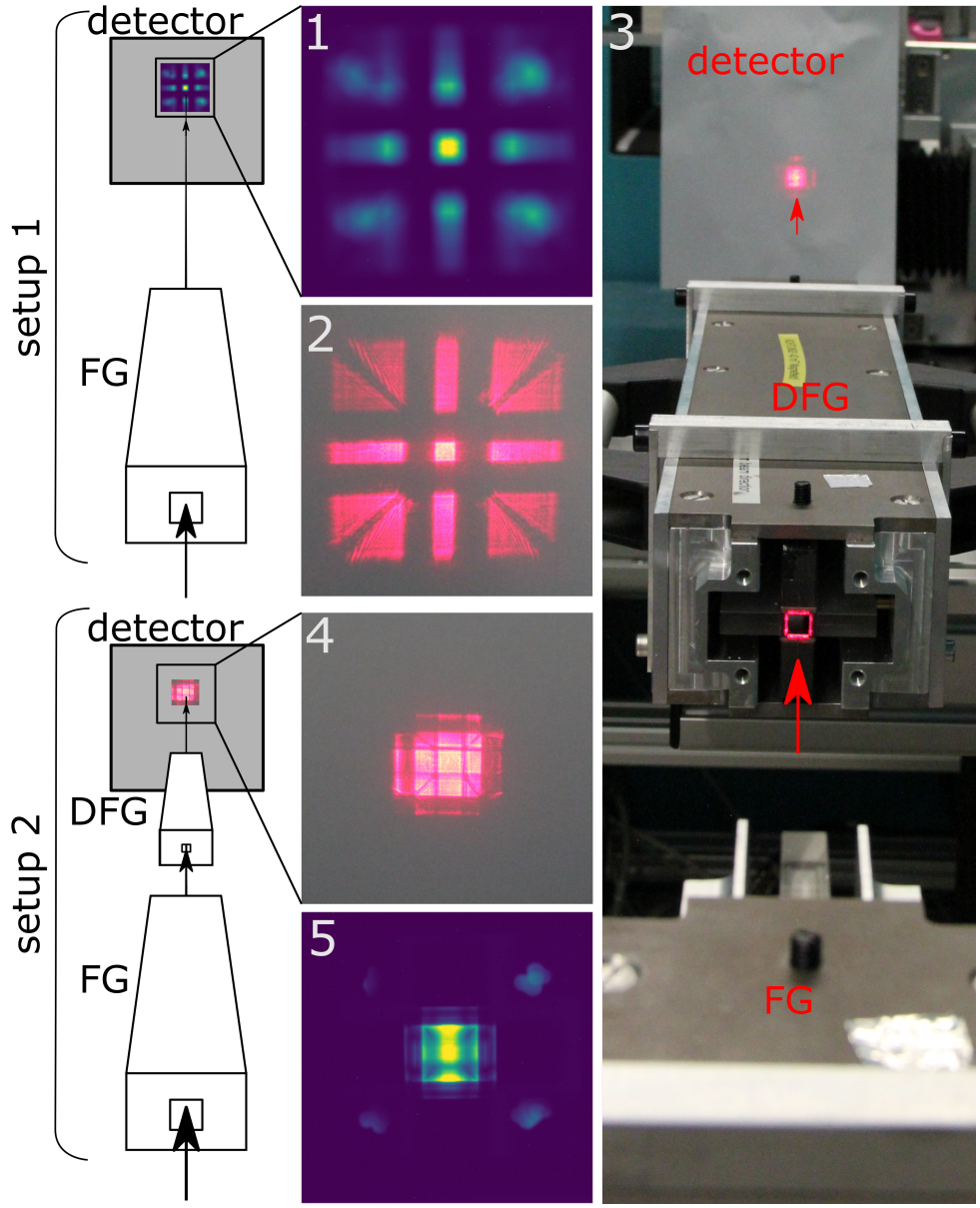

Figure 2.27: Alignment procedure between focusing and defocusing guides. 1 :Focusing guide (FG) alone is aligned with the neutron beam. 2: Laser lamp is placed in front of the FG and aligned to reproduce a similar symmetric pattern. 3: Defocusing guide (DFG) is then placed in and its entrance is centered with the laser beam. 4: DFG is aligned to reproduce a highly symmetric pattern. 5: The lamp is removed and a neutron image through both guides is made to confirm the alignment.

less bright that the top and bottom. The sides of the defocusing guide are made of polarizing supermirror, thus they only reflect one spin state reducing the intensity to the half, as in this stage the neutron beam is unpolarized. The top and bottom part of this pattern corresponds to neutrons only reflected by the top and bottom sections of the the guide which are made of non-polarizing Ni/Ti coating, they reflect both spin states.

Once the guides are properly aligned they are removed to allow for proper alignment of the v-shape cavity. The cavity should be brought perfectly parallel to the neutron beam for an optimal performance. This is easily done by observing neutron images along a few rocking scans. Thanks to the 3 point mount, the guides can be placed afterwards back at the exact same position. At this point the spin flipper is also installed, it is important to verify that the guide field along the neutron path between analyzer and polarizer is at least 0.5 mT in strength and in the same direction. A Gaussmeter and a magnetic compass can be used to this purpose. Two small supplementary guide fields are placed at the same distance before and after the spin flipper to ensure that the guide field at the spin flipper position is highly homogeneous.

The spin flipper can be tuned to allow for a perfect 180° (π flip) turn of the neutron spin. This procedure is very common and will not be describer in detail. Mezei flippers are made of two coils, compensating and flipping coils. The compensating coil creates a magnetic field in the same direction of the neutron guide field but in opposite direction, it is tuned to the current value which allows a perfect compensation of the guide field. Having a homogeneous guide field around the spin flipper ensures a more efficient compensation. The flipping coil creates a magnetic field in a direction perpendicular to the local guide field. Within this coil the direction of the neutron spin rotate due to the Larmor precession. The current along the flipping coil is tuned so that, along the path inside the spin flipper, this rotation is exactly 180° (π). This current is obviously different for different neutron velocities and has to be readjusted when the neutron wavelength is modified.

After the focused depolarization module is aligned and tuned, the sample or pressure cell can be mounted inside the cryostat and placed on the sample table. The main requirement is that the sample has to be centered with respect to the axis of the cryostat tail. When using pressure cells, it is very important to place the cryostat such that the optical aperture of the neutron beam is roughly facing the neutron beam. The 20° conical angle of this aperture is forgiving to small misalignment. To adjust the focal spot of the neutron beam exactly on the sample, the vertical motor on the sample stage, and the horizontal motor on the guide module, should be used. Removing the guides and taking neutron images of the sample allows for an easy coarse positioning, as the relative position between the pinhole and the center of the focusing guides will be known by comparing the two neutron images.

For a finer positioning, the guides are placed back and successive images are taken with very small steps (50 μm steps) of the positioning motors in a cross pattern (i.e. first scan one motor, the come back to the central position and scan the second one). Usually a first coarse scan is performed where the center position is determined by visually choosing the image where the transmitted intensity is highest. The optimal positions is determined as the center of the bell shaped profile of the integrated intensity transmitted through the cell obtained in a subsequent scan. Figure 2.28 shows an example of the intensity profile when doing such scan. This allows for a highly accurate (within 100 μm) and reproducible positioning of the sample with respect to the neutron beam.

At this point the instrument is ready to start a measurement. As it is done in standard neutron depolarization techniques, images are taken with the spin flipper turned on (spin-up state) and with the spin flipper turned off (spin-down state). To minimize non-statistical sources of noise

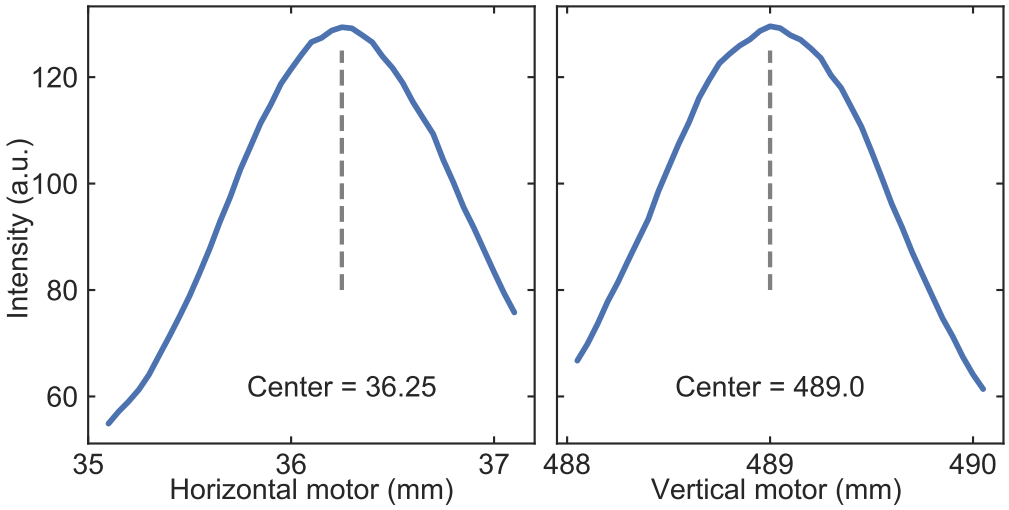

Figure 2.28: Plots of the intensity profile when scanning the horizontal and vertical motors to find the sample position. Central position is determined as the center of the bell shaped intensity profile obtained.

(e.g. gamma rays), each image is computed as the median of 3 successive images, preferably alternating between on and off images to minimize error due to temperature drifts. Using the formula given in equation 2.5, spin up and down images are combined to create a polarization image. I_{Dark} is an offset image taken with the beam shutter closed at the end of the experiment. Each individual image is taken with 30 seconds of exposure time, summing up to 180 seconds exposure time for a polarization image.

$$P_{image} = \frac{I_{\text{Up}} - I_{\text{Down}}}{I_{\text{Up}} + I_{\text{Down}} - 2I_{\text{Dark}}} \tag{2.5}$$

Figure 2.29 shows typical images obtained during an experiment and how they are combined to create a polarization image. Only the side (right and left sections) of the defocusing guide have polarizing supermirror (Fe/Si) coating, thus only neutrons on the sides of the neutron beam (reflected by the lateral sections) are polarized. As it has been argued in the beginning of this section, all spatially resolved information is lost, thus a single polarization value is obtained from a neutron polarization by averaging over a region of interest (ROI) of the neutron image. The ROI is chosen in the area where the beam is both polarized and the neutron intensity is high. The integrated intensity through the same pressure cell measured in a standard NDI experiment is 15 times smaller than what we obtain with the enhanced neutron depolarization experiment.

Temperature scans are measured by obtaining a polarization value at successive temperatures steps. Once the temperature reaches a particular value, a waiting time of 1 or 2 minutes can be implemented to ensure the whole cell has reached this temperature before the measurement is started. Placing a thermometer directly onto the side of the pressure cell is preferable to avoid temperature gradients between the control and sample temperature. Nonetheless, the lack of hysteresis between cooling and heating scans in all measurements indicates that this thermalization is sufficiently fast in comparison to the downtime between temperature steps (between 3 to 5 minutes).

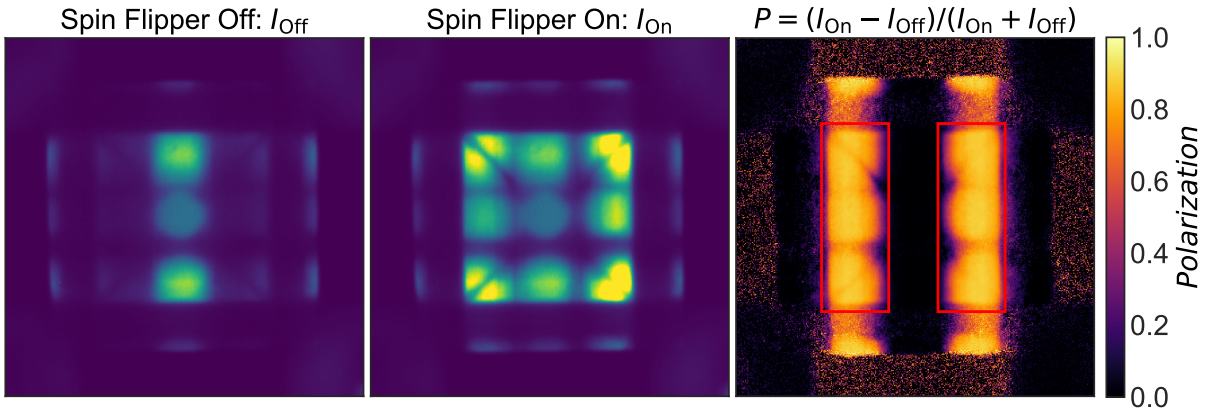

Figure 2.29: Neutron images obtained with the spin flipper turned off (left), and turned on (center), are combined to create polarization images (right). A single polarization value is obtained by averaging over a Region Of Interest (ROI), highlighted by the red rectangles.

The beam polarization is rarely 1, it is the result of the combined efficiency of the polarizer, analyzer, and the flipping ratio of the spin flipper. Instead of evaluating these efficiencies which are highly dependent on the neutron wavelength and the quality of the alignment procedure, the polarization is usually normalized to 1. The normalization factor is obtained by averaging the beam polarization measured in the paramagnetic state of the sample, where the empty beam polarization is reproduced. For this purpose, the temperature range is always chosen across a ferromagnetic phase transition, starting or ending in a paramagnetic state. Magnetic field or neutron wavelength scans can be done by tuning the different parameters in a similar way. Normalizing the polarization in these cases is more complex.

At the beginning of every measurement the effect of the afterglow of the detector has to be balanced. The detector consists of a CCD camera observing a scintillator placed in front of the neutron beam. Once the scintillator has been excited by neutrons, it has a finite down-time where it can still emit light, the so called afterglow. When the scintillator is successively exposed to neutrons, like in an NDI experiment, the gain will thus depend on previous exposure and downtime since the last one. Assuming a constant rate of exposure, it takes some time until the gain of the scintillator reaches a stable gain value, and this value can change when the rate of neutron exposure is changed. To compensate for the afterglow, successive sets of images (at least 4 complete polarization images) with the same exposure time as for the experiment, and a similar down time between them as between the temperature steps, are taken before the start of a temperature scan. This way, by simulating the experiment conditions on the scintillator, equilibrium is reached before the start of the experiment. This effect is usually small, in fact it is smaller than the measurement noise obtained with standard NDI, but when measuring very small signals with the enhanced ND setup it becomes a significant spurion. For the same reason, it is important to keep the downtime between temperature steps constant during a scan, otherwise the gain level of the scintillator might variate.

2.2.4 Performance and characteristics

The performance of the enhanced depolarization setup was evaluated at different neutron wavelengths and collimation values. This is summarized in figure 2.30 where the dependence of the beam intensity and polarization to the neutron wavelength is shown for 2 different collimation values. There was no sample on the motorized stage during this experiment. As mentioned before, the flipping coil of the spin flipper must be adjusted to a given wavelength. For this measurement, the current through the flipping coil was swept from 0 to 3 ampere for each wavelength step. The beam polarization is calculated observing the sinusoidal intensity profile obtained when sweeping the current. The ratio between the amplitude and the average value of the oscillation produced gives the maximum achievable beam polarization.

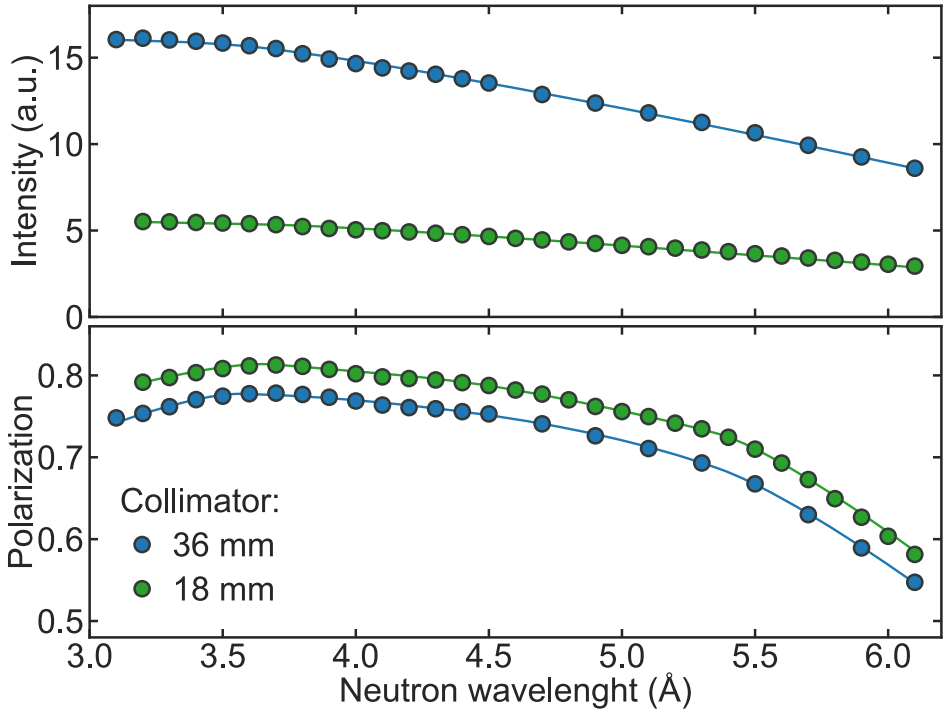

Figure 2.30: Performance of the enhanced neutron depolarization setup. Empty beam intensity and polarization as a function of the neutron wavelength for two collimation values. The solid lines are a guide to the eye.

The integrated intensity at the detector decreases with higher wavelengths, this is expected from the wavelength profile of the cold source which is maximum around 1.6 Å and decreases rapidly. Predictably, with the larger collimator hole there is a significant increase in neutron intensity. The polarization profile is more complex. Both polarization profiles have a maximum around 3.7 Å and decrease very slowly until 5.5 Å where the slope becomes more significant. The beam polarization is a product of the polarization efficiency of the polarizer, close to 80 % and analyzer, close to 99 %. The flipping ratio of the spin flipper is approximated to 1 as a narrow wavelength band is shaped by the velocity selector. With increasing neutron wavelengths, the efficiency of the v-shaped polarizer increases, while the efficiency of the analyzing focusing guide decreases. The competition between this two effects explains that a maximum

where the crossover between the two efficiency slopes is obtained. The v-shape polarizer is most effective with a well collimated neutron beam, therefore the polarization is slightly higher with the smaller collimator. The achieved beam polarization is significantly higher, around 75 % for a wavelength below 5 Å, compared to the typical beam polarization obtained in standard ND experiments (65 %).

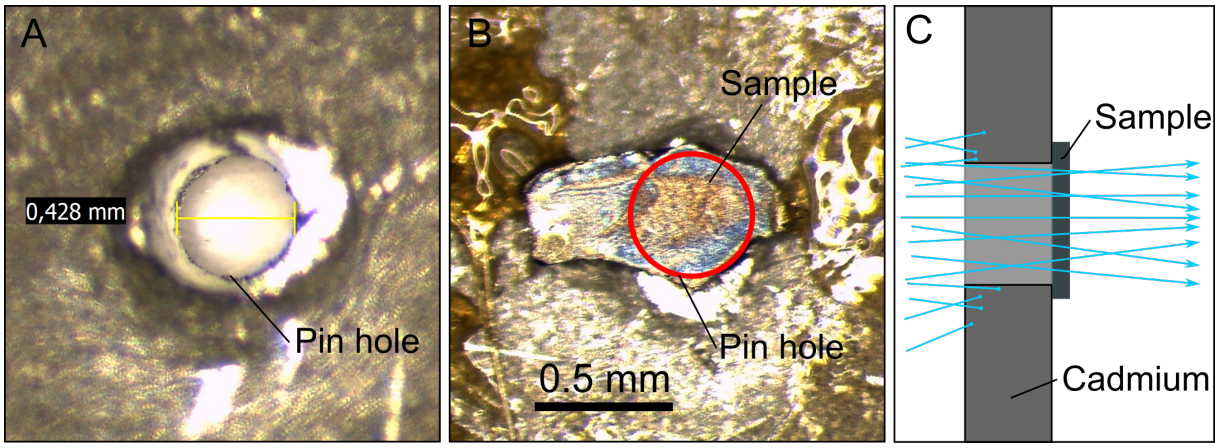

Figure 2.31: Single crystal FM sample placed on a cadmium mask. A: Picture of the 430 µm diameter pin hole pierced into a 0.5 mm thick cadmium foil. B 100 µm thick $HgCr_2Se_4$ sample glued over the hole using low temperature varnish, the red circle highlights the position of the pin hole. C: Schematic side view of the sample and the cadmium foil. Blue arrows represent neutron trajectories.

The previous experiment has been repeated with a ferromagnetic sample placed at the focal spot of the neutron beam. A $HgCr_2Se_4$ single crystal, shaped in a irregular slab of constant thickness (100 µm) has been used. To ensure that all neutrons go through the sample, it is placed over a a 430 µm diameter pinhole of a 0.5 mm thick cadmium foil, as shown in figure 2.31. The sample, with a Curie temperature of 106 K is cooled to 80 K for the duration of the experiment. The results are presented in figure 2.32. Like in the previous experiment, the beam intensity has been obtained by integrating over a ROI, and the beam polarization by fitting the intensity profile when sweeping the current in the flipping coil of the spin flipper. This time, the beam polarization is a product of the polarization of the instrument (measured before), with the depolarization factor of the sample. Thanks to the empty beam polarization measured earlier it is possible to untangle these two quantities.

The neutron depolarization produced by a ferromagnetic sample depends strongly on the neutron velocity, slow neutrons (i.e. long neutron wavelength) spend more time inside the sample and are thus more depolarized by it. This is confirmed in this experiment, the sample depolarization increases strongly with increasing wavelength and reaches 100 % at 5 Å, the neutron beam is no longer polarized. The intensity profile is very similar as before with a rapid decrease of intensity with increasing wavelength.

From these two experiments, the most efficient parameters to use when investigating $HgCr_2Se_4$ under pressure are chosen. First, the larger collimator aperture (38 mm) is favorable as it offers

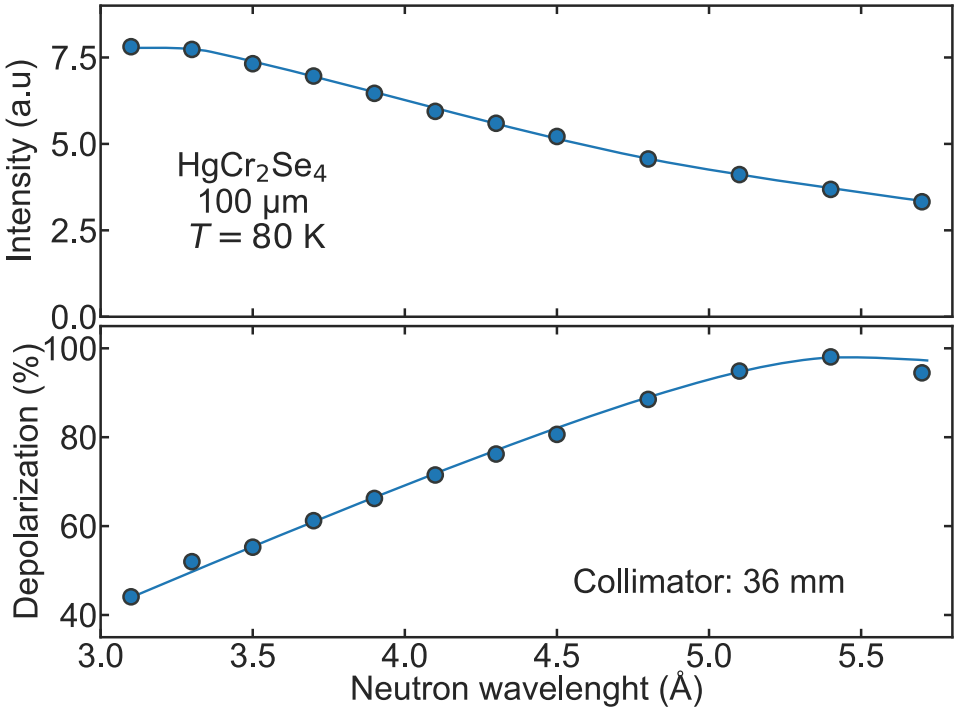

Figure 2.32: Beam intensity and sample depolarization measured as a function of the neutron wavelength. The $HgCr_2Se_4$ sample is shown in figure 2.31. The sample depolarization is calculated by normalizing the beam polarization observed through the sample with the beam polarization measured in figure 2.30. The solid line is a guide to the eye.

not only a larger beam intensity (therefore shorter exposure times), with only a small decrease of the beam polarization, but it also achieves a more homogeneous beam flux across the sample as seen with the McStas simulations. As for the appropriate neutron wavelength to use, a compromise between intensity and depolarization signal is found. For most of the experiments, the velocity selector is tuned at 5 Å. At this wavelength, the sample depolarization is very high, while the overall beam polarization is good, and the neutron intensity is still significant.

Finally, figure 2.33 compares two temperature scans obtained on the same $HgCr_2Se_4$ sample shown in figure 2.31 with a standard ND experiment and with the enhanced depolarization setup described above. Here the beam polarization is normalized to the mean value obtained above the Curie temperature. For the standard ND experiment and the one using focusing guides the neutron wavelength was 4.14 and 4.3 Å, respectively, while the magnetic guide field at the sample position was 5 mT and 20 mT. These slightly different experimental parameters might account for the small differences in the overall shape of the depolarization profile. Nonetheless, the two curves are very similar. The significant factor here is that while the exposure time is kept at 180 seconds per point for both experiments, the standard deviation around the mean value is reduced from 2 % with standard ND, to less than 0.3 % using focusing guides to enhance the ND experiment. By significantly increasing the neutron flux at the sample position the measurement noise has been reduced by an order of magnitude at no cost in exposure time.

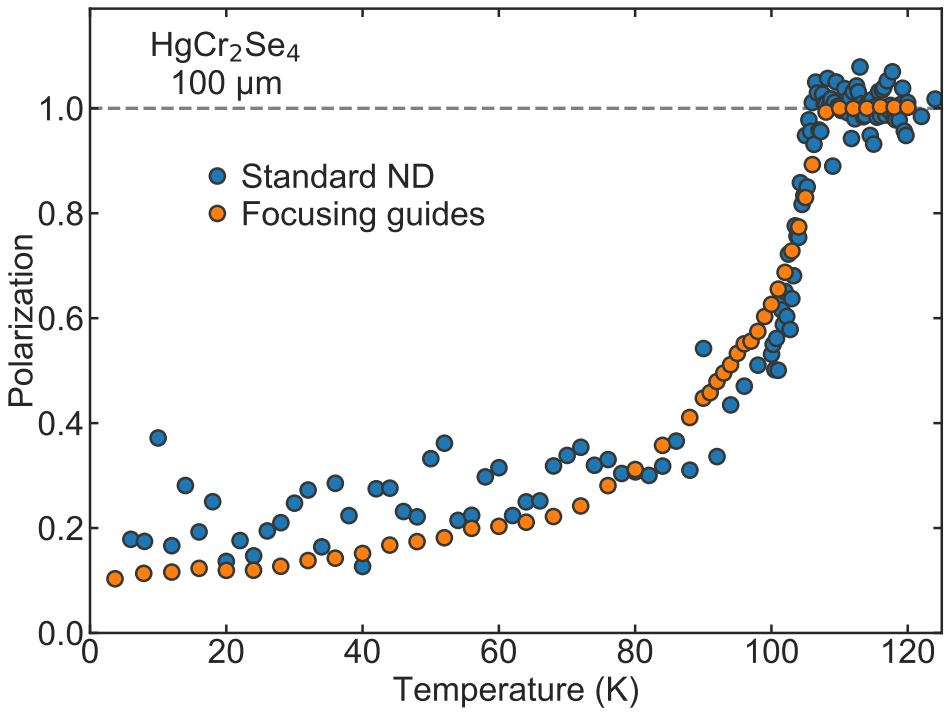

Figure 2.33: Neutron depolarization of a 100 µm thick $HgCr_2Se_4$ sample versus temperature. Two different measurement methods are compared, standard ND (blue), and enhanced neutron depolarization using focusing guides (green). The dashed line indicates the beam polarization level at the paramagnetic state to which the polarization has been normalized.

2.2.5 Proof of principle experiment on superconductors

It is known that superconductors can depolarize a neutron beam [38, 39]. The study of superconductors under pressure is of great interest, for instance the record high superconducting transition had been recently lifted to 260 K in lanthanum hydrides under a pressures of 170 GPa [20, 89], and more recently has reached the milestone of room temperature superconductivity in carbonaceous sulfur hydrides at the staggering pressure of 267 GPa [90]. Superconductivity can also be found as an emergent phase around the quantum critical point of pressure driven ferromagnets [18]. Studying superconductors under pressure becomes technically challenging, specially towards the higher pressures. The different techniques usually used, as high pressure transport and susceptibility measurements, require a highly skilled experimenter capable of correctly placing electrical wires into a very small (sub millimeter) sample space. In contrast for a high pressure neutron depolarization experiment, it is sufficient to load a sample into the pressure cell without any electrical leads or coils. Moreover, unlike transport measurements, neutron depolarization tests superconductivity in bulk.

Neutron depolarization at ambient pressure on a niobium sample, small enough to fit into a diamond anvil cell, was measured using the experimental setup described in this section. Nio-

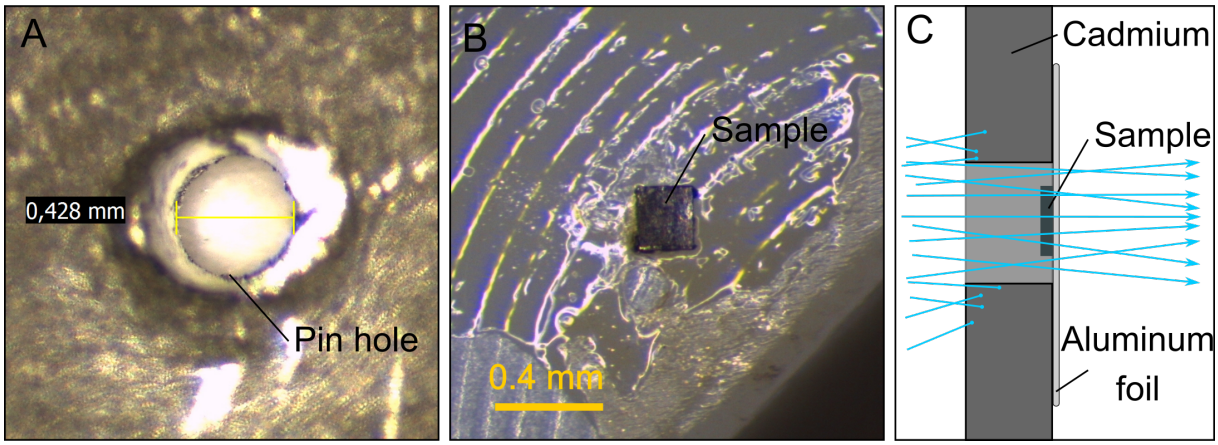

Figure 2.34: Single crystalline niobium sample mounted on a cadmium mask was placed at the focal spot of the neutron guides. A: Photography of the cadmium mask with a 430 µm diameter pin hole. B: Photography of the slab-like niobium sample with dimensions: 240x240x70 µm. C: Sketch of how the sample is placed at the center of the pinhole with the help on aluminum tape. Blue arrows represent neutron trajectories.

bium is a Type II superconductor with a critical temperature of 9.26 K. Figure 2.34 show the cadmium mask used as a diaphragm, the single crystalline sample itself which has been cut into a regular slab-like sample with 250 µm lateral dimensions and 70 µm thickness, and a sketch showing how the sample is placed into the cadmium mask using aluminum tape. The mask is used to absorb neutrons that do not go through the sample and and are thus not depolarized by it, resulting in an increased depolarization signal. The sample is cooled using a standard closed cycle cryostat, and a water cooled electromagnet applies a magnetic field in a direction parallel to the neutron beam. Additionally, magnetization measurements were also performed after the experiment on the same niobium sample to compare the amplitude of the magnetization signal with the neutron depolarization. The magnetization measurements were performed in a standard magnetic properties measurement system (MPMS) from Quantum Design. In absence of any magnetic field a superconductor does not produce any measurable magnetization, and similarly no neutron depolarization. Temperature and field scans were performed in order to better understand how the magnetic shielding and trapped magnetic flux depolarize the neutron beam.

The niobium sample was measured as the temperature was increased across the expected transition value with different applied magnetic fields and cooling histories. Due to a malfunction of the cryostat temperatures below 4 K were not easily reached. The results are shown in figure 2.35 were the changes incurred in the neutron beam polarization are compared to the absolute value of the measured magnetization. Interestingly, the trends observed with both techniques are very similar. In both cases when the sample is cooled under 20 mT of applied magnetic field and measured as it is warmed up under the same field, there is no perceptible signal. For the other field histories, the relative signal amplitude, and the overall temperature profile of the neutron polarization, matches the trend observed with magnetization. The only relevant difference appears for the measurement were the sample is cooled at 180 mT and warmed up at 65 mT, here the signal observed with neutron depolarization seems stronger than for the other field histories,

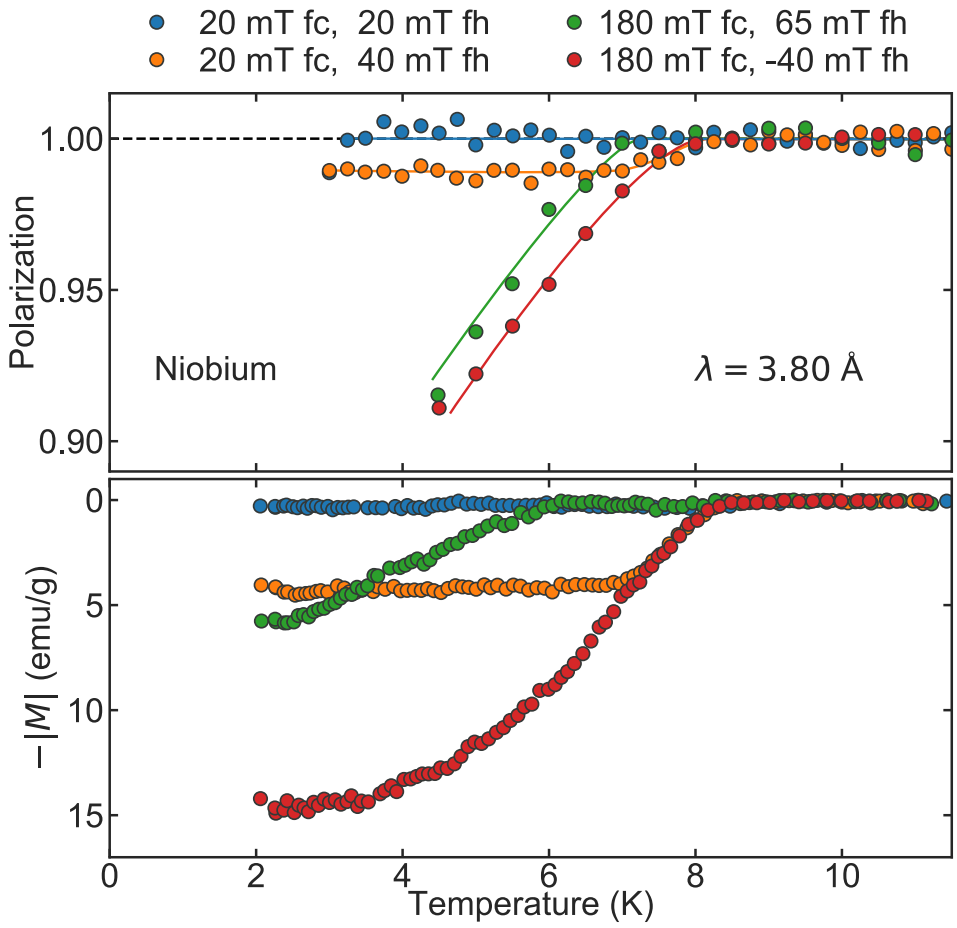

Figure 2.35: Temperature dependence of the neutron depolarization of niobium compared to its magnetization for different field histories. The niobium sample was field cooled (fc) at a given magnetic field, and measured during field heating (fh) at another magnetic field, as indicated in the legend. Top panel shows the neutron polarization (neutron wavelength $\lambda = 3.8$ Å), the solid lines are used as a guide to the eye, while the dashed line indicates the beam polarization level at the paramagnetic state. Bottom panel shows the absolute value of the magnetization as measured on the same niobium sample with the same field history.

when compared to what is observed in the magnetization measurements.

These temperature dependent measurements suggest that the level of neutron depolarization scales with the magnetization and thus with the strength of the magnetic shielding present in the sample. This can in principle be used to map the field dependence of the critical temperature. Unfortunately, at low fields the shielding effect from from niobium is too small to change the neutron beam polarization beyond the measurable range. Therefore, an exact measurement of the critical temperature at zero magnetic field would not be possible with this technique. The temperature dependence of the neutron polarization through a superconductor is also significantly different that what is observed with a ferromagnet (e.g. as in figure 2.33). Here the beam polarization decreases rapidly from the critical temperature to a saturation point where

the sample becomes a perfect diamagnet and then stagnates at this value. As expected from a superconductor, the critical temperature depends strongly on the applied magnetic field.

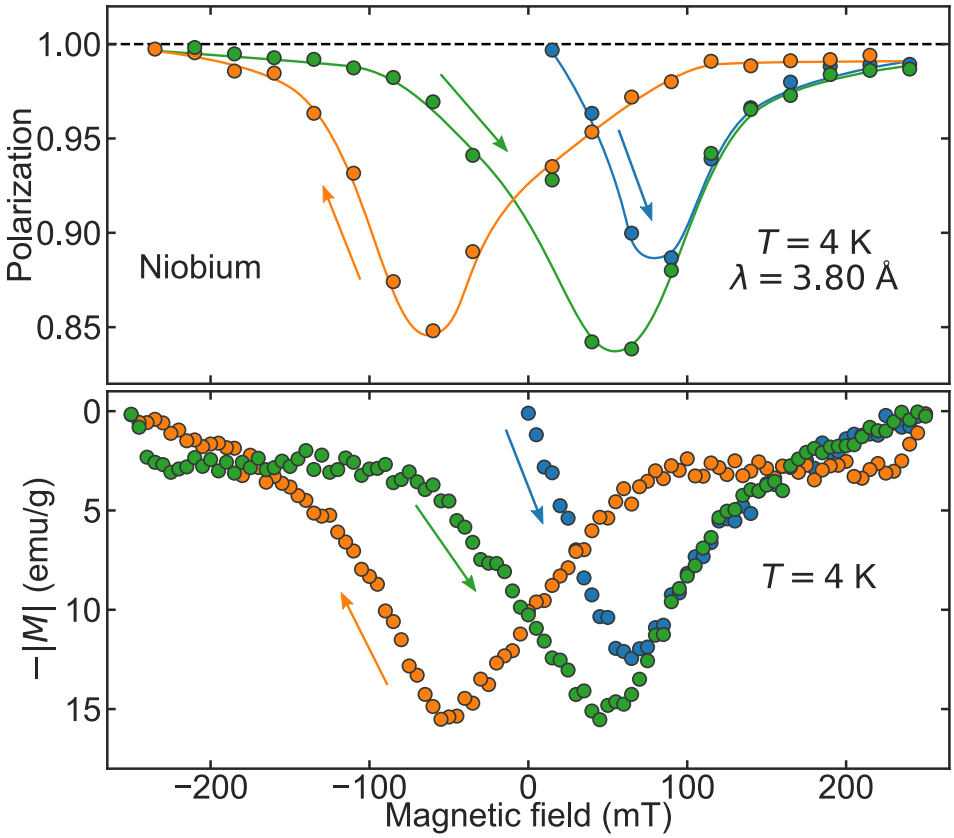

Figure 2.36: Magnetic field dependence of the neutron depolarization of niobium compared to its magnetization across a hysteresis loop at 4 K. The sample was zero field cooled to 4 K. The data points obtained in the 3 branches of the hysteresis loop are plotted in different colors and the sweep direction is indicated with arrows. The top panel shows the neutron polarization (neutron wavelength λ was set around 3.8 Å), the solid lines are used as a guide to the eye, while the gray dashed line indicates the beam polarization level at the paramagnetic state. The bottom panel shows the absolute value of the magnetization as measured on the same niobium sample with the same temperature and field history.

Figure 2.36 shows the neutron depolarization and the absolute value of the magnetization of superconducting niobium across a hysteresis loop at 4 K. The sample was first cooled to 4 K at zero field, then measured as the field is successively increased to 250 mT (virgin curve), decreased to -250 mT (down sweep), and increased again to 250 mT (up sweep). A significant hysteretic behavior is observed. The neutron polarization decreases from the full polarization state as the magnetic field is increased, and at around 70 mT it increases first rapidly until 140 mT and then slowly up to 250 mT where it reaches the full polarization again, i.e. the paramagnetic value. In the down sweep, where the magnetic field is decreased, the neutron polarization remains very close to the fully polarized state down to 100 mT were the neutron polarization starts to

decrease reaching a minimum at around -70 mT with a larger depolarization value than for the new curve. Then, as in the new curve, the beam polarization increases rapidly to -140 mT and then slowly up to -250 mT where it reaches again full beam polarization. The third branch of the hysteresis (up sweep) has a mirror symmetry with respect to the zero field axis of the second branch (down sweep). Interestingly, the profile of the neutron polarization is matched with great detail by the profile of the absolute value of the magnetization, except for a small jump observed in the magnetization measurement at the beginning of the up and down sweeps.

This hysteresis loop measurement further indicates a close relation between the magnetization of a superconductor and the level of neutron depolarization obtained. Furthermore it hints towards the origin of the neutron depolarization. In the new curve, at low magnetic fields, the niobium sample is in a complete shielding state, thus the neutron depolarization can be attributed only to the shielding effect. Above an below the sample, the magnetic field changes abruptly leading to a loss of neutron polarization. At higher fields, once the neutron flux is able to penetrate the sample in the vortex phase, the ability of the superconducting sample to disrupt the polarization of the neutron beam is strongly reduced. The larger signal is obtained when reaching a small field value, before reaching the vortex state and coming from a large field value of opposite sign. This suggest that the trapped magnetic field of opposite polarity inside the superconductor contributes additionally to the shielding effect leading to stronger stray fields around the sample further depolarizing the neutron beam. This particular hysteretic behavior can be used as a unique signature of neutron depolarization through a superconductor to distinguish it from other magnetic orders.

A single crystal lead sample was also measured as part of this proof of principle experiment. Lead, as a type I superconductor ($T_C = 7.2$ K), has smaller critical fields and therefore smaller magnetic shielding can be generated. The lead sample has similar dimensions and is mounted in the same way as the niobium sample showed in figure 2.34. A hysteresis experiment, similar to the one performed on niobium sample, but at 3.5 K was performed. The lead sample was similarly cooled to 3.5 K at zero field, the magnetic field was then driven to 90 mT, -90 mT, and 90 mT, successively. The results are shown in figure 2.37. The hysteretic behavior of the neutron depolarization profile is similar than the one observed for niobium. The main difference is that the amplitude of the signal has been reduced by and order of magnitude (maximum depolarization observed has decreased from 15 % to 1.5 %) leaving it at the edge of the measurable range. This is also in accordance to a strong reduction of the amplitude of the magnetization measurement indicating that lead has a more limited capability than niobium to repel magnetic fields, as expected. Type II superconductors are therefore more easily observed with neutron depolarization measurements than type I.

Finally the effect of the neutron wavelength on the neutron depolarization through superconductors is also addressed. Temperature dependent measurements were performed on a niobium sample using different neutron wavelengths from 3.2 to 5.3 Å. For all measurements, the niobium sample was cooled under 20 mT of applied magnetic field. The field was then increased to 60 mT, and the neutron polarization was measured as the sample warmed up through the transition temperature. The results are shown in figure 2.38. Despite the small amount of data points measured, it is obvious that the larger neutron depolarization is obtained for the longest neutron wavelength. Similarly to neutron depolarization through a ferromagnet, slower neutrons spend longer time inside a area with a given magnetic field and are therefore more depolarized.

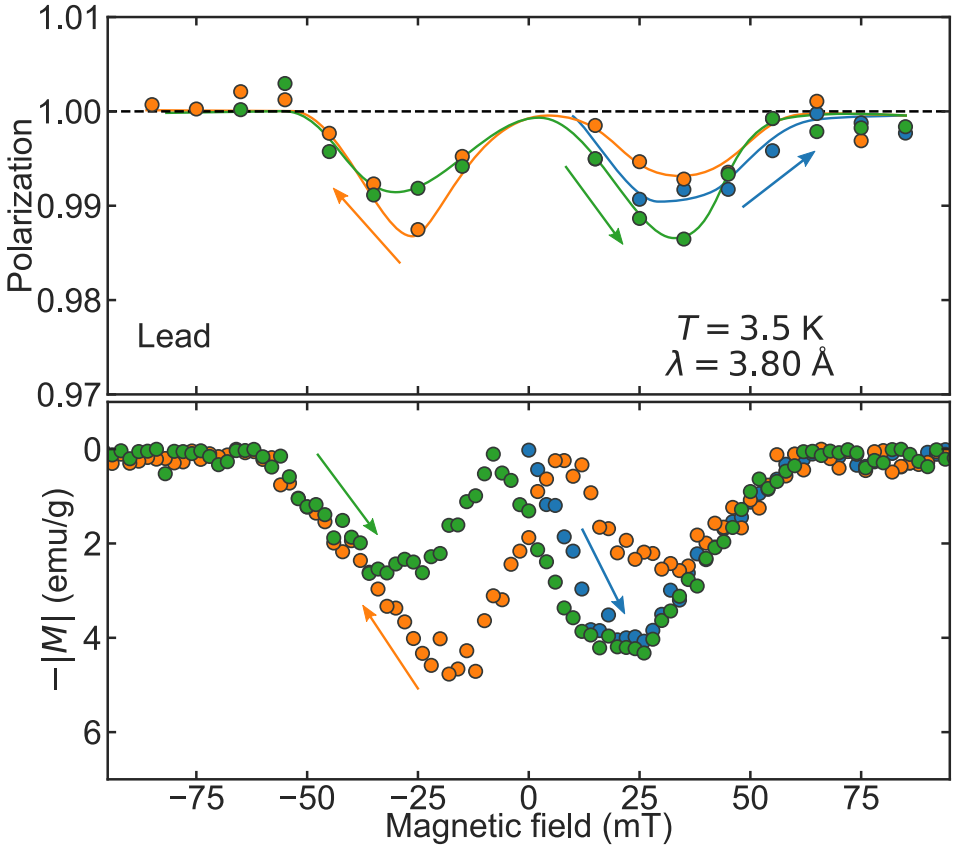

Figure 2.37: Magnetic field dependence of the neutron depolarization of lead compared to its magnetization across a hysteresis loop at 3.5 K. The sample was zero field cooled to 3.5 K. The data points obtained in the 3 branches of the hysteresis loop are plotted in different colors and the sweep direction is indicated with arrows. The top panel shows the neutron polarization (neutron wavelength $\lambda = 3.8$ Å), the solid lines are used as a guide to the eye, while the dashed line indicates the beam polarization level at the paramagnetic state. The bottom panel shows the absolute value of the magnetization as measured on the same niobium sample with the same temperature and field history.

Although the neutron depolarization seems to decrease linearly with the wavelength down to 3.6 Å, it suddenly collapses at 3.2 Å. This suggests that there might be a threshold in the magnetic inhomogeneity of shielding effect under which neutron depolarization does not occur. The exact mechanism of that effect are unclear.

It is important to point out that these measurements were performed in an early stage where the design and use of the neutron focusing guides was still being tested and improved. The quality of the measurements here presented can be substantially improved with the current optimized experimental setup. Most notably, at the time of the measurements, the alignment of the neutron focusing guides was not ideal, this was further worsen by the fact that the magnetic field of the magnet could slightly induce a tilt on the neutron guides. A stiffer guide mount with a clamping mechanism to fix the guides was later introduced.

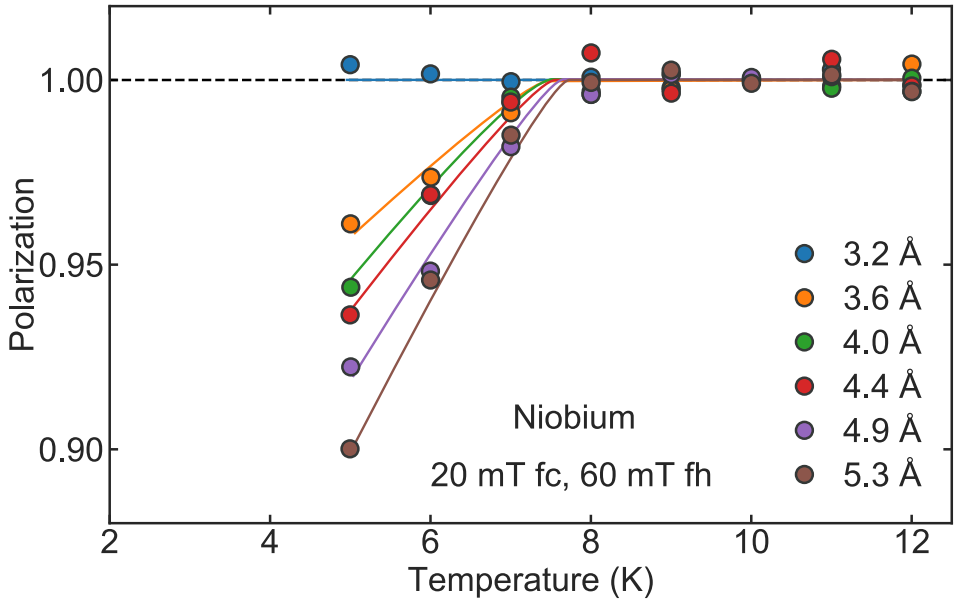

Figure 2.38: Neutron wavelength dependence of the neutron depolarization through a niobium superconducting sample. The sample was field cooled (fc) under an applied magnetic field of 20 mT and then measured as it is heated (fh) up to 12 K under a magnetic field of 60 mT. This process was repeated for different neutron wavelengths as indicated in the legend. The solid lines are used as a guide to the eye, while the dashed line indicates the beam polarization level at the paramagnetic state.

2.2.6 Summary and outlook

In this section we have described how neutron depolarization (ND) measurements were adapted to measure small samples inside diamond anvil cells by using focusing neutron supermirror guides to increase the neutron flux at the sample position. The use of parabolic focusing guides is specially suited to efficiently focus and defocus a collimated beam. The mechanical parts designed to place and align the guides were optimized to ensure an easy and stable guide alignment. McStas simulations were performed to evaluate the size and shape of the focal spot, and to understand which are the relevant neutron trajectories. The procedure of aligning the neutron guides and placing the sample at the focal spot of the guides is also described in detail, and the guidelines on how to analyze the raw data are given. The performance of the new enhanced neutron depolarization technique is tested against different experimental parameters and with different samples. $HgCr_2Se_4$, a ferromagnetic sample, was measured with a standard ND experiment and the enhanced ND here described. The comparison shows that by introducing the focusing guides the signal to noise ratio was reduced by an order of magnitude while requiring the same exposure time. Finally, we have used this enhanced ND technique to measure the neutron depolarization of superconducting niobium and lead samples small enough to fit inside a diamond anvil cell. Beyond demonstrating as a proof of principle that enhanced ND can be used to investigate superconductors under pressure, our measurements indicate that the level

of neutron depolarization produced by a superconductor scales quite linearly with the absolute value of its magnetization. Moreover, the neutron depolarization of a superconductor across a hysteresis loop shows a distinctive behavior which can be used to distinguish it from other magnetic textures. Regarding the neutron wavelength, although a larger neutron intensity is obtained with shorter wavelengths, it is preferable to increase the ND signal by using slower neutrons, i.e. longer wavelengths. A neutron wavelength of 5 Å is long enough to produce a sizable neutron depolarization while the empty beam polarization is still significantly large, this value will be used for most of the experiments performed hereafter.

The focusing guide module constructed in the scope of this thesis can in principle be adapted to any instrument capable of ND experiments and provided of a 2D neutron detector. The guides used here were designed to enhance neutron scattering experiments, guides designed specifically for ND experiments with cold neutrons ($\lambda > 4$ Å) could lead to much larger increases of neutron flux at the sample position. The experimental setup could also be made much more compact by having polarizing supermirror coating on both focusing and defocusing guides, thus not requiring an extra polarizer in front of the guides and shortening the section of the beam between analyzer and polarizer. The challenge here is to fit a efficient spin flipper in the small space between the two guides where strong magnetic fields are present. A possibility would be to adapt some of the miniaturized spin flippers, also called mu-pads and used in spin echo and MIEZE experiments, that use mu-metal to shield the spin flipper from external magnetic fields.

CHAPTER 3

Competing interactions in chromium spinels

In this section we investigate the unconventional magnetic properties of the antiferromagnet $HgCr_2S_4$ by means of magnetic susceptibility, magnetization, and neutron depolarization measurements. Additionally, the pressure dependent magnetic phase diagram of the parent compound $HgCr_2Se_4$ is investigated with high pressure neutron depolarization measurements. The results are discussed and used to clarify the nature of the exchange interactions in the Chromium spinel family. Interestingly, although a FM at ambient pressure, $HgCr_2Se_4$ under sufficient pressure, seems to reproduce similar unconventional magnetic properties as $HgCr_2S_4$, suggesting that the same underlying mechanism is at work. Rather than redefining the exchange interaction in place, arguments are given for a more careful investigation of structural distortions appearing at low temperatures as an escape route from a QCP.

3.1 Motivation

3.1.1 Chromium spinels

The chromium spinel family is a very interesting playground for investigating competing magnetic interactions and the interplay between structural and magnetic degrees of freedom [46]. The chemical formula of these spinels is ACr_2X_4 where A^{2+} is a divalent cation from the last column of the transition metals (Zn, Cd, Hg) and X^{2-} is a divalent anion from the chalcogen group (O, S, Se). A and X atoms get filled d and p orbitals respectively, thus not having a net magnetic moment. The chromium cations Cr^{3+}, in a spin polarized $3d^3$ configuration, carry a magnetic moment with a total spin $S = 3/2$. As shown in figure 3.1, this family of compounds crystallizes to a cubic $Fd\bar{3}m$ (N227) structure [44]. The figure highlights Cr_4X_4 distorted cubes formed by 2 chemically pure interlocked tetrahedrons. Another interesting structure are the edge sharing CrX_6 octahedron with the chromium site at the center. Finally, it is important to mention that the chromium ions form a pyrochlore lattice of corner sharing tetrahedron.

The nature of the exchange interactions between the chromium ions in these spinels is being studied since more than 50 years [44, 45]. The combination of structure and orbital filling gives a good insight into the origin of these interactions. Due to the octahedral environment around the

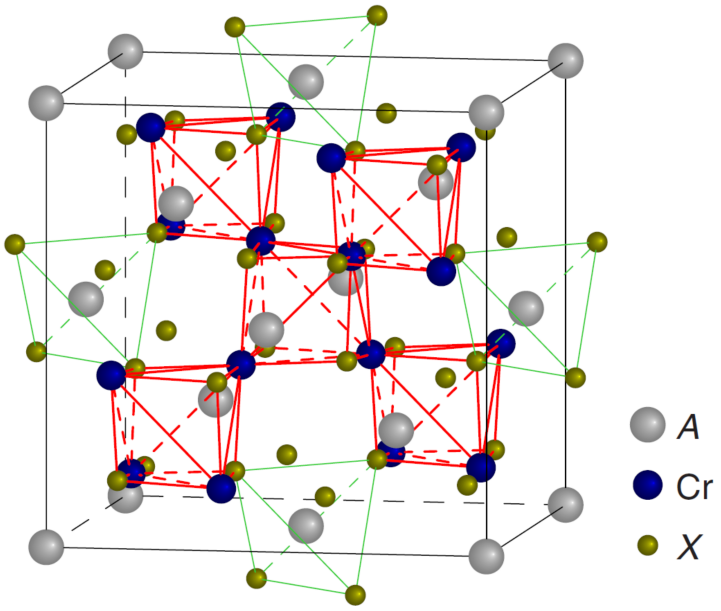

Figure 3.1: Crystal structure of the chromium spinels (ACr_2X_4) at room temperature with an A ion shifted to the origin. Distorted Cr_4X_4 cubes and AX_4 tetrahedra are highlighted by thick red and thin green lines, respectively. [44]

chromium ions, the crystal electric field breaks the energy degeneracy of the d orbitals between the low energy t_{2g} states (d_{xy}, d_{xz}, and d_{yz}) which are half filled, and the empty high energy e_g states (d_{z^2} and $d_{x^2-y^2}$) [46]. The hybridization between the half filled t_{2g} states of neighboring chromium atoms results in an AFM exchange due to the kinetic exchange as the one found in Mott insulators. In the CrX_6 octahedron, the t_{2g} and e_g states, form relatively weak pd$\pi-$ and much stronger pd$\sigma-$ type bonds with the p states of the X atoms [44] situated on the octahedral corners. The resulting hybridization between e_g and p states stabilizes the octahedron, but more importantly it opens the possibility of an indirect 90° FM superexchange between two neighboring chromium ions mediated by the p orbitals of the X ions [44, 46]. Second, third and even fourth nearest neighbors exchange interactions are also considered [44], though being significantly weak, their large multiplicity results in a finite overall contribution.

The resulting competition between the direct AFM exchange and the indirect FM superexchange is at the origin of the interesting variety of ground states in these compounds. The direct AFM exchange decreases rapidly with increasing distance between neighboring chromium ions, as the overlap between the t_{2g} orbitals decreases. Due to the larger directional nature of p orbitals, the strength of the FM superexchange is less susceptible to changes in the volume of the unit cell [44, 46]. Though sharing the same crystal structure at room temperature, the lattice parameter and the bond distances between the atoms changes significantly across the family of compounds. Oxides, sulfurs and selenides show successively larger lattice parameter as the atoms forming the compound are successively larger. Additionally, within compounds that share the same atom at the X site, the compounds with zinc, smaller than cadmium and mercury, have a significantly lower lattice parameter. Figure 3.2 shows the chromium-chromium bond length and the measured Curie Weiss (CW) temperature, obtained form the paramagnetic sus-

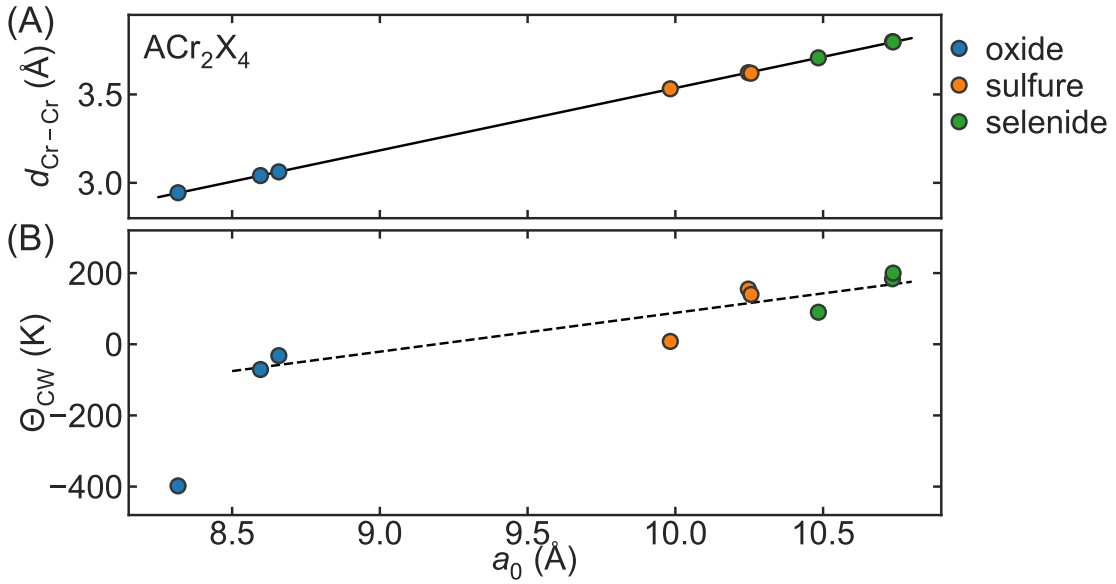

Figure 3.2: Chromium-chromium distance (d_{Cr-Cr}) and Curie Weiss temperature (Θ_{CW}) of the chromium spinels (ACr_2X_4) scales with the lattice parameter. A: Inter-chromium bond distance with respect to the lattice parameter, the solid line is a linear fit over all data points. B: Curie Weiss temperature measured at high temperatures with respect to the lattice parameter, the dashed line is a guide to the eye. The values are taken from [44, 46].

ceptibility at high temperatures, with respect to the lattice parameter of the chromium spinels. The distance between two neighboring chromium atoms scales linearly with the lattice parameter. Likewise, the Curie Weiss temperature also scales with the lattice parameter and goes from negative values for the oxides indicating a dominant AFM exchange, to positive values at larger lattice parameter, indicating a dominant FM exchange. Interestingly, the compounds with zinc have a comparatively lower CW temperature as otherwise expected from their lattice parameter.

Figure 3.3 shows the schematic magnetic phase diagram of the chromium spinels, where the magnetic ordering temperature is plotted with respect to the CW temperature. As expected, the oxide compounds, having a smaller lattice parameter and therefore negative CW temperatures, have an AFM ground state. Despite the large CW temperatures, the Néel temperatures are in the order of 10 Kelvin. The Chromium ions sit in a pyrochlore lattice formed by corner sharing tetrahedrons, hence strong geometrical frustration takes place lowering the Néel temperature. The compounds with the larger lattice parameter and therefore positive CW temperatures order ferromagnetically with relatively large Curie temperatures. In the other hand, $ZnCr_2Se_4$ and $HgCr_2S_4$, despite having positive CW temperatures, have an AFM ground state. The bond frustrated $ZnCr_2S_4$, with a CW temperature close to zero denoting an almost perfect balance between AFM and FM exchange, also shows an AFM ground state.

These observations suggest that a more complex mechanism than a linear dependence to the nearest neighbor distance is in place. The question remains whether the discrepancies between the sign of the CW temperature and the magnetic ground states can be explained in

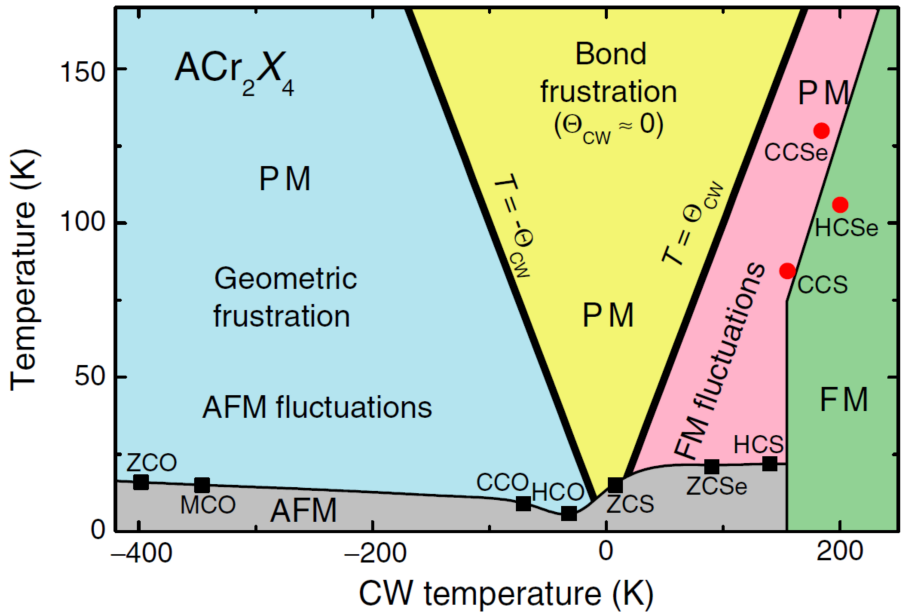

Figure 3.3: Schematic magnetic phase diagram of the chromium spinels, where magnetic ordering temperatures (FM red circles and AFM black squares) are plotted versus the CW temperature. The name of the compounds are abbreviated by removing the stoichiometric proportion and the sentence key letter of the atomic species, except for selenium. Hypothetical magnetic ordering temperatures ($T = \pm\Theta_{\mathrm{CW}}$) are indicated by thick solid lines. Thin solid lines separate magnetic phases and are drawn as a guide to the eye. [46]

simple terms by an underlying physical phenomenon that is shared by all the members of the chromium spinel family. Different interaction schemes are used to explain FM order in $HgCr_2Se_4$ and $CdCr_2Se_4$ [45], and the AFM ground state in $ZnCr_2Se_4$ [91]. As pointed out by N. W. Grimes and E. D. Isaac [92], it seems unlikely that materials that are so similar require different interaction schemes to account for their properties. They suggest that the exchange interactions, which are considered temperature independent in the theoretical models, can change significantly with temperature. Strong evidence of exchangestriction [93] and off-center displacement of the chromium ions in spinel systems at lower temperatures strongly support this claim [94]. More recent discoveries like ferroelectricity in $CdCr_2Se_4$ [95], and phonon anomalies in $CdCr_2S_4$ [96] seem to point out that slight lattice displacements occurring at lower temperatures could be responsible for the observed coupling of magnetic and dielectric moments in these systems.

Beyond a purely theoretical interest, these compounds present a large variety of interesting physical properties within one chemical structure. Electrical properties range from AFM insulators to FM semiconductors [44]. The oxide compounds show complex AFM ground states [46], and even emergent complex magnetic states [97]. Sulfur and selenide compounds show metamagnetic behavior [98], magnetostriction and negative thermal expansion [99], and even multiferroic behavior [95, 100]. By understanding the magnetic interactions in this family of compounds, and their interplay with structural and electronic degrees of freedom, one could build highly functional materials based on chromium spinel heterostructures.

3.1.2 $HgCr_2S_4$ and $HgCr_2Se_4$ compounds

One of the most interesting compounds of the chromium spinel family is $HgCr_2S_4$. Despite having a large positive Curie-Weiss temperature (142 K), it shows AFM order below $T_N = 22$ K. This compound shows an incommensurate spiral order with the propagation vector $\boldsymbol{k}$ parallel to the symmetry axis of the spiral [101]. The magnetic structure below T_N consists of ferromagnetic layers in the ab-plane stacked in a spiral arrangement along the c-axis. The propagation vector $\boldsymbol{k}$ increases from (0,0,0.18) at the Néel temperature to (0,0,0.25) at saturation [102]. When an external magnetic field is applied, the Néel temperature decreases and long range FM order takes place. In a wider temperature range above the Néel temperature, a so called incipient ferromagnetic (IFM) order has been proposed. This IFM state is characterized by a rapid magnetization increase towards the saturation value of 6 μ_B per formula unit under magnetic field, but with zero remnant field. This suggest that, although under large magnetic fields, the sample behaves like a FM, no long range FM order remains when the external field is removed. Furthermore, the temperature dependence of the specific heat (figure 3.4) only shows an anomaly at the Néel temperature, indicating the absence of a sharp phase transition into the IFM state [98].

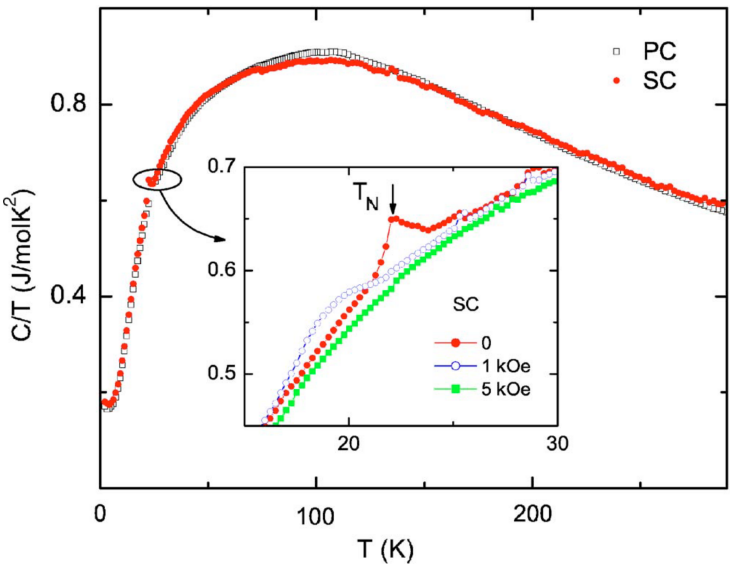

Figure 3.4: Temperature dependence of the specific heat of $HgCr_2S_4$. Open and closed symbols correspond to polycrystal and single crystal measurements, respectively. The inset represents C/T vs T at around T_N for the single crystalline data at different applied fields up to 5 kOe on an enlarged scale. Taken from [98]

Within the range of the IFM, below 60–80 K, the dielectric constant of $HgCr_2S_4$ becomes strongly enhanced, and ferroelectric order is observed below 70 K. Moreover, under applied magnetic fields up to 5 T, colossal magnetocapacitance and magnetoresistance have been observed coinciding with the temperature and field dependent phase space of the IFM phase [100]. These physical phenomena are rather unexpected considering the cubic $Fd\bar{3}m$ structure hitherto assumed, which is incompatible with ferroelectricity. Far from an isolated phenomenon, similar

states are observed in other compounds of this series [95].

The chromium spinel with the larger lattice parameter ($a = 10.737$ Å), and thus the larger CW temperature (200 K), is $HgCr_2Se_4$ [44]. The selenium compound has a ferromagnetic transition temperature of 105.5 - 106 K [24, 45], which is significantly lower than the CW temperature. The reasons for this discrepancy are unclear, a study suggests that magnetoelastic interactions could be responsible for the lower onset of long range magnetic order [103]. This compound has been identified as a semiconductor with a band gap of 0.8 eV at room temperature [104], that drops significantly to 0.2 eV at liquid helium temperatures [105]. The electrical resistivity depends strongly to small changes in sample composition or surface quality, nonetheless, a clear drop of a few orders of magnitude towards a more metallic behavior appears at the ferromagnetic transition. This drop shifts towards higher temperatures under applied magnetic field, leading to a large magnetoresistance [106].

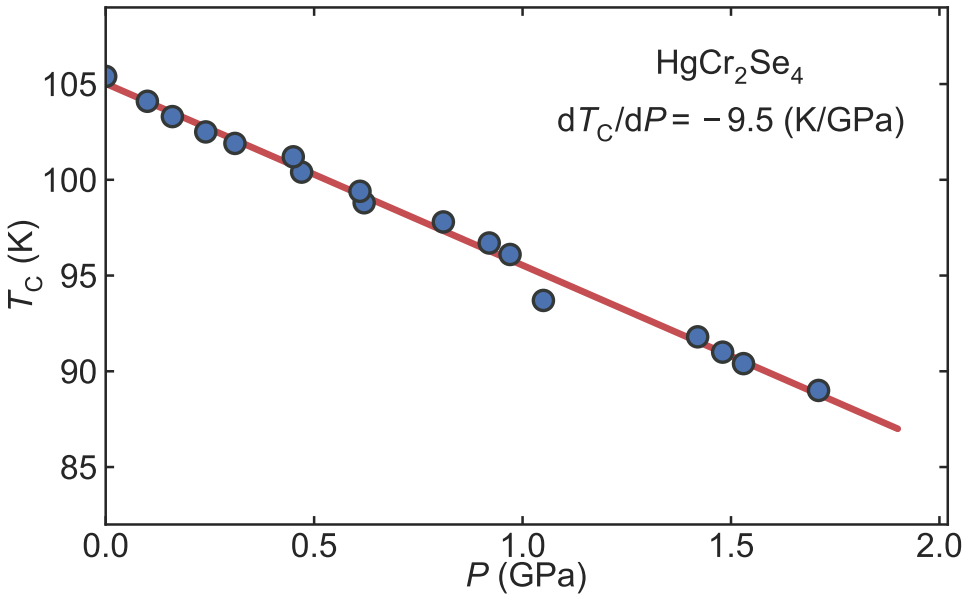

Figure 3.5: Curie temperature of $HgCr_2Se_4$ as function of applied hydrostatic pressure. The red line is a linear fit of the data. [47]

$HgCr_2Se_4$ has raised recent interest for being a candidate of a Chern semimetal with topologically unavoidable band crossings at the Fermi level. This state is a condensed-matter realization of Weyl fermions in (3+1) dimensions, and should exhibit remarkable features, such as magnetic monopoles and Fermi arcs [107]. Experimental evidence support this claim identifying the ground state of this ferromagnetic semiconductor as a half metal with spin polarization levels up to 97 % [108].

Early studies have identified a linear decrease of the Curie temperature for the 3 ferromagnetic compounds ($HgCr_2Se_4$, $CdCr_2Se_4$, and $CdCr_2S_4$) under applied pressure up to 1 GPa [24]. More recently, Michael Wagner made detail measurements on the magnetization of $HgCr_2Se_4$ under hydrostatic pressure up to 2 GPa as part of his doctoral thesis [47]. As shown in figure 3.5, this study confirms that Curie temperature decreases linearly within the explored range with

a rate of 9.5 ± 0.2 GPa/K. No changes in the magnetization curve with respect to the critical temperature were observed, confirming that $HgCr_2Se_4$ remains a Heisenberg ferromagnet under moderated pressures. Moreover, it was confirmed that the saturation magnetization of 6 μ_B per formula unit, remains constant over the whole pressure range.

Hydrostatic pressure is a unique tuning parameter to investigate the interplay between structure and magnetism in the chromium spinels. It offers a clean way to tune the lattice parameter and thus change the relative strength between FM and AFM exchange in a continuous way and without changing the chemical composition. High pressure x-ray scattering on $HgCr_2Se_4$ at room temperature shows no structural transformations up to 15 GPa [109], as the structure is maintained, the exchange mechanisms described earlier is not expected to change. Moreover, the lattice parameter decreases almost linearly with pressure, thus the linear decrease of the critical temperature is expected to continue to higher pressures down to zero Kelvin around 10 GPa. At this point a quantum critical point could be expected [5] where the strength of the competing exchange interactions is perfectly compensated.

3.2 Magnetic properties of $HgCr_2S_4$ at ambient pressure

This section presents the magnetic properties of $HgCr_2S_4$ at ambient pressure. First, the magnetization and magnetic susceptibility are measured as function of temperature and external field using a magnetic properties measurement system (MPMS) from Quantum Design equipped with a 14 Tesla superconducting magnet. The same sample is then used to measure neutron depolarization as function of temperature and field. The sample, shown in figure 3.6, has a quasi regular octahedral shape with 1 mm long edges, where the regular facets are along the (111) crystal planes.

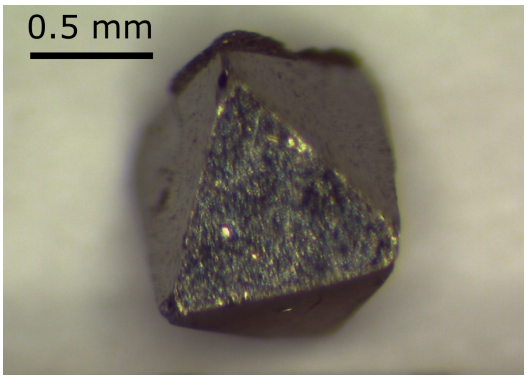

Figure 3.6: Picture of the single crystal $HgCr_2S_4$ sample measured in this section. The sample has a quasi regular octahedral shape with 1 mm long edges. The regular facets are along the (111) crystal planes.

The samples used in these experiments have been prepared by Vladimir Tsurkan. Single crystals are grown by means of chemical transport reactions using pre-synthesized high-purity polycrystals as starting materials. The growth experiments are performed at temperatures between 850° and 800° Celsius [98].

3.2.1 Temperature and field dependence

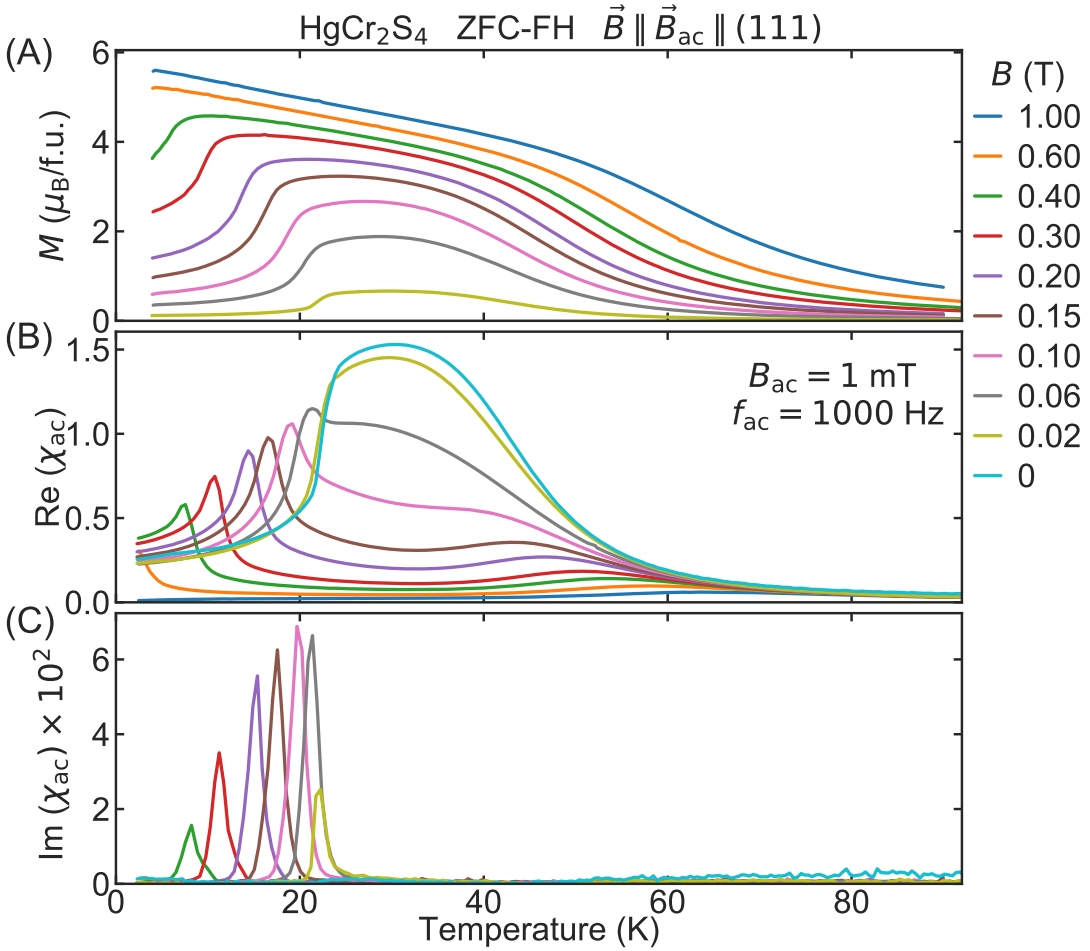

Figure 3.7: Temperature dependence of the magnetic properties of $HgCr_2S_4$. Temperature dependence of the magnetization (M), and the real and imaginary part of the magnetic susceptibility (Re (χ_{ac}) and Im (χ_{ac})), for different applied magnetic fields (B). The sample is zero field cooled (ZFC) and measured upon field heating (FH). The applied field is parallel to the ac excitation (B_{ac}), and the (111) crystallographic direction. The amplitude and frequency of the excitation are 1 mT and 1 kHz, respectively.

The temperature dependence of the magnetization and ac susceptibility was measured under several applied magnetic fields ranging from 0 to 14 T. The sample was first cooled at zero field from a temperature of at least 150 K, then the measurements were performed upon heating the sample from 2 K up to 90 K under a given applied magnetic field. Additionally, two field cooled measurements were performed at 10 T and 100 mT revealing no difference with the zero field cooled measurements. The temperature dependence of the magnetization and ac susceptibility for different applied fields is shown in figure 3.7, only relevant measurements (from 0 to 1 T) are shown. The magnetization curve under applied fields of 0.6 T and 1 T, show the typical behavior of a FM where the magnetization increases more rapidly above the Curie temperature. For all curves with an applied field of 0.4 T or less, there is a clear downturn in the magnetization at low temperatures corresponding to the onset of the AFM ground state, which starts at 22 K for

the lower applied field and is pushed towards lower temperatures for increasing magnetic fields. At zero field, the real part of the magnetic susceptibility shows a large signal in the intermediate temperature region between 60 K and 20 K. At the Néel temperature the magnetic susceptibility decreases strongly. As the magnetic field is increased, the broad large signal decreases rapidly, and at the same time a rather sharp peak appears at the Néel temperature which is pushed to lower temperatures. At 150 mT a small broad peak is revealed around 50 K, for increasing fields this peak decreases in intensity and becomes broader while the peak temperature increases. Finally, the imaginary part of the susceptibility shows a sharp peak at the Néel temperature, except for the zero field measurement where no peak is observed. The intensity of the peak increases rapidly with applied field, it becomes maximal at 100 mT, and decreases slowly for higher fields.

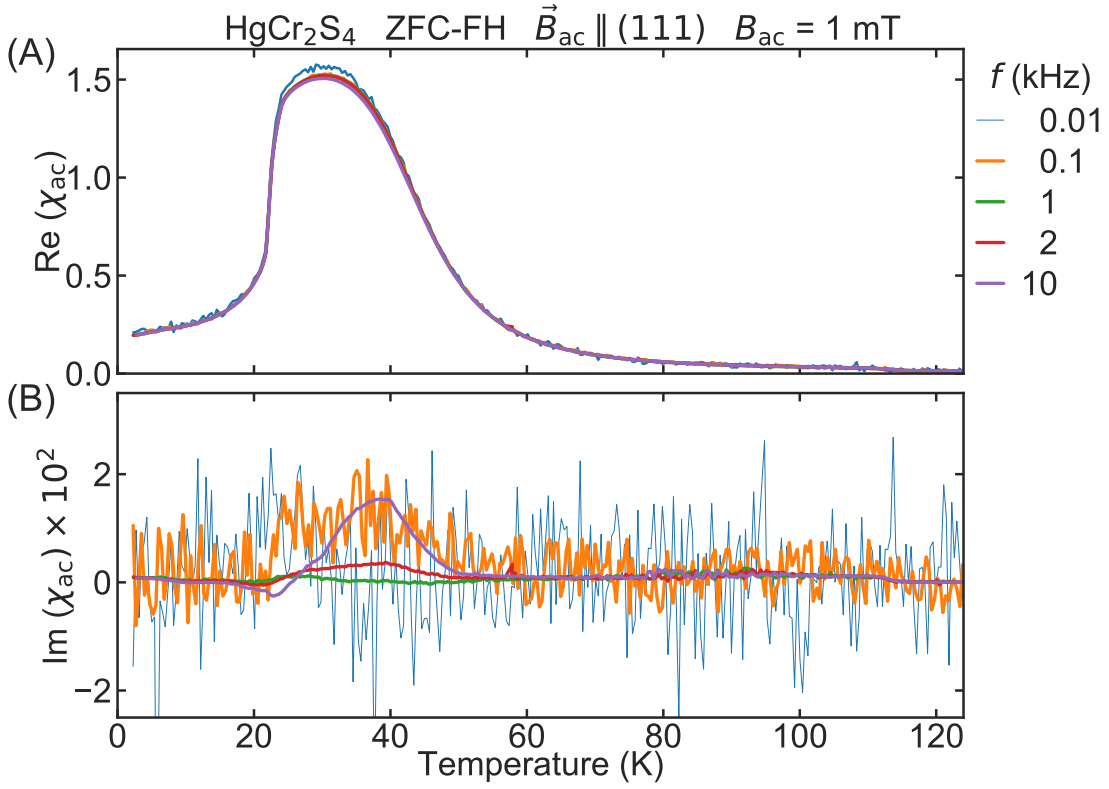

Figure 3.8: Frequency dependence. Temperature dependence of the real (A) and imaginary (B) part of the magnetic susceptibility (Re (χ_{ac}) and Im (χ_{ac})) of $HgCr_2S_4$ at zero field for different excitation frequencies. The sample was cooled at zero field (ZFC) and measured upon zero field heating (ZFH). The ac excitation field (B_{ac}) with an amplitude of 1 mT is parallel to the (111) crystallographic direction.

These measurements are in good agreement with the results presented by Tsurkan et. al. [98], where the reduced magnetization in the AFM phase is well reproduced. In addition, the high density of ac susceptibility measurements allows us to do supplementary observations. First, the large signal in the intermediate region between 60 and 20 K, which coincides with the incipient ferromagnetic phase (IFM), is rapidly suppressed under field. Moreover, a clear peak appears at the Néel temperature for both the real and imaginary part of the magnetic susceptibility.

Looking at the real part of the susceptibility, it is not clear whether at very low fields this peak cannot be distinguished from the broader signal at intermediate temperatures or it is not present. Interestingly, at zero field there is no peak in the imaginary part of the susceptibility, suggesting that changes occur in the transition into AFM state when a magnetic field is applied.

The magnetic susceptibility at zero field was repeatedly measured with different excitation frequencies ranging from 10 Hz to 10 kHz, and two different excitation amplitudes (1 and 0.5 mT). No significant difference has been observed. The temperature dependence of the magnetic susceptibility at zero field for different excitation frequencies is shown in figure 3.8. The real part of the susceptibility is almost identical for all investigated frequencies. There is a very small signal in the imaginary part present at 100 Hz and 10 kHz suggesting that a dissipation phenomenon (e.g. magnetic domain walls moving) could be taking place.

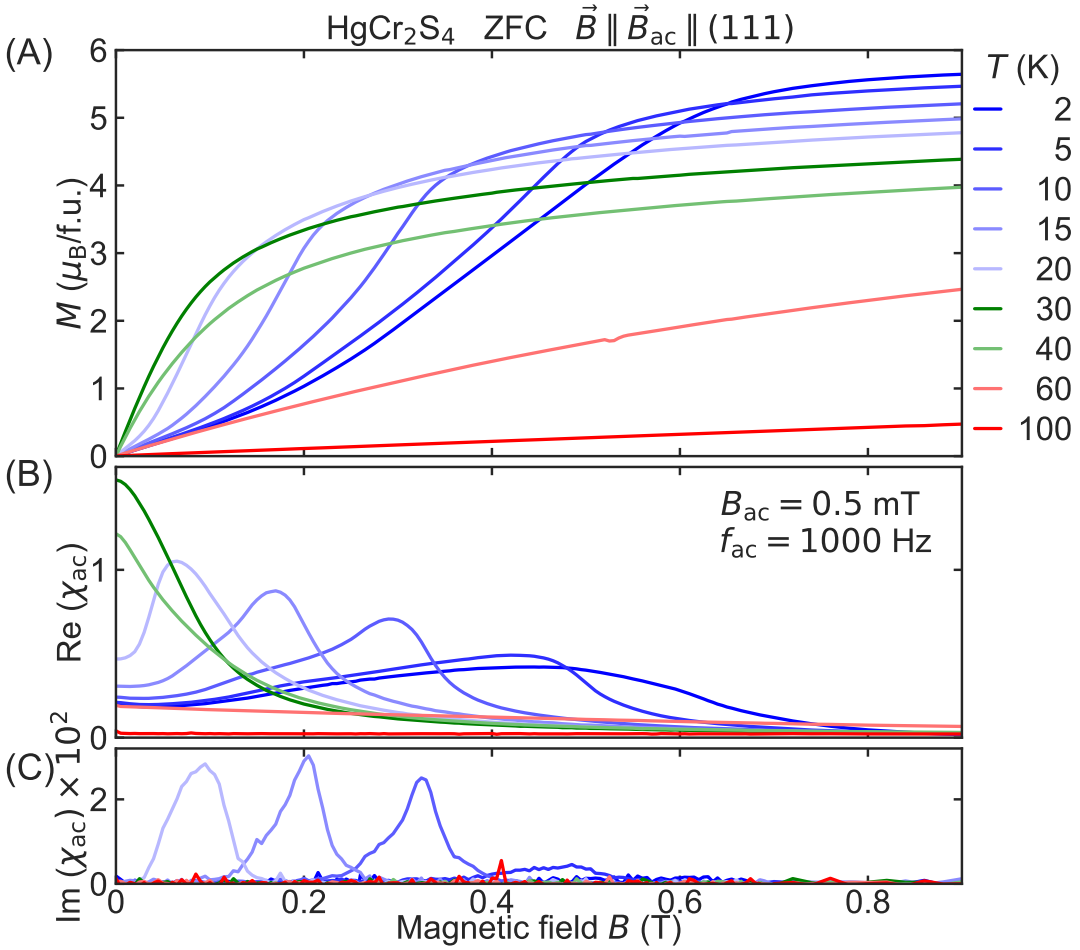

Figure 3.9: Magnetic field dependence. Magnetic field dependence of the magnetization (M), and the real and imaginary part of the magnetic susceptibility (Re (χ_{ac}) and Im (χ_{ac})), for different temperatures. The samples were zero-field cooled (ZFC) before each field sweep. The curves in blues, greens, and reds correspond to the AFM , intermediate, and high temperature PM regimes, respectively.

The field dependence of the magnetic properties of $HgCr_2S_4$ was studied in detail at several temperatures. The sample was cooled from 150 K to the measurement temperature at zero field. Once this temperature was reached, the magnetization and AC susceptibility were measured as the magnetic field increased to +4 T and subsequently decreased to −4 T.

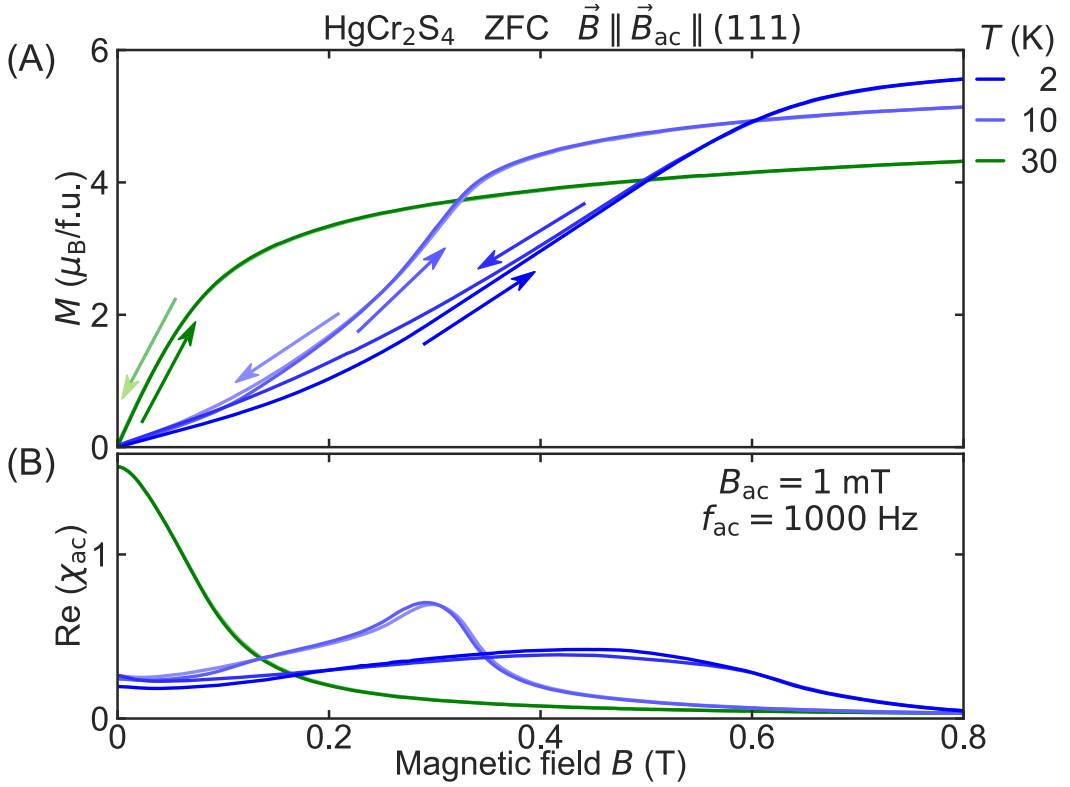

Figure 3.10: Magnetic hysteresis. Magnetic field dependence of the magnetization (M), and the real part of the magnetic susceptibility (Re (χ_{ac})), at different temperatures, for increasing (darker color) and decreasing (lighter color) field.

Figure 3.9 shows the magnetization and magnetic susceptibility as the field was increased from the zero field cooled state (virgin curves). Three distinct regimes can be observed in the magnetization, AFM, intermediate temperature, and high temperature PM regimes. In the AFM regime, corresponding to the blue curves, at first, the magnetization increases slowly with field, following the paramagnetic curve at 60 K. Arriving at the meta-magnetic transition into the incipient FM phase (IFM), for a given field which becomes lower for higher temperatures, the magnetization increases then more rapidly until it reaches saturation. The real and imaginary part of the susceptibility show a broad peak at the meta-magnetic transition. The meta-magnetic transition from the AFM ground state into the IFM state, as a function of field, seems to becomes sharper as the temperature is increased towards the Néel temperature. The rise of the magnetization across this transition becomes faster for increasing temperatures. Similarly, below 10 K, the peak in the real part of the susceptibility becomes extremely broad while it disappears in the imaginary part. In the intermediate regime, the magnetization rises quickly from zero field towards saturation like in a FM, while the large susceptibility signal becomes suppressed under field as previously observed.

Figure 3.10 shows the magnetization and magnetic susceptibility at 2 K, 10 K, and 30 K for increasing and decreasing fields. Hysteresis is only observed in the AFM regime, and it is largest at 2 K and decreases with increasing temperature to disappear completely at 20 K. Upon lowering the magnetic field across the meta-magnetic transition, the magnetization remains slightly higher than for the virgin curve before crossing through the origin. The field reversing curves are not shown because the superconducting electromagnet produces a remnant field, of circa 10 mT, which cannot be compensated for in this branch and adds a slight spurious deformation of the curve. Nonetheless its seems that upon reversing the magnetic field (the third branch of the hysteresis), the magnetization curve remains somewhat between the previous two curves. This has also been reported in the literature and it is suggested that is is due to the reorientation of the three possible domains of the AFM spiral [98]. In the intermediate and high temperature regimes no hysteresis is observed, i.e. no remnant magnetization. The intermediate temperature regime is not truly a FM.

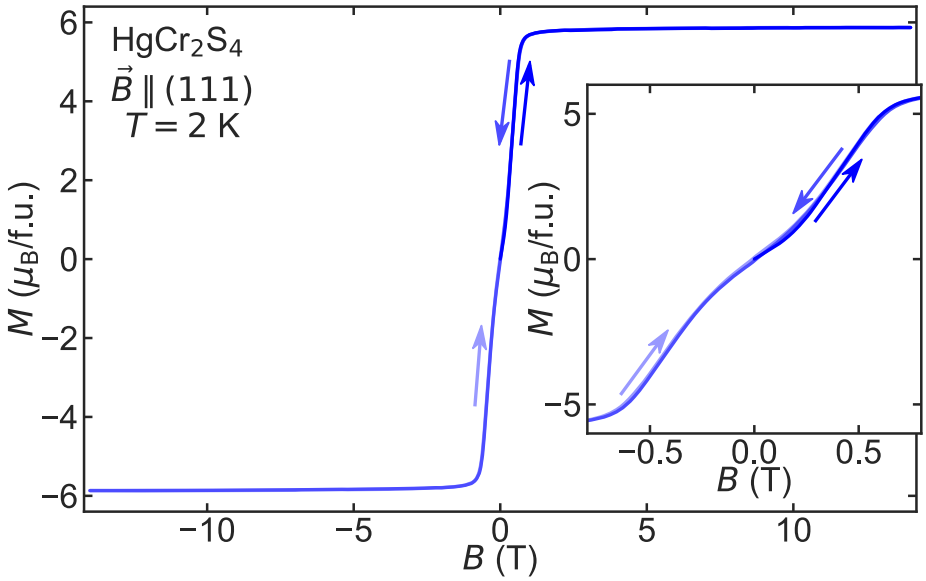

Figure 3.11: Full range hysteresis curve of $HgCr_2S_4$. Magnetic field dependence of the magnetization (M) at a temperature of 2 K, for successive magnetic field sweeps from 0 to +14 T, +14 T to −14 T, and −14 T to +14 T (respectively lighter tones of blue). The inset shows the same data with the field axis zoomed-in around the origin.

The magnetization of $HgCr_2S_4$ was investigated across the full range of the 14 Tesla magnet at $T = 2$ K. Figure 3.11 shows the 3 branch hysteresis curve of the magnetization from −14 T to +14 T at a temperature of 2 K. Despite the anomaly at small magnetic fields described above and attributed to the meta-magnetic transition into the IFM phase, no other significant feature is observed. The magnetization tends asymptotically towards saturation at the full value of 6 μ_B/f.u. as expected for two Cr^{3+} ions per formula unit. The inset in figure 3.11 highlights the absence of a remanent field, as expected from the AFM ground state. It becomes difficult to establish whether a very small remanent field is still present in the sample because the electromagnet used has itself a sizable remanent field, of circa 10 mT, depending on the field history.

3.2.2 Spin clustering at 114 K

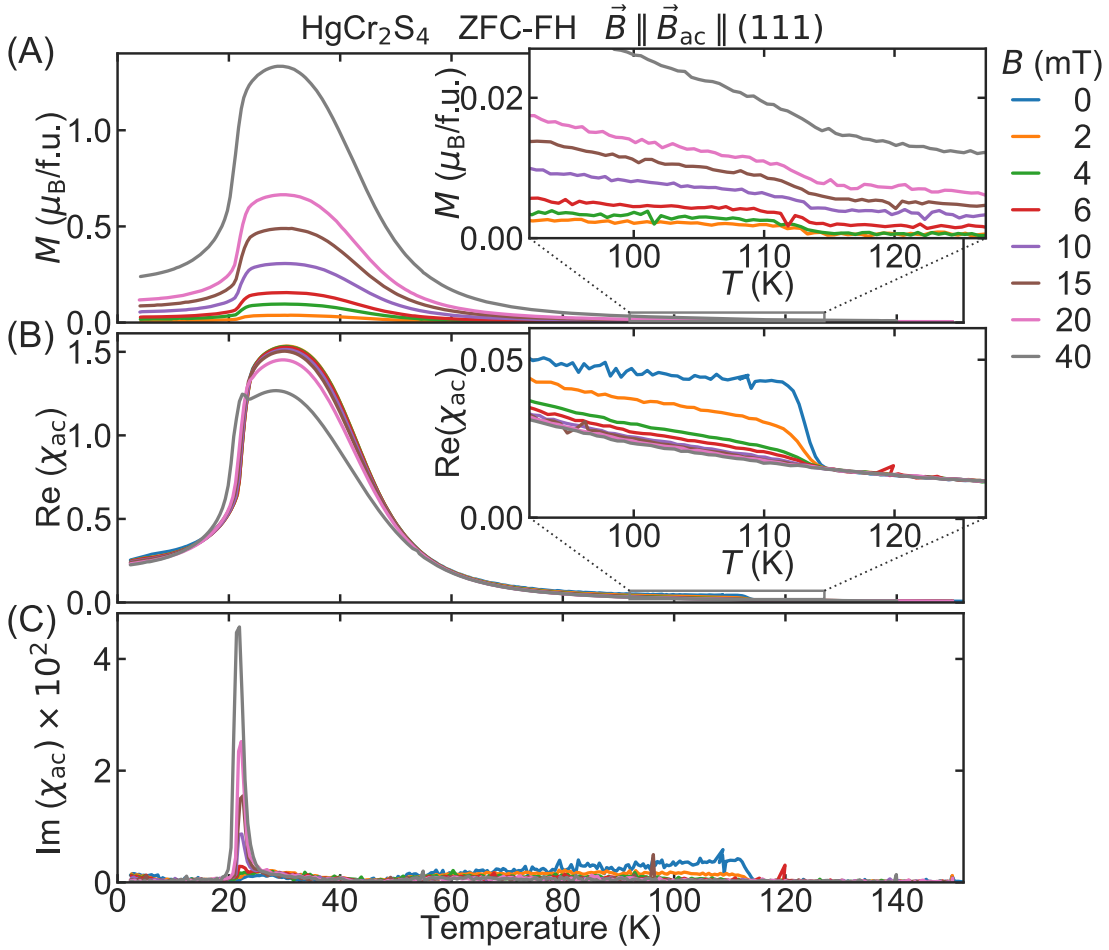

Figure 3.12: Temperature dependence of the magnetic properties of $HgCr_2S_4$ at very low magnetic fields. Temperature dependence of the magnetization (M), and the real and imaginary part of the magnetic susceptibility (Re (χ_{ac}) and Im (χ_{ac})), for very small applied applied magnetic fields (B). The 2 insets expand figures in the area delimited by the gray squares where an unexpected behavior can be observed. The amplitude and frequency of the excitation field are 0.5 mT and 1 kHz, respectively.

In addition to the previous observations, which build up on the hitherto known magnetic properties of $HgCr_2S_4$, an interesting behavior has been discovered in the paramagnetic regime. This behavior is highlighted in figure 3.12, where the temperature dependence of the magnetic properties of $HgCr_2S_4$ under very low applied magnetic field are shown, by taking a closer look at the data between 90 K and 120 K. Independently of the applied field, there seems to be a subtle but clear increase in the magnetization at 114 K. In the real part of the magnetic susceptibility, a much more significant increase can be observed at zero field, although it becomes strongly suppressed under field. With an applied field of 2 mT the jump in the susceptibility is

reduced by half, disappearing completely at 20 mT. With decreasing temperature, the anomaly decreases gradually. In the imaginary part of the susceptibility, there is a very small signal appearing below 114 K for zero applied field, but it is not clear whether is has to do with a real dissipative phenomenon, or it is due to a small phase shift between X and Y channels. Additionally, the development of the peak in the imaginary part of the susceptibility at the Néel temperature can be clearly seen.

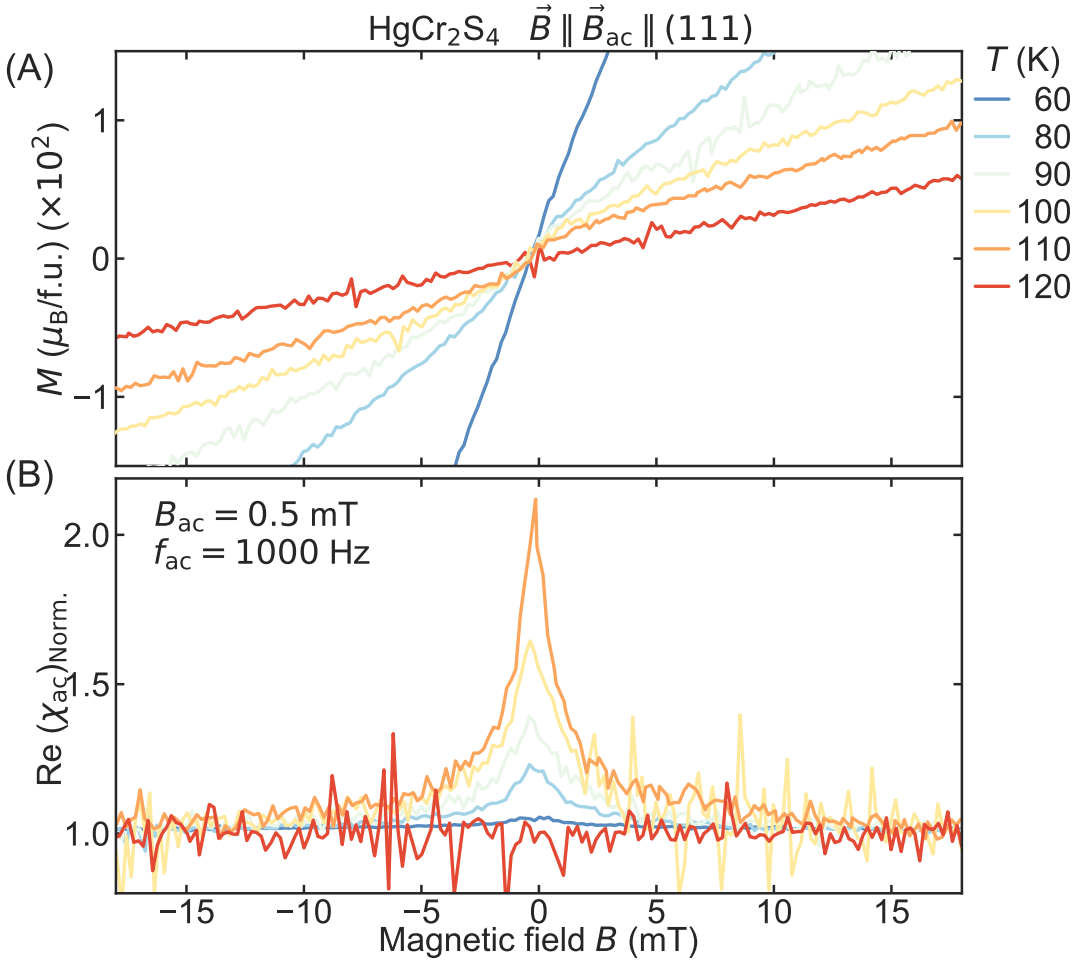

Figure 3.13: Field dependence of the anomaly below 114 K. Magnetization (M) and real part of the ac susceptibility (Re (χ_{ac})) of $HgCr_2S_4$ as the magnetic field is decreased across zero from 50 to −50 mT at different temperatures. The amplitude and frequency of the excitation field are 0.5 mT and 1 kHz, respectively. The real part of the magnetic susceptibility is normalized to its average value for fields with an absolute value higher than 20 mT.

The field and temperature dependence of the observed anomaly was further investigating by carefully sweeping the magnetic field at different temperatures. The sample was cooled from 150 K to the measurement temperature at zero field. Once this temperature is reached, the magnetization and AC susceptibility are measured as the magnetic field was increased to +50 mT and subsequently decreased to −50 mT. No significant difference can be observed between the

virgin curve and the field reversing curves. The field dependence of the anomaly observed below 114 K in the magnetization and real part of the ac susceptibility is shown in figure 3.13 for different temperatures. Although small, an s-shaped anomaly can be seen in the magnetization around zero field for all temperatures between 110 K ans 80 K. At 120 K this anomaly is completely gone. At 60 K the magnetization slope is significantly steeper, making it hard to clearly determine whether there is an s-shaped anomaly. The real part of the ac susceptibility, as seen in figure 3.9, has a rather flat variation with field in the currently studied temperature regime. Here it has been normalized to its average value for fields with an absolute value higher than 20 mT. The anomaly here can clearly be seen as a sharp peak in the susceptibility around zero field, which decreases rapidly until 2 mT, and then decreases more slowly to 15 mT where the signal is completely gone. This peak is highest at 110 K where the amplitude is doubled, and decreases with decreasing temperature. At 120 K no peak can be observed.

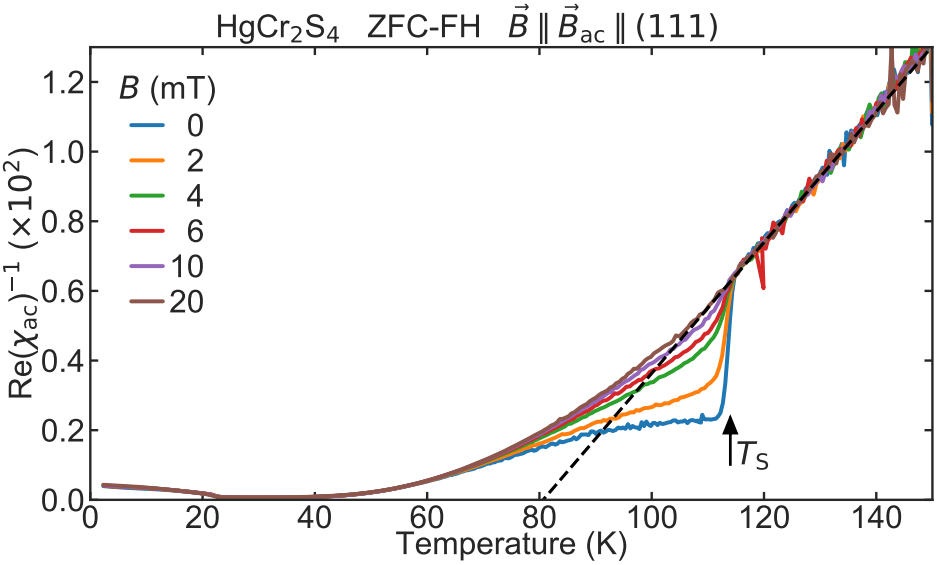

Figure 3.14: Spin clustering in $HgCr_2S_4$ at $T_S = 114$ K. Inverse of the real part of the magnetic susceptibility as function of temperature for different applied magnetic fields. The dashed line corresponds to a linear fit of the data at 20 mT in the range between 120 and 150 K.

Figure 3.14 shows the temperature dependence of the inverse of the magnetic susceptibility. The expected linear behavior in the PM phase is strongly disturbed at $T_S = 114$ K and zero field. As before, the anomaly seems to be strongly suppressed under magnetic field. This anomaly in the paramagnetic regime indicates the presence of short-range ferromagnetic clusters (spin clusters), where the magnetic field reduces the correlation length between the spins, decreasing the size of the clusters and thus the magnetic susceptibility [110].

Interestingly, this spin clusters have also been observed in the parent compound $CdCr_2S_4$, where it is shown to originate due to the dynamic off-centering of the chromium ions from their octahedral position and linear coupling between the magnetic and polar order parameters [111]. Although both compounds share the same $Fd\bar{3}m$ structure as the rest of the chromium spinels, unlike $HgCr_2S_4$ which has a spiral AFM ground state, $CdCr_2S_4$ becomes ferromagnetic be-

low 86 K. Despite this stark difference, both show a sharp spin clustering signal appearing at 116 K and 114 K for the cadmium and mercury compounds, respectively. Similarly to $HgCr_2S_4$, $CdCr_2S_4$ is also known to show ferroelectricity and a strong magnetocapacitive coupling [95]. These observations are in conflict with the reported $Fd\bar{3}m$ structure which strictly forbids ferroelectric order. For $CdCr_2S_4$ the dynamic off-centering of the chromium coupled with a second order phase transition into the distorted $F\bar{4}3m$ structure allow magneto-electric coupling [96]. Our findings, suggest that a similar mechanism is at the origin of the observed ferroelectric order in $HgCr_2S_4$.

The anomaly in the magnetic susceptibility has also been studied for different excitation frequencies ranging from 10 Hz to 10 kHz, no difference can be observed. Pair distribution function analysis of the X-ray powder diffraction of $CdCr_2S_4$ suggest that the off-centering frequency of the chromium ions is close to 10 MHz and temperature independent [111]. The detection frequency is probably to low to study the time dependence of these excitation. Within the range of the linear fit in figure 3.14, 120 K to 150 K, the Curie-Weiss temperature appears to be 80 K which still suggest dominant FM correlations. This value is much lower than the 140 K obtained upon fitting the high temperature susceptibility [98], suggesting that the FM correlations are reduced at lower temperatures.

3.2.3 Neutron depolarization measurements

Neutron depolarization at ambient pressure was measured on the same $HgCr_2S_4$ single crystalline sample used for the magnetization measurements. The sample was placed in front of a cadmium mask with a pinhole of circa 0.5 mm diameter, as it is shown in figure 2.31, and inside a closed cycle cryostat. Figure 3.15 shows the neutron polarization profile through a $HgCr_2S_4$ single crystal at ambient pressure for different applied magnetic fields. When only a very small guide field of 1 mT is applied, there is small depolarization between 22 and 43 K. When the field is increased to 5 mT, significant neutron depolarization starts to take place below 50 K, and at 22 K (Néel temperature) the beam polarization abruptly comes back to 100 %. As the magnetic field is further increased to 100 mT, the onset of neutron depolarization is displaced to higher temperatures, and the depolarization levels are more pronounced. At the same time, the beam polarization in the AFM phase is no longer 100 % suggesting that some signature of FM component is present. At 200 mT of applied magnetic field, as the saturation field is approached, the depolarization level becomes less pronounced. Nonetheless, it is also obvious that the Néel temperature decreased to 12 K, similarly to what was observed in the magnetization measurements.

Despite a relatively large depolarization, these observations are in strong contrast to what would be observed on a regular FM. In a regular FM, for the lowest applied magnetic field the sample is in its magnetically most inhomogeneous state (magnetic domains have no preferred orientation), leading to the largest depolarization. For $HgCr_2S_4$, and extrapolating the data, one can assume that at zero external field there would be no neutron depolarization in the sample. Interestingly, when magnetic field is applied, the sample starts to strongly depolarize the neutron beam, albeit in a lesser degree of what would be expected for a FM like $HgCr_2Se_4$. Finally, it is worth noting that the onset of polarization in the IFM phase is not abrupt as for a typical FM (see ambient pressure $HgCr_2Se_4$ in figure 2.33) but rather smooth, suggesting that

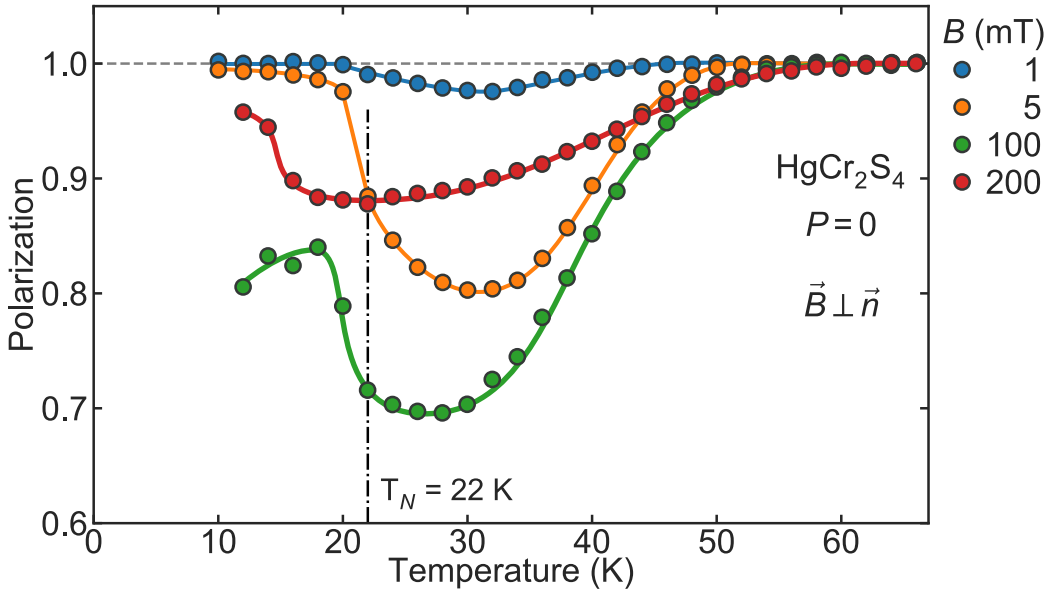

Figure 3.15: Temperature dependence of the neutron polarization through a $HgCr_2S_4$ sample at ambient pressure for different applied magnetic fields. The magnetic field is applied in a direction parallel to the neutron beam. The vertical dot-dashed line indicates the Néel temperature at zero field. The solid lines are guides to the eye.

there is no sharp phase transition from the paramagnetic state to the IFM state.

The ambient pressure measurements performed on $HgCr_2S_4$ are summarized in the magnetic phase diagram shown in figure 3.16. The color plots were obtained with a 2-dimensional interpolation of the temperature scans shown in figures 3.7 and 3.12, where some of the different features as maxima (i.e. peaks) and inflection points are indicated with markers. The different features observed in the neutron depolarization are also plotted.

The meta-magnetic transition from the AFM ground state into the IFM state seems to be quite well defined with a good overlap of the features in the different measured quantities. The Néel temperature decreases linearly with applied magnetic field. Nonetheless at low temperatures and high magnetic fields the features become increasingly broad diluting the sharpness of the transition. When the applied field becomes larger a substantial neutron depolarization is observed in the AFM state, as well as a sizable magnetization, raising the question whether the state remains purely antiferromagnetic. The cross-over from the IFM state into PM state is not well defined. The onset of neutron depolarization marks an upper limit while the broad peak in the magnetic susceptibility appearing at higher fields marks the lower limit. The pocket of enhanced susceptibility at low fields in the IFM region is potentially at the origin of, or related to, very interesting physical phenomena. In this region, additionally to the observed neutron depolarization and enhanced magnetization, there is a strong enhancement of the dielectric constant. Moreover, ferroelectric order appears below 70 K, and colossal magnetocapacitance and magnetoresistance are also observed [100].

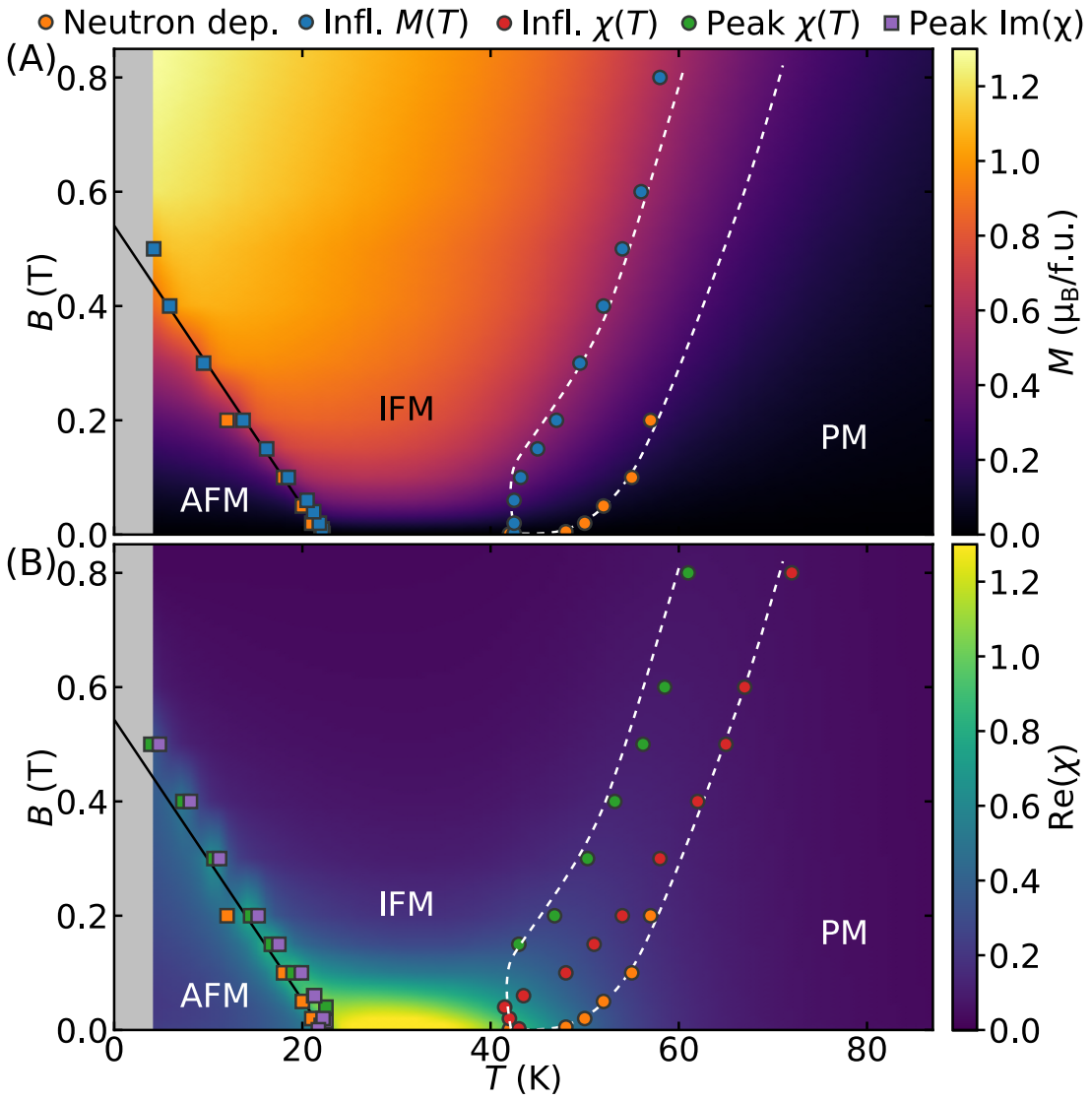

Figure 3.16: Magnetic phase diagram of $HgCr_2S_4$ at ambient pressure. A: Magnetization (M) and B: real part of the magnetic susceptibility (Re (χ_{ac})), as function of temperature and magnetic field (B). Features tracked from the different measurements are indicated with circular and square markers, for the PM to IFM and IFM to AFM transitions, respectively. The transition from the AFM state into the IFM state is marked by a solid line. The dashed gray lines bound the upper and lower limits of the crossover transition from the PM into IFM state.

3.3 Neutron depolarization experiments on $HgCr_2Se_4$ under pressure

Neutron depolarization (ND) on, $HgCr_2Se_4$ under pressure was measured using the enhanced ND setup described in the previous chapter (2.2). As before, the samples used were prepared by Vladimir Tsurkan. Single crystals were grown by means of chemical transport reactions using pre-synthesized high-purity polycrystals as starting materials. The growth experiments are performed at temperatures between 850° and 800° Celsius [98]. For the high pressure experiments,

single crystals were carefully ground from both sides obtaining irregular slab-like samples of constant thicknesses ranging from 50 to 70 µm. These samples were later manually pieced using a scalpel into smaller slabs that fit the 400 µm diameter space in the pressure cells. The (111) crystal direction is perpendicular to the surface of the slabs.

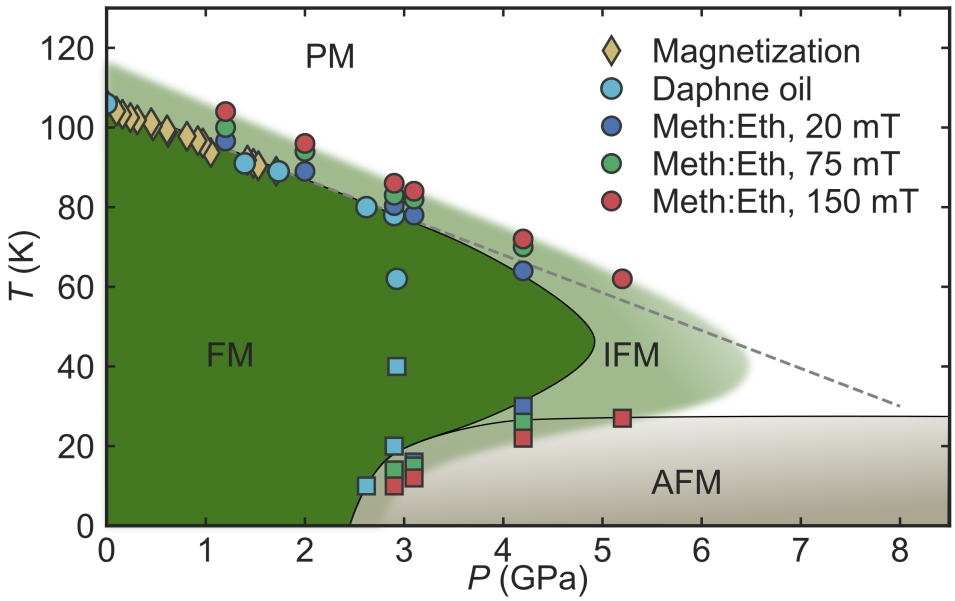

Figure 3.17: Pressure dependent magnetic phase diagram of $HgCr_2Se_4$. The Curie, and re-entrant temperatures obtained from the depolarization measurements are marked with circles and squares, respectively. Yellow diamonds mark the Curie temperatures from [47] shown in figure 3.5. The FM phase is highlighted in green and the AFM phase is filled in gray, the semi-transparent green area shows the incipient ferromagnetic (IFM) phase, and the PM phase is left white. Solid black lines are a suggestion of where phase transitions take place. The gray dashed line follows the predicted linear decrease of the Curie temperature.

The neutron depolarization measurements on $HgCr_2Se_4$ under pressure can be summarized in the pressure dependent magnetic phase diagram presented in figure 3.17 which is built from transition temperatures obtained from the different experiments. Namely, the high pressure magnetization measurements performed by Michael Wagner as part of his thesis [47], and two ND experiments where two different pressure transmitting mediums (PTM) were used, Daphne oil (low hydrostaticity) and methanol:ethanol mixture (high hydrostaticity). The Curie temperature follows the expected linear decrease, but only up to 4.2 GPa where long range FM order seems to break down. Above 2.5 GPa the measurements show a re-entrant behavior below 20 K. This gives an interesting shape to the FM phase. The hypothesized QCP seems to be covered by the emergence of a new ground state. When a magnetic field is applied, the Curie temperature is gradually increased, and the transition temperature to this new phase is suppressed. Due to the striking similarities with the ambient pressure ND measurements performed on $HgCr_2S_4$, we suggest that the ground state corresponds to AFM order. Moreover, at 5.2 GPa, when sufficiently strong magnetic field is applied (circa 70 mT), a sizable neutron depolarization is observable. This seems to point towards the presence of an incipient FM order (IFM), like in

$HgCr_2S_4$, which might be related to quantum criticality. Finally, when using a pressure medium with low hydrostatic conditions (i.e. Daphne oil), there is a premature collapse of the FM phase at only 3 GPa, and no IFM phase can be observed.

In the following these observations will be corroborated by neutron depolarization measurements. This will be followed by a discussion of the nature of the exchange interactions in the chromium spinels.

3.3.1 $HgCr_2Se_4$ under hydrostatic pressure

For the measurements presented here, V2 pressure cells fitted with moissanite anvils (0.8 mm diameter culet) were used to pressurize $HgCr_2Se_4$ single crystalline samples. Most of the data shown here was obtained during a single pressure run where the pressure was first increased to 3.1 GPa and 5.2 GPa successively, followed by a decrease to 4.2 GPa, 2.9 GPa, 2.0 GPa, and 1.0 GPa. In this particular experiment the magnetic field was applied in a direction parallel to the neutron beam. Due to the technical limitations of this configuration, the guide field was unable to penetrate through the yoke of the electromagnet. Therefore, a magnetic field of at least 20 mT should be applied with the electromagnet in order to obtain a continuous guide field through the neutron path. It is important to note that during the loading procedure the slab-like sample broke in a few smaller pieces. Subsequent pressure measurements were also performed with different sample shapes and different magnetic field configurations to confirm the validity of our findings. A 4 to 1 mixture of methanol and ethanol was used as pressure transmitting medium (PTM). Although this mixture freezes below 100 K, it ensures almost hydrostatic conditions at cryogenic temperatures in the studied pressure range [70].

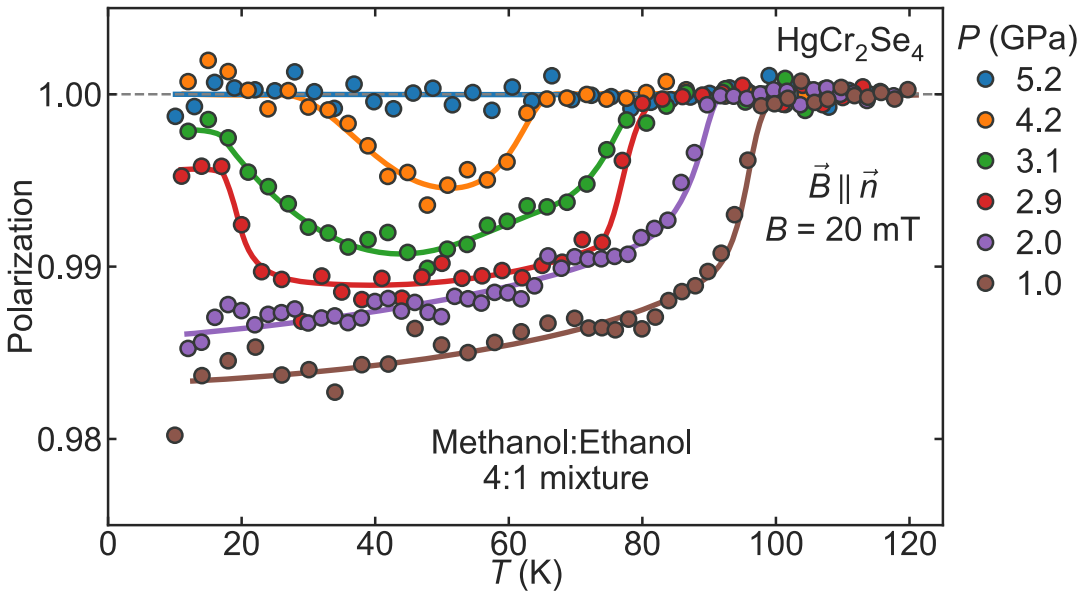

Figure 3.18: Temperature dependence of the neutron polarization through a $HgCr_2Se_4$ sample at different hydrostatic pressures. A 4:1 mixture of methanol and ethanol was used as PTM. A local magnetic guide field of 20 mT was applied parallel to the neutron beam. The solid lines are guides to the eye.

Figure 3.18 shows the temperature dependence of the beam polarization through $HgCr_2Se_4$ under 20 mT of applied magnetic field for different pressures. At low pressures, below 2.9 GPa, the neutron polarization displays typical ferromagnetic behavior, with the beam fully polarized at high temperatures, and a sudden drop at the Curie temperature, followed by a more gentle decrease of the beam polarization towards lower temperatures. At 2.9 GPa, 3.1 GPa, and 4.2 GPa, we have as before a sudden drop at the Curie temperature, but surprisingly, at lower temperatures, the beam polarization increases rapidly reaching an almost fully polarized neutron beam. At 5.2 GPa, there is no sign of depolarization, the neutron beam remains fully polarized over the whole temperature range, suggesting a complete suppression of long-range FM order. Overall, the decrease of the curie temperature fits the expected linear behavior. The fact that FM behavior was recovered at lower pressures after having reached 5.2 GPa, indicates that the transitions through which the sample has been taken are reversible. Finally it is worth noticing that the amplitude of the neutron depolarization seems to slightly decrease with applied pressure.

Note that the depolarization is only of a few percent of the total, which is much smaller than what can be observed at ambient pressure. Inside the pressure cell it is not possible to place a mask, the samples only fill a small section of the neutron beam, therefore many neutrons are not depolarized by the sample, leading to a strong reduction of the average beam depolarization.

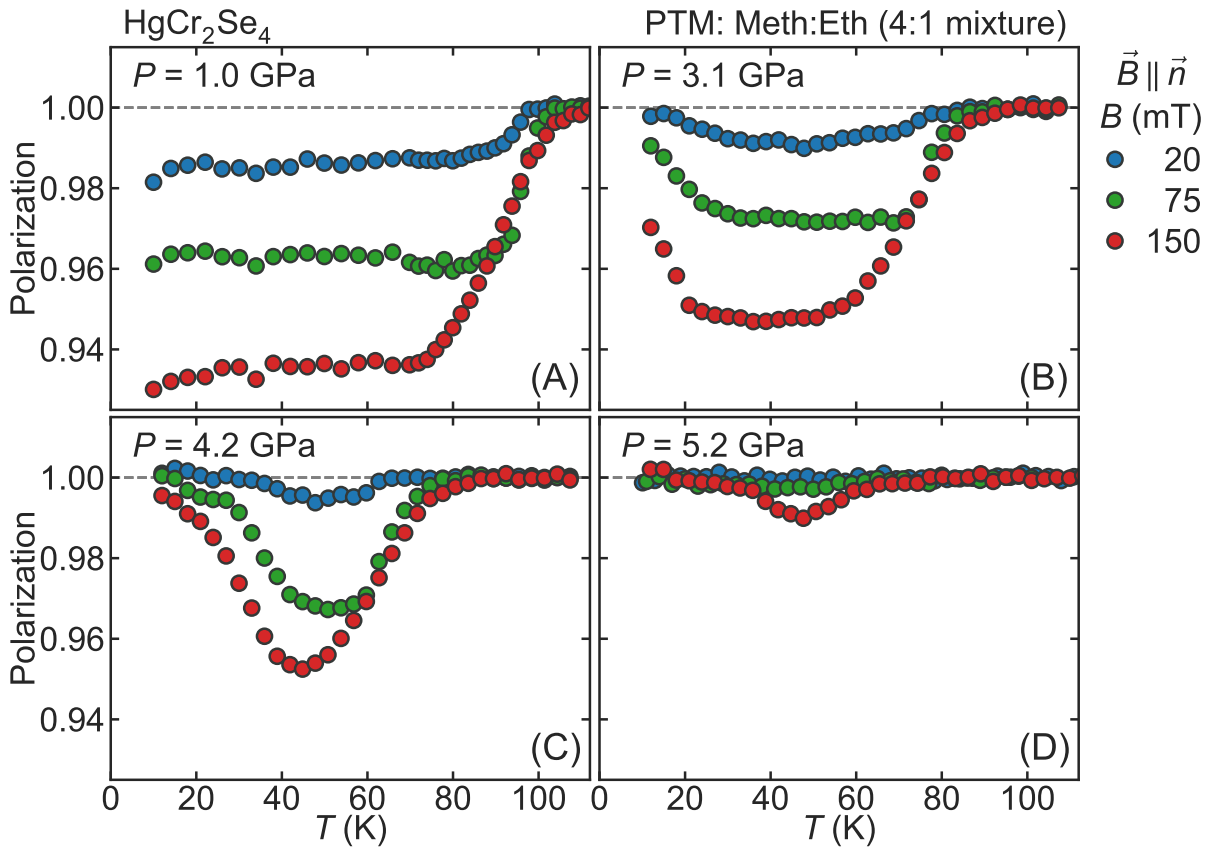

Figure 3.19: Comparison of the temperature dependence of of the neutron polarization through a $HgCr_2Se_4$ sample under different applied fields at some pertinent pressures.

The use of focusing neutron guides and the improved statistics described in the technical development section allowed for the field dependence of the depolarization profiles to be investigated within the limited experiment time available at the neutron source. Therefore, temperature sweeps were performed at different applied magnetic fields for each studied pressure. Figure 3.19 shows the temperature dependence of the polarization at 20 mT, 75 mT, and 150 mT of applied field for 4 different pressures. In this magnetic field configuration, with the field applied parallel to the neutron beam and perpendicular to the slab like sample, the neutron depolarization increases very significantly with the applied magnetic field. This is also observed at 1.0 GPa, where it is known that the ordered moment does not change with magnetic field. The increased depolarization must then be due to the reorientation of magnetic domains inside the sample, in this configuration (magnetic field perpendicular to a very flat sample) the demagnetizing factors are very large, moreover as the sample is broken into smaller pieces, the domain dynamics can be very complex. Besides the change in amplitude of the depolarization signal, it is interesting to see how the Curie and re-entrant temperatures are pushed towards higher and lower temperatures respectively. This phenomenon was observed at all applied pressures. Moreover, at 5.2 GPa some depolarization takes place between 65 K and 35 K when sufficiently strong magnetic field is applied, suggesting the onset of long-range FM order.

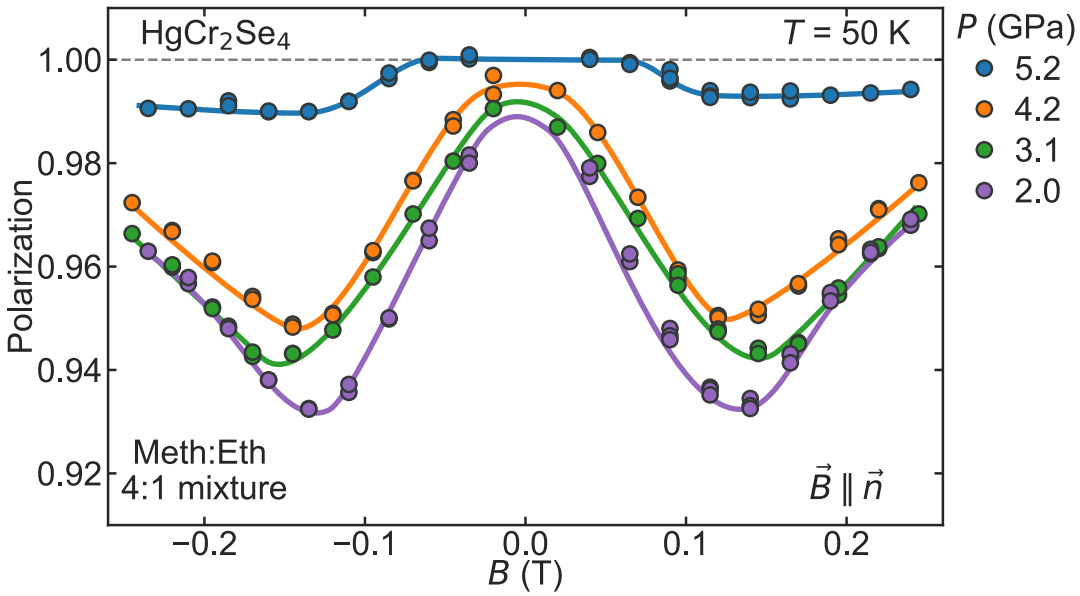

Figure 3.20: Magnetic field dependence of the neutron depolarization of $HgCr_2Se_4$ at 50 K under different hydrostatic pressures. The magnetic field was parallel to the neutron beam. The solid lines are guides to the eye.

The field dependence of the beam polarization at 50 K under different pressures is shown in Figure 3.20. For all the pressures from 2 GPa to 4.2 GPa (i.e. in the FM phase) a similar trend is observed, indicating no change in the nature of the magnetic order. There is a reduced neutron depolarization at small magnetic fields, the depolarization increases significantly to 120 mT and then decreases again towards higher magnetic fields. At 5.2 GPa an interesting dependence of the beam polarization is observed, at first the beam is fully polarized (indicating no long range FM order), but under 150 mT of applied magnetic field, the polarization drops slightly

indicating the presence of magnetic inhomogeneity which suggests that long-range FM order is taking place. These observations are well in agreement with what is observed in figure 3.19.

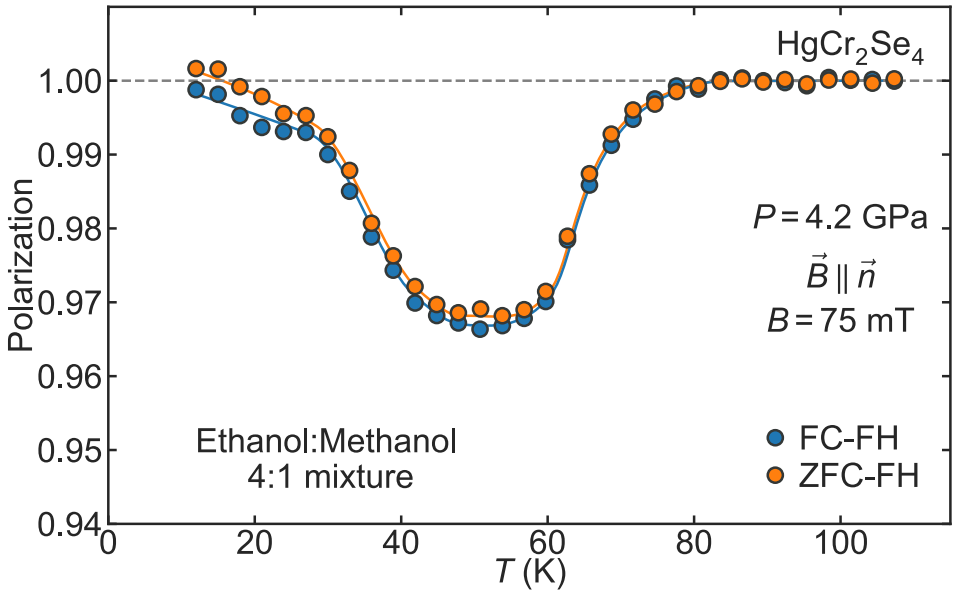

Figure 3.21: Temperature dependence of the neutron polarization through a $HgCr_2Se_4$ sample at 4.2 GPa for different cooling histories. FC-FH refers to field cooled - field heated measurement, ZFC-FH refers to zero field cooled - field heated measurement.

Different magnetic states that fit with a reduced sample depolarization in the re-entrant phase could be considered. Given the strong competing interactions in place and the temperature range, paramagnetic order can be discarded, specially having a long range FM order at higher temperatures. Re-entrant phases associated to spin glasses and other spin freezing behaviors have commonly been observed with neutron depolarization measurement [36, 37, 112]. In these scenarios, the comparison between zero field cooled (ZFC) and field cooled (FC) measurements reveals the frozen nature of these states. Figure 3.21 shows that the depolarization profile is independent of the cooling history. Moreover, spin glasses are also known to show a significant neutron depolarization depending on their properties [37, 112].

The strong similarities, when measuring neutron depolarization, between the re-entrant phase in $HgCr_2Se_4$ under pressure and the AFM phase in $HgCr_2S_4$ at ambient pressure, strongly suggest that the re-entrant phase observed is associated with the onset of AFM order. Furthermore, AFM order is also the ground state of other members of the chromium spinel family with smaller lattice parameter. An ideal antiferromagnet should leave the neutron beam fully polarized, but as observed in figure 3.18, the re-entrant phase does not always reach 100 % beam polarization. This has also been observed in the AFM phase of $HgCr_2S_4$ at ambient pressure.

Additionally, the pressure distribution inside the sample space is not homogeneous and can vary strongly from much higher pressures at the center, to lower pressures towards the gasket walls [27]. The observed temperature dependence of the polarization represent a convolution of the temperature dependence at different pressures. The main consequence is the smearing out

of features (e.g the sudden drop at T_C). As it can be observed from the reasonably sharp drop of the beam polarization at the Curie temperature over the whole pressure range, this effect is rather small. Nonetheless, hybrid states were the central parts of the sample are already in the AFM phase while the parts of the sample closer to the gasket are still in the FM phase are possible when a sudden change with respect to the pressure occur, like at 2.8 GPa, where within a change of ± 0.2 GPa, the ground state changes from FM to AFM.

The parallels between the selenium compound and the sulfur compound under pressure go even further. The selenium compound at 5.2 GPa, also shows no depolarization at low magnetic fields, while a significant signal appears at intermediate temperatures when sufficiently strong magnetic field is applied, suggesting that a similar IFM phase takes place above the Néel temperature. Finally, for both compounds, the transition temperature to this IFM phase increases with applied magnetic field, and the transition becomes less pronounced.

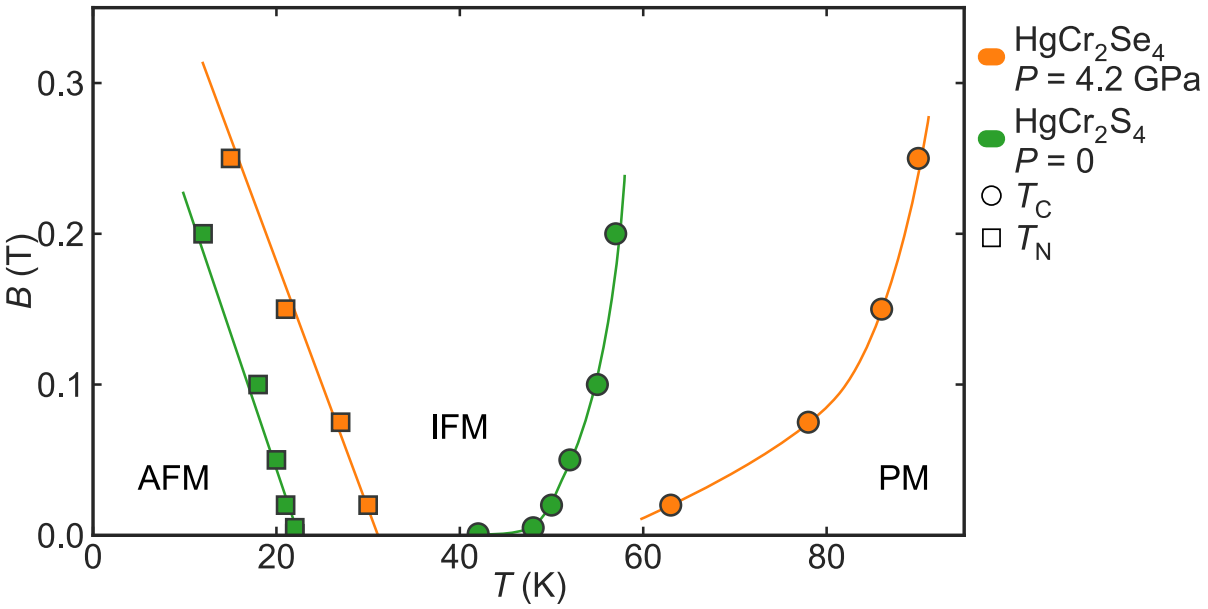

Figure 3.22: Change of the characteristic temperatures of $HgCr_2Se_4$ at 4.2 GPa, and $HgCr_2S_4$ at ambient pressure (0.1 MPa), as a function of applied magnetic field. The circles and squares indicate the FM transition (T_C) and the re-entrant temperature (T_N), respectively. The data points have been visually extracted from figures 3.19 and 3.15. The solid lines are a guide to the eye

The comparison of the high pressure measurements on the selenium compound ($HgCr_2Se_4$) with the ambient pressure measurements on the sulfur compound ($HgCr_2S_4$) suggests that under sufficiently large pressure, the selenium compound has been brought to a similar state than the sulfur compound at ambient pressure. In both cases, there is an intermediate pressure range with a reduced neutron depolarization signal, and a re-entrant phase at low temperature where the depolarization signal vanishes. Not only the overall shape of the polarization profiles are similar, but in both cases there is an opening of the intermediate temperature regime under applied field, where the onset of the depolarization signal occurs at higher temperatures and the

re-entrant behavior is shifted towards lower temperatures.

Figure 3.22 shows the change of the characteristic temperatures of $HgCr_2Se_4$ at 4.2 GPa and $HgCr_2S_4$ at ambient pressure (0.1 MPa) as a function of applied magnetic field. For both cases, the critical temperature corresponding to the onset of FM or IFM order shifts somewhat logarithmically with the applied magnetic field, while the re-entrant temperature corresponding is shifted linearly with pressure. This strongly suggests that the transition temperatures in the different compounds are of similar nature. These experiments have been performed with the magnetic field applied in different direction and are not corrected for demagnetization effects which could explain the difference in the slope of the evolution of the Néel temperature.

To confirm that the re-entrant phase indeed corresponds to a spiral AFM ground state, neutron diffraction measurements on $HgCr_2Se_4$ under pressure and at low temperatures should be performed. Due to the relatively small amplitude of the magnetic peaks of the expected magnetic structure [102], the experiment should offer a good signal to noise ratio. Neutron scattering experiments at pressures exceeding 2 GPa tend to be technically challenging, as the sample volume is significantly reduced.

3.3.2 Low hydrostaticity measurements

A first set of measurements was obtained with standard NDI, previously to the construction of the enhanced ND setup. A $HgCr_2Se_4$ single crystal, loaded in a V2 pressure cell, and a cadmium mask with a small aperture (1 mm diameter) was placed in front of the pressure cell, aligned with the optical aperture of the cell and the sample. Due to the very low counting rate of this experiment, long exposure times (6 minutes for a single polarized image) were needed, thus several hours were necessary to obtain a single temperature scan. Here Daphne oil was used as a PTM, it has the advantage of being easier to use as it does not evaporate quickly. Daphne oil freezes at 200 K at ambient pressure, and at 2 GPa the freezing temperature reaches 300 K [80]. When used as a PTM in combination with cryogenic temperatures, Daphne oil is known to develop large non-hydrostatic components at pressures as low a 2 GPa [70].

Figure 3.23 shows the evolution of the neutron polarization through a $HgCr_2Se_4$ sample with temperature for different applied pressures. At low pressures, below 2.5 GPa, the polarization profile has a typical ferromagnetic behavior, with the beam fully polarized at high temperatures, and a sudden drop at the Curie temperature, followed by a more gentle decrease of the beam polarization towards lower temperatures. At 2.6 and 2.8 GPa, there is as before, a sudden drop at the curie temperature, followed by a re-entrant phase at lower temperatures indicated by an increase of the polarization back to an almost fully polarized neutron beam. The decrease of the Curie temperature up to 2.8 GPa follows the expected linear drop. At 2.9 GPa, there is almost no signs of beam depolarization, but for a small region between 30 and 60 K. Finally, at 3.3 GPa the neutron beam remains fully polarized over the whole temperature range indicating a lack of long range ferromagnetic order.

The depolarization values are larger than in the previous experiments using focused neutron depolarization. The increase in depolarization signal is explained by the fact that a small pinhole to shape the neutron beam, and a sample with a larger cross section are used here. Thus a larger proportion of the measured neutron beam goes through the sample. It is not possible

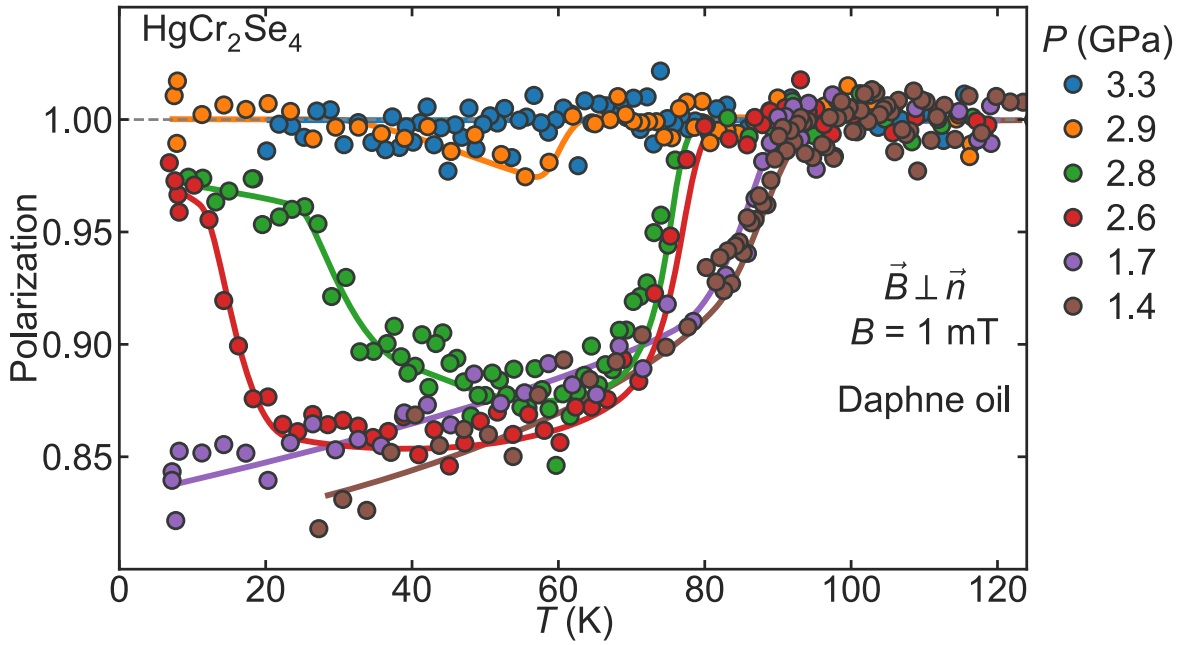

Figure 3.23: Temperature dependence of the neutron polarization through a $HgCr_2Se_4$ sample at different pressures. Daphne oil is used as PTM. A local magnetic guide field of 1 mT was applied perpendicular to the neutron beam. The solid lines are guides to the eye.

to do a quantitative comparison of the depolarization levels of two different experiments with different sample shapes and different magnetic field configurations.

The evolution of the beam depolarization with applied field for the known paramagnetic and ferromagnetic states, at 120 and 8 K respectively, is presented in figure 3.24 (A). At 120 K, within the range of the applied field, the sample remains paramagnetic, thus the beam polarization remains unchanged. At 8 K, the field dependent polarization profile is consistent with a ferromagnetic behavior. At low applied fields there is a small depolarization increase, apparently as magnetic domains reorganize under field they depolarize the beam more efficiently. As the magnetic field approaches the saturation field, the magnetic domains align with the local neutron guide field and the magnetic inhomogeneity of the sample is reduced, thus the depolarization is reduced. At the saturation field, the sample becomes a single domain with the magnetization aligned with the neutron guide field, thus no neutron depolarization takes place. This would be different for an anisotropic sample. Note that in the current field configuration, the demagnetization values are very small as the magnetic field is applied parallel to the surface of the slab-like shape of the sample. No significant hysteresis is observed.

In figure 3.24 (B), the change of polarization under applied field at base temperature is shown for different pressures. At 2.6 GPa the polarization recovers a certain ferromagnetic behavior when a magnetic field is applied, which is consistent with the metamagnetic behavior observed in the hydrostatic case. This effect becomes much smaller at 2.8 GPa and completely disappears at 2.9 GPa, indicating a certain hardening of the putative AFM re-entrant phase.

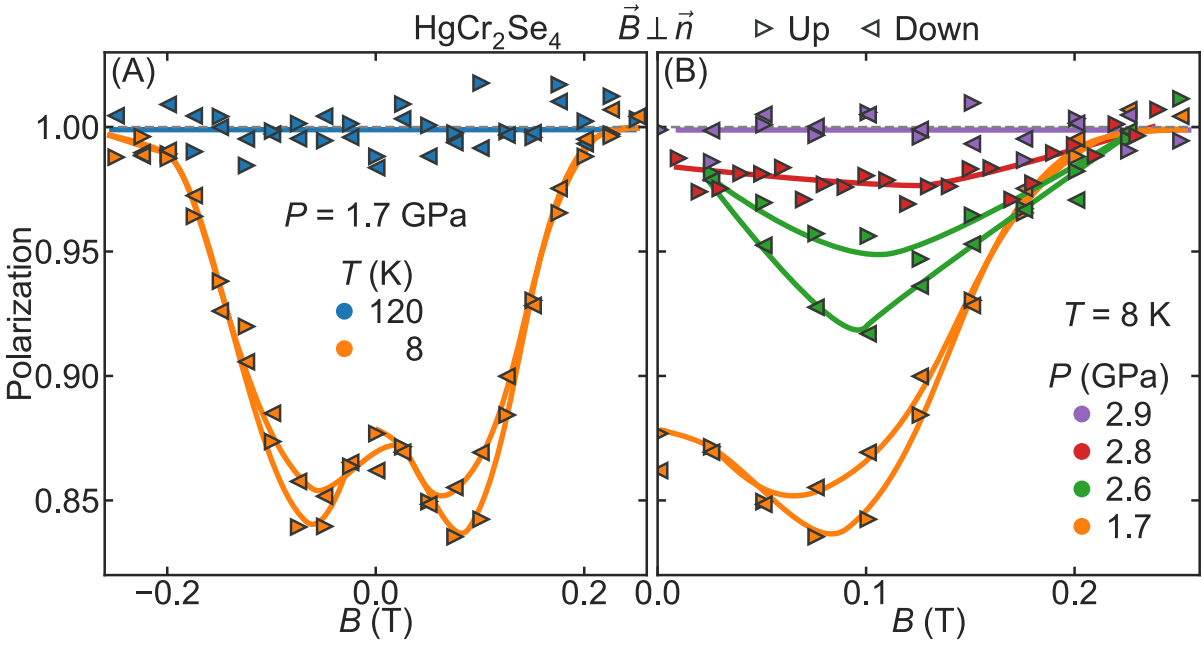

Figure 3.24: Magnetic field dependence of the neutron polarization through a $HgCr_2Se_4$ sample at different pressures and temperatures. A: typical profiles of the ferromagnetic state (green) and paramagnetic state (blue) over a complete hysteresis loop. B: Polarization profile at base temperature for different applied pressures. Each measurement point is indicated by a triangle, triangles pointing to the right or to the left are measured when increasing (Up) or decreasing (Down) the magnetic field, respectively. The solid lines are guides to the eye.

3.3.3 Improved measurement technique

In section 2.2 it was discussed that the quality of the data improved during the course of this thesis by optimizing different parameters. When comparing figures 3.18 and 3.23, the improvement of the statistics obtained with the use of focusing neutron guides does not seem very significant. The main reason would be that in the measurements using the enhanced neutron depolarization setup the magnetic field was parallel to the neutron beam. This leads to a reduced neutron depolarization at low magnetic fields, as discussed in the previous sections. For further measurements, the configuration with the magnetic field perpendicular to the neutron direction was used unless it is strictly necessary to do otherwise (e.g. when measuring superconductors).

The quality of the data was also reduced by pressure inhomogeneities across the sample space. In order to maximize the signal to noise, samples as large as possible were used. This resulted in two main problems. First, the sample might be crushed by the gasket or the anvils, because the sample space shrinks due to the compressibility of the pressure medium. Secondly, the pressure is usually maximal at the center of the sample space and decreases towards the gasket, leading to a pressure gradient across the sample. For larger samples this effect is enhanced and the results obtained will be a convolution of the sample properties at these different pressures. Therefore smaller samples are preferable, as long as they are large enough to produce a significant signal.

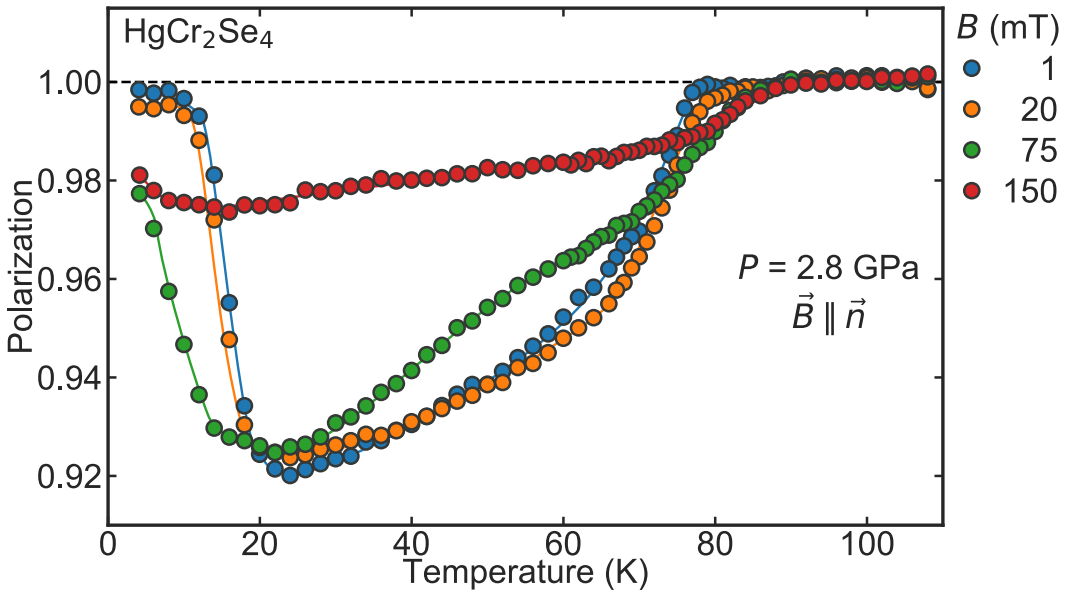

Figure 3.25: Temperature dependence of the neutron polarization through a small $HgCr_2Se_4$ sample at 2.8 GPa for different applied magnetic fields. In this experiment the field was applied perpendicular to the neutron beam. The solid lines are a guide to the eye.

A typical example of the level of improvement that can be achieved when the different parameters are optimized is shown in figure 3.25. Here a sample with a very small cross section (100x100 μm^2) was loaded in a pressure cell at 2.8 GPa and the magnetic field was applied perpendicular to the neutron beam. The main features observed in the previous experiments could be reproduced. The Curie temperature decreases by 27 K as expected, and a re-entrant phase appears around 20 K which is shifted towards lower temperatures under applied magnetic field. More significantly, the transition from the FM phase to the re-entrant phase is very sharp, and at low fields, there is no neutron depolarization at the re-entrant phase as would be expected for an AFM. The smaller sample size reduces the range of the pressure distribution across the sample, revealing a profile closer to the intrinsic behavior of the sample at a given pressure. Moreover, the results presented in figure 3.25, using the enhanced ND technique, have a very large signal to noise ratio compared to those in figure 3.23, where the standard NDI was used instead. Typical depolarization amplitudes obtained with both measurement techniques are of the order of 10 %, while the measurement noise was reduced from 2 % to 0.2 % with the use of focusing optics.

3.3.4 Intrinsic behavior of $HgCr_2Se_4$ under hydrostatic pressure

Differences in sample shape or magnetic field configuration modify the strength of the depolarization in a given experiment and even seem to modify the temperature dependence of the polarization. It is not possible to fit the temperature dependence of the polarization measured in these experiments as with a standard FM by using equation 1.7 presented in the introduction. Many of the assumptions made to derive this equation are seemingly no longer valid under the current experimental conditions due to the extreme limitations of the sample space inside the

pressure cells. Halpern and Holstein take advantage of the fact that a neutron will pass through a large number of magnetic domains to average across several terms in their calculations [34], when the sample thickness becomes 60 µm or less, this assumption might no longer be valid as the magnetic domains in $HgCr_2Se_4$ are expected to be in the order of 20 µm. Moreover, the slab-like shape of the sample introduces a strong anisotropy while Halpern and Holstein assume isotropic domains. The levels of neutron depolarization can therefore only be compared meaningfully within a given pressure run, where the same sample and the same magnetic field configuration are used. Nonetheless, the critical temperatures for a given pressure and magnetic field, independently of sample shape and field configuration, should remain the same.

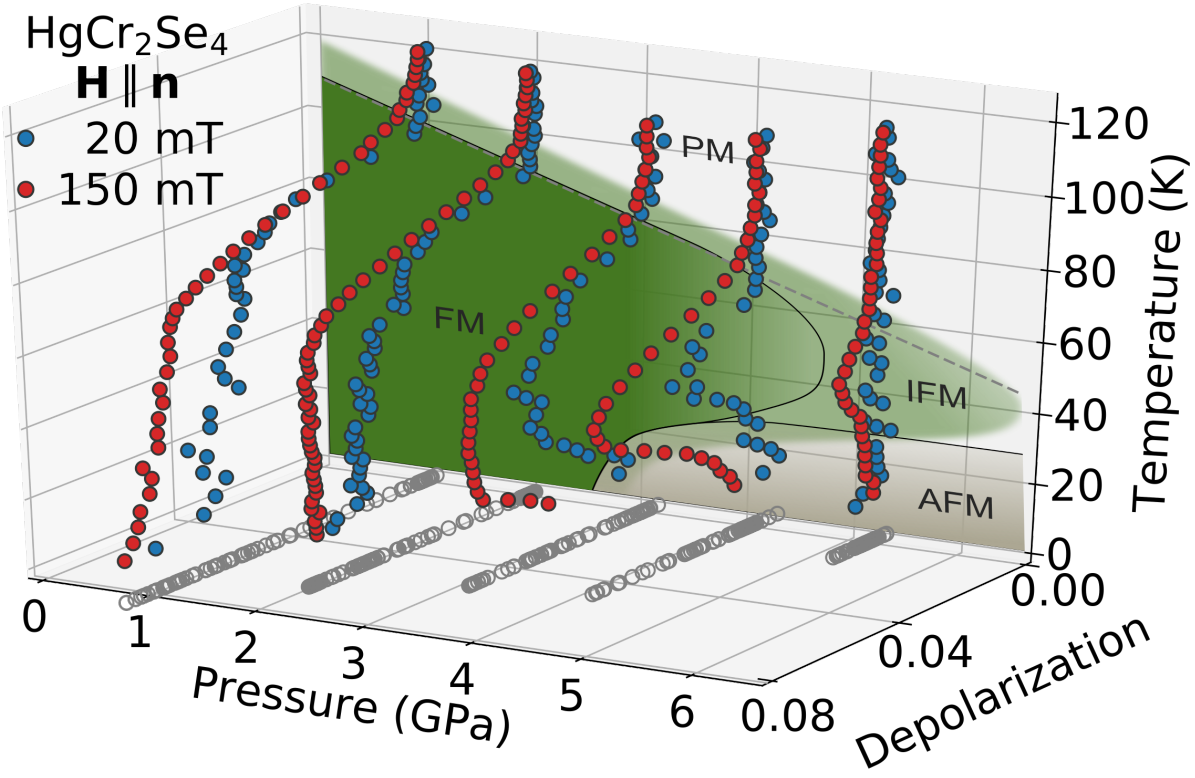

Figure 3.26: Neutron depolarization of $HgCr_2Se_4$ under hydrostatic pressure at low and high magnetic fields, across the proposed phase diagram. The temperature dependent measurements shown in subsection 3.3.1 are presented in a 3 dimensional plot with temperature as vertical axis, hydrostatic pressure in the horizontal axis, and the level of depolarization in the depth. The proposed pressure and temperature dependent phase diagram is shown on the back plane. The depolarization level has been multiplied by 4 for the data obtained at 20 mT. Each data set belongs to a plane of constant pressure. The projection of each data point on the horizontal plane is marked with gray circles to improve clarity. The magnetic field H is applied in a direction parallel to the neutron beam.

The discrepancy between the data sets obtained using different pressure transmitting mediums, must be due to the effects of pressure anisotropies. While the 4 to 1 methanol:ethanol

mixture is known to ensure almost ideal hydrostatic conditions up to 10 GPa, Daphne oil becomes poorly hydrostatic above 2 GPa, most notably at low temperatures [70]. The intrinsic behavior of $HgCr_2Se_4$ under hydrostatic pressure, summarized in the phase diagram presented in figure 3.17, is therefore observed only with the measurements obtained using methanol:ethanol mixture as pressure transmitting medium. The phase diagram was constructed with the transition temperatures inferred from the temperature dependence of the polarization. The neutron polarization as function of temperature, hydrostatic pressure, and magnetic field, can be better visualized in a 3 dimensional depiction as shown in figure 3.26. The temperature dependent measurements shown in subsection 3.3.1 are presented in a 3 dimensional plot with temperature as vertical axis, hydrostatic pressure in the horizontal axis, and the level of depolarization from the sample in the depth. To improve the comparison of the data obtained with high and low applied magnetic field, the amplitude of the depolarization levels at low magnetic field are multiplied by 4. This representation of the experimental data highlights the the reentrant phase diagram which is shown in the back plane. The FM phase is indicated by a marked neutron depolarization, which seems to weaken at higher pressures. The proposed AFM phase corresponds to a re-entrant behavior which is modulated with the magnetic field. Finally, the proposed incipient FM order is marked by a slight depolarization pocket which only appears at high fields.

3.4 Discussion

In $HgCr_2Se_4$ the relative strength of the FM and AFM exchange interactions changes with pressure as the Curie temperature decreases over a large pressure range. A secondary effect of the decrease of the exchange interaction can be seen in the decrease of the depolarization amplitude with increasing pressure in figure 3.18. In a FM, the depolarization decreases exponentially with the saturated magnetization and the mean domain size (see equation 1.7). Magnetization measurements show that the saturated magnetization is constant up to 1.8 GPa [47], and can be expected to remain constant at higher pressures. The contribution of the Bloch walls to the internal energy scales with the exchange interaction [113], thus lowering of the exchange interactions would lead to a decreasing of the mean size of the magnetic domains due to demagnetization effects. Therefore, the observed decrease of the depolarization amplitude is likely due to the decrease of the mean domain size due to the weakening of the exchange interaction.

High pressure X-ray powder diffraction reveals that the chromium-chromium bond distance at room temperature changes linearly with pressure within the range studied [109]. According to the mechanism described by Baltzer et.al. [45] the exchange interaction should also decrease linearly with pressure, ensuring a FM ground state at least up to 10 GPa. Surprisingly, the pressure dependent magnetic phase diagram of $HgCr_2Se_4$ shows that for pressures as low as 2.8 GPa the ground state is no longer ferromagnetic. At such pressures, the bond distance between neighboring chromium atoms is only slightly reduced from 3.797 to 3.757 Å. These values are significantly larger than the bond distance in the AFM compounds $ZnCr_2Se_4$ and $HgCr_2S_4$ with 3.707 Å, and 3.622Å respectively. Additionally, theoretical calculations have been performed to predict the magnetic ground state of $HgCr_2Se_4$ under pressure. Local spin density approximations (LSDA) predicted a spin-spiral ground state with a pressure-dependent incommensurate wave vector for the whole pressure range. A more accurate calculation was obtained via local density approximations accounting for the strong electron correlations (LDA + U) which then

predicts a FM ground state over the whole pressure range [109]. Density-functional-theory investigations suggest that $HgCr_2Se_4$ remains FM up to 12 GPa [114]. This discrepancy between theory and experiment indicates that important aspects are missing in the theoretical models.

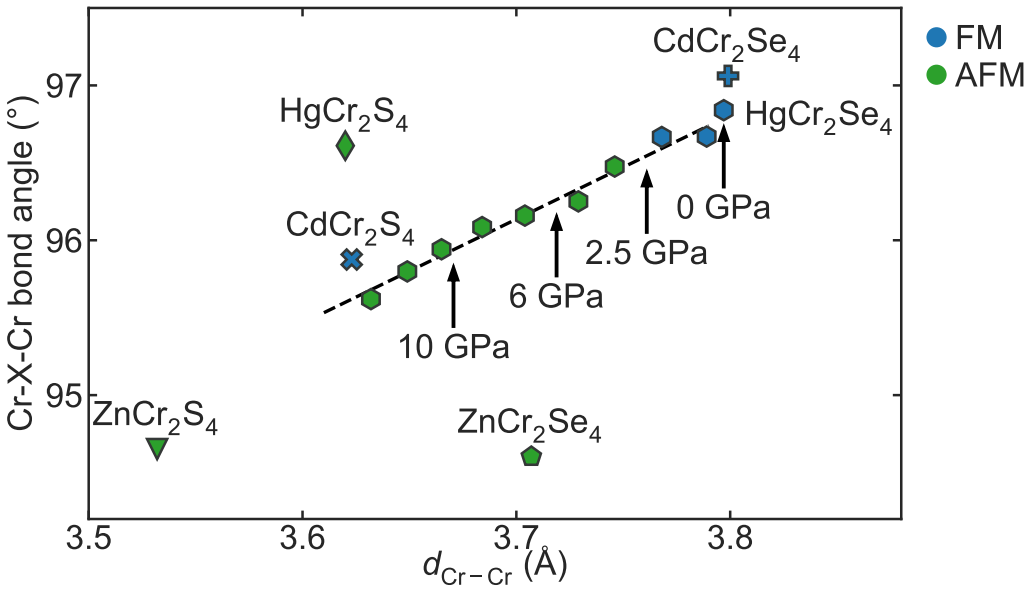

Figure 3.27: Cr-X-Cr bond angle and Cr-Cr bond distance of $HgCr_2Se_4$ under applied hydrostatic pressure compared with the selenide members of the chromium spinel family ACr_2X_4. The pressure series of $HgCr_2Se_4$ is indicated by hexagons, the arrows indicate which pressure is necessary to reach a given Cr-Cr bond distance. The dashed line is a linear fit of the pressure series. Markers in blue and green indicate FM and AFM ground states, respectively. Values for $HgCr_2Se_4$ under pressure are calculated from the crystallographic data in [109], the rest are taken from references [44, 115–119] .

The Cr-X-Cr bond angle has been suggested to play a significant role in the chromium spinels [45, 47]. The strength of the FM super-exchange mediated by the X atoms (O, S, or Se) is susceptible to change with the bond angle, it is expected to be at a maximum at 90°. It was suggested that these angles are further deformed under pressure accelerating the collapse of the FM order [47]. Figure 3.27 shows how the Cr-X-Cr bond angle and the Cr-Cr bond distance change when applying pressure on $HgCr_2Se_4$ with respect to other compounds of the chromium spinel family. The Cr-X-Cr bond angle for $HgCr_2Se_4$ is close to 96.7° at ambient pressure and it is slightly reduced under pressure. This trend under pressure is also shared by other compounds of this series [116, 117, 119]. Contrary to what would be expected, some compounds with smaller bond angle, i.e. closer to the 90° mark, have an AFM ground state. $CdCr_2S_4$, with a FM ground state, has similar bond angles and length as in the high pressure phase of $HgCr_2Se_4$, which is expected to be deeply in an AFM phase. Hydrostatic pressure tends to reduce the distortion in the octahedra, naturally occurring at ambient pressure, bringing the bond angles back to the optimal 90° mark. These observations indicate that changes of the Cr-X-Cr bond angle under pressure are presumably not directly responsible for the sudden collapse of FM order.

Our observations show that in $HgCr_2Se_4$ above 2.5 GPa, the relative strength of the exchange interaction seems to be reversed upon cooling, the sample goes from FM to AFM coupling. Such exchange inversion with temperature, i.e. the exchange interaction changes sign, is observed in numerous compounds. Kittel, recognizing the impossibility to describe these compounds with temperature-independent interactions, describes a magnetization model were, similarly to the chromium spinels, the lattice parameter drives the relative strength of the exchange interactions [120]. It is simply understood, that due to thermal contraction, as the sample is cooled down, the lattice parameter decreases changing the sign of the exchange interaction. The change of lattice parameter a_0 from room temperature to a few Kelvin in $HgCr_2Se_4$ is on the order of 0.02 Å [103]. The change due to thermal contraction is relatively small compared to the change under pressure $da_0/dP = -0.034$ [Å/GPa] [109]. Although the change of lattice parameter upon cooling participates in the early collapse of the FM ground state, and partially explains the reentrant behavior observed in $HgCr_2Se_4$ under pressure, it is too small to explain the pressure phase diagram and the discrepancy between Curie-Weiss temperatures and ground state in the chromium spinel series.

The oxide members of the chromium spinel family ($ZnCr_2O_4$, $CdCr_2O_4$, and $HgCr_2O_4$) show negative Curie-Weiss temperatures (see figure 3.2) as expected from the smaller lattice constant. The chromium ions seat in a pyrochlore lattice which consist of corner sharing tetrahedra introducing a large geometrical frustration, as neighboring spins at the edges of a tetrahedra cannot be all mutually anti-parallel. This geometrical frustration prevents the spins from ordering, giving rise to the much lower Néel temperatures observed in figure 3.3. To achieve an ordered phase, spins tend to couple with some available degree of freedom, such as orbital or structural degrees of freedom. In the particular case of the oxide members of the chromium spinels, and given the widely reported spin-phonon coupling [46, 121, 122], the Néel transition is coincides with a structural transition into a tetragonal distorted phase which lifts the geometrical frustration [123–125].

Similarly, in the bond frustrated $ZnCr_2S_4$, with a Curie-Weiss temperature close to zero and and AFM order below 22 K, the Néel transition is accompanied by a transition from the cubic $Fd\bar{3}m$ structure to a tetragonal $I4_1/amd$ structure. Upon further cooling, $ZnCr_2S_4$ gets a $Imma$ orthorhombic crystal structure with a more complex AFM order [126]. This suggests strongly that the chromium spinels are near a structural instability, and lowering the thermal energy has more significant changes in the structural degrees of freedom than the simple thermal contraction. Furthermore, under large applied pressure the majority of chromium spinels follows the same sequence (cubic, tetragonal, and orthorhombic) of structural transitions [109, 115–119] suggesting that when sufficient energy is available, the structure stabilizes into the tetragonal phase. Figure 3.28 shows the critical pressure of the tetragonal structural transition compared to the Curie-Weiss temperature. In this representation the compounds with the same ground state are grouped together, suggesting a correlation between the Curie-Weiss temperature, the critical pressure, and the magnetic ground state. Paradoxically, the elements with FM ground state have lower critical pressure indicating that they are potentially closer to the tetragonal instability.

We postulate here that the reason certain elements of the chromium spinel family order antiferromagnetically despite having a large positive Curie-Weiss temperature is due to tetragonal transitions (or distortions) occurring at lower temperatures, and that a similar phenomenon

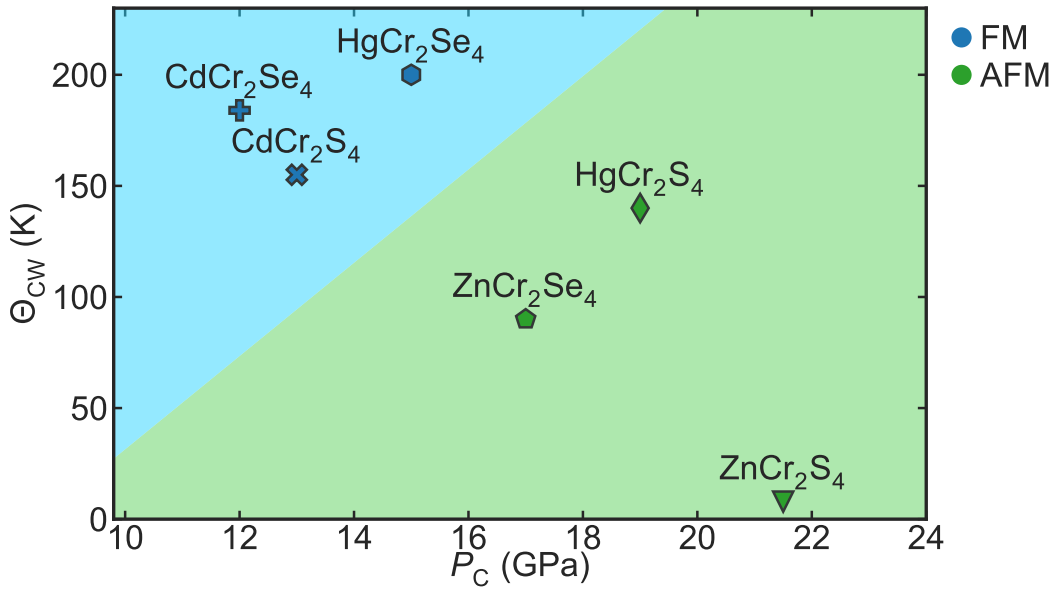

Figure 3.28: Curie-Weiss temperature (Θ_{CW}) compared to the critical pressure (P_C) where the first structural phase transition occurs for the chalcogenide elements of the Chromium spinel family (ACr_2X_4). The color indicates the magnetic ground state of each compound. Data taken from [44, 109, 115–119]. The colored areas suggest a correlation between the Curie-Weiss temperature and the critical pressure determining the magnetic ground state.

occurs to $HgCr_2Se_4$ under pressure. These structural changes might be very subtle and only revealed through high resolution synchrotron X-ray diffraction combined with an accurate structural refinement. For instance, different studies on $ZnCr_2Se_4$ with a spiral AFM ground state below 21 K, have reported different structural transitions occurring at the Néel temperature or even non at all. Yokaichiya et. al. only observed negative thermal expansion below T_N and argue that if a structural transition takes place it is beyond the resolution of their instrument [126]. Previously it was proposed that an orthorhombic phase transition occurs at the Néel temperature [127], while more recently the transition has been identified to be the same tetragonal structure $I4_1/amd$ found in $ZnCr_2S_4$ [128]. Unfortunately, no such detailed studies at low temperatures have been performed on $HgCr_2S_4$ or $HgCr_2Se_4$ under pressure.

The AFM order obtained in the tetragonal phases of $ZnCr_2S_4$, and $ZnCr_2Se_4$ is shown in figure 3.29. It corresponds to a simple spiral propagating along the (001) (or c) crystallographic direction, and a ferromagnetic arrangement in the ab-plane [126]. This is consistent with a smaller Cr-Cr bond distance in the c direction and and larger Cr-Cr bond distance in the a-b plane due to the tetragonal structure. The interactions within the plane become dominantly FM due to the larger distance while the interactions in the c direction become slightly more AFM as the distance is reduced. Furthermore, Dzyaloshinskii-Moriya interactions are enabled by the symmetry lowering of the crystal structure. This combination allows for a material in which FM exchange dominate, to develop a spiral AFM ground state.

$HgCr_2S_4$ shows a very similar magnetic ground state [102] from which we can speculate that

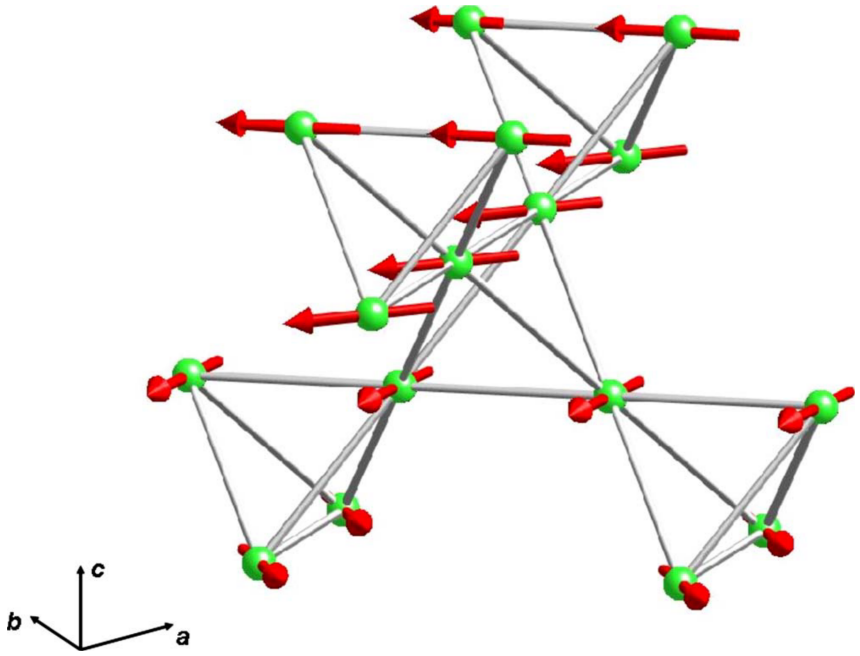

Figure 3.29: Schematic representation of the magnetic structure of $ZnCr_2Se_4$. For clarity only the Cr atoms are displayed [126].

a tetragonal structural transition or distortion with a reduced bond distance out of the plane and an increased bond distance in the ab plane is present. The re-entrant phase observed in $HgCr_2Se_4$ under high pressure is likely to be due to the same spiral AFM order and thus similar tetragonal crystallographic changes. As seen in figure 3.28, hydrostatic pressure brings the system closer to the tetragonal instability, thus allowing a system with very large chrome-chrome distance, to show AFM order through the mechanism previously described. It is worth noting, that all the AFM states discussed here are characterized by a Néel temperature around 20 K shifting towards lower temperatures under magnetic field. Furthermore, the premature loss of FM order when using daphne oil as PTM introducing anisotropic stresses into the sample, seems to support this hypothesis. The increased anisotropic stress breaks the cubic symmetry artificially introducing a sort of tetragonal distortion.

It also has been established that the dynamic off-centering of the Chromium ions present in $CdCr_2S_4$ is also present in $HgCr_2S_4$ inferred by a large signal observed in the reciprocal susceptibility (see figure 3.14) due to FM clustering. Additionally to negative thermal expansion, the formation of FM clusters in the regime between the Néel temperature and 100 K was also reported in $ZnCr_2Se_4$ [128]. The other members of the chromium spinel family with dominant FM exchange (i.e. positive Curie-Weiss temperature) are likely to exhibit similar FM clustering above the ordering temperature. The dynamic off-centering of the chromium ions can also be related to the structural instability as the chromium ions hop between equivalent potential energy minima as the system is driven closer towards a phase transition [129]. Furthermore, this mechanism may be competing with FM order, explaining the lower Curie temperatures observed in these compounds with respect to the large Curie-Weiss temperatures. In the extreme case of $HgCr_2S_4$ this mechanism could even be responsible for the absence of conventional FM order.

Comparing the amplitude of the signal observed in $CdCr_2S_4$ and $HgCr_2S_4$, it is comparatively larger in the mercury compound, suggesting a stronger effect. The dynamic lattice distortions are of great interest as they are likely enabling the ferroelectric properties observed in these compounds [96, 111], further expanding the functionality of chromium spinel based devices.

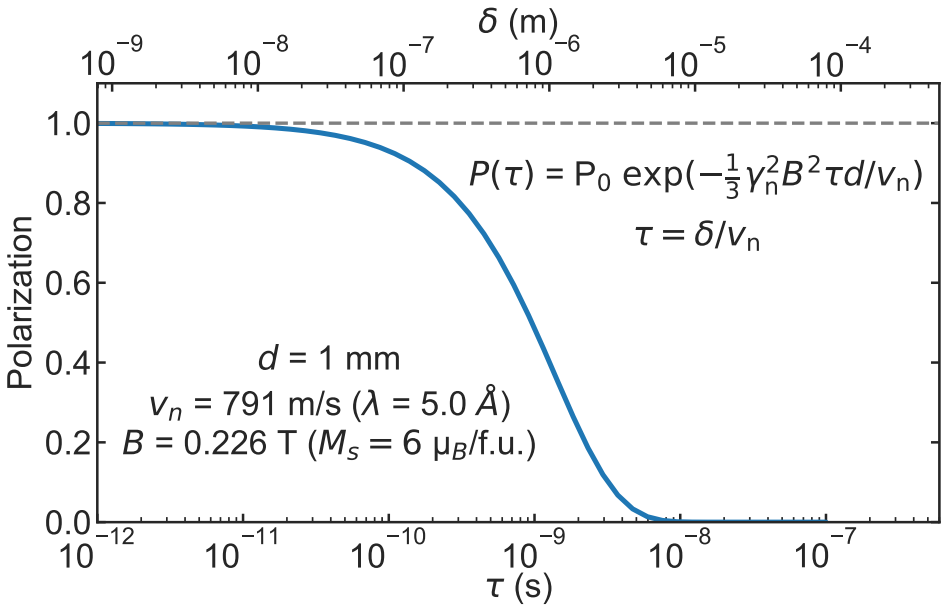

Figure 3.30: Neutron depolarization with respect to the mean time τ of fluctuating FM domains, or alternatively, as function of the mean domain size δ in a static FM. The polarization levels are calculated according to equation 1.7. Sample thickness d and neutron velocity v_n are matched to the experimental values used in figure 3.15. The magnetic field B inside a domain is obtained from the saturated magnetization of 6 μ_B/f.u. .

The incipient FM (IFM) region observed in $HgCr_2S_4$, which is likely to be present in $HgCr_2Se_4$ at high pressures, is highly unconventional. Beyond the already discussed ferroelectric properties, neutron depolarization measurements give a deeper insight into the purely magnetic properties of this phase. Neutron depolarization occurs only in the presence of finite magnetization on mesoscopic scales, e.g. magnetic domains inside a FM. The very low magnetic field pocket of the IFM state, where a large magnetic susceptibility signal is observed, is characterized by a strongly reduced neutron depolarization signal (see figure 3.15), which, extrapolating to zero field, goes to zero. This clearly indicates that no conventional FM order takes place in the IFM state. Considering that the chromium ions are part of a pyrochlore lattice, and the AFM ground state, a spin liquid type of phase could be considered at low fields. Diffuse neutron scattering measurements could help to identifying if these magnetic correlations have a certain structure. Nonetheless, given the large FM correlations in this system, a spin liquid type order seems unlikely. Another plausible situation is that applying magnetic field strengthens the FM correlations through an unknown mechanism triggering FM order. This is also unlikely, since once the system enters the FM state, its own magnetization would keep the system ordered, which would lead to a distinct signal in the hysteresis measurements (see figure 3.10).

Finally, we propose that some sort of rapidly fluctuating FM order could be in place, where external magnetic field slows down the system rendering it almost identical to a conventional FM at sufficiently high fields. The equation presented in the introduction to quantify the neutron depolarization through a FM (equation 1.7) is equally valid for a neutron with velocity v_n traveling through static magnetic domains with a mean size δ than for a static neutron (i.e. much slower than the domain fluctuations) in time fluctuating domains with mean lifetime $\tau = \delta/v_n$. Figure 3.30 shows the expected neutron polarization through such a system as function of the mean fluctuation time τ of the domains. This figure is a vertical slice of figure 1.12 along the the value $M = 6\,\mu_B/f.u.$, which is the saturated magnetization of $HgCr_2Se_4$ and $HgCr_2S_4$ under a large field. Significant neutron depolarization takes place for mean fluctuation times in the order of 10 picoseconds or slower, for faster fluctuating times the neutrons spend to little time within a given magnetic domain to undergo sufficiently large Larmor precession to be detectable. The timescale of the fluctuations in the proposed exotic FM order should therefore be in the order of 10 ps or faster at zero field to fit our experimental data. With applied magnetic field the timescale of the fluctuations should slow down to the nanosecond regime.

3.5 Summary and outlook

The magnetic properties of $HgCr_2S_4$ were thoroughly investigated by means of neutron depolarization, magnetization, and ac susceptibility measurements. The hitherto known phase diagram was reproduced, with the already mentioned AFM order at low temperatures and the incipient ferromagnetic (IFM) phase at intermediate temperatures. The absence of neutron depolarization at zero field further confirmed that the IFM phase shows stark differences to conventional FM order. Additionally, evidence of spin clustering below 114 K has been observed in the magnetization and ac susceptibility data. This feature, also present above ferromagnetic order in $CdCr_2S_4$, is related to the dynamic off centering of the chromium ions, and is believe to play an important role in breaking the cubic symmetry of the compounds enabling, for instance, ferroelectric order.

The pressure and field dependent magnetic phase diagram of $HgCr_2Se_4$ was investigated by means of high pressure focused neutron depolarization measurements. The previously observed linear decrease of the Curie temperature was confirmed and extended to pressures as high as 4.2 GPa. A low temperature phase appeared above 2.5 GPa with transition temperatures around 20 Kelvin. This phase has been identified with a spiral AFM order as the one observed in $HgCr_2S_4$, $ZnCr_2Se_4$, and $ZnCr_2S_4$. The similarity of the signal observed in high pressure $HgCr_2Se_4$ and ambient pressure $HgCr_2S_4$, together with the metamagnetic behavior, i.e. lowering of the critical temperature under applied field, are strong arguments supporting this claim. Finally, as in $HgCr_2S_4$, an IFM phase where long range magnetic order is triggered by an external magnetic field seems to appear at intermediate temperatures above 5 GPa.

The impact of these results on the understanding of the competing interactions present in the chromium spinel family has been discussed. Pressurizing $HgCr_2Se_4$, the different magnetic phases occurring across the different compounds of this spinel family could be observed. This strongly suggest that the same exchange mechanism is at place in all the compounds of this series and that discrepancy in the ground state of the different compounds of this series can be understood in terms of slight structural distortions. These compounds lie close to a structural

instability towards a tetragonal structure. The lattice dependent exchange interaction, allows the magnetic and structural degrees of freedom to couple with each other creating the various observed physical phenomena.

High pressure neutron diffraction on $HgCr_2Se_4$ should allow to identify the proposed AFM spiral order. Magnetic satellites at $\begin{pmatrix} 0 & 0 & \pm q \end{pmatrix}$ should appear around the Bragg peaks. At pressures exceeding 2.5 GPa detection might become technically challenging and dedicated pressure equipment and beamlines have to be used. As it has been observed, these systems are rather sensitive to pressure anisotropies and highly hydrostatic pressure transmitting mediums should be used. To fully model these compounds, the temperature dependence of the structure of the different chromium spinels should be investigated by means of high pressure synchrotron X-ray diffraction measurements. Special attention should be made to subtle and even dynamic distortions. Moreover, traces of spin clustering in the remaining elements of the series should be investigated by performing ac susceptibility measurements at very low magnetic fields. Finally, diffuse neutron scattering measurements on $HgCr_2S_4$ should help to characterize the spin fluctuations taking place in the IFM phase.

CHAPTER 4

Pressure and current driven phase transitions in Ca_2RuO_4

The antiferromagnetic Mott insulator Ca_2RuO_4 is close to a structural instability making it very susceptible to small perturbations. For instance, hydrostatic pressure and electric currents have a strong effect on the magnetic and electrical properties of Ca_2RuO_4. Here, FM order appearing at high pressure is investigated with the help of neutron depolarization. The results allow for a different interpretation of the hitherto known pressure phase diagram. Additionally, the temperature dependence of the magnetization and resistivity at different applied electric currents are measured in detail. A gradual decrease of the Néel temperature is observed at small current densities. The metal-insulator transition, reported in the literature, is not observed even at current densities exceeding the reported critical currents. Nonetheless the resistivity decreases by several orders of magnitude under current. We propose a combination of current induced charge carrier injection and gap suppression to explain the observed temperature dependence of the resistivity.

4.1 Motivation

Ruthenates, containing the oxyanion of ruthenium RuO_4^{2-}, show a large variety of ground states, ranging from FM metals to AFM insulators. Particularly, the Ruddlesden–Popper series $(Ca, Sr)_{n+1}Ru_nO_{3n+1}$, constitutes an interesting series of elements to study metal-insulator transitions (MIT) [130]. Among these, the single layer $n = 1$ system $Ca_{2-x}Sr_xRuO_4$ is of great interest. The end of the series member of this system, Sr_2RuO_4, is the only layered-perovskite superconductor containing no copper, with a critical temperature much below that of the Cuprates ($T_C = 1.35$ K)[131]. In contrast, the compound studied in this chapter, located at the other end of the series, shows a Mott insulator AFM ground state. Moreover, Ca_2RuO_4 appears to be at the verge of a structural instability which makes it very susceptible to chemical substitution [48, 49], hydrostatic pressure [50], and even electrical current [132].

Ca_2RuO_4, with an orthorhombic *Pbca* structure at room temperature, has a highly distorted K_2NiF_4 single layered-perovskite structure, as seen in figure 4.1. The smaller size of the calcium Ca^{2+} ions, as compared to strontium or ruthenium, induces strong rotation and tilt angles in the

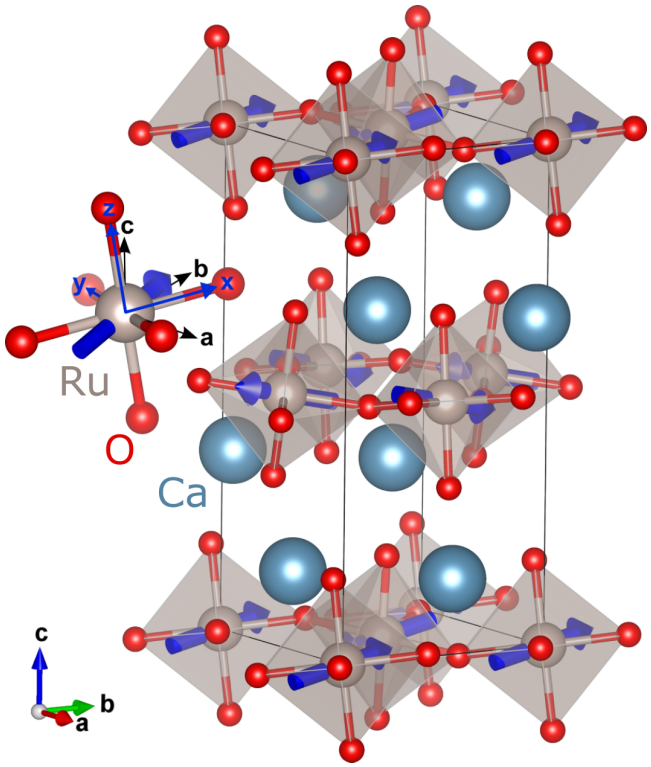

Figure 4.1: Crystal structure of Ca_2RuO_4. Gray, light blue, and red spheres indicate ruthenium, calcium, and oxygen sites, respectively. The rotated and tilted RuO_6 octahedra are highlighted in gray. Blue arrows indicate the magnetic moment on each Ru site in the AFM state. Taken from [133].

RuO_6 octahedra. Long range AFM order sets in below 110 K, with the spins aligned along the b axis, and an ordered moment close to 2 μ_B as expected from the Ru^{4+} cations, which are responsible for the magnetism [134]. Recent resonant elastic X-ray scattering (REXS) measurements have identified a spin canting towards the orthorhombic c axis of about 10% (see figure 4.1) [133]. As temperature is increased, the structural distortions decrease, and at 357 K a transition to a near metallic phase is triggered by a structural transition from the low-temperature orthorhombic to a high-temperature tetragonal phase [135].

Under moderate hydrostatic pressure, close to 0.7 GPa, Ca_2RuO_4 becomes a FM metal. The low saturated magnetization (0.35 μ_B/Ru-ion), and the metallic conductivity, indicate that the magnetic order is itinerant [54]. Establishing a magnetic and structural phase diagram becomes complicated, as both structure and magnetic information are difficult to retrieve at high pressures. The structural information is mostly limited to room temperature measurements while some of the magnetic transition temperatures are obtained through indirect quantities, i.e. changes in the resistivity. In figure 4.2 the hitherto known structural and magnetic pressure dependent phase diagrams are shown. Between the ambient pressure short-orthorhombic phase (*S-Pbca*) and the long-orthorhombic (*L-Pbca*) phase found at higher pressures, there is an intermediate mixed phase between 0.5 and 2 GPa. The transition from the pure *S-Pbca* phase into the mixed state is also a MIT transition where a discontinuous change of the lattice constants,

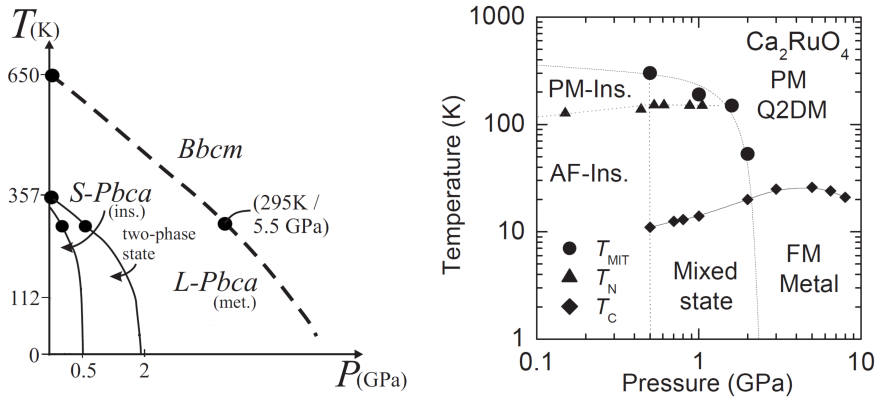

Figure 4.2: Structural, magnetic, and electric pressure dependent phase diagrams taken from references [54, 55]. Left: Pressure dependent structural phase diagram where *S-Pbca* and *L-Pbca* indicate the short and long orthorhombic phases respectively, and *Bbcm* indicates the increased symmetry phase observed at higher pressures when the tilt angle is suppressed. Right: Magnetic and electric phase diagram. The different transition temperatures are indicated as follows, circles indicate the MIT transition, triangles the Néel temperature, and diamonds the Curie temperatures.

is observed [55]. The structural phase diagram has been extrapolated from room temperature measurements by the authors of this study where the main assumption is that lowering the temperature is likely to increases the pressures of the structural transition [55]. The magnetic phase diagram seems to mimic this behavior with an overlap of AFM and FM states in the structural mixed state, suggesting that the AFM order could be a consequence of the *S-Pbca* phase while FM order would be related to the *L-Pbca* phase. The Curie temperature seems to be around 10 K up to 2 GPa, and then increases to 25 K at 5 GPa to slowly decrease at higher pressures forming a dome shaped phase. The signal in the magnetic susceptibility allowing to track the Curie temperature disappears above 8 GPa, a QCP could be expected around 10 GPa, and possibly coincide with the transition to the *Bbcm* phase. Furthermore evidence of superconductivity has been found at 9 GPa with ac susceptibility measurements [51].

The structural changes observed at room temperature in Ca_2RuO_4 under pressure are detailed in figure 4.3. The high pressure orthorhombic L-*Pbca* structure is characterized by a discontinuous elongation of the *c*-axis, while the *a* and *b* lattice parameters are slightly shortened and become almost identical. The jump in the lattice volume and the phase coexistence between the short and elongated phases are characteristic of a first order phase transition. Additionally, the tilt angle of the octahedra is also reduced in the L-*Pbca* phase and completely disappears above 5.5 GPa leading to the higher symmetry structure *Bbcm*. The rotation angle is almost unchanged under pressure.

Recently Ca_2RuO_4 has received great interest due to its unusual behavior under applied current. Electric DC currents seem to be able to control the electronic, magnetic, and structural degrees of freedom. The I-V curve shows clear non-Ohmic behavior with the onset of a negative-differential-resistivity (NDR), where for a sufficiently high current, the voltage starts to drop instead of increasing [132, 136]. An electric field induced insulator to metal transition

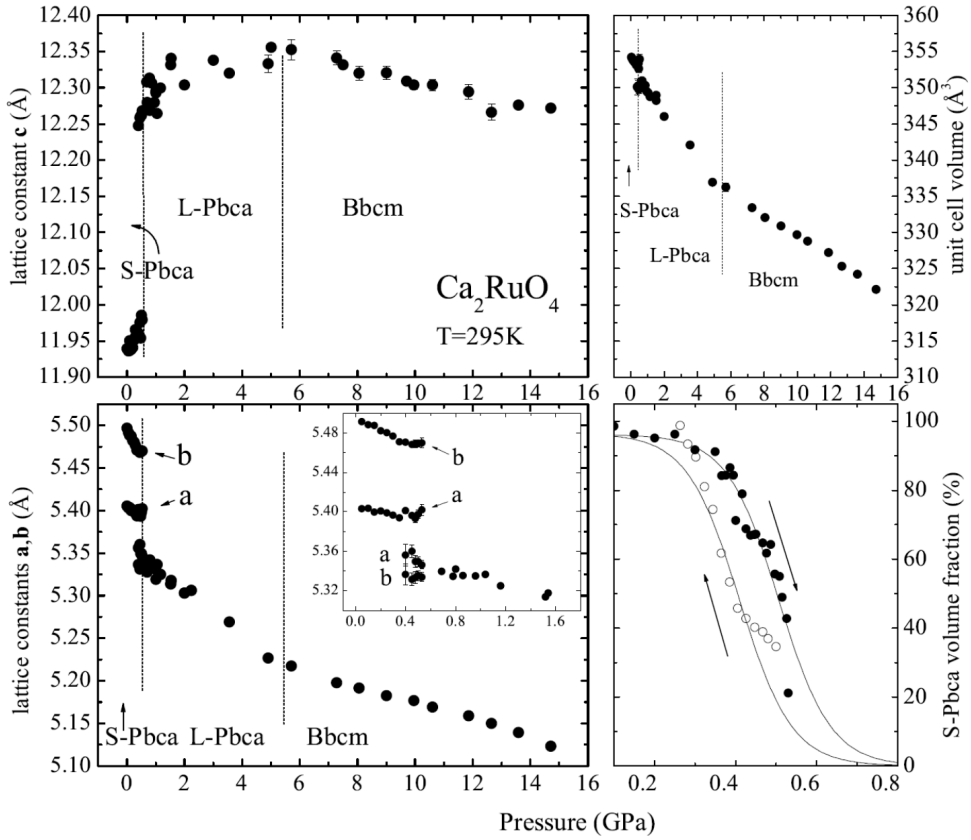

Figure 4.3: Structural changes in Ca_2RuO_4 under pressure. Left: pressure dependence of the lattice constants. The inset shows a and b near the phase transition from S-Pbca to L-Pbca. Top right: Unit cell volume versus pressure. Bottom right: hysteresis of the S-Pbca volume fraction at the transition. The corresponding space groups are indicated, the phase transitions are marked by dashed lines. Taken from [55].

maintained by current was first reported in 2013 [52], but since then the putative transition is believed to be induced by current, as evidenced by the change from "electrical-field-induced" to "current-induced" transition in the literature [132, 132]. So far there has been no comprehensive study on the electrical transport properties of Ca_2RuO_4 under applied DC current which has defined a critical current density of the MIT and its dependence to the crystallographic directions. Evidence to claim that a metallic state is reached is not sufficient, as almost all temperature dependent curves presented to identify the metallic phase show a strong increase of the resistivity with lowering temperature, which would indicate an insulating or semiconductor state [132, 136, 137].

The magnetic properties of Ca_2RuO_4 are also strongly affected by the current density. At very small current densities the AFM order is expected to disappear. As shown in figure 4.4, the (100) neutron scattering peak produced by the AFM order is suppressed under current. Although an alternate AFM order could be in place this seems unlikely, no new magnetic reflection have been observed [137].

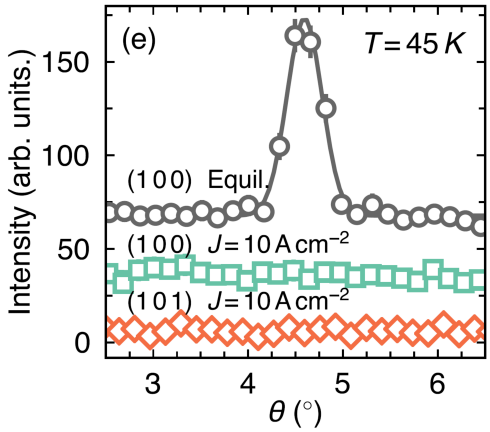

Figure 4.4: Magnetic neutron scattering. The (100) magnetic reflection at $T = 45$ K in the equilibrium state (zero current) is suppressed under current. The (101) reflection that can arise due to an alternate AFM pattern is also not present. [137]

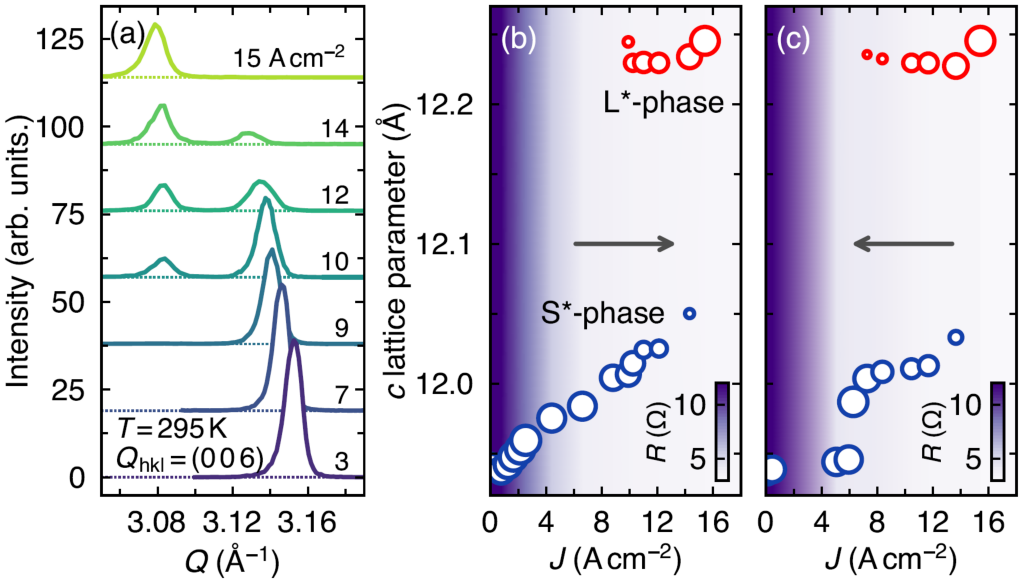

Figure 4.5: Current induced structural transition. (a) X-ray diffraction scans around the (006) reflection for increasing current densities applied along the c-axis. (b) Evolution of the c-axis lattice parameter with increasing current density, J, where short (S*-phase) and elongated (L*-phase) phases are differentiated with blue and red colors, respectively. The symbol size indicates the integrated intensity and background color grading represents the in-situ resistance (R) (c) A hysteresis in the structural behavior is seen upon reducing the applied voltage. [137]

The changes in the crystal structure under electrical current are shown in figure 4.5. There is first an elongation in the c axis of the ambient pressure structure, followed by an intermediate state, with current densities between 10 and 15 A.m^{-1}, where the initial phase coexists with a new one showing even longer lattice parameter in the c direction. At higher current densities,

the initial phase is completely suppressed. The low-current phase can be identified to be the equilibrium short orthorhombic phase, referred to as S*-phase, where the star stands for out-of-equilibrium. The new phase appearing at higher currents with an even longer c axis is referred to as L*-phase, similarly to the elongated phase found under pressure. The hysteretic behavior across the transition is indicative of a first order phase transition. Further neutron diffraction studies showed that besides the structural elongation along the c-axis, the tilt and rotation of the RuO_6 octahedra are reduced under current [137].

Hydrostatic pressure and electric current reduce the structural disorder in Ca_2RuO_4 in a similar way, notably with a discontinuous elongation of the *c*-axis lattice parameter and reduction of tilt of the RuO_6 octahedra. Moreover, both bring the system away from the AFM Mott insulating state. However, under pressure the system becomes FM, while under current is shows strong diamagnetism. We intend to study more deeply the magnetic properties of Ca_2RuO_4 under current and pressure to understand this discrepancy and the connections between structure and magnetic order. We also intend to shed light into the multiple current induced phase transitions and the interplay between the different degrees of freedom. Unlike hydrostatic pressure, current is a non-equilibrium tuning parameter which opens the possibilities to a new class of phase transitions.

4.2 Pressure phase diagram

Neutron depolarization was measured on Ca_2RuO_4 single crystalline samples under pressure using the enhanced depolarization set up described in section 2.2. High quality single crystals were prepared using a floating zone mirror furnace with a RuO_2 self-flux [138]. During the preparation process, upon cooling to room temperature, a first order structural transition is crossed at $T_M = 357$ K which shatters the crystal mostly along the (001) planes (or *c* planes). Some of the resulting pieces were carefully ground from both sides obtaining irregular slab-like samples of constant thicknesses ranging from 50 to 70 µm with the *c* direction perpendicular to the large surface. These samples have later been manually pieced using a scalpel into smaller slabs that would fit the 400 µm diameter space in the pressure cells. Pressure was applied using V2 pressure cells described in section 2.1, fitted with moissanite anvils of 0.8 mm culet size. A 4 to 1 mixture of methanol and ethanol has been used as pressure transmitting medium (PTM).

The results presented in this section were obtained during 2 pressure runs on 2 different samples. Images of the 2 samples inside the pressure cells are shown in figure 4.6. During the first pressure run (1^{st} Run), where a copper-beryllium gasket was used, the pressure was successively increased to 1.7, 2.8, 4.8, and 6.3 GPa, before the sample shattered and the gasket started deforming irreversibly by dangerously enlarging the sample space. At this point the pressure run was terminated and the pressure cell opened. For the second pressure run (2^{nd} Run), a rhenium gasket was used instead. Here the pressure was successively increased to 1.4, 1.9, 4.0, and 8.8 GPa. Although the use of a rhenium gasket allowed us to reach a higher pressure, the experiment had to be terminated when the gasket hole started deforming dangerously while trying to increase the pressure beyond 9 GPa. At 8.8 GPa, already substantial gasket deformation in comparison to the mostly circular initial shape could be observed (see figure 4.6).

The temperature dependence of the neutron depolarization obtained during the first pressure

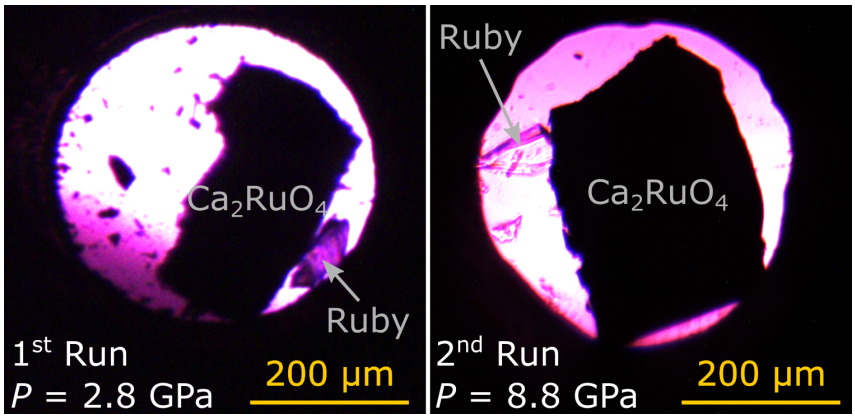

Figure 4.6: Images of the Ca_2RuO_4 samples inside the pressure cell for the 2 pressure runs. The pressure P at which each image has been obtained is indicated as well as the location of the ruby crystal used for manometry.

run are shown in figure 4.7. The depolarization is very small, on the order of 0.5 %, as expected from the small saturated magnetization of 0.35 μ_B/f.u. [54]. After testing different parameters, the measurement protocol comprised to cool the samples under zero field, and measure as the sample is warmed up under an applied field of 20 mT. Despite the small signal, a clear change from a flat neutron polarization dependence at high temperatures, to a gradually decreasing dependence at lower temperatures can be seen. For all the pressure studied, the transition temperature is around 25 K. The experimental error in determining the exact transition temperature is rather high due the large dispersion of the data in comparison to the signal. Nonetheless it is clear that the Curie temperature of the weak itinerant FM phase appears under pressure and depends weakly on pressure.

This first set of measurements performed on Ca_2RuO_4 proved rather challenging. Any change of the neutron intensity during the experiment can potentially produce a spurious signal. During this experiment the afterglow of the detector, discussed in section 2.2.3, where the neutron scintillator efficiency depends on the neutron exposure, was first noticed. The effect at ANTARES is usually small enough to be ignored in most ND experiments, but in this case it produces a large spurious signal in comparison to the signal produced by the sample. This spurious signal disappears once the detector reaches a steady state, which usually happens after 2 or 3 data points. More information on this topic may be found at the end of section 2.2.3. Due to this, the first few data points for each pressure were discarded. Additionally, during this experiment, due to technical problems with the cryostat's helium compressor, temperatures below 5 K were hardly reached. For these reasons 7 K is the lowest temperature reached during this measurement.

Figure 4.8 shows the temperature dependence of the neutron polarization recorded during the second pressure run. Similarly to what was observed for the first pressure run, the neutron polarization drops slightly at temperatures between 20 and 25 K, and the depolarization values reached at 10 K are around 0.5 %. For the measurements at 1.4 and 1.9 GPa, around 7 K there is a second more pronounced drop in the neutron polarization. At 4 K, the lowest achievable temperature in this experiment, the polarization drop is on the order of 2 %, suggesting a much

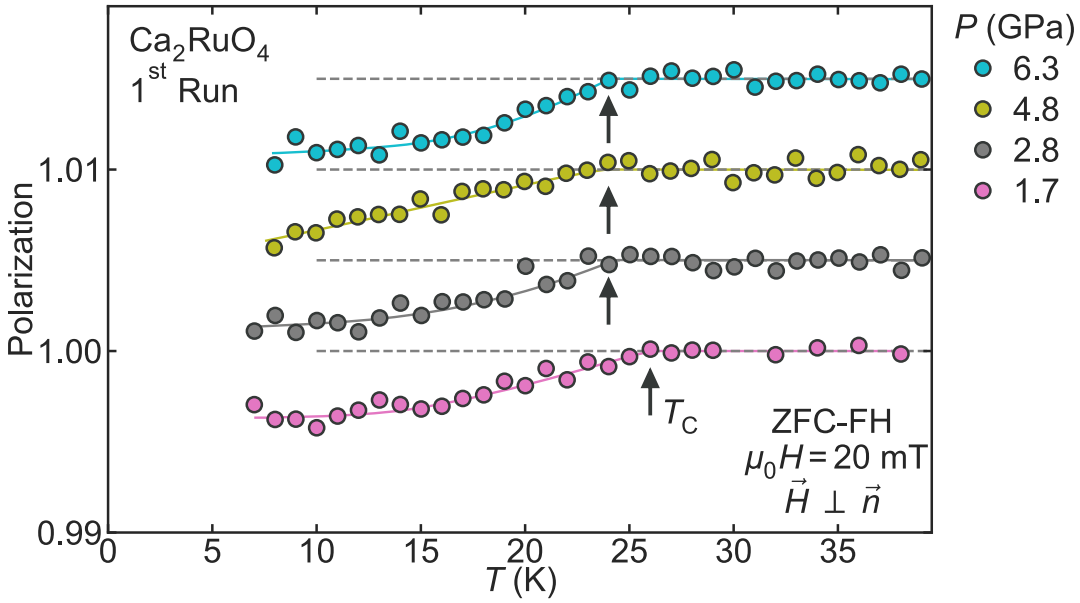

Figure 4.7: Temperature dependence of the neutron depolarization of Ca_2RuO_4 under different applied pressures during the 1st pressure run. A magnetic field (H) was applied perpendicular to the neutron beam, i.e, parallel to the sample surface. The sample was first cooled at zero field (ZFC) and then measured upon field heating (FH). Data is shifted upwards for clarity, the gray dashed line indicates full polarization ($P = 1$) for each pressure. The arrows indicate the transition temperature. The lines are a guide to the eye.

larger ordered magnetic moment. This discontinuity in the polarization profile clearly illustrates the presence of a distinct low temperature phase.

For the first pressure point of the second run, at 1.4 GPa, different cooling histories and magnetic fields were used. Typical data is presented in figure 4.9. At a field of 5 mT, the first drop in the polarization, corresponding to the weak FM phase, seems to be slightly more pronounced than for higher fields while the second drop corresponding to the new phase is smaller. In zero field cooled - field heated, and field cooled (fc) measurements, the temperature dependence of the polarization is qualitatively similar, although it seems that the neutron depolarization due to the new low temperature phase is stronger for field cooled measurements. This might indicate that the new low temperature phase has a spin glass type behavior.

Further insights into the nature of the different phases, was inferred from the field dependencies of the polarization shown in figure 4.10. As expected, in the paramagnetic phase (at 30 K), the neutron beam is not depolarized by the sample at any applied field. At 12 K, deep in the weak FM phase, the beam polarization is lowest at very small applied fields (as already evident in figure 4.9), and increases with increasing magnetic field reaching a fully polarized beam (i.e. saturation) at only 80 mT. The relatively low saturation field together with the low depolarization values suggest that this phase is characterized by a very small ordered moment, and a small saturation field, thus we labeled it "weak FM phase". In contrast, at 4 K, into the low temperature phase, the polarization drops quickly for small applied fields and reaches

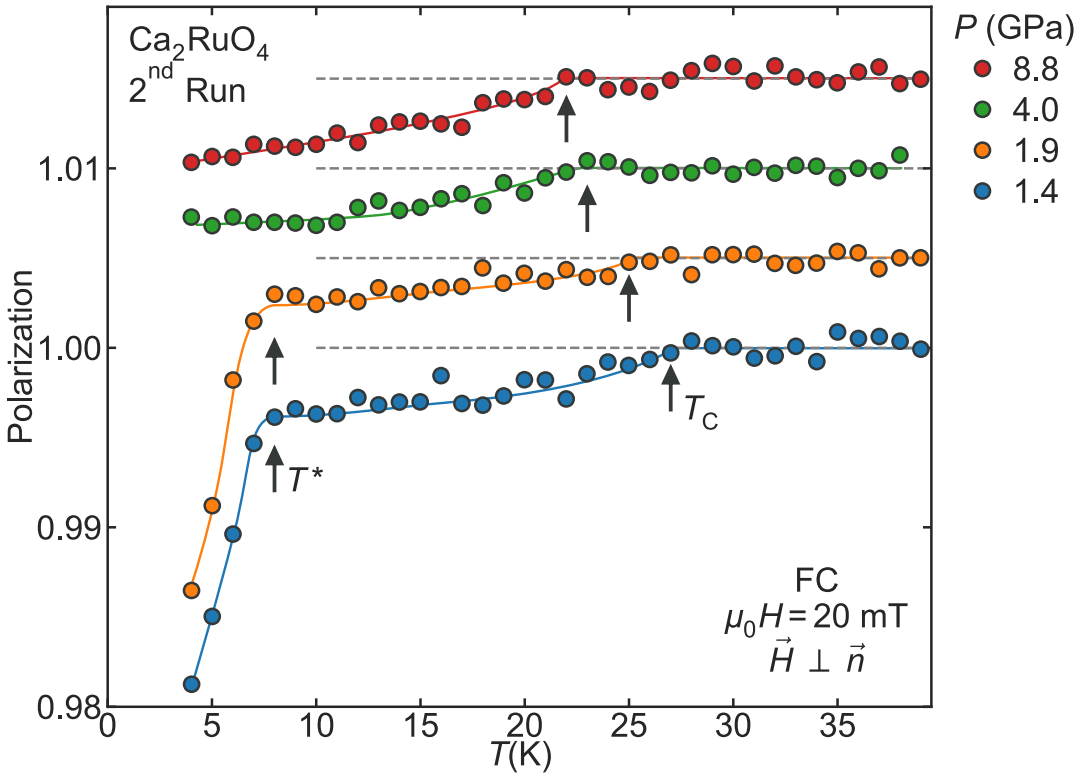

Figure 4.8: Temperature dependence of the neutron depolarization of Ca_2RuO_4 under different applied pressures during the 2nd pressure run. A magnetic field (H) was applied perpendicular to the neutron beam, i.e, parallel to the sample surface. The sample was measured during field cooling (FC). Data is shifted upwards for clarity, the gray dashed line indicates full polarization ($P = 1$) for each pressure. The arrows indicate the transition temperature. The lines are a guide to the eye.

a minimum 70 mT before slowly increasing as it approaches saturation above 250 mT. The different profile suggest that this second phase is not a typical isotropic FM. The increase in neutron depolarization observed at low fields could be due to domain reorganization, but given the magnetic field configuration (parallel to the sample surface), demagnetization fields should be small. This profile could be observed in a FM with a hard axis in a different direction than the applied field, or with some sort of spin glass. The overall large increase in neutron depolarization, in comparison to the weak itinerant FM phase, indicates that long range magnetic order is in place with a rather large ordered moment.

The neutron depolarization measurements are summarized in figure 4.11 with a proposed magnetic and structural temperature versus pressure phase diagram. The critical temperatures plotted in this figure was determined graphically as shown in figures 4.7 and 4.8. The results clearly point towards a different magnetic phase diagram as the one proposed in the bibliography, where a single dome shaped FM phase spans a pressure range from 0.5 GPa to 7.5 GPa [51, 55]. We observe instead two distinct FM phases. In the mixed S-L structure phase, i.e between 0.5 and 2 GPa, a low temperature phase appears below 8 K. This phase is characterized by large

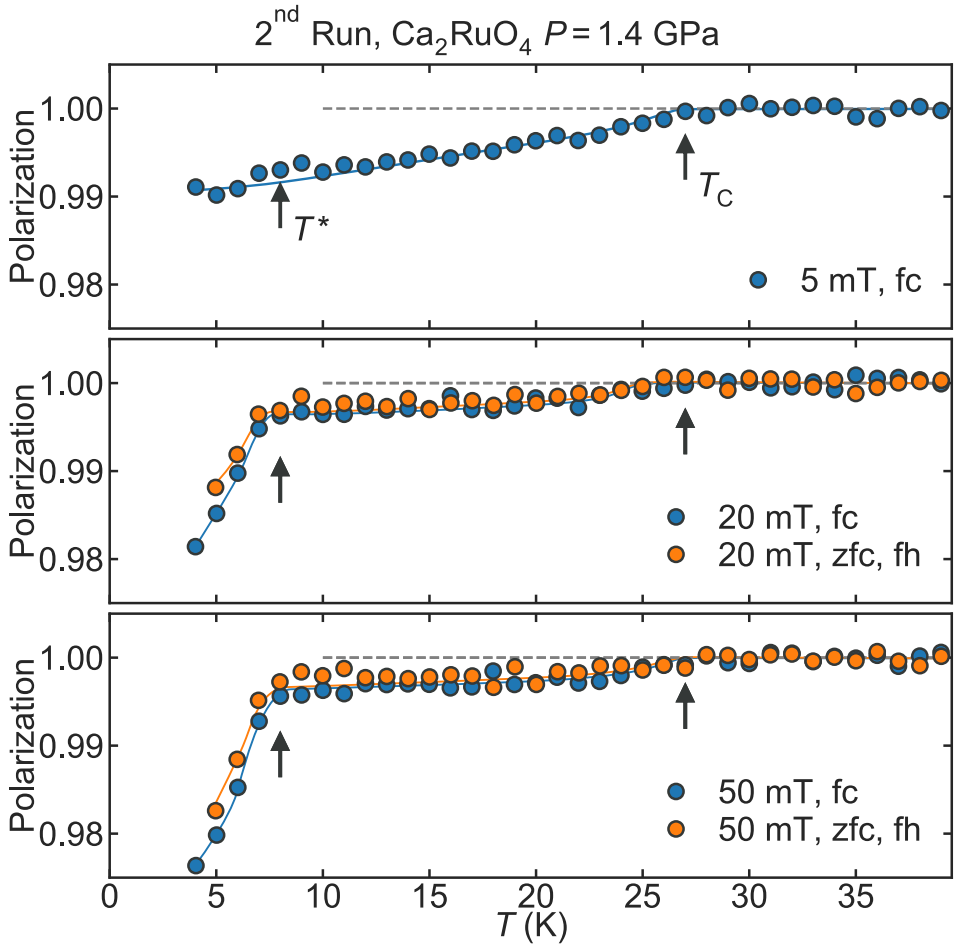

Figure 4.9: Temperature dependence of the neutron polarization of Ca_2RuO_4 at 1.4 GPa for different cooling histories and magnetic fields. The magnetic field is applied in a direction perpendicular to the neutron beam, i.e parallel to the sample surface. The arrows indicate the transition temperature. The lines are a guide to the eye.

neutron depolarization which indicates a large ordered moment. The simplest explanation would be that a local-moment FM state forms, were the magnetic moment reaches the full 2 μ_B/f.u. as expected from Ru^{4+} ions. Alternatively, a glassy system with strong FM correlations might from, similarly to what is observed in the element $x = 0.5$ of the $Ca_{2-x}Sr_xRuO_4$ series [14, 139] (see figure 1.3 b). At higher temperatures, and for all measured pressures, a weaker FM phase can be observed over both S-L mixed state and L-*Pbca* structural phases. The Curie temperatures for this phase does not change strongly with applied pressure, ranging between 25 and 22 K. The Curie temperature seems to slightly decrease in the pure L-*Pbca*, but due to the large measurement errors it is hard to know for certain. No signs of collapse of the FM order can be observed up to 8.8 GPa.

The transition lines shown in the phase diagram represent an empirical suggestion. The error bars shown in figure 4.11 reflect the large experimental uncertainty when determining the transition temperatures and pressures. The error for the Curie temperature is estimated to ± 2 K,

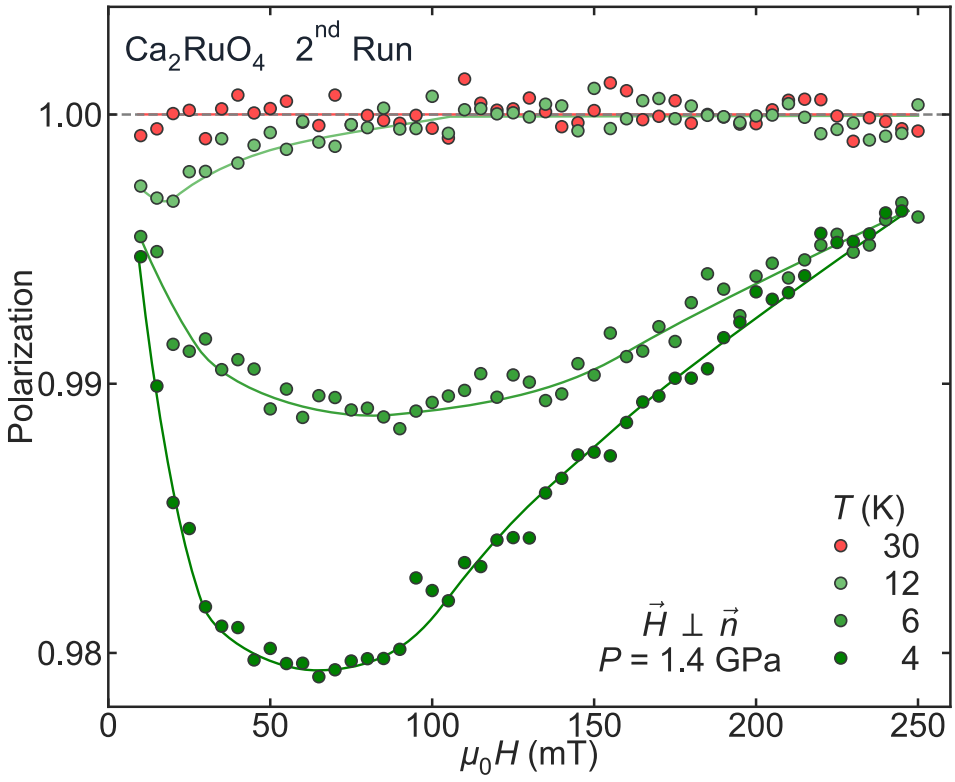

Figure 4.10: Field dependence of the neutron depolarization of Ca_2RuO_4 at 1.4 GPa and different temperatures. The magnetic field is applied in a direction perpendicular to the neutron beam, i.e parallel to the sample surface. The lines are a guide to the eye.

while it is only $\pm$ 1 K for T^*. The error of the pressure determination is chosen arbitrarily large and increasing with the pressure amplitude. Although the ruby fluorescence technique allows to determine the pressure of the ruby crystal with high accuracy, a large systematic error must be taken into account. There are two main contributions to this experimental error. First, as described in chapter 2, the pressure at low temperatures is extrapolated from measurements at room temperature. Secondly, a pressure gradient builds up inside the sample space where the pressure is maximal at the center and lower towards the edge of the gasket. Both of these error sources would increase under increasing pressure. Moreover, for the two experiments, the ruby crystals were particularly close to the edge of the gasket in comparison to the sample (see figure 4.6) which might lead to an underestimation of the pressure.

Neutron depolarization is superior to other techniques when it comes to the identification of FM phases, as there is no signal in the PM region (in contrast with inductive methods), and the signal drops strongly as long range FM order appears. There is no sign of the dome shaped FM phase suggested by transport measurements [50]. The presence of two distinct FM-like phases has been demonstrated. The presented phase diagram is far from accurate as both pressure and temperature values have relatively large error bars. The exact shape of the weak FM phase is hard to determine as the signal to noise ratio is very low especially close to the phase transition. Interestingly, despite this discrepancies, most of the data found in the literature fits the present phase diagram [51, 54]. It seems likely that the strong FM phase is unique of the mixed

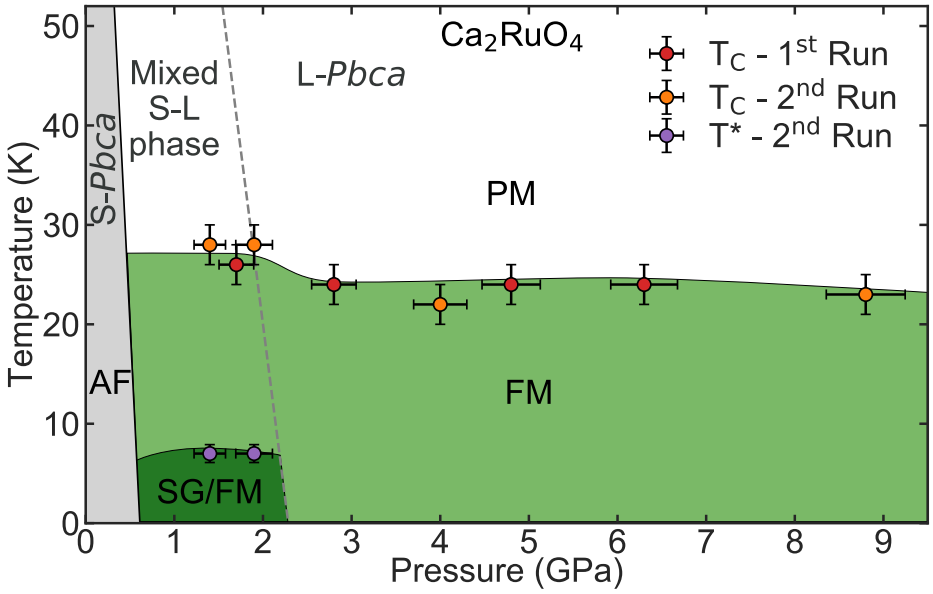

Figure 4.11: Pressure dependent magnetic and structural phase diagram of Ca_2RuO_4. The distinct magnetic phases, paramagnetic (PM), antiferromagnetic (AFM), weak ferromagnetic (FM), and spin-glass/strong-ferromagnetic (SG/FM) are labeled in black and separated by thin continuous lines. The structural phases, short orthorhombic (S-*Pbca*), long orthorhombic (L-*Pbca*), and mixed phase, are labeled in gray. The S-*Pbca* phase is superposed to the AFM phase and a dashed line separates the mixed phase from the L-*Pbca* phase. The temperatures are obtained from the neutron depolarization measurements, T_C refers to the transitions into the weak FM state while T^* indicates the transition into the low temperature state. The structural phases are taken from [55].

structural phase, while the weak FM phase belongs to the S-*Pbca* phase. More measurements would be necessary to determine the interplay between structure and magnetic order, especially at low temperatures and low pressures, where the mixed structure phase appears. Up to the highest pressures measured, namely 8.8 GPa, the strength of the weak FM phase seems to be relatively constant with no indication of a QCP at higher pressures. Above 9 GPa, the magnetic susceptibility of the transition appears to be suppressed [51], similar measurements at higher pressures using the superior V2 pressure cell design and diamond anvils should be performed in order to clarify these questions.

Finally, thin films exhibit low temperature itinerant ferromagnetism and a significantly suppressed MIT due to epitaxial strain [140]. FM order is not particularly sensible to crystallographic distortions, thus suggesting that it is also not very sensitive to pressure anisotropies.

4.3 Current-induced phase transitions

The temperature dependence of the magnetization and electrical resistivity of a Ca_2RuO_4 single crystalline sample were simultaneously measured under different applied electric DC currents. A standard helium gas flow cryostat was used to control the temperature. The measurements were performed in a vibrating sample magnetometer (VSM), where the sample stick was modified to allow for transport measurements to be conducted in situ. To avoid shattering the sample when crossing the structural phase transition at $T_M = 357$ K, the sample should not be warmed above this temperature. To avoid heating, silver epoxy was used to contact the sample. The electrical contacts and sample geometry are shown in figure 4.12. A Keithley 6221 current source was used to apply DC current to the sample. The electrical current was supplied by thick insulated copper wires (0.25 mm diameter). The voltage drop through the sample due to the applied current was measured 3 cm upstream of the copper wires, in a 2 point contact fashion, with a Keithley 2182A nanovoltmeter.

Given the large resistance values of the sample compared to the thick copper wires, the contact resistance was considered zero. Inside the cryostat, the wires were twisted in pairs (see figure 4.12) to minimize noise. A small Cernox thermometer from Lake Shore was used to measure the sample temperature. Most thermometers contain relatively strong magnetic elements. To minimize parasitic magnetic signals from the thermometer, it was placed 2 cm away from the sample. The thermal contact between sample and thermometer was ensured via the thick copper wires used for the electrical contacts. The directions of the applied current and magnetic field, as well as the measured magnetization and resistivity were parallel to each other, and perpendicular to the c axis of the sample. The exact directions of the a and b axes are unknown, from the magnetization data it seems likely that the magnetization was measured in a direction somewhat in between a and b.

Ca_2RuO_4 undergoes a structural phase transition under applied current [137] which induces cracks in the sample as the current is increased and decreased. A few samples turned into a coarse powder during the preliminary tests of the experimental setup. Therefore, the different curves were measured in a single experiment where the applied current was increased successively between measurements without ever decreasing the current or turning off the current source. The sample seems particularly vulnerable when the changes in the current density occurred at low temperatures, therefore, the current was only changed when the sample was at room temperature. Due to the large resistance values of the sample, notably at low current densities and low temperatures, the compliance voltage of the current source (100 V) was reached, limiting the temperature range available. At higher current densities, the sample resistance was significantly lower and the compliance voltage was never reached.

The temperature dependence of the magnetization and resistivity of Ca_2RuO_4, for various DC currents, is shown in figure 4.13. The magnetization curve at very low currents is characteristic of the intrinsic behavior of Ca_2RuO_4, with a peak at 110 K corresponding to the AFM transition. This peak shifts towards lower temperatures as the applied current increases, it completely disappears for applied current densities above 1 A/cm^2. Above this value, the magnetization curve is rather flat with the start of a downturn at low temperatures (around 40 K).

At the lowest applied currents, the resistivity increases exponentially for decreasing temper-

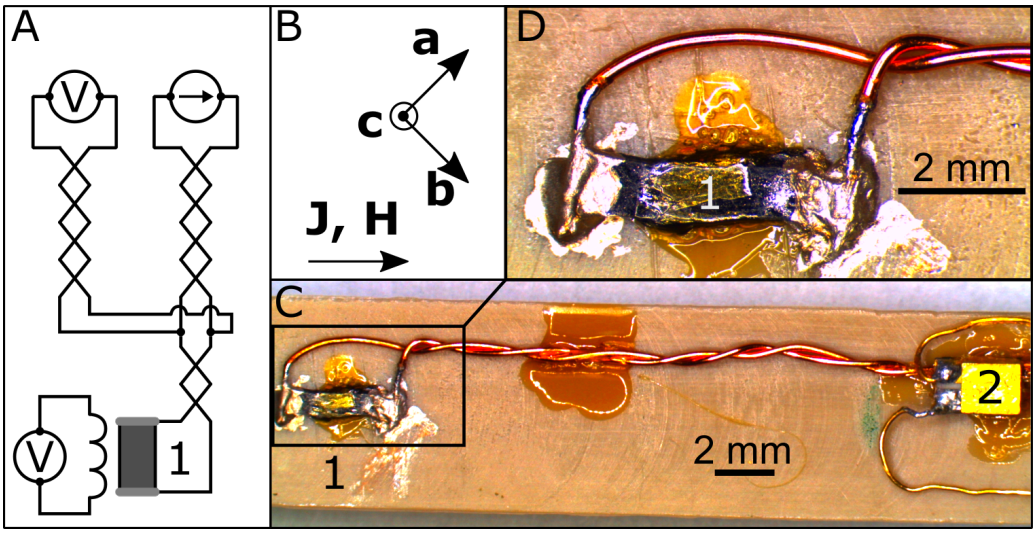

Figure 4.12: Schematic circuit, and pictures of the Ca_2RuO_4 single crystal. A: Schematic circuit showing the nanovoltmeter and current source connected to the sample (1), as well as the voltage induced in the pick-up coils by the sample's magnetization. B: Relative direction of the current (J) and magnetic field (H), with respect to the crystallographic directions of the sample. C: The sample is glued with GE varnish on the VSM sample holder made of PEEK (plastic). A Cernox thermometer (2) is attached on the copper wires 2 cm upstream of the sample. D: Enlarged image of the sample, silver epoxy is used to contact the thick insulated copper wires.

atures, as expected from the insulating nature of the intrinsic state. As the current density J increases, the resistivity decreases significantly, most notably at low temperatures where it is reduced by several orders of magnitude. Still, even at the highest current densities the resistivity increases for decreasing temperatures, over the whole temperature range, suggesting that no purely metallic state is achieved.

It was not possible to routinely reach temperatures below 40 K with the current setup. At low current densities the high resistivity values mean that the compliance voltage of the nanovoltmeter is reached. At higher current densities, although the resistivity drops considerably, it is still large at low temperatures, and combined to the larger current densities it leads to considerable Joule heating. The temperature of the helium gas flow (i.e. the temperature in the cryostat) was much lower than the temperature read on the sample thermometer. When we tried to increase the cooling power of the cryostat by increasing the helium flow we observed a steep decrease of the magnetization as a function of apparent sample temperature. Given the large temperature gradients we did not trust the data and attributed the downturn to the solder near the pick-up coils containing superconducting material. Interestingly a similar and much stronger downturn was also observed by Sow et. al. and first interpreted as the onset of strong diamagnetism [53]. The publication was later retracted when this downturn was identified as a spurious signal arsing from the sample holder due to the large thermal gradients building around the sample [141]. To avoid any controversy the data below 50 K, where the thermal conductivity of the PEEK sample holder becomes marginal and the Joule heating significant, will not be considered.

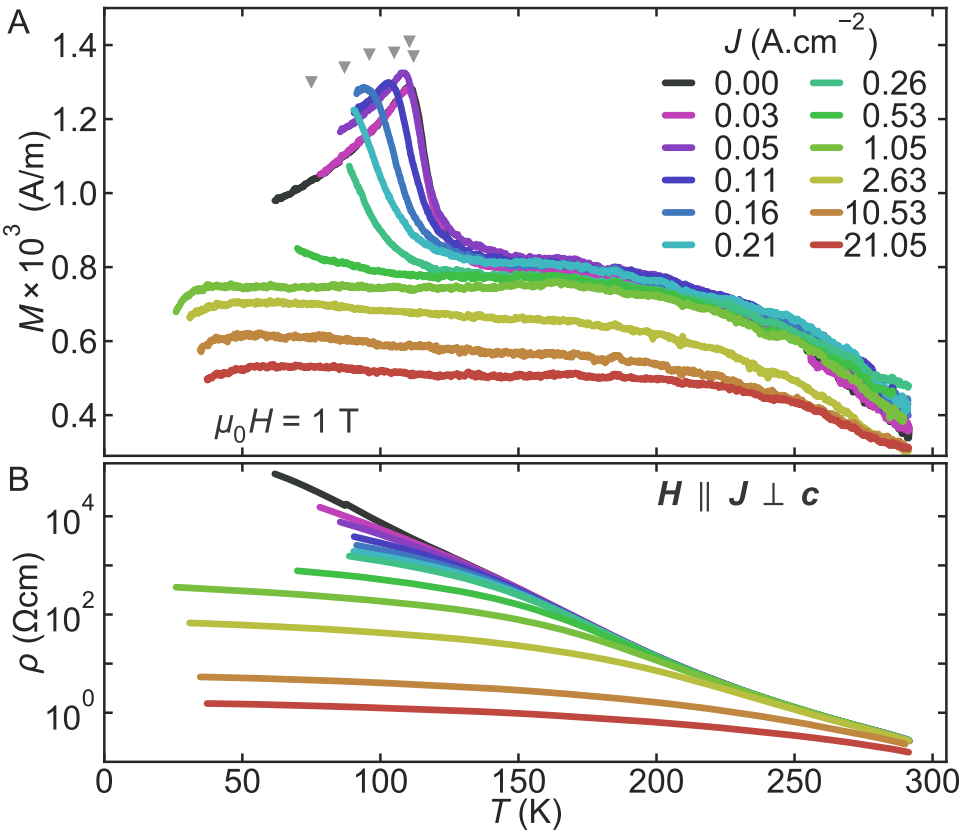

Figure 4.13: Temperature dependence of (A) the magnetization M, and (B) electrical resistivity ρ, of a Ca_2RuO_4 single crystalline sample under different applied DC electrical currents. The applied current (J) and magnetic field (H), as well as the direction of the measured quantities are parallel to each other and perpendicular to the c axis of the sample. Small gray triangles indicate the peak in the magnetization corresponding to the AFM transition.

From the magnetization curves, namely the AFM peak positions, a current density dependent magnetic phase diagram may be considered. This diagram is presented in figure 4.14, were some points falling out of the measurable range have been extrapolated. It illustrates how the Néel temperature is gradually suppressed for small current densities. Unfortunately due to the experimental limitations mentioned above we cannot infer any information about a QCP or a different magnetic order appearing at lower temperatures. Since the structure under current undergoes similar changes as under pressure, one could expect a similar FM order appearing below 25 K for large current densities.

Following the measurements presented in figure 4.13, current sweeps were determined at room temperature on the same sample. The results were identical when measuring both increasing and decreasing current, showing no hysteresis in the resistivity curve. The electrical field that builds up across the sample with respect to the current density is shown in figure 4.15. The convex curvature indicates that the resistivity decreases with increasing current. Up to the maximum current density measured, there is no evidence of a sharp phase transition to a conductive

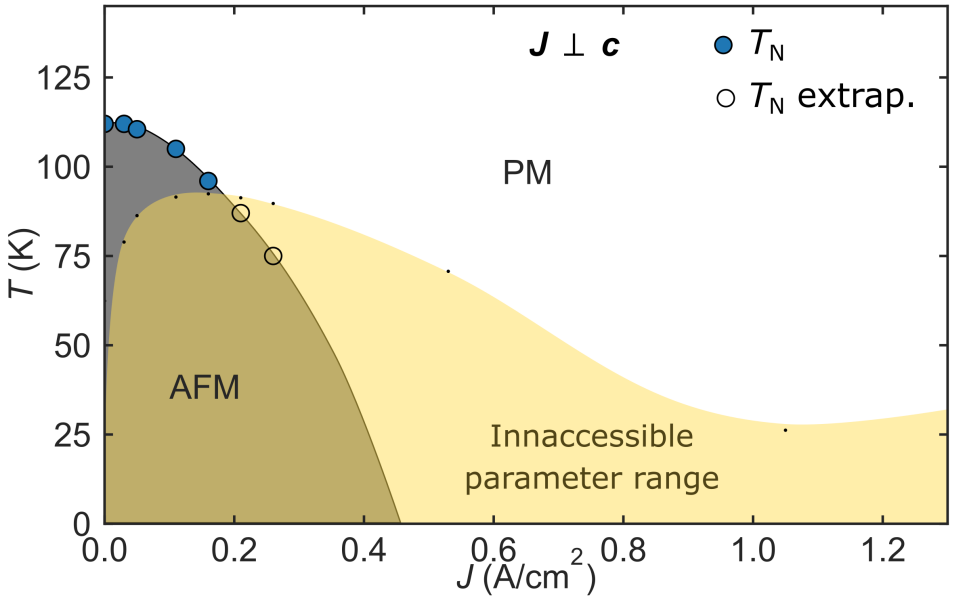

Figure 4.14: Current density dependent magnetic phase diagram of Ca_2RuO_4. The antiferromagnetic (AFM) phase is highlighted in gray. The Néel temperature is taken from figure 4.13, where the blue points are maximums in the resistivity, while the empty points have been extrapolated. The semi-transparent yellow area identifies the inaccessible parameter range.

state as suggested in the literature [52]. It can also be seen that the measured magnetization is unchanged by the current density, therefore all parasitic signal induced into the measurement coils due to the applied current density can be discarded.

The differential resistance (dE/dJ) tends to zero at similar current densities as reported by Okazaki et. al. [132], and might potentially evolve into a negative differential resistivity (NDR) at higher current densities. Unlike in this experiment, most measurements in the literature are done with the current along the c axis, which might explain discrepancies in the current density values to which different features are observed. The observation of a discontinuity in the resistivity, associated with the MIT transition, as reported in the literature was done using a constant voltage source [132]. Negative differential resistance can lead to an uncontrolled increase of the applied current when using a constant voltage source. Interestingly, NDR is also observed in the AFM insulating state of the the bi-layered parent compound $Ca_3Ru_2O_7$. The phenomenon produces similar current versus voltage dependencies than those where the MIT is observed [52, 142]. In this case no MIT was suggested. Current sweeps at different ramp rates and with different sample geometries should be performed in a more consistent way to clarify whether such discontinuous transitions take place and which are the critical values. Due to naturally occurring cracks in the Ca_2RuO_4 samples, and the degradation of the sample under current make it difficult to obtain reproducible results.

Independently of the putative MIT, it is clear form the temperature dependence of the resistivity that no metallic state has been found in this experiment. Different transport mechanisms may be assumed to model the change of charge carrier density with temperature for a Mott

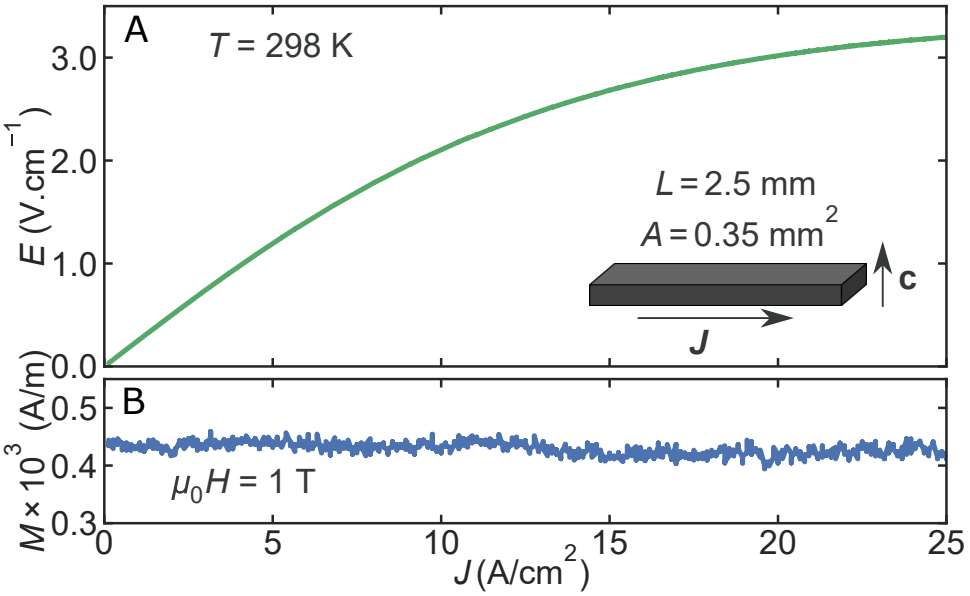

Figure 4.15: Current density sweep. A: Electric field E versus current density J in the measured Ca_2RuO_4 sample at room temperature, the sample geometry needed to convert electrical field into resistivity is detailed. B: The magnetization M is measured simultaneously during the current sweep.

insulator. Two different models were used in the literature to describe the transport mechanism [143, 144], activation type with $\rho \propto \exp(E_G/2k_BT)$, and Variable-Range Hopping (VRH) with $\rho \propto \exp(T_0/T)^\beta$ where β depends on the dimensionality D of the hopping mechanism as $\beta = 1/(D+1)$ [145]. The first model is based on a thermal activation of the charge carriers across an energy gap E_G, while the second model is used to describe carrier transport in a disordered semiconductor or in amorphous solids with a less well defined energy gap.

The validity of these different models is evaluated in figure 4.16 by plotting the resistivity in a logarithmic scale with respect to the inverse temperature with different exponents. The VRH model for 2 and 3 dimensions provides a slightly better fit, but all models fail below 160 K, which is the range where, in particular, the VRH model is supposed to be better defined. A more complex transport mechanism seems to be in place, especially at low temperatures. This could already have been foreseen in figure 4.13, where the resistivity curve at low current densities changes from a positive curvature at high temperatures to a negative curvature at lower temperatures, indicating that the exponential increase of the resistivity slows down at low temperatures.

Assuming that an activation type mechanism is in place, in addition to other mechanisms that modify the resistivity at low temperatures, a gap energy at room temperature can be extracted by fitting the resistivity from 292 to 270 K. For very low currents we obtain a value close to $E_G = 0.48$ meV, which seems to be a good estimate of the gap energy as it is close to the results obtained with recent angle-resolved photoemission spectroscopy (ARPES) measurements [146]. The fitted values of the activation energy for different applied currents are shown in figure 4.17. As the current density increases, the activation energy decreases linearly with a slope of about 10 meV.A^{-1}cm^2, indicating a gap closing with applied DC current. This suppression of the Mott

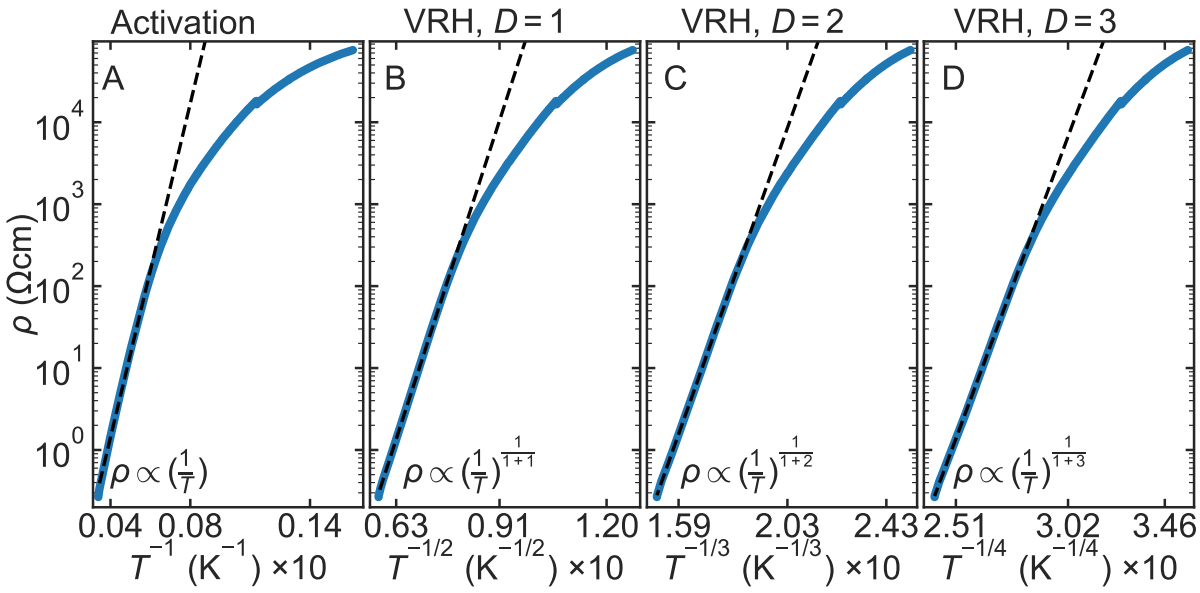

Figure 4.16: Different transport models. The resistivity ρ is plotted in a logarithmic scale with respect to $1/T$ with different exponents β. The exponent corresponds to the different transport mechanisms discussed, A: activation type across an energy gap ($\beta = 1$), B: one dimensional VRH ($\beta = 1/2$), C: two dimensional VRH ($\beta = 1/3$), and D: three dimensional VRH ($\beta = 1/4$). The dashed line corresponds to a linear fit in the temperature range between 300 and 160 K. The ticks in the x-axis correspond to fixed temperatures of 250, 120 and 70 K.

gap with current has previously been observed by Ryuji Okazaki, et. al. [132]. In their study they discard spurious effects due to Joule heating directly determining the sample temperature with infrared radiation. Interestingly, at very low current densities, the activation energy seems to be constant, and only starts to decrease above 1 A/cm^2. Nonetheless, even at the highest current density the activation energy is still considerable, indicating that the Mott gap is not closed and the conducting state has not been achieved.

The limited reduction of the Mott gap is not sufficient to understand the large drop in resistivity with increased current at low temperatures. We propose that a current induced injection of electrons in the conduction band (and/or holes in the valence band), can qualitatively explain the temperature dependence of the measured resistivity curves. For this purpose, we consider a model based on a textbook semiconductor with simple parabolic band edges that approximates the intrinsic electron concentration as a function of temperature due to thermal activation across the Mott gap. To this intrinsic electron density we add an electron doping density n_{D}, constant in temperature and with values ranging from 10^{12} to 10^{16} cm^{-3}. For simplicity, a constant mobility μ is assumed. To obtain similar values as the measured ones, the effective mass m_{eff} is set to 3 times the electron mass, and the mean free time is fixed to 2 ns. Figure 4.18 shows curves corresponding to such model where to simulate the effect of the current on the resistivity, the doping concentration n_{D} is successively increased, and the gap energy is decreased within the range shown in figure 4.17.

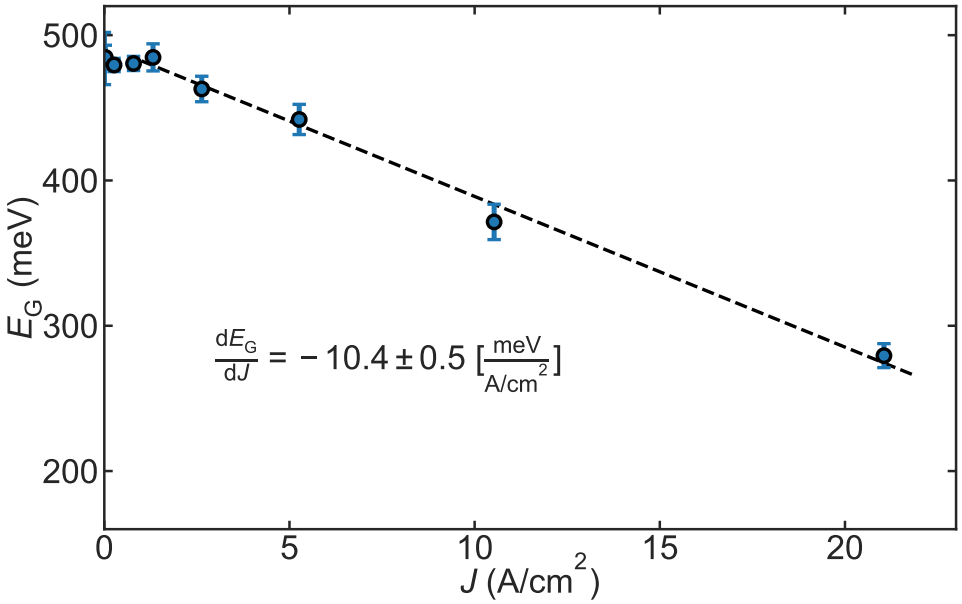

Figure 4.17: Gap energy versus current density. The gap energy E_G is obtained by fitting the conductivity to an activation energy model between 292 and 270 K. The error bars are given by the fit uncertainty. The dashed line is a linear regression of the gap energies obtained for a current density larger than 1 A/cm^2, the slope of the regression is shown.

These curves show a qualitative similarity to the measured resitivity curves (see figure 4.13), and capture the main trends observed, namely a strong reduction of the resistivity at low temperatures, and a quasi stagnation of the resistivity at low temperatures and large currents (i.e. larger electron doping concentration). The observed change from a positive to a negative curvature as the temperature decreases is also well reproduced. Note also that the inflection point between the two curvatures occurs also at higher temperatures for increasing current density. Despite this qualitative similarity, the model is incomplete and does not properly account for the data.

For instance, the band structure of Ca_2RuO_4 is more complex [146] and the mobility most likely has a temperature dependence which modifies the curve shape. In the model the resistivity reaches a stagnation value, even for the lower doping concentrations (i.e. low current densities), it does not in the measured curves. This can be explained by the different nature of the doping mechanism in place. In the model the electron doping is assumed to be temperature independent. In contrast, the charge carrier doping in the sample has two origins, the proposed current induced doping which is also temperature independent but negligible at very small current densities, and the doping due to donor (and/or acceptor) impurity concentration which decreases significantly at low temperatures allowing the resistivity to increase.

The model described in the previous paragraph is capable of qualitatively predicting the changes in the temperature dependence of the resistivity. Additionally, a gradual change of the carrier concentration with current is consistent with a gradual decrease of the Néel temperature, since itinerant AFM is susceptible to the carrier concentration. More particularly, a

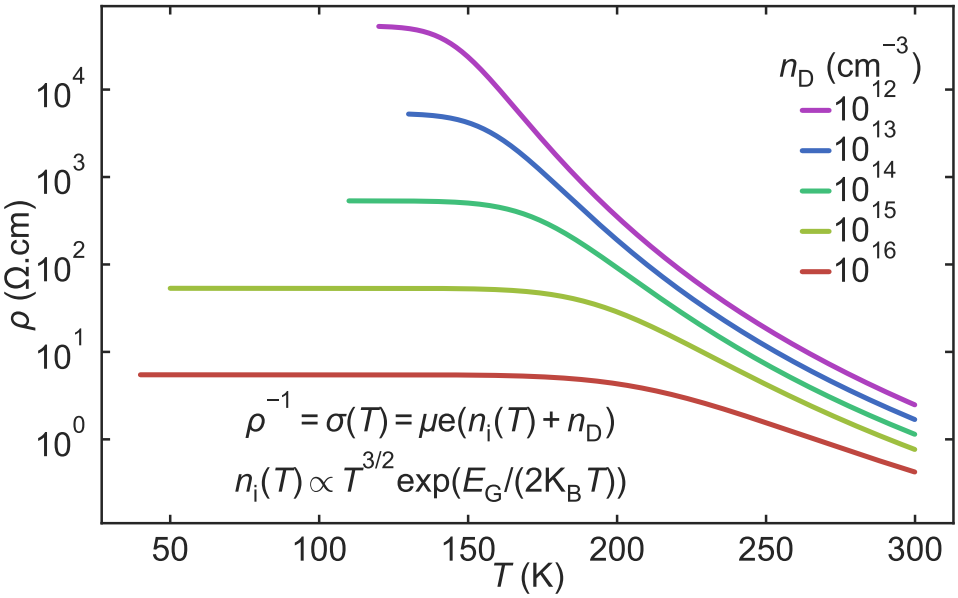

Figure 4.18: Current density induced doping model. Temperature dependence of the resistivity ρ of a theoretical semiconductor with increasing electron doping density n_D. As indicated on the figure, the resistivity is calculated from the intrinsic density of states n_i of a semiconductor and the induced electron density n_D which simulates the effect of the current density.

theoretical study suggests that electron doping in d^4 Mott insulators like Ca_2RuO_4 with strong orbit-coupling favors FM order in detriment to AFM order [147].

The exact mechanism by which charge carriers might be injected into the conduction band when a current is applied is not clear. Negative differential resistivity (NDR) has also been observed in similar systems presenting oxygen octahedra as the parent compound $Ca_3Ru_2O_7$ [142], Sr_2IrO_4 [49], or $BaIrO_3$ [148]. Some of the authors suggest a charge propagation through an unpinning of a charge density wave (CDW) which would add a polaronic transport channel to the already existing activation type transport. Further hypothesis include a current induced promotion of charge carriers from a low to a high mobility band due to impact ionization. Ryuji Okazaki, et. al. [132] argue that the NDR observed in Ca_2RuO_4 is unlikely to be consequence of a ionization of electrons across the band gap or of Zener tunneling as the electric fields needed for those phenomenon to occur are much larger than the ones measured. They propose instead a current induced reduction of the gap energy through the Jahn-Teller distortion of RuO_6 octahedra.

We argue here that both a current control of the gap energy and a charge promotion of carriers to the conduction band seems to be in place. Bandwidth control and doping drive the different elements of the Ruddlesden-Popper series of layered ruthenates [130] to different electronic states. The gap bandwidth is controlled by structural distortions, i.e., the multiple tilting angles of the RuO_6 octahedra [134]. Small distortions to the crystal structure, either due to hydrostatic pressure or to chemical substitution with Sr or La, result in drastic changes in both the electronic and magnetic properties of Ca_2RuO_4 [48, 49, 54]. The small structural

distortions that have been observed under current [137], in combination with the temperature dependent distortions [134] which could be enhanced under current, account for the reduction of the Mott gap. In contrast, unlike the present results, the temperature dependence of the resistivity under pressure or due to chemical substitution does not tend to a saturation at low temperatures. Indicating, that a second transport channel is opened under current which is less temperature dependent than the energy activation type. This second channel could be of polaronic nature given the strong electron-phonon coupling present in Ca_2RuO_4 [149], and that the critical quantity seems to be current concentration and not electric field as it would be for a impact ionization process.

4.4 Summary and outlook

The pressure dependent magnetic phase diagram of Ca_2RuO_4 was investigated by means of high pressure focused neutron depolarization measurements. The results obtained are in conflict with the hitherto know phase diagram clearly showing two distinct FM-like phases coexisting at an intermediate pressure range between 0.5 and 2 GPa. A weakly depolarizing FM phase below 25 K, and a strongly depolarizing phase below 10 K which can be attributed to a FM or a spin-cluster phase with a large ordered moment. At higher pressures, above 2 GPa only the weak FM phase prevails, with a Curie temperature which remains mostly constant up to 8.8 GPa with a slight tendency to decrease with increasing pressure. Given the similarities with the structural phase diagram, where a mixed structural phase is expected at the same pressure range as the observed mixed FM order, it seems very likely that these magnetic orders are associated to a given crystal structure. A careful investigation of the magnetization of Ca_2RuO_4 under pressure with the help of vibrating sample magnetometry inside a beryllium copper clamp cell could help shading light into the controversy between the present results and the bibliography. We also plan to perform additional high pressure neutron depolarization measurements in the future. XRD measurements at low temperatures and high pressures would also be necessary to understand the interplay between structure and magnetic orders.

The temperature dependence of the magnetization and electrical resistivity of Ca_2RuO_4, were also measured simultaneously under different applied current densities with help of a vibrating sample magnetometer in a helium flow cryostat. The resistivity of the sample increases by several orders of magnitude as it is cooled down, making the experiment technically challenging due to the increased power output and the large detection range needed. Nonetheless, the onset of a gradual decrease of the Néel temperature as function of current density was observed below 0.4 A/cm^2. Exploring the low temperature behavior for small current densities is potentially interesting, for instance there could be an emergent phenomena consequence of the suppression of the AFM order. At higher current densities a similar FM phase as the one observed under pressure could take place due to the similarity in the structural changes. Unfortunately the Joule heating at the sample position makes it hard to cool down below 50 K. To overcome the technical challenges, a dedicated large voltage and large power measurement setup would be required. In addition the sample temperature should be measured directly and more efficient sample cooling should be provided. The use of a very small sample should help to reduce the heating output, while aluminum heat exchangers could be used to further thermalize the sample with the helium gas.

The resistivity of $Ca_2Ru)_4$ is strongly reduced under current, specially at low temperatures, but no sign of a first order insulator to metal transition was observed. From the slope of the resistivity at room temperature, an estimation of the electronic band gap was extracted. This energy decreases under current but stays significantly does not go to zero (i.e. gap closing), up to the highest current density measured (20 A/cm^2). To explain the resistivity profiles, we propose that in addition to the closing of the band gap, a current induced promotion of charge carriers may be in place. The exact mechanism is not clear, but it is likely to be related to a reorganization of the orbital population that accompanies the tilting and rotation of the RuO_6 octahedra known to occur under current. Moreover the increase of charge carrier density is very likely a precursor of the gradual suppression of the Néel temperature. More precise and systematic transport measurements would be needed to retrieve reliable critical current densities as well as the anisotropy of the transport properties. For this purpose special effort should be made to obtain single crystal samples with a well defined length and sections along different crystallographic directions.

Conclusions

Quantum phase transitions (QPTs), i.e. phase transitions driven by a non-thermal control parameter, and quantum criticality in general, are a source of novel physical phenomena which can help to challenge existing theoretical models, and drive the development of new functionalities in material sciences. The introduction of this thesis (1) presents the theoretical framework describing QPTs as well as several experimental examples. Hydrostatic pressure is described as a unique control parameter allowing to continuously change the lattice volume of a crystal without changing its chemical composition or introducing unwanted disorder. Applying pressure requires the use of bulky pressure vessels that complicates the data acquisition, particularly for magnetic materials. Neutron depolarization (ND), is described in detail. This technique is very sensitive to the presence of magnetic inhomogeneities on a mesoscopic scale, such as FM or a spin-glass behavior. Additionally, neutrons readily penetrate cryogenic equipment, pressure cells and bulk metal samples. ND is therefore particularly suited to investigate pressure driven QPT in magnetic materials.

Chapter 2 describes the developments of dedicated pressure cells (2.1) and how ND experiments were enhanced by the use of focusing neutron optics (2.2). The adequacy of different pressure cell designs is discussed, and diamond anvil cells (DACs) are chosen due to their compact size and huge versatility. Three different pressure cell models were built presenting increasing high pressure capabilities. Additionally to a good pressure cell design, the technical expertise to operate these cells had to be developed. A short account of the utilization and characteristics of the cells is also given, with a special emphasis in the pressure determination and low temperature behavior.

The sample space inside a DAC is typically limited to a few tenth of microns in thickness, and less than a millimeter in diameter. A pair of focusing neutron supermirror guides were used to enhance the neutron flux at the sample position, increasing the signal intensity by a factor 20. An instrumental module was built to accommodate the neutron guides in the ANTARES beamline at the Maier-Leibnitz Zentrum (MLZ). The mounting and aligning procedures are described in detail as well as the data acquisition. The test experiments and simulations carried out to characterize the instrument are also presented. The use of the enhanced ND module allows for an increase in the signal to noise ratio by an order of magnitude with the same measurement time. A proof of principle experiment shows that ND can be used to investigate the shielding effect of a superconductor sample, small enough to fit inside a DAC.

In chapter 3, two members of the chromium spinel family, are investigated. High pressure neutron depolarization measurements were performed on the ferromagnetic semiconductor $HgCr_2Se_4$, where the linear decrease of the Curie temperature is expected to end in a quantum critical point (QCP) at 10 GPa. Interestingly a more complex phase diagram emerged, where a low temperature re-entrant phase appeared at pressures as low as 2.8 GPa, which is associated with AFM order. Moreover, the reentrant FM phase seems to weaken at higher pressures, turning into an incipient FM (IFM), where depolarization only appears when sufficient external magnetic field is applied.

The high pressure state of $HgCr_2Se_4$ is very similar to what was observed in the parent compound $HgCr_2S_4$ at ambient pressure. Although this compound has a large positive Cure-Weiss temperature of 142 K, it has an AFM ground state below 22 K. Detailed magnetization and ac susceptibility measurements were also performed on $HgCr_2S_4$. The field dependent phase diagram was carefully mapped. Additionally, spin clustering was observed at 114 K. This feature, also present above ferromagnetic order in $CdCr_2S_4$, is related to the dynamic off centering of the chromium ions, and is believe to play an important role in breaking the cubic symmetry of the compounds enabling, for instance, ferroelectric order. The results are discussed in detail within the framework of the chromium spinel family.

Applying pressure to $HgCr_2Se_4$ allowed to retrieve the different ground states observed in the spinel family, strongly suggesting that the same exchange mechanism is in place within the whole series. The decrease of the lattice parameter under pressure in $HgCr_2Se_4$, even including thermal contraction and bond angle changes, is not sufficient to explain the AFM ground state. We propose that the reason $HgCr_2S_4$ orders antiferromagnetically despite having a large positive Curie-Weiss temperature is due to tetragonal transitions (or distortions) occurring at low temperatures, and that a similar phenomenon occurs to $HgCr_2Se_4$ under pressure. The dynamic off-centering of the chromium ions, observed in $HgCr_2S_4$ can also be related to the structural instability and is potentially present in other elements of the series. The dynamic lattice distortions are of great interest as they are likely enabling the ferroelectric properties observed in these compounds, further expanding the functionality of chromium spinel based devices. Finally, it was proposed that a rapidly fluctuating FM order, where external magnetic field slows down the system rendering it almost identical to a conventional FM at sufficiently high fields, would fit the experimental observations of the IFM phase.

Chapter 4 reports our studies of the pressure and current induced phase transitions in the AFM Mott insulator Ca_2RuO_4. This compound is characterized by a highly distorted single layered-perovskite structure. Interestingly, despite the stark difference between pressure and current control parameters, both seem to lead the sample through similar structural transitions characterized by a first order transition into a new elongated phase, and the reduction of the tilt angles of the RuO_4 octahedra. High pressure neutron depolarization measurements revealed a hitherto unknown phase in the mixed structural region between 0.5 and 2 GPa with a critical temperature of 10 K. This new phase is characterized by strong FM correlations, and a larger ordered moment as compared to the itinerant FM phase observed previously.

The temperature dependence of the magnetization and electrical resistivity of Ca_2RuO_4, were also measured simultaneously under different applied current densities with help of a vibrating sample magnetometer and a helium flow cryostat. The onset of a gradual decrease of the Néel temperature as a function of current density was observed below 0.4 A/cm^2. The resistivity is strongly reduced under current, especially at low temperatures, but no sign of a first order

insulator to metal transition were observed up to a current density of $20\,\mathrm{A/cm^2}$. The activation energy, extracted from the slope of the resistivity at room temperature, decreases under current. We propose that in addition to the closing of the band gap, a current induced promotion of charge carriers seems to be in place to explain the measured resistivity profiles. The exact mechanism is not clear, but it is likely to be related to a reorganization of the orbital population that accompanies the tilting and rotation of the RuO_6 octahedra known to occur under current.

Publications

1. **An ultra-low temperature scanning Hall probe microscope for magnetic imaging below 40 mK**
   Özgür Karcı, Julian O. Piatek, Pau Jorba, Münir Dede, Henrik M. Rønnow, and Ahmet Ora
   Review of Scientific Instruments **85**, 103703 (2014)

2. **High-resolution neutron depolarization microscopy of the ferromagnetic transitions in Ni_3Al and $HgCr_2Se_4$ under pressure**
   Pau Jorba, Michael Schulz, Daniel S. Hussey, Muhammad Abir, Marc Seifert, Vladimir Tsurkan, Alois Loidl, Christian Pfleiderer, Boris Khaykovich
   Journal of Magnetism and Magnetic Materials **475**, 176–183 (2019)

3. **Unique Crystal Structure of Ca_4RuO_4 in the Current Stabilized Semimetallic State**
   J. Bertinshaw, N. Gurung, P. Jorba, H. Liu, M. Schmid, D. T. Mantadakis, M. Daghofer, M. Krautloher, A. Jain, G. H. Ryu, O. Fabelo, P. Hansmann, G. Khaliullin, C. Pfleiderer, B. Keimer, and B. J. Kim
   Physical Review Letters **123**, 137204 (2019)

Acknowledgments

I would like to acknowledge here several people that have, in one way or another, through their advice, suggestions, work, or support of any kind, helped me to complete this thesis.

- Christian Pfleiderer trusted in my abilities as an experimental scientist to carry on and expand the high pressure research in his group. I am ever grateful for his guidance and support and the confidence he showed on my work these last years. As a supervisor he creates a great work atmosphere were you feel like you can talk your mind.

- Peter Böni shared with me some of his extensive knowledge on neutron instrumentation and the physics of polarized neutrons. Additionally he provided the parabolic neutron guides from SwissNeutronics, they became a key element of the experimental setup.

- Astrid Schneidewind mentored me during the first years of my thesis. From her I could learn specific scientific knowledge like inelastic neutron scattering, but also how to organize and plan my research and reflect about a career in science.

- Jim Schilling is a never ending source of knowledge on high pressure physics. I wish he would have been around since the beginning of my thesis, my learning curve would had probably been much steeper. I am grateful for his support, and the opportunities he offered me sharing his connections in the high pressure community.

- Stuart Gilder and Rudi Hackl introduced me to diamond anvil cells and took time to guide me in the right direction during my first year.

- Christoph Morkel helped me with some theoretical aspects of neutron scattering.

- All my colleagues (E51 and former E21) were part of the great work atmosphere and the companionship that so many times spilled beyond work hours. Coffee breaks, discuss data, plan a barbecue, help with the measurement software, birthday cake, beamtime in the reactor, poker night, transfer helium, football games, 'I have a couple of questions', Oktoberfest days, practice presentations, conference trips, hiking/skiing trips, sample changes, afterwork beers, sample loading, etc... Jan Spallek, Marko Halder, Steffen Säubert, Georg Benka, Felix Rücker, Alfonso Chacón, Franz Haslbeck, Philipp Schmakat, Marc Seifert,

Andreas Bauer, Christian Franz, Wolfgang Simeth, Anh Tong, Alexander Regnat, Christopher Schnarr, Christoph Duvinage, Jonathan Leitner, Grace Causer, Alexander Engelhardt, Nico Huber, Christian Oberleitner, Markus Kleinhans, Andreas Wendl, Marc Wilde, Michael Wagner, Robert Ritz, Tim Adams, Jonas Kindervater, Anna Kusmartseva, Georg Brandl, Tommy Reinmann, Tobias Neuwirth, and many more... Thank you all for your help and friendship. So many good memories!

- The entire staff at the ANTARES beamline of the MLZ reactor who assisted me during countless days of beamtime. Michael Schulz not only organized all necessary means for the measurements but was also a constant source of information on neutron depolarization. Phlipp Schmakat spent many hours of beamtime giving me hands on experience. Dominik Bausenwein and Elbio Calzada were very helpful with the technical aspects when designing the neutron guides module.
- The central workshop of the physics department made an excellent job manufacturing the diamond anvil cells. Manfred Pfaller and Manfred Reiter helped me during the conception and design process and put the resources of the workshop on the complex task of manufacturing diamond anvil cells. Norbert Heimerl and his staff at the precision mechanics, as well as Michael Novotny and many more technicians of the central workshop, spent hours working on my intricate technical drawings with increasingly tightening tolerances.
- The staff at the Crystal laboratory of the physics department who helped me with aligning and cutting the single crystalline samples I measured during my thesis. Susanne Mayr and Katarzyna Danielewicz very patiently dealt with my constant demands of smaller and smaller samples.
- Giacomo Pesche, whom I met during the Hercules school, shared with me his wide experience operating diamond anvil cells as a geologist. His insights gave me the confidence to use the newly built cells at the beginning of my second year, no broken diamond would stop me.
- To the ODE instrument scientists at the SOLEIL Synchrotron that assisted me during a week long high pressure XMCD experiment. Special thanks to Lucie Nataf who helped me with the high pressure instrumentation and the whole measurement process, and even brought me chocolate to withstand the long nights alone.
- Alois Loidl and Vladimir Tsurkan contributed their expertise with the chromium spinels. Vladimir synthesizes the valuable single crystalline chromium spinel samples.
- Bernhard Keimer and the members of his group working on the calcium ruthenates, in particular Joel Bertinshaw and Namrata Gurung. As part of our collaboration, I had many discussions with Joel and Namrata on the physics and experimental challenges of investigating current induced and pressure induced phase transitions in $CaRuO_4$.
- My partner and life companion Sabine was always there to cheer me up and motivate me through the ups and downs. Thank you for your support and care!
- Mònica and Rafael, my parents. My siblings and me were raised with care and love. My parents supported my education all along the way encouraging me to follow my own goals. They both have been role models and a source of inspiration along the way. This is also their success. Gràcies per tot!

Bibliography

[1] N. F. Mott and R. Peierls, Discussion of the paper by de Boer and Verwey, Proc. Phys. Soc. **49**, 72 (1937).

[2] B. Brandow, Theory of Mott Insulators, in *Narrow-Band Phenomena—Influence of Electrons with Both Band and Localized Character*, edited by J. C. Fuggle, G. A. Sawatzky, and J. W. Allen (Springer US, 1988) p. 97.

[3] R. Blatt and D. Wineland, Entangled states of trapped atomic ions, Nature **453**, 1008 (2008).

[4] S. Sachdev, Quantum phase transitions, in *Handbook of Magnetism and Advanced Magnetic Materials* (American Cancer Society, 2007).

[5] M. Vojta, Quantum phase transitions, Rep. Prog. Phys. **66**, 2069 (2003).

[6] C. Pfleiderer, Why first order quantum phase transitions are interesting, J. Phys.: Condens. Matter **17**, S987 (2005).

[7] M. E. Fisher, The theory of equilibrium critical phenomena, Rep. Prog. Phys. **30**, 615 (1967).

[8] K. G. Wilson, The renormalization group and critical phenomena, Rev. Mod. Phys. **55**, 583 (1983).

[9] G. R. Stewart, Non-fermi-liquid behavior in d- and f-electron metals, Rev. Mod. Phys. **73**, 797 (2001).

[10] C. Pfleiderer, Superconducting phases of f-electron compounds, Rev. Mod. Phys. **81**, 1551 (2009).

[11] N. D. Mathur, F. M. Grosche, S. R. Julian, I. R. Walker, D. M. Freye, R. K. W. Haselwimmer, and G. G. Lonzarich, Magnetically mediated superconductivity in heavy fermion compounds, Nature **394**, 39 (1998).

[12] G. R. Stewart, Unconventional superconductivity, Adv. Phys. **66**, 75 (2017).

[13] P. Gegenwart, Q. Si, and F. Steglich, Quantum criticality in heavy-fermion metals, Nature Phys **4**, 186 (2008).

[14] S. Nakatsuji, D. Hall, L. Balicas, Z. Fisk, K. Sugahara, M. Yoshioka, and Y. Maeno, Heavy-mass Fermi liquid near a ferromagnetic instability in layered ruthenates, Phys. Rev. Lett. **90**, 137202 (2003).

[15] D. Moroni-Klementowicz, M. Brando, C. Albrecht, W. J. Duncan, F. M. Grosche, D. Grüner, and G. Kreiner, Magnetism in $Nb_{1-y}Fe_{2+y}$: Composition and magnetic field dependence, Phys. Rev. B **79**, 224410 (2009).

[16] Y. Shimizu, D. Braithwaite, B. Salce, T. Combier, D. Aoki, E. N. Hering, S. M. Ramos, and J. Flouquet, Unusual strong spin-fluctuation effects around the critical pressure of the itinerant ising-type ferromagnet URhAl, Phys. Rev. B **91**, 125115 (2015).

[17] S. Acharya, D. Dey, T. Maitra, and A. Taraphder, Quantum criticality associated with dimensional crossover in the iso-electronic series $Ca_{2-x}sr\_xruo\_4$\$, J. Phys. Commun. **2**, 075004 (2018).

[18] M. Brando, D. Belitz, F. M. Grosche, and T. R. Kirkpatrick, Metallic quantum ferromagnets, Rev. Mod. Phys. **88**, 025006 (2016).

[19] D. Belitz, T. R. Kirkpatrick, and J. Rollbühler, Tricritical behavior in itinerant quantum ferromagnets, Phys. Rev. Lett. **94**, 247205 (2005).

[20] A. P. Drozdov, P. P. Kong, V. S. Minkov, S. P. Besedin, M. A. Kuzovnikov, S. Mozaffari, L. Balicas, F. F. Balakirev, D. E. Graf, V. B. Prakapenka, E. Greenberg, D. A. Knyazev, M. Tkacz, and M. I. Eremets, Superconductivity at 250 K in lanthanum hydride under high pressures, Nature **569**, 528 (2019).

[21] I. Errea, F. Belli, L. Monacelli, A. Sanna, T. Koretsune, T. Tadano, R. Bianco, M. Calandra, R. Arita, F. Mauri, and J. A. Flores-Livas, Quantum crystal structure in the 250-kelvin superconducting lanthanum hydride, Nature **578**, 66 (2020).

[22] R. F. Smith, D. E. Fratanduono, D. G. Braun, T. S. Duffy, J. K. Wicks, P. M. Celliers, S. J. Ali, A. Fernandez-Pañella, R. G. Kraus, D. C. Swift, G. W. Collins, and J. H. Eggert, Equation of state of iron under core conditions of large rocky exoplanets, Nat Astron **2**, 452 (2018).

[23] J. S. Schilling, The use of high pressure in basic and materials science, J. Phys. Chem. Solids **59**, 553 (1998).

[24] V. C. Srivastava, Pressure dependence of ferromagnetic phase transitions of chromium chalcogenide spinels, J. Appl. Phys. **40**, 1017 (1969).

[25] T. Vojta, Disorder-induced rounding of certain quantum phase transitions, Phys. Rev. Lett. **90**, 107202 (2003).

[26] N. Kimura, N. Kabeya, H. Aoki, K. Ohyama, M. Maeda, H. Fujii, M. Kogure, T. Asai, T. Komatsubara, T. Yamamura, and I. Satoh, Quantum critical point and unusual phase diagram in the itinerant-electron metamagnet UCoAl, Phys. Rev. B **92**, 035106 (2015).

[27] M. I. Eremets, *High Pressure Experimental Methods* (Oxford University Press, 1996).

[28] A. Dewaele, P. Loubeyre, F. Occelli, O. Marie, and M. Mezouar, Toroidal diamond anvil cell for detailed measurements under extreme static pressures, Nat Commun **9**, 1 (2018).

[29] A. Furrer, J. Mesot, and T. Strässle, *Neutron Scattering in Condensed Matter Physics* (World Scientific Publishing Company, 2009).

[30] P. A. Seeger and L. L. Daemen, Numerical solution of Bloch's equation for neutron spin precession, Nucl. Instr. Meth. Phys. Res. A **457**, 338 (2001).

[31] F. Mezei, Neutron spin echo: A new concept in polarized thermal neutron techniques, Z. Physik **255**, 146 (1972).

[32] P. Jorba, M. Schulz, D. S. Hussey, M. Abir, M. Seifert, V. Tsurkan, A. Loidl, C. Pfleiderer, and B. Khaykovich, High-resolution neutron depolarization microscopy of the ferromagnetic transitions in Ni_3Al and $HgCr_2Se_4$ under pressure, J. Magn. Magn. Mater. **475**, 176 (2019).

[33] H. Schober, An introduction to the theory of nuclear neutron scattering in condensed matter, J. Neutron Res. **17**, 109 (2014).

[34] O. Halpern and T. Holstein, On the passage of neutrons through ferromagnets, Phys. Rev. **59**, 960 (1941).

[35] M. T. Rekveldt, Study of ferromagnetic bulk domains by neutron depolarization in three dimensions, Z. Physik **259**, 391 (1973).

[36] I. Mirebeau, S. Itoh, S. Mitsuda, T. Watanabe, Y. Endoh, M. Hennion, and R. Papoular, Neutron depolarization in a reentrant spin-glass system: Amorphous Fe-Mn, Phys. Rev. B **41**, 11405 (1990).

[37] S. Mitsuda, H. Yoshizawa, and Y. Endoh, Neutron-depolarization studies on re-entrant spin glass, Phys. Rev. B **45**, 9788 (1992).

[38] H. W. Weber, Properties of the flux line lattice in hysteretic type II superconductors. II. neutron depolarization experiments, J Low Temp Phys **17**, 49 (1974).

[39] W. Treimer, O. Ebrahimi, and N. Karakas, Imaging of quantum mechanical effects in superconductors by means of polarized neutron radiography, Phys. Procedia **43**, 243 (2013).

[40] B. P. Toperverg and J. Weniger, On polarized neutron scattering from magnetized samples and the spin echo effect, Z. Physik B **71**, 95 (1988).

[41] B. P. Toperverg and J. Weniger, On neutron depolarization in magnetized media, Z. Phys. B **74**, 105 (1989).

[42] R. Rosman and M. T. Rekveldt, Neutron depolarization theory in the Larmor and the scattering approach, Z. Phys. B **79**, 61 (1990).

[43] M. Takahashi, S. Itoh, and M. Takeda, Neutron depolarization study on the magnetic critical fluctuation in Rb_2CrCl_4, J. Phys. Soc. Jpn. **64**, 268 (1995).

[44] A. N. Yaresko, Electronic band structure and exchange coupling constants in $a\mathrm{Cr}_2x_4$ spinels (a = Zn, Cd, Hg; x = O, S, Se), Phys. Rev. B **77**, 115106 (2008).

[45] P. K. Baltzer, P. J. Wojtowicz, M. Robbins, and E. Lopatin, Exchange interactions in ferromagnetic chromium chalcogenide spinels, Phys. Rev. **151**, 367 (1966).

[46] T. Rudolf, C. Kant, F. Mayr, J. Hemberger, V. Tsurkan, and A. Loidl, Spin-phonon coupling in antiferromagnetic chromium spinels, New J. Phys. **9**, 76 (2007).

[47] M. Wagner, *Suche Nach Topologisch Nichttrivialen Eigenschaften Stark Korrelierter Materialien*, PhD thesis, TU München Physik Department E21 (2014).

[48] S. Nakatsuji and Y. Maeno, Quasi-two-dimensional mott transition system $\mathrm{Ca}_{2-x}\mathrm{Sr}_x\mathrm{RuO}_4$, Phys. Rev. Lett. **84**, 2666 (2000).

[49] G. Cao, S. McCall, V. Dobrosavljevic, C. S. Alexander, J. E. Crow, and R. P. Guertin, Ground-state instability of the Mott insulator $\mathrm{Ca}_2\mathrm{RuO}_4$ impact of slight La doping on the metal-insulator transition and magnetic ordering, Phys. Rev. B **61**, R5053 (2000).

[50] F. Nakamura, T. Goko, M. Ito, T. Fujita, S. Nakatsuji, H. Fukazawa, Y. Maeno, P. Alireza, D. Forsythe, and S. R. Julian, From mott insulator to ferromagnetic metal: A pressure study of $\mathrm{Ca}_2\mathrm{RuO}_4$, Phys. Rev. B **65**, 220402 (2002).

[51] P. L. Alireza, F. Nakamura, S. K. Goh, Y. Maeno, S. Nakatsuji, Y. T. C. Ko, M. Sutherland, S. Julian, and G. G. Lonzarich, Evidence of superconductivity on the border of quasi-2d ferromagnetism in $\mathrm{Ca}_2\mathrm{RuO}_4$ at high pressure, J. Phys.: Condens. Matter **22**, 052202 (2010).

[52] F. Nakamura, M. Sakaki, Y. Yamanaka, S. Tamaru, T. Suzuki, and Y. Maeno, Electric-field-induced metal maintained by current of the Mott insulator $\mathrm{Ca}_2\mathrm{RuO}_4$, Sci. Rep. **3**, 2536 (2013).

[53] C. Sow, S. Yonezawa, S. Kitamura, T. Oka, K. Kuroki, F. Nakamura, and Y. Maeno, Current-induced strong diamagnetism in the mott insulator $\mathrm{Ca}_2\mathrm{RuO}_4$, Science **358**, 1084 (2017).

[54] F. Nakamura, Pressure-induced Mott transition and related novel quantum phenomena in $\mathrm{Ca}_2\mathrm{RuO}_4$, J. Phys. Soc. Jpn. **76**, 96 (2007).

[55] P. Steffens, O. Friedt, P. Alireza, W. G. Marshall, W. Schmidt, F. Nakamura, S. Nakatsuji, Y. Maeno, R. Lengsdorf, M. M. Abd-Elmeguid, and M. Braden, High-pressure diffraction studies on $\mathrm{Ca}_2\mathrm{RuO}_4$, Phys. Rev. B **72**, 094104 (2005).

[56] J. Bertinshaw, N. Gurung, P. Jorba, H. Liu, M. Krautloher, A. Jain, G. H. Ryu, O. Fabelo, G. Khaliullin, C. Pfleiderer, B. Keimer, and B. J. Kim, A Unique Crystal Structure of $\mathrm{Ca}_2\mathrm{RuO}_4$ in the Current Stabilized Metallic State, ArXiv (2018), arXiv:1806.06455 [cond-mat] .

[57] A. Jayaraman, Diamond anvil cell and high-pressure physical investigations, Rev. Mod. Phys. **55**, 65 (1983).

[58] J.-a. Xu and H.-k. Mao, Moissanite: A window for high-pressure experiments, Science **290**, 783 (2000).

[59] D. J. Dunstan and I. L. Spain, Technology of diamond anvil high-pressure cells: I. principles, design and construction, J. Phys. E: Sci. Instrum. **22**, 913 (1989).

[60] J.-a. Xu, H.-k. Mao, R. J. Hemley, and E. Hines, Large volume high-pressure cell with supported moissanite anvils, Rev. Sci. Instrum. **75**, 1034 (2004).

[61] S. Klotz, *Techniques in High Pressure Neutron Scattering* (CRC Press, 2016).

[62] A. Palmer, D. M. Silevitch, Y. Feng, Y. Wang, R. Jaramillo, A. Banerjee, Y. Ren, and T. F. Rosenbaum, Sub-kelvin magnetic and electrical measurements in a diamond anvil cell with in situ tunability, Rev. Sci. Instrum. **86**, 093901 (2015).

[63] A. Zerr, A. Diegeler, and R. Boehler, Solidus of earth's deep mantle, Science **281**, 243 (1998).

[64] A. P. Drozdov, M. I. Eremets, I. A. Troyan, V. Ksenofontov, and S. I. Shylin, Conventional superconductivity at 203 kelvin at high pressures in the sulfur hydride system, Nature **525**, 73 (2015).

[65] J. Thomasson, Y. Dumont, J.-C. Griveau, and C. Ayache, Transport measurements at low temperatures in a diamond anvil cell with helium as pressure medium, Rev. Sci. Instrum. **68**, 1514 (1997).

[66] S. Yomo and S. W. Tozer, Moissanite-anvil cells for the electrical transport measurements at low temperatures, J. Phys.: Conf. Ser. **215**, 012181 (2010).

[67] E. D. Marquardt, J. P. Le, and R. Radebaugh, Cryogenic Material Properties Database, in *Cryocoolers 11*, edited by R. G. Ross (Springer US, 2002) p. 681.

[68] A. Tong, *Building and Testing a Coil System for AC Susceptibility Measurements in a Diamond Anvil Pressure Cell*, Bachelor thesis, Technical University of Munich (2017).

[69] I. L. Spain and D. J. Dunstan, The technology of diamond anvil high-pressure cells: II. Operation and use, J. Phys. E: Sci. Instrum. **22**, 923 (1989).

[70] N. Tateiwa and Y. Haga, Evaluations of pressure-transmitting media for cryogenic experiments with diamond anvil cell, Rev. Sc. Instrum. **80**, 123901 (2009).

[71] K. Syassen, Ruby under pressure, High Press Res **28**, 75 (2008).

[72] G. J. Piermarini, S. Block, J. D. Barnett, and R. A. Forman, Calibration of the pressure dependence of the R1 ruby fluorescence line to 195 kbar, J. Appl. Phys. **46**, 2774 (1975).

[73] A. Regnat, *Low Temperature Poperties of CrB_2, MnB_2, and CuMnSb*, Thesis, TU München Physik Department E21 (2019).

[74] A. R. Rosenfield and B. L. Averbach, Effect of stress on the expansion coefficient, J. Appl. Phys. **27**, 154 (1956).

[75] R. J. Corruccini and J. J. Gniewck, *Thermal Expansion of Technical Solids at Low Temperatures: A Compilation from the Literature* (US. Gov. Printing Office, 1961).

[76] A. D. Krawitz, D. G. Reichel, and R. Hitterman, Thermal expansion of tungsten carbide at low temperature, J. Am. Ceram. Soc. **72**, 515 (1989).

[77] P. S. Gaal and D. E. Apostolescu, eds., *Thermal Conductivity 24: Thermal Expansion 12: Joint Conferences, October 26-29, 1997, Pittsburgh, Pennsylvania, Usa* (Technomic Pub. Co, 1999).

[78] F. Sigger, *Ruby fluorescence manometry at low temperatures*, Bachelor thesis, TU München Physik Department E21 (2013).

[79] K. Nakano, Y. Akahama, Y. Ohishi, and H. Kawamura, Ruby scale at low temperatures calibrated by the NaCl gauge: Wavelength shift of ruby R1 fluorescence line at high pressure and low temperature, Jpn. J. Appl. Phys. **39**, 1249 (2000).

[80] M. S. Torikachvili, S. K. Kim, E. Colombier, S. L. Bud'ko, and P. C. Canfield, Solidification and loss of hydrostaticity in liquid media used for pressure measurements, Rev. Sc. Instrum. **86**, 123904 (2015).

[81] M. Schulz, P. Böni, C. Franz, A. Neubauer, E. Calzada, M. Mühlbauer, B. Schillinger, C. Pfleiderer, A. Hilger, and N Kardjilov, Comparison of polarizers for neutron radiography, J. Phys.: Conf. Ser. **251**, 012068 (2010).

[82] M. Schulz, A. Neubauer, P. Böni, and C. Pfleiderer, Neutron depolarization imaging of the hydrostatic pressure dependence of inhomogeneous ferromagnets, Appl. Phys. Lett. **108**, 202402 (2016).

[83] N. Kardjilov, I. Manke, M. Strobl, A. Hilger, W. Treimer, M. Meissner, T. Krist, and J. Banhart, Three-dimensional imaging of magnetic fields with polarized neutrons, Nature Phys **4**, 399 (2008).

[84] M. Schulz, A. Neubauer, S. Masalovich, M. Mühlbauer, E. Calzada, B. Schillinger, C. Pfleiderer, and P. Böni, Towards a tomographic reconstruction of neutron depolarization data, J. Phys.: Conf. Ser. **211**, 012025 (2010).

[85] W. Treimer, Radiography and tomography with polarized neutrons, J. Magn. Magn. Mater. **350**, 188 (2014).

[86] N. Kardjilov, A. Hilger, I. Manke, M. Strobl, M. Dawson, and J. Banhart, New trends in neutron imaging, Nucl. Instr. Meth. Phys. Res. A **605**, 13 (2009).

[87] K. Lefmann and K. Nielsen, McStas, a general software package for neutron ray-tracing simulations, Neutron News **10**, 20 (1999).

[88] P. Willendrup, E. Farhi, and K. Lefmann, McStas 1.7 - a new version of the flexible Monte Carlo neutron scattering package, Physica B **350**, E735 (2004).

[89] M. Somayazulu, M. Ahart, A. K. Mishra, Z. M. Geballe, M. Baldini, Y. Meng, V. V. Struzhkin, and R. J. Hemley, Evidence for superconductivity above 260 K in lanthanum superhydride at megabar pressures, Phys. Rev. Lett. **122**, 027001 (2019).

[90] E. Snider, N. Dasenbrock-Gammon, R. McBride, M. Debessai, H. Vindana, K. Vencatasamy, K. V. Lawler, A. Salamat, and R. P. Dias, Room-temperature superconductivity in a carbonaceous sulfur hydride, Nature **586**, 373 (2020).

[91] K. Dwight and N. Menyuk, Magnetic interactions and spiral ground states in spinels, with application to $ZnCr_2Se_4$, Phys. Rev. **163**, 435 (1967).

[92] N. W. Grimes and E. D. Isaac, A simplified interpretation of the magnetic exchange interactions for chromium chalcogenide spinels, Philos. Mag. A **35**, 503 (1977).

[93] W. Bindloss, Anomalous exchangestriction in ferromagnetic pyrite and chromium chalcogenide spinel compounds, J. Appl. Phys. **42**, 1474 (1971).

[94] N. W. Grimes, 'Off-centre' ions in compounds with spinel structure, Philos. Mag. A **26**, 1217 (1972).

[95] J. Hemberger, P. Lunkenheimer, R. Fichtl, H.-A. K. von Nidda, V. Tsurkan, and A. Loidl, Relaxor ferroelectricity and colossal magnetocapacitive coupling in ferromagnetic $CdCr_2S_2$, Nature **434**, 364 (2005).

[96] V. Gnezdilov, P. Lemmens, Y. G. Pashkevich, C. Payen, K. Y. Choi, J. Hemberger, A. Loidl, and V. Tsurkan, Phonon anomalies and possible local lattice distortions in giant magnetocapacitive $CdCr_2S_4$, Phys. Rev. B **84**, 045106 (2011).

[97] S.-H. Lee, C. Broholm, W. Ratcliff, G. Gasparovic, Q. Huang, T. H. Kim, and S.-W. Cheong, Emergent excitations in a geometrically frustrated magnet, Nature **418**, 856 (2002).

[98] V. Tsurkan, J. Hemberger, A. Krimmel, H.-A. Krug von Nidda, P. Lunkenheimer, S. Weber, V. Zestrea, and A. Loidl, Experimental evidence for competition between antiferromagnetic and ferromagnetic correlations in $HgCr_2S_4$, Phys. Rev. B **73**, 224442 (2006).

[99] J. Hemberger, H.-A. K. von Nidda, V. Tsurkan, and A. Loidl, Large magnetostriction and negative thermal expansion in the frustrated antiferromagnet $ZnCr_2Se_4$, Phys. Rev. Lett. **98**, 147203 (2007).

[100] S. Weber, P. Lunkenheimer, R. Fichtl, J. Hemberger, V. Tsurkan, and A. Loidl, Colossal magnetocapacitance and colossal magnetoresistance in$HgCr_2S_4$, Phys. Rev. Lett. **96**, 157202 (2006).

[101] J. M. Hastings and L. M. Corliss, Magnetic structure and metamagnetism of $HgCr_2S_4$, J. Phys. Chem. Solids **29**, 9 (1968).

[102] L. C. Chapon, P. G. Radaelli, Y. S. Hor, M. T. F. Telling, and J. F. Mitchell, Non-collinear long-range magnetic ordering in $HgCr_2S_4$, arXiv (2006), arXiv:cond-mat/0608031 .

[103] A. Slebarski, D. Konopka, and A. Chełkowski, X-ray investigations of temperature dependence of the lattice constants of $HgCr_2S_4$, $HgCr_2Se_4$, $CdCr_2S_4$, $CdCr_2Se_4$, $ZnCr_2Se_4$ polycrystals in a temperature range from 70 K to the decomposition temperature, Phys Lett A **50**, 333 (1974).

[104] H. W. Lehmann and F. P. Emmenegger, Crystal growth, semiconducting and optical properties of ferromagnetic $HgCr_2Se_4$, Solid State Commun. **7**, 965 (1969).

[105] T. Arai, M. Wakaki, S. Onari, K. Kudo, T. Satoh, and T. Tsushima, Magnetoabsorption in single-crystal $HgCr_2Se_4$, J. Phys. Soc. Jpn. **34**, 68 (1973).

[106] N. I. Solin, V. V. Ustinov, and S. V. Naumov, Colossal magnetoresistance of the inhomogeneous ferromagnetic semiconductor $HgCr_2Se_4$, Phys. Solid State **50**, 901 (2008).

[107] G. Xu, H. Weng, Z. Wang, X. Dai, and Z. Fang, Chern semimetal and the quantized anomalous hall effect in $HgCr_2Se_4$, Phys. Rev. Lett. **107**, 186806 (2011).

[108] T. Guan, C. Lin, C. Yang, Y. Shi, C. Ren, Y. Li, H. Weng, X. Dai, Z. Fang, S. Yan, and P. Xiong, Evidence for half-metallicity in n-type $HgCr_2Se_4$, Phys. Rev. Lett. **115**, 087002 (2015).

[109] I. Efthimiopoulos, A. Yaresko, V. Tsurkan, J. Deisenhofer, A. Loidl, C. Park, and Y. Wang, Pressurizing the $HgCr_2Se_4$ spinel at room temperature, Appl. Phys. Lett. **104**, 011911 (2014).

[110] C. Magen, P. A. Algarabel, L. Morellon, J. P. Araújo, C. Ritter, M. R. Ibarra, A. M. Pereira, and J. B. Sousa, Observation of a Griffiths-like phase in the magnetocaloric compound $Tb_5Si_2Ge_2$, Phys. Rev. Lett. **96**, 167201 (2006).

[111] G. N. P. Oliveira, A. M. Pereira, A. M. L. Lopes, J. S. Amaral, A. M. dos Santos, Y. Ren, T. M. Mendonça, C. T. Sousa, V. S. Amaral, J. G. Correia, and J. P. Araújo, Dynamic off-centering of Cr^{3+} ions and short-range magneto-electric clusters in $CdCr_2S_4$, Phys. Rev. B **86**, 224418 (2012).

[112] P. Schmakat, *Neutron Depolarisation Measurements of Ferromagnetic Quantum Phase Transitions*, PhD thesis, TU München Physik Department E21 (2015).

[113] C. Kittel, *Introduction to Solid State Physics*, eighth ed. (2005).

[114] S.-D. Guo and B.-G. Liu, Density-functional-theory investigation of pressure induced semiconductor–metal transitions in the ferromagnetic semiconductor $HgCr_2Se_4$, J. Phys.: Condens. Matter **24**, 045502 (2012).

[115] I. Efthimiopoulos, *High-Pressure Structural and Spectroscopic Studies on Transition Metal Compounds*, Ph.D. thesis, Aristotle University of Thessaloniki (2010).

[116] I. Efthimiopoulos, A. Yaresko, V. Tsurkan, J. Deisenhofer, A. Loidl, C. Park, and Y. Wang, Multiple pressure-induced transitions in $HgCr_2S_4$, Appl. Phys. Lett. **103**, 201908 (2013).

[117] I. Efthimiopoulos, Z. T. Y. Liu, M. Kucway, S. V. Khare, P. Sarin, V. Tsurkan, A. Loidl, and Y. Wang, Pressure-induced phase transitions in the $CdCr_2Se_4$ spinel, Phys. Rev. B **94**, 174106 (2016).

[118] I. Efthimiopoulos, Z. T. Y. Liu, S. V. Khare, P. Sarin, V. Tsurkan, A. Loidl, D. Popov, and Y. Wang, Structural transition in the magnetoelectric $ZnCr_2Se_4$ spinel under pressure, Phys. Rev. B **93**, 174103 (2016).

[119] I. Efthimiopoulos, T. Lochbiler, V. Tsurkan, A. Loidl, V. Felea, and Y. Wang, Structural behavior of $ZnCr_2S_4$ spinel under pressure, J. Phys. Chem. C **121**, 769 (2017).

[120] C. Kittel, Model of exchange-inversion magnetization, Phys. Rev. **120**, 335 (1960).

[121] R. Valdés Aguilar, A. B. Sushkov, Y. J. Choi, S.-W. Cheong, and H. D. Drew, Spin-phonon coupling in frustrated magnet $CdCr_2O_4$, Phys. Rev. B **77**, 092412 (2008).

[122] C. Kant, Optical phonons, spin correlations, and spin-phonon coupling in the frustrated pyrochlore magnets $CdCr_2O_4$ and $ZnCr_2O_4$, Phys. Rev. B **80** (2009), 10.1103/PhysRevB.80.214417.

[123] H. Ueda, H. Mitamura, T. Goto, and Y. Ueda, Successive field-induced transitions in a frustrated antiferromagnet $HgCr_2O_4$, Phys. Rev. B **73**, 094415 (2006).

[124] J.-H. Chung, Y. S. Song, S. Park, H. Ueda, Y. Ueda, and S.-H. Lee, Incommensurate spin spiral of the geometrically-frustrated antiferromagnet $CdCr_2O_4$, J Korean Phys Soc **62**, 1900 (2013).

[125] M. C. Kemei, P. T. Barton, S. L. Moffitt, M. W. Gaultois, J. A. Kurzman, R. Seshadri, M. R. Suchomel, and Y.-I. Kim, Crystal structures of spin-Jahn–Teller-ordered $MgCr_2O_4$ and $ZnCr_2O_4$, J. Phys.: Condens. Matter **25**, 326001 (2013).

[126] F. Yokaichiya, A. Krimmel, V. Tsurkan, I. Margiolaki, P. Thompson, H. N. Bordallo, A. Buchsteiner, N. Stüßer, D. N. Argyriou, and A. Loidl, Spin-driven phase transitions in $ZnCr_2Se_4$ and $ZnCr_2S_4$ probed by high-resolution synchrotron x-ray and neutron powder diffraction, Phys. Rev. B **79**, 064423 (2009).

[127] M. Hidaka, M. Yoshimura, N. Tokiwa, J. Akimitsu, Y. J. Park, J. H. Park, S. D. Ji, and K. B. Lee, Structural modulation induced by the incommensurate antiferromagnetic phase transitionin $ZnCr_2Se_4$, Phys. Status Solidi B **236**, 570 (2003).

[128] X. L. Chen, Z. R. Yang, W. Tong, Z. H. Huang, L. Zhang, S. L. Zhang, W. H. Song, L. Pi, Y. P. Sun, M. L. Tian, and Y. H. Zhang, Study of negative thermal expansion in the frustrated spinel $ZnCr_2Se_4$, J. Appl. Phys. **115**, 083916 (2014).

[129] E. S. Božin, C. D. Malliakas, P. Souvatzis, T. Proffen, N. A. Spaldin, M. G. Kanatzidis, and S. J. L. Billinge, Entropically stabilized local dipole formation in lead chalcogenides, Science **330**, 1660 (2010).

[130] Y. Maeno, S. Nakatsuji, and S. Ikeda, Metal–insulator transitions in layered ruthenates, Mater. Sci. Eng., B **63**, 70 (1999).

[131] Y. Maeno, H. Hashimoto, K. Yoshida, S. Nishizaki, T. Fujita, J. G. Bednorz, and F. Lichtenberg, Superconductivity in a layered perovskite without copper, Nature **372**, 532 (1994).

[132] R. Okazaki, Y. Nishina, Y. Yasui, F. Nakamura, T. Suzuki, and I. Terasaki, Current-induced gap suppression in the mott insulator Ca_2RuO_4, J. Phys. Soc. Jpn. **82**, 103702 (2013).

[133] D. G. Porter, V. Granata, F. Forte, S. Di Matteo, M. Cuoco, R. Fittipaldi, A. Vecchione, and A. Bombardi, Magnetic anisotropy and orbital ordering in Ca_2RuO_4, Phys. Rev. B **98**, 125142 (2018).

[134] M. Braden, G. André, S. Nakatsuji, and Y. Maeno, Crystal and magnetic structure of Ca_2RuO_4: Magnetoelastic coupling and the metal-insulator transition, Phys. Rev. B **58**, 847 (1998).

[135] C. S. Alexander, G. Cao, V. Dobrosavljevic, S. McCall, J. E. Crow, E. Lochner, and R. P. Guertin, Destruction of the mott insulating ground state of Ca_2RuO_4 by a structural transition, Phys. Rev. B **60**, R8422 (1999).

[136] N. Shukla, M. Jerry, H. Nair, M. Barth, D. G. Schlom, and S. Datta, Electrically driven reversible insulator-metal phase transition in Ca_2RuO_4, in *2016 74th Annual Device Research Conference (DRC)* (2016) p. 1.

[137] J. Bertinshaw, N. Gurung, P. Jorba, H. Liu, M. Schmid, D. T. Mantadakis, M. Daghofer, M. Krautloher, A. Jain, G. H. Ryu, O. Fabelo, P. Hansmann, G. Khaliullin, C. Pfleiderer, B. Keimer, and B. J. Kim, Unique crystal structure of Ca_2RuO_4 in the current stabilized semimetallic state, Phys. Rev. Lett. **123**, 137204 (2019).

[138] S. Nakatsuji and Y. Maeno, Synthesis and single-crystal growth of $Ca_{2-x}Sr_xRuO_4$, J. Solid State Chem. **156**, 26 (2001).

[139] J. P. Carlo, T. Goko, I. M. Gat-Malureanu, P. L. Russo, A. T. Savici, A. A. Aczel, G. J. MacDougall, J. A. Rodriguez, T. J. Williams, G. M. Luke, C. R. Wiebe, Y. Yoshida, S. Nakatsuji, Y. Maeno, T. Taniguchi, and Y. J. Uemura, New magnetic phase diagram of $(Sr,Ca)_2RruO_4$, Nature Mater **11**, 323 (2012).

[140] L. Miao, P. Silwal, X. Zhou, I. Stern, J. Peng, W. Zhang, L. Spinu, Z. Mao, and D. Ho Kim, Itinerant ferromagnetism and geometrically suppressed metal-insulator transition in epitaxial thin films of Ca2RuO4, Appl. Phys. Lett. **100**, 052401 (2012).

[141] C. Sow, S. Yonezawa, S. Kitamura, T. Oka, K. Kuroki, F. Nakamura, and Y. Maeno, Retraction, Science **368**, 376 (2020).

[142] R. P. Guertin, J. Bolivar, G. Cao, S. McCall, and J. E. Crow, Negative differential resistivity in $Ca_3Ru_2O_7$: Unusual transport and magnetic coupling in a near-metallic system, Solid State Commun. **107**, 263 (1998).

[143] G. Cao, S. McCall, M. Shepard, J. E. Crow, and R. P. Guertin, Magnetic and transport properties of single-crystal Ca_2RuO_4: Relationship to superconducting Sr_2RuO_4, Phys. Rev. B **56**, R2916 (1997).

[144] S. Nakatsuji, V. Dobrosavljević, D. Tanasković, M. Minakata, H. Fukazawa, and Y. Maeno, Mechanism of hopping transport in disordered Mott insulators, Phys. Rev. Lett. **93**, 146401 (2004).

[145] R. M. Hill, Variable-range hopping, Phys. Status Solidi A **34**, 601 (1976).

[146] D. Sutter, C. G. Fatuzzo, S. Moser, M. Kim, R. Fittipaldi, A. Vecchione, V. Granata, Y. Sassa, F. Cossalter, G. Gatti, M. Grioni, H. M. Rønnow, N. C. Plumb, C. E. Matt, M. Shi, M. Hoesch, T. K. Kim, T.-R. Chang, H.-T. Jeng, C. Jozwiak, A. Bostwick, E. Rotenberg, A. Georges, T. Neupert, and J. Chang, Hallmarks of hunds coupling in the Mott insulator Ca_2RuO_4, Nat. Commun. **8**, 15176 (2017).

[147] J. Chaloupka and G. Khaliullin, Doping-induced ferromagnetism and possible triplet pairing in d^4 Mott insulators, Phys. Rev. Lett. **116**, 017203 (2016).

[148] T. Nakano and I. Terasaki, Giant nonlinear conduction and thyristor-like negative differential resistance in $BaIRo_3$ single crystals, Phys. Rev. B **73**, 195106 (2006).

[149] H. Rho, S. L. Cooper, S. Nakatsuji, H. Fukazawa, and Y. Maeno, Lattice dynamics and the electron-phonon interaction in Ca_2RuO_4, Phys. Rev. B **71**, 245121 (2005).